UNIVERSITY OF Southampton

Faculty of Engineering and Physical Sciences
University of Southampton

Sophia Maria Schillai

October 2018

Autonomous Underwater Vehicle Photographic Surveys in Complex Terrain

Thesis submitted for the degree of Doctor of Philosophy

University of Southampton
Abstract
Faculty of Engineering and Physical Sciences
Civil, Maritime & Environmental Engineering
Doctor of Philosophy
Autonomous Underwater Vehicle Photographic Surveys in Complex Terrain
by Sophia Maria Schillai

Photographic seafloor surveys are a valuable tool for studying ecosystems in the benthic zone. The vehicle carrying the camera must navigate at close distance to the subject. Flight style vehicles are energy efficient and thus capable of long, cost efficient surveys. Their limited manoeuvrability however brings a high risk of terrain collision.

To improve vehicle safety and survey success, the component of the altitude tracking sensor and control system with largest impact needs to be identified. Since tests on larger vehicles are expensive, tests for comparing different configurations in simulation and on small scale test platforms need to be established.

This thesis focuses on the two flight style vehicles Autosub6000 and Delphin2. Delphin2 is equipped with additional thrusters for hover capable actuation. Both vehicles detect obstacles in the vertical plane ahead with a mechanical scanning sonar. The terrain following behaviour of Autosub6000 is analysed using data from recorded missions in combination with case studies of a vertical plane simulation of Autosub6000. An altitude tracking method based on that of Autosub6000 is implemented on Delphin2, and studied in repeated experiments over a terrain step in a lake. The addition of the vertical thrusters for enhancing the altitude tracking is tested. To compare and evaluate experiment results, measures for vehicle risk and photographic survey success are introduced. Since vertical plane obstacle detection is identified as the limiting factor, improved detection methods for mechanically scanning sonars are developed.

The simulation is validated for studying terrain following behaviour, but uncertainties about the buoyancy change at depth, and terrain detection limit the accuracy for simulating a specific vehicle. The lake experiments with Delphin2 are repeatable, and show distinction between different configurations. The vehicle risk and mission success are estimated more accurately using the known terrain profile. The tests of hover capable actuation at speed show a negative impact on the flight style actuation. The studies of Autosub6000 experiments, simulations, and Delphin2 experiments highlight that the forwards looking detection has the largest impact on success and repeatability. The causes behind the noise responsible for false detections and reduced detection range are identified, and filters for removal are applied. A Gaussian terrain prediction method is developed, increasing the detection range and the reliability thereof.

Using these results, adjustments on existing systems can optimise survey outcomes, providing researchers with better data. To enhance flight style vehicles with thrusters, selective operation at lower speed is recommended. The development focus for future systems must be on the forwards detection and better estimation of buoyancy changes.

Contents

Declaration of Authorship

I, Sophia Maria Schillai, ORCID ID 0000-0003-3349-4169, declare that this thesis entitled 'Autonomous Underwater Vehicle Photographic Surveys in Complex Terrain'
and the work presented in it is my own and has been generated by me as the result of my own original research. I confirm that:

- The work was done wholly or mainly while in candidature for a research degree at this University.
- Where any part of this thesis has previously been submitted for a degree or any other qualification at this University or any other institution, this has been clearly stated.
- Where I have consulted the published work of others, this is always clearly attributed.
- Where I have quoted from the work of others, the source is always given. With the exception of such quotations, this thesis is entirely my own work.
- I have acknowledged all main sources of help.
- Where the thesis is based on work done by myself jointly with others, I have made clear exactly what was done by others and what I have contributed myself.
- Parts of this work have been published as:

Evaluation of terrain collision risks for flight style autonomous underwater vehicles
Schillai, S. M., Turnock, S. R., Rogers, E., Phillips, A. B., & Harris, C. A. (2016). In IEEE/OES Autonomous Underwater Vehicles (AUV) (pp. 311–318). Tokyo.

Experimental Analysis of Low Altitude Terrain Following for Hover Capable Flight Style Autonomous Underwater Vehicles
Schillai, S. M., Turnock, S. R., Rogers, E., & Phillips, A. B. submitted to Journal of Field Robotics.

Signature

Date

List of Figures

List of Tables

Symbolslist

A_{pseudo}	Pseudo altitude, distance parallel to the heave direction, measuring the height of the horizon in the vehicle fixed coordinate frame. Positive direction is in the positive heave direction.
A	Start/end position of the Testwood lake mission path.
A	Plan area e.g. of a wing, for lift and drag estimates.
BG	Distance between the Centre of Buoyancy and the Centre of Gravity in the z-direction. For stability this should be positive, with the centre of buoyancy above the centre of gravity.
B	Start/end position of the Testwood lake mission path.
B	Absolute sum of the buoyant forces.
C_{ai}	Correction factor for shortening the aspect ratio correction formula (see Equation 4.10).
Cd	Drag coefficient.
Cl	Lift coefficent.
CoB	Centre of Buoyancy.
D_z	Constant factor of the derrivative term of the depth PID controller.
D_θ	Constant factor of the derrivative term of the pitch PID controller.
D	Vehicle diameter.
$E_{battery}$	Electrical energy available from the battery.
F_D	Drag force.
F_L	Lift force.
$F_{Th,d}$	Thruster force demand.
F_{aft}	Force applied by the aft thruster.
F_{front}	Force applied by the front thruster.
F_{th}	Thruster force.
Fr	Froude number $Fr = \frac{u}{\sqrt{g \cdot l}}$.

I_z	Integral term of the depth PID controller.
I_{yy}	Moment of inertia.
L	Vehicle length.
M, M_i	Moments arount the pitch centre of rotation.
$M_L^{(N_\alpha x N_b)}$	Matrix of lookup values for removing the noise from internal reflections, for each of the bins N_b and the scan angles N_α.
$M_{\delta_s uu}, Z_{\delta_s uu}$	Moments and forces from sternplanes.
M_{aft}	Moment induced by the aft thruster.
M_{front}	Moment induced by the front thruster.
$M_{winglet}$	Moment applied by the winglets.
N_b	Number of bins of one sonar measurement.
N_α	Number of distinct angles in one mechanical scanning sonar scan.
P_z	Constant factor of the proportional term of the depth PID controller.
P_θ	Constant factor of the proportional term of the pitch PID controller.
$Range_{horizon}$	Horizon range, detection range at the largest sonar scan angle that still returns a valid detection.
$Rate_z$	Depth change rate.
$Rate_\theta$	Pitch change rate.
Re	Reynolds number $Re = \frac{u \cdot l}{\nu}$.
R	Detection range of the terrain in a sonar scan.
S_r	Reduction of the sliding threshold per metre range from the maximum applied threshold.
S_{th}	Detection threshold for the obstacle detecion in testwood lake. In case of the sliding threshold, the maximum applied threshold.
TC_z	Integration time of the integral term of the depth PID controller.
$WB, W - B$	Difference between the absolute sum of the gravitational and the absolute sum of the buoyant forces. Positive if the buyoyant forces are larger.
W	Absolute sum of the gravitational forces.
X, X_i	Force in the global frame x direction.
Z, Z_i	Force in the global frame Z direction.
$Z_{qu}, M_{\dot{q},etc.}$	Hydrodynamic derivatives.
$Z_{winglet}$	Force applied by the winglets.
$\Delta\Psi$	Heading error.

$\Delta\alpha$	Scan step angle, the angle between two consecutive measurements of the mechanical scanning sonar..
Δx_d	X distance at which an obstacle can first be detected.
Δx_u	Progress made by the vehicle in x-direction whilst new terrain is detected.
$\Delta x_{\alpha_{hz}}$	X-distance of the terrain detection at α_{hz}, the shallowest scan angle that still detects the terrain, relative to the position of the vehicle at the time of the measurement..
Δx_{gap}	Progress in x-direction made by the vehicle during one full scan from α_{max} to α_{min} and back again..
Δx_{gap}	Gap area between continuous scans of the seafloor due to the vehicle moving faster than the mechanical scanning sonar coverage of the seafloor during one scan..
$\Delta x_{scanned}$	Distance in x-direction that is scanned during one full sector scan of the mechanical scanning sonar.
α_w	Winglet angle of attack.
$\alpha_{horizon}, \alpha_{hz}$	Horizon angle, the largest sonar scan angle that still returns a valid detection. For flat terrain this is also the shallowest angle at which the terrain is detected..
α_{max}	Largest scan angle of the mechanical scanning sonar, pointing upwards..
α_{max}	Smallest scan angle of the mechanical scanning sonar, pointing downwards..
α	Angle between the vehicle surge direction and the sonar beam, a positive sonar scan angle points towards the water surface.
β	Angle of the fixed winglet.
δ_{sp}	Sternplane angle, position of the sternplane actuators. Zero sternplane angle is parallel to the surge direction, a positive sternplane angle induces forces towards the water surface (in the negative heave direction).
δs_d	Sternplane angle demand.
δt	Time increment.
$\dot{q}$	Pitch acceleration.
$\dot{w}$	Acceleration in the heave direction..
γ	Terrain slope angle.

ν	Kinematic viscosity.
ρ	Water density.
σ_{base}	Predefined value to calculate $\sigma_{predicted}$, the standard deviation for weighting the sonar return values around the expected detection range $r_{predicted}$. This value is also used if the scan angle α is close to 90^o..
$\sigma_{predicted}$	Standard deviation around the predicted terrain detection range $r_{predicted}$, used to weight the sonar return values. This standard deviation is calulcated from predefined base value of the standard deviation σ_{base}, to account for the scan angle..
σ^*_{sp}	Width of the sternplane transition zone.
σ^*_{th}	Width of the thruster transition zone.
$\theta_{horizon}$	Pitch angle of the vehicle when the horizon was last detected by the mechanical scanning sonar.
θ_{now}	Most recent pitch angle measurement.
θ_{steady}	Pitch angle of the AUV when it has reached a steady state, keeping a constant depth.
θ	Pitch angle, angle of the vehicle rotation around the sway axis. A positive pitch angle indicates motion towards the surface.
$\tilde{\theta}$	Pitch error.
$\tilde{a}$	Altitude error.
$\tilde{z}$	Depth error.
$\vec{m}(t)$	Mechanical scanning sonar measurement at time t.
$\vec{m}(t-i)$	The i-th mechanical scanning sonar measurement before the measurement at time t.
$\vec{m}^f(t)$	Sonar measurement vector $\vec{m}$ compensated for different noise sources due to internal reflections of the sonar beam..
$\vec{m}$	Sonar return values for each bin of a measurement, in vector form.
a_d	Altitude demand.
a_{pseudo}	Pseudo altitude.
a	Altitude, ditance between vehicle and terrain, measured orthogonal to the vehicle x-Axis.
$b_{pattern}$	Largest bin index for which a visible pattern due to reflections on the vehicle is apparent.

b	Index of one of the N_b bins per sonar beam, lower number indicates closer proximity to the sonar device.
g	Standard acceleration due to earth gravity, $g = 9.81\,\mathrm{m/s^2}$.
h_{max}	Height of the tallest step that can be correctly detected for a given altitude a, sonar detection range r_d and maximum scan angle α_{max}.
h_{min}	Height of the smallest step that can be detected for a given altitude a, sonar detection range r_d and minimum scan angle α_{min}.
h	Obstacle height for a step approximation of an obstacle.
l_{aft}	Leaver arm of the aft thruster.
l_{bin}	Length of one bin in a sonar scan, in metres. Converted from the discrete time intervals of the sonar detection, and the speed of sound in water..
l_{front}	Leaver arm of the front thruster.
l	Characteristic length, e.g. vehicle or control surface length.
$m_{\alpha,b}$	Individual mechanical scanning sonar measurement at a given bin index and angle.
m	Vehicle mass.
q	Pitch velocity.
r_{max}	Upper limit of the predicted detection range to account for zero degree angles and detection inaccuracy at long detection ranges..
$r_{predicted}$	Prediction of the likely terrain detection range of a measurement, based on the previous detection range..
t_{scan}	Time per scan step, the timespan the mechanical sonar needs to measure one sonar range and move the sonar head by one scan step..
u^*_{sp}	Vehicle surge speed at which the sternplane transition is centered for transition between flight- and hover style control.
u^*_{sp}	Mid-transition speed of the sternplane weight function, where the function value is 0.5.
u^*_{th}	Vehicle surge speed at which the thruster transition is centered for transition between flight- and hover-style control.
u^*_{th}	Mid-transition speed of the thruster weight function, where the function value is 0.5.

u	Surge velocity, vehicle velocity in the surge direction of the vehicle fixed reference frame. Positive indicates forwards direction.
w_{sp}	Sternplane weight function.
w_{sp}	Sternplane weight function for speed based actuation transition.
w_{th}	Thruster weight function.
w_{th}	Thruster weight function for speed based actuation transition.
w	Velocity in the heave direction, in the vehicle fixed frame.
z_d	Depth demand.
z	Depth.
$\vec{m}_I(t)$	Vector for the compensation of the scan angle independent noise, which is due to internal reflections bouncing of the terrain, the water surface, or other structures that are not in the path of the main beam. Vector rows are the compensation values for the individual bins..

Acronyms

3D	three dimensional.
ABS	Acrylonitrile Butadiene Styrene (a type of plastic).
ADC	Analog to Digital Converter.
ADCP	Acoustic Doppler Current Profiler.
AESA	Autonomous Ecological Surveying of the Abyss.
AUG	Autonomous Underwater Glider.
AUV	Autonomous Underwater Vehicle.
CoB	Centre of Buoyancy.
COT	Cost Of Transport.
CPU	Central Processing Unit.
D	Research cruise index prefix of RRS Discovery.
DVL	Doppler Velocity Log.
FOG	Fibre Optic Gyro.
GPS	Global Positioning System.
HIL	Hardware In the Loop.
HOV	Human Occupied Vehicle.
IMU	Intertial Measurement Unit.
INS	Inertial Navigation System.
JC	Research cruise index prefix of RRS James Cook.
laser	Light Amplification by Stimulated Emission of Radiation.
LR	Long Range.
MARS	Marine Autonomous and Robotic Systems.
MARS	MArine Robotics Simulator.
MATLAB	MATrix LABoratory, proprietary programming language and environment for numerical computation.
MPC	Model Predictive Control.
NACA	National Advisory Committee for Aeronautics.

NASA	National Aeronautics and Space Administration.
NED	North-East-Down (axis conventions for global reference frame).
NOAA	National Oceanic and Atmospheric Administration.
NOC	National Oceanography Centre.
OAS	Obstacle Avoidance System.
PC	Personal Computer.
PHINS	Photonic Intertial Navigation System.
PID	Proportional Integral Derivative.
RAM	Random-Access Memory.
ROS	Robot Operating System.
ROV	Remotely Operated Vehicle.
RPM	Rotations Per Minute.
RRS	Royal Research Ship.
SI	Système International (d'unités), International System of Units.
SLAM	Simultaneous Localization And Mapping.
sonar	SOund Navigation And Ranging.
TRN	Terrain Relative Navigation.
UTM	Universal Transverse Mercator (map projection).
UWSIM	UnderWater Simulator.
YAML	YAML Ain't Markup Language (originally Yet Another Markup Language).

Acknowledgements

This work is funded by the National Oceanography Centre and the University of Southampton.

Beyond this, I would like to thank the following individuals for their support: My supervisors Prof. Stephen R. Turnock, Prof. Eric Rogers, Dr. Maaten Furlong and Dr. Alexander B. Phillips, who not only supported me throughout this work, including two Delphin2 debugging and recovery emergencies at the lake side, but went above and beyond their responsibilities by also supporting me in organising the World Robotic Sailing Championship 2018. Sébastien Lemaire, Alistair R. P. Lynn and Tobias Schneider for their assistance in working at the lakeside with Delphin2. Dr. Catherine Harris for sound advice and a helpful hand on many occasions. Dr. John Downes for providing Delphin2 and me with a well equipped lab as a safe haven for repairs and recovery after (and some times in the middle of) experiments. Dr. Kantapon Tanakitkorn, for introducing me to the details of Delphin2 and the interesting discussions and meals shared outside of the lab or the towing tank. Dr. Nick Townsend and the Southampton Sailing Robot Team, particularly Yu Cao, Thomas Kluyver, and Sébastien Lemaire for three years of 'hanging out with a purpose' at lakes and the seaside. Club Killick, and Killick herself, for teaching me the basics of sailing. Everyone within my extended definition of family.

Chapter 1

Introduction

> We have better maps of Mars than of the oceans that cover 70% of our planet.
>
> *- almost everyone presenting maritime research to the public*

The above expression is as widely used, as it is true. The absorption of most of the electromagnetic spectrum in water is the reason why maps and photos of objects in space are easier to obtain than the equivalent in the oceans. This same property is the reason behind a wide spectrum of problems almost unique to robotic applications in water.

On the earth's surface and in space electromagnetic waves are relied upon for communication, navigation, mapping, and sensing; in water, by contrast, none of these methods are available. To obtain photos of the seafloor, a vehicle has to get very close to its subject, do so with limited communication to the surface, and without beforehand maps of the area in which it is navigating.

The ocean floor, often called the benthic zone in an ecological context, is home to a large number of organisms. Across most of the oceans it has never been mapped, the few existing studies of temporal variations highlight that significant variations occur, making regular mapping of larger areas a desired goal [Glover et al., 2010]. Whilst still struggling to learn more, mankind has an increasing effect on this system. From applications such as monitoring the adverse effects of climate change [Ling et al., 2016], managing food supply [Smale et al., 2012, Nishida et al., 2014a], or understanding the impact of mining activity at the seafloor [Nakajima et al., 2015], to understanding human and the planet's history, photographic surveys taken with AUVs can enhance existing approaches, reliably perform repeat surveys [Nakajima et al., 2015, Smale et al., 2012], and replace alternatives that are damaging to the survey area or that put human divers at risk [Smale et al., 2012].

For photographic surveys, the vehicle must come to within three to ten metres of the sea or lake bed to be able to sufficiently illuminate its subject and record photos thereof.

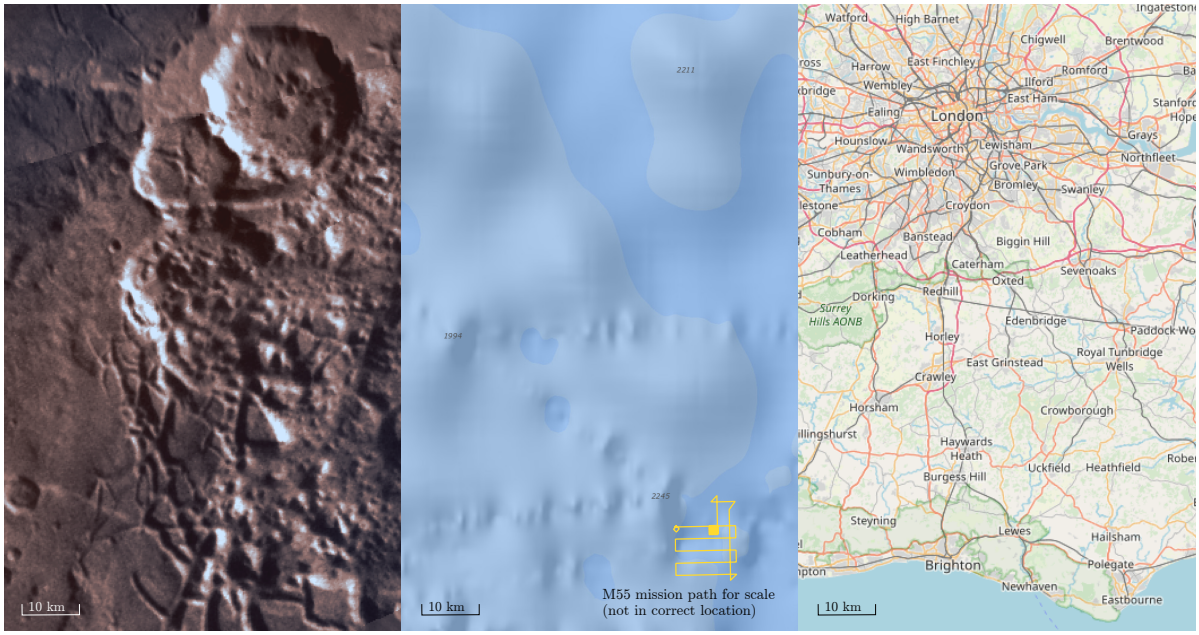

Figure 1.1: Contrasting map resolutions from Mars, the bottom of the North Atlantic Ocean, and, to give a land based reference, Southern England. All maps are at the same scale. The maps of Mars and the North Atlantic Ocean come directly from institutions researching these areas. In the seabed map, the higher resolution traces of a sonar map collected at sea can clearly be distinguished. Maps are provided by NASA [NASA], the NOAA [NOAA], and OpenStreetMap.org [OpenStreetMap] respectively.

In vehicle operation, terms from land based robot operation are often used, referring to the sea bed or lake bed "terrain", and describing the vehicle as "flying" over the terrain.

Ironically, the data underpinning global ocean maps are obtained from space, using satellites to measure gravitational effects of the seafloor on the water surface and create low resolution (as low as 5 km by 5 km per pixel) maps. Mapping and range measurements in water rely on sound, using sonar sensors that emit beam shaped acoustic waves and record the reflections of these waves returning from objects. Whilst seemingly similar to light, these acoustic beams interact with matter differently: for example, sound waves travel at much slower speeds than light waves. They cannot be formed in tight, laser-like beams, and often part of the beam passes through an object, whilst part of it is reflected. As a consequence of these differences, maps recorded from the water surface before launching an Autonomous Underwater Vehicle (AUV) are still not of a high enough resolution to determine safe vehicle trajectories whilst planning the mission on deck of the research vessel before deployment.

Underwater vehicles for photographic surveys can either be controlled from a ship by a tether that is permanently attached to the vehicle (towed or remotely operated vehicles) or they can be controlled using preprogrammed autonomous behaviours to reach and photograph the area of interest (autonomous underwater vehicles). Currently photo-

graphic surveys are mostly executed by towed vehicles or Remotely Operated Vehicles (ROVs), since the programmed autonomous behaviours have not yet reached the complexity of the decision making of the human operator and the endurance of such vehicles is not limited by battery capacity, since power can be supplied via the tether. However, ROVs also have some significant disadvantages: during ROV operations, the research ship cannot be used for other purposes, and the tether limits the vehicle speed, depth, and the area the vehicle can operate in for instance, under ice.

AUVs have the advantage that their speeds are not limited by a wires, and their operation is independent of the movement of a research ship. Currently, the areas not accessible to ROVs often also prove challenging for AUVs, but navigation has been demonstrated [McPhail et al., 2009]. Whilst they are not constrained by a tether, the software on the AUV needs to take over the role of the human controller. Since the vehicle cannot get energy through a tether either, the energy available for running the control systems and analysing the environment is limited to the batteries on board. The vehicle choice is essentially a choice between manouevrability and energy efficiency. Whilst the more energy efficient flight style AUVs both operate at higher speeds and have a higher endurance, their use in complex terrain is limited by their slow response to actuator actions and forwards sensing and planning capability.

Whereas other oceanographic data, like sonar maps, can be acquired from a relatively high altitude (100 m and above), the desired altitude for photographic surveys varies between 0.4 m and 12 m, depending on survey goals, available light sources, photographic equipment, and water quality [Marouchos et al., 2015, Bodenmann et al., 2013, Houts and Rock, 2015, Morris et al., 2014]. The scientifically interesting areas often lie in rough terrain, making it challenging to navigate an underwater vehicle without collision. Once a goal altitude has been decided, the vehicle must stay in a small band around this altitude, so that suitable light conditions and the camera field of view are maintained. Figure G.1 shows photos of the same species obtained at a variety of altitudes by the flight style AUV Autosub6000, illustrating the impact of small altitude changes on the photo quality, due to the attenuation of light in water.

Amongst autonomous underwater vehicles, three main propulsion styles can be distinguished: buoyancy engine propulsion along a sawtooth depth profile, flight style propulsion with a single thruster and control surfaces for pitch and yaw, and hover capable propulsion using only thrusters. Since the propulsion with buoyancy engines requires a continuous change in depth [Bachmayer et al., 2003], it is not suited for photographic surveys. Flight style AUVs (or 'cruising AUVs') are typically torpedo shaped, they have a forwards propulsion system and yaw, pitch and roll are controlled with sternplanes, movable surfaces that have airfoil shaped cross sections. Hover capable AUVs are typically box shaped and their movement is controlled by a larger number of thrusters pointing in different directions [Thornton et al., 2007]. Examples of the two propulsion styles are given in Figure 1.2. Further propulsion styles exist, but they are either not suitable or not widely used.

The energy consumption for propulsion is dominated by the number of thrusters, so

Flight style AUV Autosub6000.
Photo provided by the National Oceanography Centre, reproduced with permission.

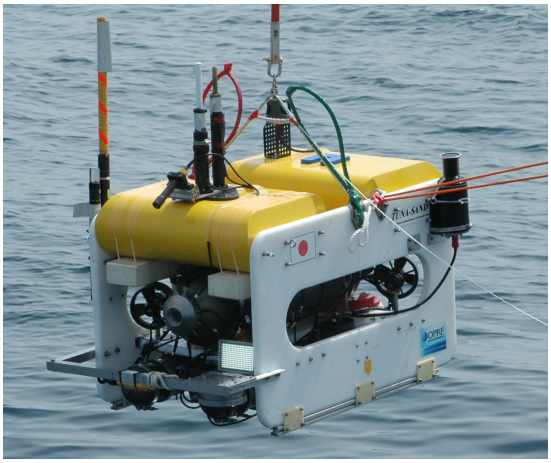

Hover capable AUV TUNA-SAND.
Image from [Nishida et al., 2014a], reproduced with permission.

Figure 1.2: Autosub6000 and TUNA-SAND, examples of hover capable and flight style vehilces.

flight style AUVs can generally deliver longer endurances. Using only one thruster for forwards propulsion also leads to less disturbance of the seafloor, allowing a better image quality. Flight style AUVs have successfully been used for photographic surveys [Houts et al., 2012, McPhail et al., 2010a] but their control for low altitude terrain following is challenging, since they need to maintain at a minimum speed to remain controllable [Burcher and Rydill, 1994].

When performing surveys at a low altitude, the AUV faces sensor, planning, and control challenges. Information about the terrain ahead must be obtained, the vehicle state relative to the terrain ahead must be determined, and the correct control actions for achieving the goal altitude or avoiding an obstacle must be chosen and applied. On flight style vehicles, this must all be done whilst maintaining a constant forwards speed. For Autosub6000, a 5.5 m long AUV, this speed is 1 m/s.

1.1 Aims, Objectives, and Work Plan

An increasing requirement, driven mainly by increasing scientific interest, is to undertake AUV surveys in more complex terrain, where one driver is that the biodiversity in such areas can be higher [Durden et al., 2015a]. This places additional demands on the AUV used, since, for example, gathering high quality photographic data requires very close following of the area of the sea bed concerned. To successfully undertake such a mission, measures to quantify the risks to the vehicle are required, and where possible changes to the operation, to limit or remove this critical operational factor.

Many currently available AUVs are rejected for such missions as it cannot be determined how high the risk to the vehicle is. The scientists involved ideally need to have information on the quality and quantity of photos that can be expected, and what effect a conservative terrain following strategy will have on this outcome. To reduce the data acquisition cost and to increase the areas where underwater photographic surveys can be conducted, it is of critical interest to make flight style AUVs, such as Autosub6000, capable of conducting photographic surveys in complex terrains. However, these energy efficient vehicles are limited by the missmatch between their manoeuvrabiliy frequency response and the terrain complexity.

The aim of this research is to develop new results and methods to increase the altitude tracking capabilities and applicability of AUVs for photographic surveys in more complex domains. To address this issue, the following general objectives will be pursued:

1. The development of measures for the vehicle collision risk and photographic survey success to enable quantitative analysis and comparison.
2. To establish key parameters of altitude tracking and understand the mechanims by which they impact the results of imaging surveys.
3. To identify the components of the altitude tracking control and sensor system where further development has the highest impact on improving survey success.

The work packages to address 1-3 above are:

i Analysis of the existing altitude tracking results and sensor data of the flight style AUV Autosub6000.

ii Development and validation of a vertical plane simulation of flight style altitude tracking close to terrain.

iii Determine the suitability of the Delphin2 AUV, a 2 m long scaled version of Autosub6000, as a test platform for altitude tracking with Autosub6000 and other flight style AUVs.

iv Design, validate, and implement a range of experiments to test different configurations of the altitude tracking system on the flight style, hover capable AUV Delphin2, and the repeatability thereof.

v Investigation into the feasibility of advanced controllers for altitude tracking.

1.2 Organisation of Thesis

This thesis is structured in four chapters, prior to concluding remarks followed by the references, appendices, and glossary.

Chapter 2 begins with a review of existing studies, analysing the demands and success factors of photographic surveys, the AUVs undertaking these studies, the sensors used for terrain detection and the information available on their altitude tracking strategies. Since often the altitude control is implemented as a depth control with a modified control demand input, controllers used for depth control on AUVs are included in the review.

This is followed by a detailed description of the flight style vehicle Autosub6000, and the smaller flight style, hover capable test platform Delphin2 in chapter 3. An emphasis is put on the systems relevant for undertaking altitude tracking missions, analysing altitude tracking performance, and simulating the vehicle in the vertical plane.

Chapter 4 introduces the methods used for analysing existing Autosub6000 mission data, simulating Autosub6000 altitude tracking in the vertical plane, and conducting lake experiments with Delphin2. The reference system and sign conventions used for all three approaches are specified, and numeric quantification methods for assessing the experimental data and the simulation results. The simulation implementation and the re-implementation of the altitude tracking method of Autosub6000 on Delphin2 are described. Finally the test locations and data processing steps of the experiments with Autosub6000 and Delphin2 are reported.

The results are presented in chapter 5, beginning with an overview of the altitude tracking data available from Autosub6000, using statistical analysis and mission plots to select missions for further analysis. Then, the Autosub6000 simulation is validated with test cases of increasing complexity. For each validation step, parameters of the vehicle are varied, giving further insights on the impact of these parameters on simulation accuracy and altitude tracking performance. The final test cases are based on Autosub6000 missions, comparing the simulation results with the actual mission data and investigating the vehicle performance during the experiment further through parameter variations in the simulation.
Next, the results of the Delphin2 experiments are analysed. Besides the altitude tracking analysis, similar to that used for Autosub6000, the lake experiments are analysed further. The advantages of repeated experiments over a known terrain are demonstrated, comparing the results of flight style and hover capable actuation and investigating if and how a flight style vehicle can profit from adding thrusters for vertical actuation. A bridge between the engineering perspective and the mission planner's considerations is created by extrapolating the results over a short terrain section to full scale missions.
Since all three analysis methods consistently highlight the terrain detection as the weakest link in the current state of the art, whether operating at depth or in shallow water, the efforts of improving altitude tracking are dedicated to analysing the requirements for reliable terrain detection, removing sources of noise from the data where possible, and increasing the detection reliability through a newly developed detection prediction based on Gaussian weighting.

Chapter 6 concludes this thesis, discusses how the results can directly be applied to mission planning, and suggests directions for future work.

Chapter 2

Current Photographic Survey Techniques

Operation close to the seabed requires an understanding of the terrain ahead in order to avoid collision. Considerations of Obstacle Avoidance Systems (OASs) using sonar can be found as early as 1987, in [Cyr, 1987] one proposed application of a sonar with 15 beams in an arc alignment is a "terrain and obstacle forward sonar in both horizontal and vertical space". At that time, photographic surveys were still a rarity, [Weinberg, 1981] includes photographic surveys in a comparison with other, manual, surveying techniques. Whilst the results were encouraging, at the time it was concluded that the complexity of photographic surveys was prohibitive.

Technology has since progressed. Now, almost 30 years later, the two techniques can be combined on AUVs, enabling large area surveys in previously inaccessible regions of the ocean floor.

Before going into the details of merging the technologies, this literature review first looks at the requirements of photographic surveys. This is followed by an overview of autonomous underwater vehicles, an overview of the sensors they use and an in-depth exploration of vehicles for which altitude tracking performance details are currently documented. Then available methods for mapping, and vehicle command and control developments are analysed.

Finally the current state of AUV simulations is looked into, to identify the different goals of simulating AUVs, what simulations exist, an which may be integrated in a study of vertical plane altitude tracking.

2.1 Photographic Surveys

The ocean floor, in an ecologic context often called the benthic zone, is a region of interest since it is home to a large number of organisms. For most of the oceans it has never been mapped at an adequate resolution. The few existing studies of temporal changes point out that more temporal changes than expected occur, making regular mapping of larger areas a desired goal [Glover et al., 2010].

Benthic surveys are undertaken for many reasons, including ground truthing sonar images, mapping of habitats, sediment transport, deposition or the location and activity of hydrothermal vents and volcanoes [Caress et al., 2008, Wynn et al., 2014]. This may occur for research purposes, for planning of human made structures or for monitoring human made structures and their impact on ecosystems.

Photographic surveys are a vital tool for surveying the ocean floor. The applications range from mapping and exploring ecosystems [Bodenmann et al., 2013, Morris et al., 2014], to monitoring the adverse effects of climate change [Ling et al., 2016], managing food supplysmale2012regional,nishida2014investigation, or understanding the impact of mining activity at the seafloor [Nakajima et al., 2015].

Compared to trawling methods or human diver surveys, the ocean floor is disturbed less by surveys with autonomous vehicles [Morris et al., 2014, Smale et al., 2012]. Studies find that the representation of species, especially those of smaller studies, is better [Morris et al., 2014] compared to trawling methods. Working in shallower water and comparing with divers, the performance was found to be dependant on species and fauna cover, which sometimes lead to human divers outperforming AUVs [Ling et al., 2016].

With hover capable AUVs, photographic surveys can already access more complex terrain than other sampling methods [Morris et al., 2014]. Since the specimen are recorded in their habitat, besides recording populations the photos can also be used to deduce details like group behaviour of fish [Nishida et al., 2014a].

[Wynn et al., 2014] highlights the special interest in extreme environments like volcanoes or hydrothermal vents, terrains that are difficult to navigate with obstacles that are often small in the vertical direction but bring a large change in ocean floor height.

For construction activities at the seafloor, information about the sea bed in that area is necessary for selecting a site and planning the construction [Hughes et al., 2014]. Maps for this purpose can profit from photographic surveys, to get detailed information about the sediment types, and for ground truthing of sonar side scan images. Once structures are created, they need close monitoring. Additionally scientific interest can arise in how habitats are influenced by the creation of human made structures [Nakajima et al., 2015].

From a mission planning perspective, photographic surveys vary widely in water depth and size of the survey area, from grids over a $25\,\mathrm{m} \times 25\,\mathrm{m}$ area at 15 m depth and less [Smale et al., 2012], to large scale grids over a $10\,\mathrm{km} \times 10\,\mathrm{km}$ area at 5000 m depth [Morris et al., 2014]. All photographic surveys have in common that a very low vehicle altitude

needs to be maintained, determined by the required image resolution, available means of lighting [Bodenmann et al., 2013, Morris et al., 2014, Otsuki et al., 2016], and the attenuation and scattering qualities of the water in that area [Jaffe, 1990, Akkaynak et al., 2017]. In practice the goal altitudes vary between 12 m and 0.4 m[Marouchos et al., 2015, Bodenmann et al., 2013].
The vehicle path planning is typically split between the vertical and horizontal plane. In the horizontal plane, the waypoints are usually evenly spaced in a grid, or following other patterns composed of long linear paths, as required by sampling strategies for habitat mapping or for a large area reconstruction [Weinberg, 1981, Smale et al., 2012, Morris et al., 2014, Foster et al., 2014], and though recent work investigates more complex path planning in the horizontal plane [Otsuki et al., 2016], a separation of horizontal waypoints and vertical altitude goals remains.
The success of a photographic survey is sometimes expressed through the number of photos with sufficient photos that were acquired [Morris et al., 2014], or, after further processing, the total area that could be reconstructed above a given resolution [Otsuki et al., 2016]. Due to the high cost associated with ship time, the mission success improves if the number of suitable photos per ship time spent can be increased. One of the advantages of using autonomus vehicles is that ship time during deployment can be used for other work as well, so of the overall mission time of a vehicle, the deployment and recovery time is a key factor. As a result, increasing the number of photos per battery charge can have a positive effect on the associated cost, even in cases where the number of photos per time unit might reduce.

2.2 Photo Quality

The quality of a photo taken underwater is determined by the area it covers, the resolution of the photo, how well it is illuminated, how sharp it is, how strong the contrast in the image is, and how much noise is present [Morris et al., 2014, Corchs and Schettini, 2010]. For connecting multiple photos in a larger scene, or reconstructing larger areas, a minimum image overlap may also be required. Figure 2.1 gives an overview of these quality factors, and how they are impacted by mission parameters. The small arrows next to the quality factors indicate if the goal is to maximise (upwards arrow) or minimise (downwards arrow) this factor. The vehicle design, vehicle equipment and mission plan aim to maximise the total area covered, ensure required photo overlap, and sufficient resolution, ilumination, sharpness, and contrast whilst reducing noise, so the species in question can be identified. Photo overlap and illumination also have an upper limit; a too large overlap is not required for reconstruction and indicates that a larger are could have been covered at a faster speed, while too much illumination will lead to over exposed images. However, these upper limits are rarely a problem so they were neglected to simplify 2.1.

In the second column of Figure 2.1, mission plan, vehicle design, and vehicle equipment

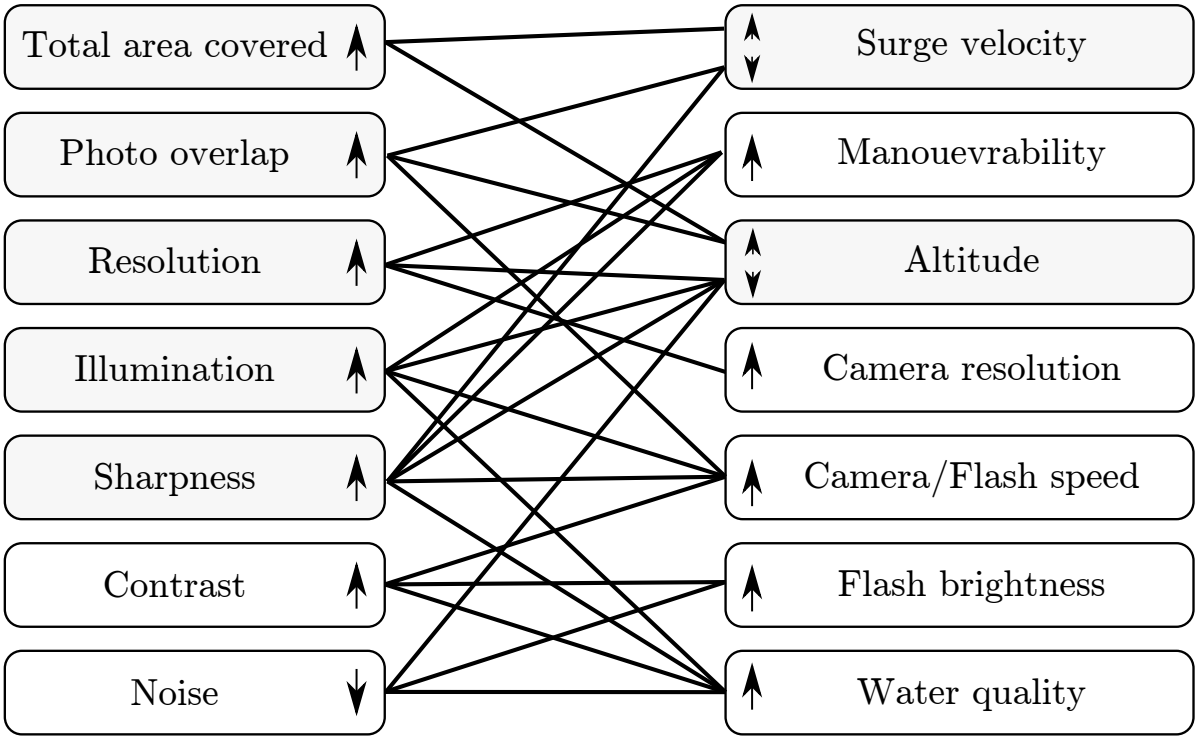

Figure 2.1: Illustration of the photo quality indicators and which mission and vehicle parameters have an impact. Arrows indicate the direction of change, e.g. an increase in flash brightness can increase the contrast and reduce the noise in the recorded image.

parameters impacting the photo quality factors are given. The lines connecting the two columns indicate which photo quality factor is impacted by which parameter, and vice versa. Most parameters are optimised by increasing them, with the exception of surge velocity and altitude. In those cases the arrow next to where a line begins indicates if the parameter needs to increase (upwards arrow) or decrease (downwards arrow) to improve the connected photo quality factor. The area covered by one pixel (resolution), the area covered by one photo (number of pixels · area of one pixel), and thus the total area covered, depend on the altitude of the vehicle and the camera. The optimal illumination is determined by the flash on the vehicle and the sensitivity of the camera, it is reduced by absorption and scattering in water. The absorption and scattering are increased by floating particles in the water turbidity and larger particles). As a result the illumination is reduced with increasing altitude, however depending on the camera settings, a too small altitude can also result in over exposure of the camera. The sharpness of the images is determined by the optical properties of the camera. Its focal length determines the altitude at which the best sharpness can be achieved, but even at this distance image features can be blurred due to forwards scattering [Corchs and Schettini, 2010]. The effect of forwards scattering reduces as the altitude is reduced. The contrast of an image depends on the illumination, in water it is also reduced by backward scattering [Corchs and Schettini, 2010], which also is reduced if the altitude is reduced. Additional noise can come from camera properties and floating particles, due to the latter noise increases with altitude. Finally, if the amount of floating particles is too large, a so-called "murky" seafloor, at a too large altitude only particles in the water ("turbidity") will be recorded, and the seafloor will remain hidden in the photos. This can be illustrated with photo examples from different scientific surveys. As part of the AESA project, the Autosub6000 AUV recorded photos that are suitable for demonstrating how changes in distance to the ocean floor influence the lighting and thus the image quality that can be achieved. Figure G.2 shows an example of different species that were observed as part of a photographic survey. The photographs in G.1 all show a selection from larger recorded images that captured one specimen of the Aperima species (see G.2 (E) for clearer photo and scale). The goal distance for the survey was 3.2 m [Morris et al., 2014]. The images have all been processed as described in [Morris et al., 2014], but it is clearly visible that there are limitations to what can be achieved. An error of one metre already shows how the strong attenuation of light in water limits the range at which photos with the correct light condition can be taken: whilst the pictures from a distance of $5.1m$ and $3.2m$ in Figure G.1 are too dark, the photograph from a $2m$ distance already looks overly bright, making contours more difficult to distinguish.

Another approach to taking photos of the ocean floor is described in [Thornton, 2015]. With more lighting the distance at which the photos can be taken can be increased, if the water turbidity is not too high. This makes obstacle avoidance easier and requires less accuracy in terrain following. But besides increasing the energy consumption and therefore reducing the endurance, this approach also reduces the resolution of the recorded photos: one pixel of a picture taken at 10 m distance in [Thornton, 2015] represents a 20 mm by 20 mm area of the seafloor.

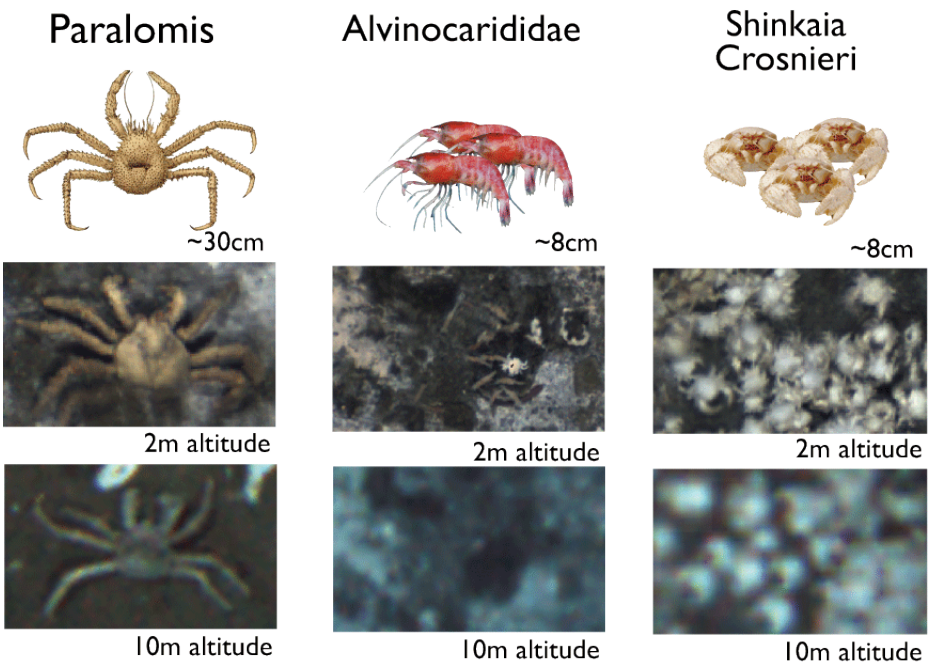

Figure 2.2: Comparison of species recorded at different altitudes. From Thornton, Pizzaro, Williams, Bodenmann (Unpublished, reproduced with permission of the rights holder).

Figure 2.2 illustrates how well different species can be recognised in the pictures taken at different altitudes. The photos recorded at a 2 m distance have a resolution of 1.5 mm, and are thus much easier to recognise. Comparing this with the scale of species shown in G.2, it is already clear that most of the species that are coloured similar to the seafloor will hardly be recognisable. The small anemone in Figure G.3 would be represented by a single pixel, demonstrating that a large number of species will be missed completely.

2.3 Underwater Vehicles

Current solutions to terrain following photographic surveys choose two approaches: The photographic system can either be positioned directly on the ocean floor or it can attempt to follow the seabed terrain, trying to keep the distance constant. Whilst systems that make contact with the ocean floor can guarantee little changes in distance, they disturb the seabed significantly. Besides the long term consequences, this influences the outcome of the survey directly by influencing the distribution of organisms and causing turbidity which reduces image quality [Morris et al., 2014].

Vehicles trying to follow the terrain at a small constant altitude are reliant on data collected during the mission. Either an operator or the on-board system then have to

determine the appropriate actuator settings. Whilst human operators might currently give a faster, more reliable evaluation, vehicles operated on a tether (Remotely Operated Vehicle (ROV) or Human Occupied Vehicle (HOV)) struggle with the forces on the tether. Human operated untethered vehicles are a possibility, however they are very costly, difficult to manoeuvre due to their large size, and only few such vehicles are available.

AUVs stand out since they are fast, relatively low cost, low risk, and high in endurance (see Figure 2.3). Their ability to react to the seafloor is currently the most limiting factor. When trying to reduce the cost and increasing the quality and scope of photographic surveys, improving the autonomous terrain following capabilities of AUVs is a promising strategy.

All AUVs consist of at least the following systems: energy supply, propulsion system, water proof pressure vessel, hull, computer system for vehicle operation and mission control, and basic sensors needed for the control systems. Depending on the mission type, the set of sensors for perception may be varied and the type of control can change. Typical navigation sensors for an AUV include a depth sensor, an Intertial Measurement Unit (IMU) and a compass to aid navigation. Often a Doppler Velocity Log (DVL) is used to track the velocity of the vehilce over the seafloor, detecting offsets due to current and reducing the positioning inaccuracy due to IMU integration errors. The mission specific sensors constitute the payload. They typically include active or passive sonar, chemical sensors or photographic systems. Unlike surface and air vehicles, AUVs can not be controlled from a long distance with radio links. This type of wireless communication over long distances is hindered by the attenuation for most electromagnetic wavelengths, including light. Acoustic waves are an alternative for both wireless communication and contactless sensors in water. Often navigation sensors, scientific sensors as well as communication rely on sound, so the timing and frequency of each system needs to be chosen carefully. With the achievable data rates for acoustic communication significantly lower than for electromagnetic waves, and the requirement of an acoustic transmitter and receiver at the water surface above the AUV, most vehicles keep the acoustic communication at a minimum.

The difference in propulsion has consequences for the abilities of the AUVs: Flight style AUVs typically have endurances of several days, some can even go on half a year long missions [Furlong et al., 2012]. Similar to airplanes that can only fly once a minimum speed is reached, flight style AUVs need to have a minimum speed so the sternplanes with airfoil shaped cross section can be effective. A reduction in operating speed comes at the cost of reducing the maximum achievable pitch angle and increasing the required pitch to keep a constant depth [Eng and Chitre, 2015]. Below a minimum speed, the vehicle control is lost [Burcher and Rydill, 1994, p. 169].

The more manoeuvrable hover capable AUVs are typically fitted with thrusters, providing actuation with more degrees of freedom. The vehicles can manoeuvre more slowly and accurately, as long as no water currents move the vehicle faster than the actuators can counteract. While capable of performing surveys in complex terrain, the water

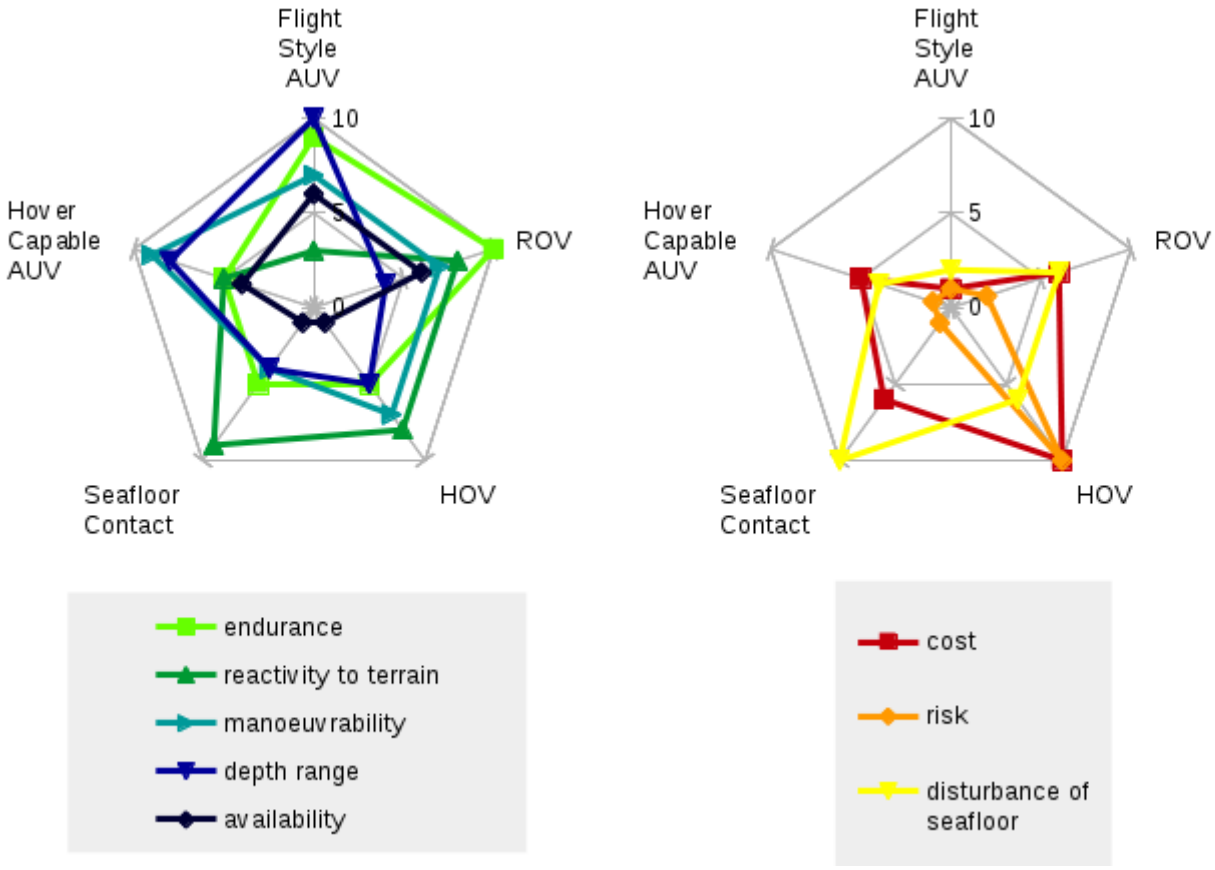

Figure 2.3: Subjective ratings of various qualities relevant for photographic surveys at the ocean floor for the existing solutions.

flow caused by the thrusters will disturb the sediment and the lower operational speeds [Smale et al., 2012, Marouchos et al., 2015, Nishida et al., 2014b] combined with the power consumption of the thrusters increase the time and energy cost for covering the same area [Smale et al., 2012].

Attempting to compromise between the two options, several hover enhanced flight style vehicles have been developed, e.g. [Wynn et al., 2014, Phillips et al., 2013, Packard et al., 2010].

Table 2.1 gives an overview of a selection of flight style and hover capable AUVs with documented use for photographic surveys. For a better understanding of the dynamic behaviour and to demonstrate the comparability of the vehicles, the (dimensionless) Reynolds number Re (Equation 2.1) and Froude number Fr (Equation 2.2) are calculated, using the vehicle length as the characteristic length l and the available information on maximum speed as the velocity u. A value of $9.81\,\mathrm{m/s^2}$ is used for g, the standard acceleration due to earth gravity. It is assumed that the vehicles are operated in seawater,

in the deep isothermal layer at 4° C [Robert, 1967]. According to the kinematic viscosity values of seawater tabulated in [26th ITTC Specialist Committee on Uncertainty Analysis, 2011, Table 3], a kinemativ viscosity of $\nu = 1.68 \cdot 10^{-6} \frac{m^2}{s}$ is used.

$$Re = \frac{u \cdot l}{\nu} \tag{2.1}$$

$$Fr = \frac{u}{\sqrt{g \cdot l}} \tag{2.2}$$

AUV	Length $[m]$	Diameter/ Cross Section $[m]$	Maximum Depth $[m]$	Endurance $[hrs]$	Minimum Speed $[m/s]$	Maximum Speed $[m/s]$	Reynolds number for $4^{o}C$ sea water, at maximum speed	Froude number at maximum speed	Actuators	Source
Autosub6000	5.5	0.9	6000	36	0.8	2.0	$6.5 \cdot 10^6$	0.27	1 rear propeller 4 control surfaces	[McPhail, 2009a] [Furlong et al., 2009]
Delphin2	1.96	0.26	50	8	0	1.0	$1.2 \cdot 10^6$	0.23	1 rear propeller 4 control surfaces 2 vertical thrusters 2 horizontal thrusters	[Phillips et al., 2013]
TUNA SAND	1.1	0.7x0.7	1500	8	0	0.9	$0.59 \cdot 10^6$	0.27	6 thrusters	[Nishida et al., 2013]
BOSS-A	3.0	1.2x1.3	3000	6	0.0	0.5	$0.89 \cdot 10^6$	0.092	2 vertical thrusters 2 horizontal thrusters	[Nishida et al., 2015]
D. Allan B. (Dorado class)	5.2	0.53	6000	18	1.0	1.5	$4.6 \cdot 10^6$	0.21	articulated aft propeller	[Caress et al., 2008]
Sirius (Seabed class)	1.9	0.34x1.5	$\geq$2000	8	0.0	1.0	$1.1 \cdot 10^6$	0.23	1 vertical thruster 2 horizontal thruster	[Woolsey et al., 2010] [Singh et al., 2004a] [Tolimieri et al., 2008]
Starbug	$\leq$1.5	0.15x0.8	$\geq$100	8	0.0	1.5	$1.3 \cdot 10^6$	0.39	3 vertical thrusters 2 horizontal thrusters	[Marouchos et al., 2015] [Dunbabin et al., 2005]

Table 2.1: Key data comparing flight style, flight style hover capable and hover style AUVs.

To increase the area that can be surveyed photographically with AUVs, the most relevant factors are endurance, speed, and the ability to react to the terrain. Considering that at a depth of several thousand metres, a vehicle spends over an hour manoeuvring to the seafloor (ca. 90 minutes [McPhail et al., 2008]) and positioning itself (30 minutes to one hour [McPhail et al., 2008]), an increase in endurance means less time will be lost by having to resurface and recharge the vehicle. The endurance is mainly restricted by the energy consumption of the actuators, and can be improved by more efficient actuation or better energy storage.

Current work on terrain following for AUVs is limited and often assumes an existing terrain map [Houts et al., 2012, McPhail et al., 2010b], though even when re-visiting previous experiment sites it is challenging to accurately position the vehicle within the map [Houts and Rock, 2015, Williams et al., 2012].

Flight style vehicles like Autosub6000 have already successfully used horizon following algorithms to undertake photographic surveys in unknown terrain but are currently restricted to flat terrain (with unclear interpretations of “flat”). The area of terrain following for complex, unknown terrain has a large scope for improvement, and flight style as well as hover capable AUVs can profit from terrain following solutions that do not require for the vehicle to slow down or stop.

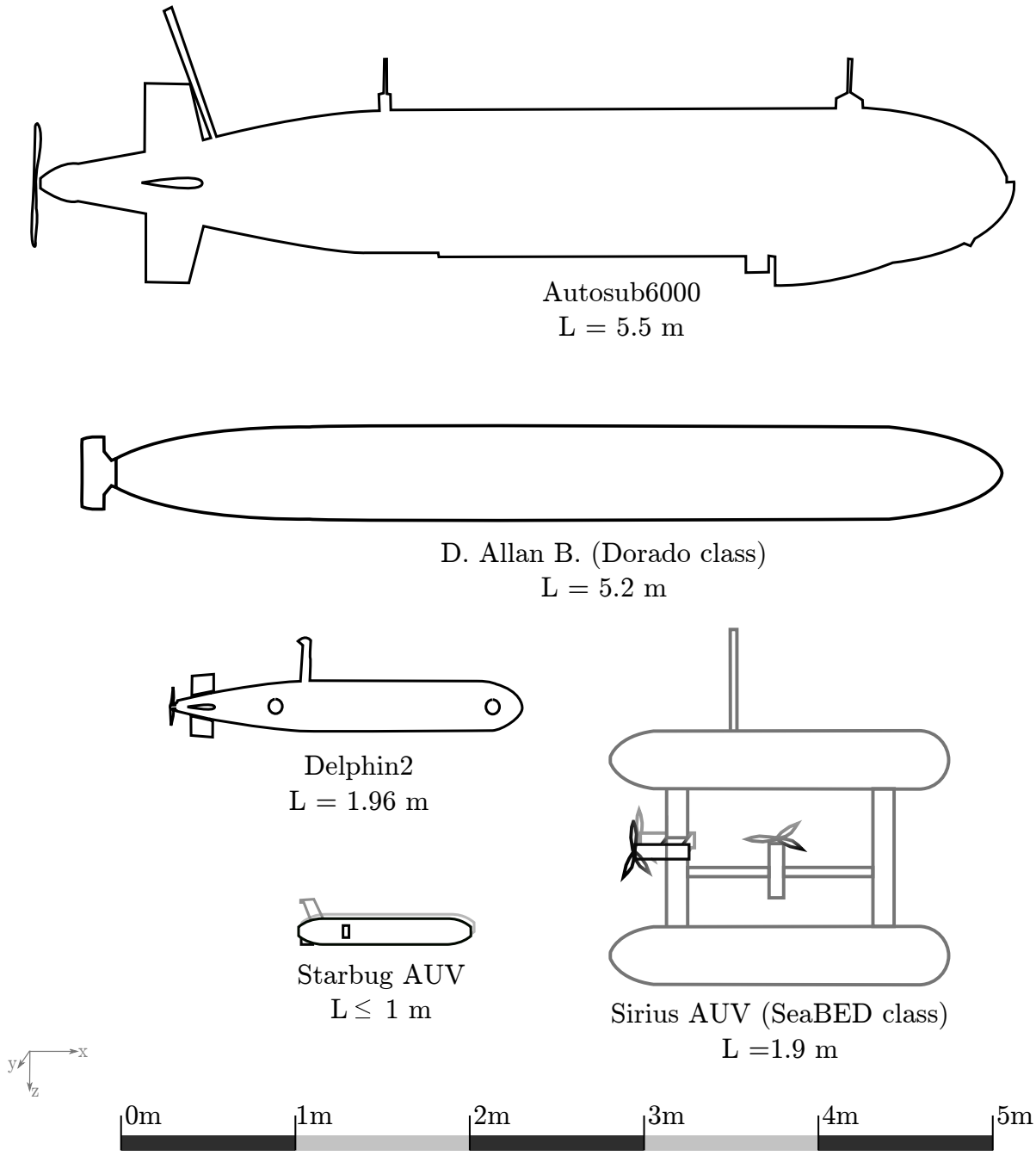

Figure 2.4: Examples of AUV outlines, to scale. Length L is given for all vehicles.

2.4 Terrain Sensors

With little to no mapping information available, AUVs need to collect and evaluate the information they need for terrain following as they go. The sensor selection needs to be based on range, power consumption, reliability of seafloor recognition, data rate and ease of data evaluation.

The range of light based sensors is limited by attenuation. Nonetheless, laser based systems using image analysis of laser points on a camera image are occasionally used in underwater ranging applications. [Kondo and Ura, 2004] uses two laser points to determine the angle of a vehicle for accurate navigation around known obstacles. [Nishida et al., 2015] uses a sheet laser underneath the BOSS-A AUV to reconstruct the topography of the seafloor based on the distortion of the projected line. The topography is then used to turn the recorded photos into three dimensional (3D) photographic maps of the seafloor and improving image quality by compensating attenuation and distortion. Instead of aiming the sheet laser downwards to the sides of the vehicle, it could be aimed forwards along the path of the AUV. With both papers recommending a range of only two to three metres, it is questionable how much information can be gained on time for terrain following.

More recent publications on underwater laser ranging look into improving the range by modulation of laser pulses in the MHz to GHz wavelength range [Laux et al., 2012, Cochenour et al., 2012] or by only recording reflected photons for a limited amount of time, with the time window corresponding to the distance of interest ('range gating') [Huang et al., 2014]. These techniques have been successfully used in air, but underwater devices are still far from ready to use sensors that can easily be added to excising AUVs.

Instead of visible light or other types of electromagnetic waves, distance sensors under water usually rely on acoustic measurements using sonar sonar (SOund Navigation And Ranging) devices. Ranges of over one hundred metres can be achieved. Active and passive sonar can be distinguished [Waite, 2005, p. xvii], however since the seafloor normally does not emit noise, only active sonar is applicable for accurately sensing ahead of the vehicle. Generally, active sonar units emit sound of a given frequency range and time and then measure the returns over time. The intensity of a return can be used for estimating what might have caused that return [Waite, 2005, chapter 4]. The time between sound emission and the observation of the reflection gives an estimate of the distance to the object [Waite, 2005, chapter 3].

The range of a sonar depends on the intensity, sensitivity and frequency of a sonar device [Waite, 2005, chapter1]. Since AUVs usually use ready made sonar units, this is usually given by the manufacturer. When looking at the sonar range given by the manufacturer, one needs to keep in mind that these numbers are for optimum conditions. [McPhail et al., 2010a] found that at flat angles, a sonar with a manufacturer given range of 300 m only detected the seafloor at distances between 67 m and 170 m. The detection range depends on the reflectivity of the seafloor, which changes with material, sonar

frequency, and angle of incident ('grazing angle') of the sonar beam. Backscattering of rocky bottoms is stronger than that of sand or mud bottoms. At shallower grazing angle, as would be expected for any forwards looking sonar beams at low altitudes, the backscattering strength is reduced [Robert, 1967, section 8.13,p.217-225]. [Robert, 1967, Fig. 8.23] shows an increase of scattering strength with increasing frequency between 50 kHz and 300 kHz over sand. Strong reflections are also produced by ice ([Robert, 1967, section 8.14]) and the water surface ([Robert, 1967, section 8.11]).

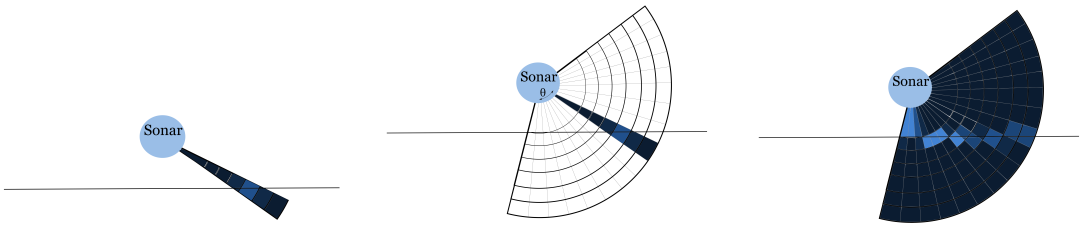

Singe beam sonar Mechanical scanning sonar Multibeam sonar

Figure 2.5: Sketches demonstrating the differences between different sonar types.

There are a variety of sensors using a combination of sonar sources and receivers. The most popular choices for ranging are single beam, mechanical scanning and multibeam. The sketches in Figure 2.5 demonstrate the basic difference between those three types of sonar: a single beam only gives returns for a single fixed beam. A mechanical scanning sonar uses a stepper motor to vary the angle at which a single beam measurement is taken. One scan is taken at a time, so covering a larger range takes time. Figure 2.7 shows two perspectives at the coverage of area in front of a vehicle using a mechanical scanning sonar. A multibeam sonar yields the same area coverage, but all angles are covered in a single measurement by measuring the sonar reflections on an array of receivers. Multibeam sonars are mainly used for building maps, often from a ship at the surface, or as payload on AUVs for generating maps through post processing after the mission [Caress et al., 2008]. Increasingly they are also added for obstacle avoidance [Houts and Rock, 2015].

To avoid the evaluation complexity and high energy consumption of multibeam sonars, [Bouxsein et al., 2007] places several transducers in selected locations at the front of the AUV to achieve low power, real time evaluation for obstacle avoidance. [Quidu et al., 2007] uses a distribution of single transducers over a horizontally scanning multibeam sonar to add vertical information (see Figure G.4).

Several vehicles use mechanical scanning sonars for forwards looking obstacle detection in the vertical or horizontal plane, from photographic missions [Nishida et al., 2015, McPhail et al., 2010a], to obstacle detection in a harbour [Chew and Chitre, 2013] or for iceberg mapping on Autonomous Underwater Glider (AUG) [Zhou et al., 2016]. Whilst limited in scanning speed compared to multibeam sonars, the device is more energy efficient and less expensive.

When using a single beam or mechanical scanning sonar, the device sends a single acous-

Figure 2.6: Getting Autosub6000 ready for a mission at the Cayman Rise. The removed front panel gives a clear view on the mechanical scanning sonar. Photo provided by the National Oceanography Centre, reproduced with permission.

tic pulse through the water. The acoustic pulse has approximately cone-shaped, with a given vertical and horizontal opening angle. The range measurement is performed in discrete time steps, so-called 'bins'. Detecting an obstacle on the returns of a single beam or mechanical scanning sonar involves analysing the numbers representing the return intensity in each bin to establish at which distance an obstacle is reflecting sound. Algorithms for such detection include using a fixed, constant threshold above which a return is considered an obstacle, automated threshold detection e.g. using Otsu thresholding [Chew and Chitre, 2013], or through a first-order infinite impulse response digital filter [McPhail et al., 2010a]. More complex analysis methods model the sound propagation within the sonar beam to calculate a probability of occupancy for a grid map [Zhou et al., 2016].

The measured intensities of the transducers of a multibeam sonar are translated into intensities along a number of beams through mathematical operations ('beamforming', [Han et al., 2014]. Rather than individually scanning one angle at a time, a single scan returns measurements for a whole set of angles. The number and resolution of these beams can be varied by changing the mathematical analysis. Typically, commercial multibeam sonars make only the resulting beams available as shown in Figure 2.5. Usually the data from the multibeam sonar is still analysed manually by a person [Caress et al., 2008]. This need for processing after completion of the mission shows how complex even the interpretation of pre-analysed multibeam data can be. Additional analysis methods are possible with the raw data. However this type of analysis is complex, of high computational cost [Bouxsein et al., 2007], and often manufacturers do not make this data available.

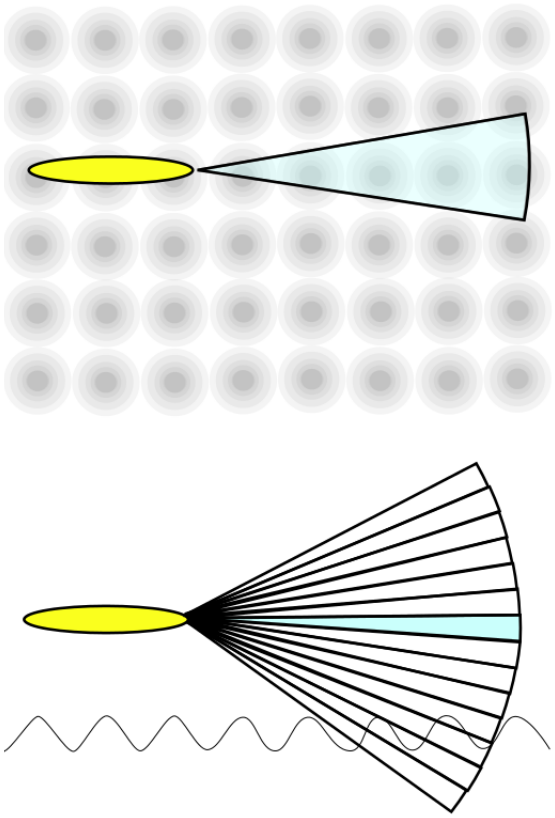

Figure 2.7: View on vehicle with mechanical scanning sonar from above and one side. The blue section marks the area that is covered in one sonar measurement. In the side view more sections are marked that can be covered if the sonar is set to a different angle.

2.5 Existing Terrain Following Strategies

Altitude tracking capabilities are often mentioned, but detailed information on the performance is rarely available. The four classes of AUV described in more detail below were selected for the detail of information available on their terrain tracking ability, and the demonstration of terrain tracking below 10 m altitude in application. An overview of all vehicles to scale is given in Figure 2.4.
The Starbug AUV and SeaBED AUV are both less than 2 m long thruster actuated AUVs. Both are constructed of two torpedo shaped hulls, but with different alignment (see Figure 2.8). The original Starbug Mk3 AUV was designed for researching navigation based on optical light and further developed into the Starbug X AUV which operates in shallow, clear water. The stereo cameras used for downwards and forwards terrain detection have a detection range of 0.2 m to 1.7 m [Dunbabin et al., 2005]. In addition to the stereo cameras, a Tritech PA500 sonar altimeter with a minimum altitude of 0.1 m and a resolution of 0.001 m is used for altitude measurements. The goal altitude for imaging is between 0.4 m and 0.9 m [Marouchos et al., 2015]. At a survey speed 0.6 m/s, with an endurance of 10 hours it can achieve a range of around 22 km [Marouchos et al.,

2015].
The SeaBED AUV was designed for low altitude surveys at the Woods Hole Oceanographic Institution [Singh et al., 2004b]. Photographic missions with the SeaBED AUV and its derivatives Mola Mola and Sirius are well documented [Tolimieri et al., 2008, Williams et al., 2009a, Woolsey et al., 2010, Singh et al., 2004a, Williams et al., 2010a,b, 2009b], however technical details on the altitude tracking are not so well reported. It uses a Proportional plus Integral plus Derivative (PID) depth control for altitude tracking, combining altimeter and depth measurements to obtain a depth demand. The Sirius AUV has been enhanced with a Tritech Micron mechanical scanning sonar for forwards detection (personal communication S. Williams, June 2018). The AUVs operate at speeds between 0.3 m/s and 1 m/s, at up to 2000 m depth [Singh et al., 2004a]. The surveyed terrain structures include a 75° slope at 3 m altitude and 0.3 m/s speed, limited in speed by the required image overlap [Singh et al., 2004a]. Plots of the vehicle path over terrain are included in [Singh et al., 2004a,b], however the vertical exaggeration of the terrain makes it difficult to read details of the altitude tracking results from the plots. With the battery capacity allowing an average endurance of 8 hours, the track length achievable within one mission is between 8.6 km at 0.3 m/s, and 28.8 km at 1.0 m/s.

The Autosub6000 AUV and Dorado class AUVs are almost 6 m long flight style vehicles, that are also capable of operation at low altitudes. Their initial obstacle detection is based on a horizon tracking method first developed for Autosub6000, relying on a mechanical scanning sonar. Surveys using this algorithm have been performed at altitudes between 3 m and 20 m at a speed of 1 m/s [McPhail et al., 2010a, Houts et al., 2012].
The obstacle avoidance system used on the Dorado class AUV has been extended for application in areas where maps are available beforehand. Relying on terrain relative navigation for accurate positioning, the knowledge of the area ahead is used to pre-plan trajectories at an altitude between 2 m and 4 m. Should unexpected obstacles be detected with the scanning sonar, the planned trajectories are overwritten by the reactive horizon tracking control [Houts et al., 2012]. The work has been further improved by including uncertainty in the trajectory planning, and by upgrading the forwards detection sensor to a multibeam sonar. Existing publications report simulations based on terrain data from previous missions, obtaining an effective turning radius of 17 m and a maximum pitch angle of 45° as altitude tracking limits; [Houts and Rock, 2015] compares three avoidance planning strategies on the example of an approximately 50 m high terrain step.

The obstacle avoidance was added onto the existing system using a Seaking mechanical scanning sonar mounted to scan the vertical plane ahead of the vehicle. The angular position of the sonar head is adjusted after each measurement, based on whether the seafloor was successfully detected in the previous measurement, thus tracking the horizon with the scan angle. Should no terrain be detected at any of the sonar settings, the scans continue over the lower half of the available sonar angles. The terrain returns are detected with a digital impulse filter [Furlong et al., 2009], due to the non-ideal shape of the sonar beam a filter for returns from sidelobes was added. From that highest angle at which the seabed is still detected, an auxiliary parameter, called the “pseudo

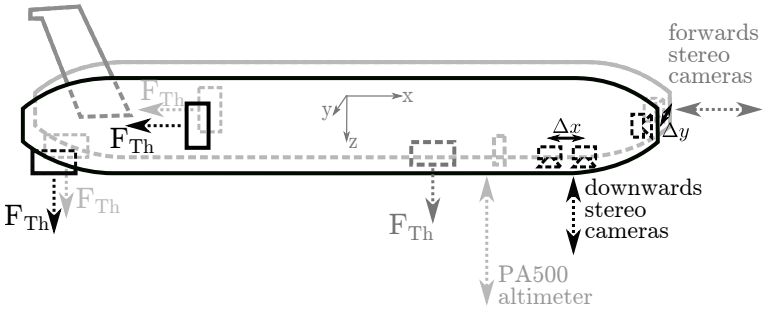

(a) Starbug AUV, $L \leq 1\,\mathrm{m}$.

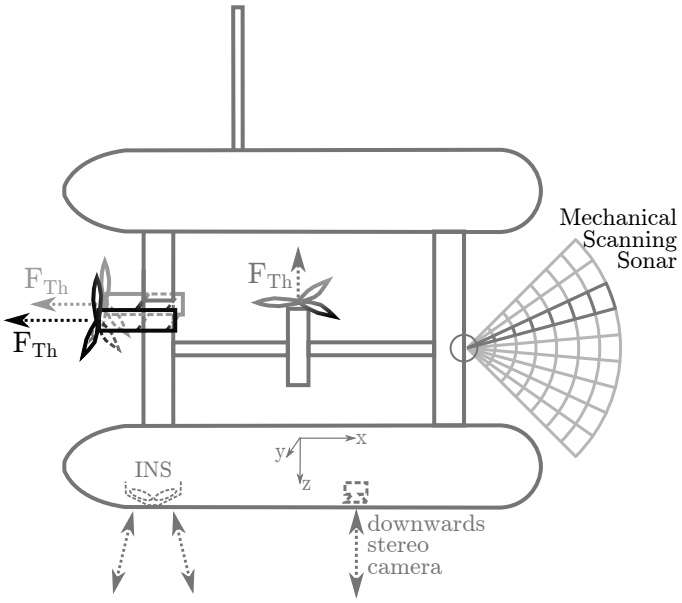

(b) Sirius AUV (SeaBED class), $L = 1.9\,\mathrm{m}$.

Figure 2.8: Side view drawings of hover-style low altitude terrain tracking AUVs. Cameras and altitude tracking sensors and actuators are indicated where known. Greyscale alludes to position in the y-direction.

altitude" a_{pseudo} is calculated (see illustration in Fig. 3.10)). The pseudo altitude a_{pseudo} is then compared to the current altitude a of the vehicle. The smaller value of the two is used to calculate the altitude error $\tilde{a}$ to the altitude demand a_d. This altitude error combined with the current depth z is used to calculate a depth demand z_d (see Figures 2.10, 3.8), which is then used in the existing depth control loop, a cascaded PID control that is shown in 2.10. In addition to this general system, on Autosub6000 further steps are implemented to filter the sonar returns for misleading returns from sidelobes of the sonar beam, and to trigger an avoidance manoeuvre in the horizontal plane by raising a 'collision immanent' flag [McPhail et al., 2010a].

Despite the obstacle avoidance system, a small number of collisions occurred when tracking the seabed with Autosub6000 and during several missions the achieved altitude was several metres above the goal altitude. However, trying to improve the system on Au-

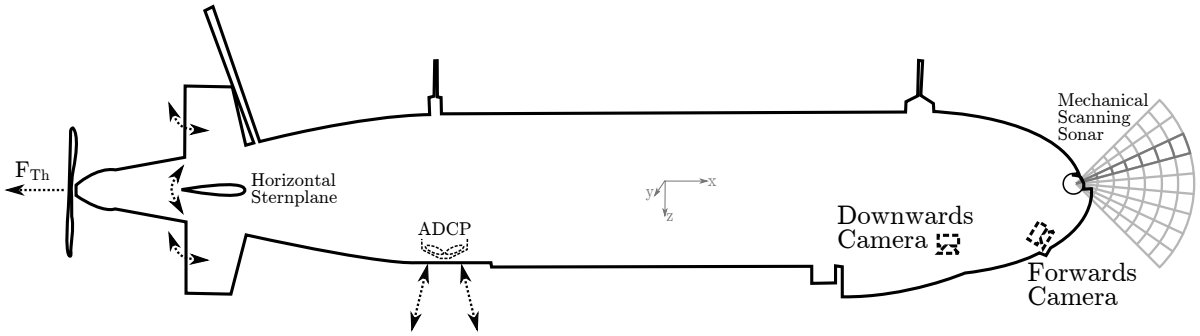

(a) Autosub6000 AUV, $L = 5.5\,\mathrm{m}$.

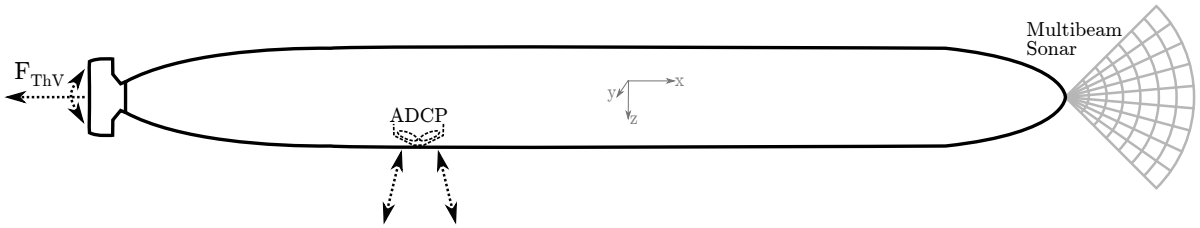

(b) D. Allan B. (Dorado class), $L = 5.2\,\mathrm{m}$

Figure 2.9: Side view drawings of flight style AUVs used in existing terrain following work. Cameras, altitude tracking sensors, and actuators are indicated where they could be identified from publications.

tosub6000 requires understanding a complex system, whilst limited in the tests that can be performed. Due to the size of Autosub6000 tests can only be performed at sea, operating from a ship, which is associated with large costs and a high risk to the AUV. Recorded mission data exists, but simulation tests can only use the collected in-situ data and the engineering details that were recorded at the time. An accurate simulation for altitudes below 10 m is difficult to achieve since due to the focus on the photographic data often engineering parameters were not recorded in sufficient detail, the actual terrain structure is only known as far as it can be re-constructed from the on-board sensor data, and suggested sensor and actuator changes can not be validated without costly and time consuming changes to the vehicle.

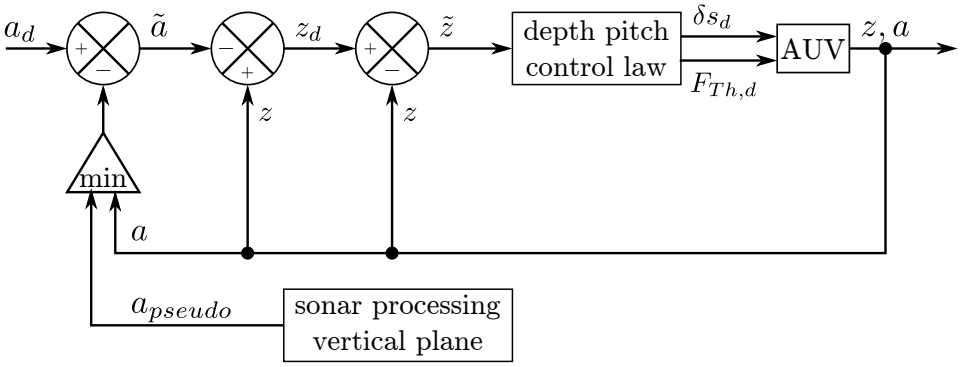

Figure 2.10: Conversion of the altitude demand a_d, the depth (z), altitude (a) and pseudo altitude (a_{pseudo}) sensor information into a depth demand input z_d for use in the existing depth control on Autosub6000 and Delphin2.

2.6 Mapping

When judging the risk and planning the needed safety margins, it would be helpful to rely on existing maps of the seafloor. The resolution of most seafloor maps is too small to show details in the size range of the vehicles undertaking surveys (see Figure 1.1, [Wilson et al., 2007]), and with increasing water depth the resolution reduces. Even maps generated with data collected by AUVs often have a resolution of 1 m to 5 m [McPhail, 2009b]. Compared to a goal altitude below 10 m, this resolution can already be useful to avoid structures that are several metres high and require longer ascends. But even these rare AUV generated maps will not suffice for the small corrections needed for keeping a constant altitude.

Few exceptions exists, for example when a vehicle revisits an area that it has previously surveyed at a close proximity. In such cases it can rely on existing maps to flight at a close proximity, if it is sufficiently confident in its position on the map. If the position of the vehicle is not clear enough, it has to increase its safety margins and go back to navigating based on local sensor readings [Houts et al., 2012]. With a loose definition of mapping, the current terrain following strategy of Autosub6000 can be seen as building a local map: different sonar angles are assigned a binary value, representing a detection of the seafloor or no detection of the seafloor, according to the most recent measurement at that angle [McPhail et al., 2010a]. [Engelhardtsen, 2007] simulates a 2D terrain with a matrix that has depth assigned. Storage efficient mapping methods, like the ROS package “octomap” [Hornung et al., 2013] use a tree based data structure called “octrees” for storing the mapping data.

Normally it is important to know the accurate location of the vehicle for building a mpa. Under water, GPS, that is usually relied on for surface localisation, is not available. The closest comparable situation on land would be indoor navigation, where often Simultaneous Localization And Mapping (SLAM) techniques are relied upon [Cadena et al., 2016]. Inertial measurement data of the robot, range sensors, and sometimes also known

landmarks, are used to update the map data and the position of the vehicle within it. The mapping required for altitude tracking differs significantly from the typical scenario of Simultaneous Localization And Mapping (SLAM) techniques: for altitude tracking purposes the vehicle only needs to be localised relative to the terrain ahead. The mapped areas are unlikely to be re-visited at a later time, thus the generated map becomes irrelevant within seconds of acquiring it. Only one sensor, the forwards looking sonar, is used to generate the map. Whilst the altimeter may be used for verification of acquired maps, or to detect offsets in the sonar scan angle, at the point when the altimeter senses the terrain, it is already too late for any contributions to the map used for the altitude tracking process.

Classical mapping techniques come from visual sensors. Widely used laser based sensors have much smaller beam opening angles than sonar devices and light waves, unlike acoustic waves, typically cannot pass through several objects or return to the sensor transceiver after multiple reflections. The widely used mapping techniques are designed to work with such thin beam, single range measurements. [Zhou et al., 2016] considers the wider beam opening angle of a mechanical scanning sonar in the map generation. The additional information from the sonar being reflected multiple times is currently dismissed as noise, and not further used.

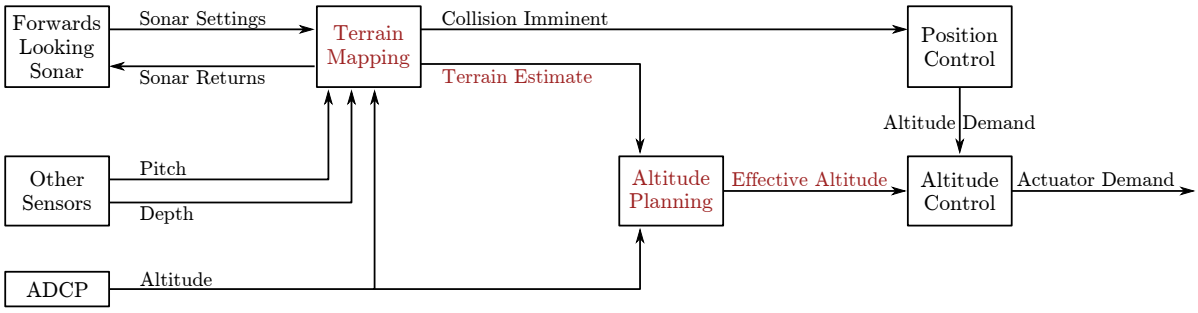

Figure 2.11: Addition of mapping to the Autosub6000 terrain following.

2.7 Command and Control

A wide variety of controllers is used for controlling flight style AUVs. A large portion of these controllers is only studied in simulation, and there is little work on comparing different controllers [Lea et al., 1999]. Autosub6000 uses a cascaded Proportional Integral Derivative (PID) controller. The depth demand is derived from an altitude demand, which is calculated based on the last horizon detection, generating a single current setpoint [Steenson et al., 2014, McPhail et al., 2010a]. The depth of Delphin2 can be controlled via a PID control that will switch between actuators based on its forwards velocity [Tanakitkorn et al., 2016]. Model Predictive Control (MPC) has been demonstrated for altitude and depth control, however the lack of foresight using only

the altimeter measurement as a control input resulted in a terrain collision [Steenson et al., 2014].

Once a mapping system has been introduced, rather than reacting to a single depth demand, trajectory planning could be used to achieve a better compromise between vehicle safety and photographic survey success. [Houts et al., 2012] demonstrates how this can be done in-situ, if existing maps can be used for the trajectory planning. The control is then given a feed-forward pitch command so the trajectory, which was planned under consideration of the maximum turning radius, will be followed.

[Naeem et al., 2005] highlights that MPC can "handle constraints in a natural way during controller design". By using a model predictive controller, the path planning step could thus be simplified to a path estimation and constraints for avoiding a terrain collision could be considered in the constraints of the controller. In the receeding horizon method, the optimal control for a fixed horizon length is determined at every timestep [Kwon et al., 1983]. Considering that the mapping information is also limited by a fixed length, the sonar range, and updated with every time step of the sonar transducer, this method seems to naturally fit with the demands of altitude control in unknown terrain. How planning for a more complex demand can be implemented with MPC is demonstrated in [Medagoda and Williams, 2012], where a cost function is used. It is based on difference between reference and planned trajectory, showing in simulation how model predictive control can improve in-situ trajectory planning, based on local water current information. [Caldwell et al., 2010] considers a simplified AUV in the horizontal plane, controlling angular velocity directly rather than through an actuator. However, constraints from the vehicle are considered and cost functions for control effort and deviations from the reference path are included. To increase the speed of the optimisation and avoid local minima a randomized sampling approach is proposed. When attempting to control a vehicle using MPC, the quality of the vehicle model is key for the performance of the controller [Badwe et al., 2009].

2.8 Simulation and Visualisation

Since using an AUV always involves multiple persons and in case of Autosub6000 usually a whole research ship, the time spent testing with AUVs is very valuable. Even in case of Delphin2, several people need to be involved and for every hour testing about an hour in preparation and cleanup need to be factored in. In addition, experiments carry the risk of damaging the AUV, and may be cancelled due to failure of a component of the vehicle or adverse weather conditions. Simulations are vital during the development of AUVs to test new control methods, verify mission plans, and select validation experiments. The need for simulation has been recognised early on in the development of AUVs.

The first step in simulating the vehicle dynamics of Delphin2 and Autosub6000 was to check if existing dynamics simulations were suitable for the terrain following simu-

lation. Many simulators focus on graphical representation of AUV and surroundings, testing of manoeuvres and control; sensors rarely include sonar. Exception to this is a simulator that was developed with the only purpose of simulating sonar beams for obstacle avoidance in coastal environments [Bouxsein et al., 2007] and the new simulator MArine Robotics Simulator (MARS) from Lübeck that was introduced in [Tosik and Maehle, 2014]. The simulators analysed in [Matsebe et al., 2008] mostly were written very vehicle specific. Often, the described simulation is even more specific, for only one area of the application. Such simulations can have the advantage that they are often is faster to develop, since they only needs consideration of few cases and can be validated on a single vehicle. In the long term, these simulators have the disadvantage that for every vehicle work needs to be redone, bringing a chance for mistakes to be made and making a comparison of multiple vehicles difficult. Nowadays various commercial, free or open source simulators that are compatible with a variety of vehicles exist. Since it was expected that the simulators would need amending for the forwards detection, only open source simulators were considered.

It was found that the wider used UnderWater Simulator (UWSIM)[Prats et al., 2012] and newly introduced MARS [Tosik and Maehle, 2015] are mainly focused on hover capable AUVs. At the time of planning the simulation, for flight style vehicles both simulators required vehicle position and speed information to be published via user provided ROS nodes. Therefore it was decided to develop a model of the AUV that outputs the AUV state in the form of ROS messages. Since model data and simulation data was available for Autosub 1 and 3/4 scale Autosub1, experiment data was available for Autosub6000 and Delphin2, and only Delphin2 is available as a dedicated testplatform, the simulation was designed to to be as flexible as possible in regards to the simulated vehicle.

2.9 Summary

The reviewed literature shows that there is a clear need for photographic surveys in complex terrain. The quality of the acquired photos depends on a number of factors, many of which are related to the vehicle altitude. In the range of vehicles that is currently being used for such surveys, flight style AUVs have the best potential for high quality data at a relatively low data acquisition cost, by virtue of their energy efficiency. To reduce the cost and risk to the vehicle and increase the range of terrain that can be surveyed, on key problem of flight style AUVs needs to be addressed: Their reaction to sternplane actions is slow, compared to the rate at which the terrain changes below them and the rate at which data about the terrain ahead can be collected with sonar sensors. To improve on existing work, the acquired looking ahead data needs to be processed more effectively to be used for mapping and planning purposes, and the planning and control strategy needs to allow more complexity, and the results need to be documented for better comparability and repeatability analysis.
The comparison with other AUVs undertaking photographic shows that the Auto-

sub6000 vehicle, Delphin2, and the horizon tracking currently used on Autosub6000 are a suitable representation of AUVs undertaking photographic surveys. The two vehicles are described in more detail in the next section.

Chapter 3

AUV Platforms Autosub6000 & Delphin2

Whilst the overall goal of this work is to gain understanding and achieve improvements that can be applied to a range of flight style AUVs, the objectives and research questions of this work are based on the photographic surveys of Autosub6000. The smaller, hover capable Delphin2 that was designed based on the Autosub vehicles is used as a more flexible test platform.

The vehicles are representative of a large range of simliar flight style AUVs, for which a transfer of the results is possible under consideration of the fluid regime they are operated in. To facilitate the transfer to other vehicles, the vehicles and their operational conditions are described in detail. This section demarcates the two AUV platforms that this thesis focuses on, giving details on the sensors and control for the vertical plane altitude tracking required for photographic surveys.

3.1 Autosub6000

The horizon tracking algorithm of Autosub6000 has been used in several science missions since first being tested in 2009. Autosub6000 uses a mechanical scanning forwards looking sonar, mounted to scan the vertical plane. From this, the highest terrain point within the sonar range ('horizon') is detected and used for generating a depth demand for the vehicle. Currently, Autosub6000 can achieve terrain following for an altitude of 3 metres in flat abyssal conditions. To increase the vehicle safety in case of terrain collisions, Autosub6000 was fitted with a sledge to protect the hull and prevent it filling with mud in case of a collision. The terrain following is very conservative: As soon as the horizon height changes, this is translated into a demand for a higher altitude, leading to the vehicle deviating from the photographic survey altitude before it is necessary. For this work, data recordings from Autosub6000 photographic missions are used to analyse

the altitude tracking success and the vertical plane altitude tracking performance. The existing system is simulated and re-implemented on the smaller vehicle Delphin2.

3.2 Delphin2

The hover capable flight style AUV Delphin2 is a 3:1 scaled model of Autosub6000 developed at the University of Southampton [Phillips et al., 2013]. For increased manoeuvrability, Delphin2 is additionally equipped with four through-body thrusters which allows hovering and operation at slower speeds. To make space for the hover actuation, the tail section was extended slightly. Figure 3.1 illustrates the similarity of the two hull shapes.

Similar to Autosub6000, Delphin2 is equipped with a mechanical scanning sonar mounted for terrain detection in the vertical plane and a camera for photographic surveys. In the past, Delphin2 has been used for altitude tracking without forwards detection in Lower Lough Erne, Ireland [Steenson et al., 2014], where photos for tracking an invasive muscle species were successfully recorded. For this study, an altitude of 0.75 m with a surge velocity of $0.5\,\mathrm{m\,s^{-1}}$ was used. As a result of the lack of forwards looking situational awareness, one crash with the lakefloor occurred during those trials [Steenson et al., 2014].

The vehicle depth and heading can be controlled over the full transition from hover to flight-style actuation using a computationally inexpensive PID based controller with a thruster and sternplane weight function based on the vehicle surge velocity [Tanakitkorn et al., 2016]. A Model Predictive Control depth control with actuator limitations as constraints [Steenson et al., 2014] and a sliding mode heading control [Tanakitkorn et al., 2017] have also been developed.

For this research, the mechanical scanning sonar was integrated in the vehicle control system. Tests were performed in towing tanks at the University of Southampton, and a set of altitude tracking experiments was recorded at Testwood Lake, an up to 4 m deep lake near Southampton. Whilst attempts were made to record photos at Testwood Lake, ultimately, it was found that the water turbidity due to algae resulted in green images without distinguishable features.

3.3 Actuation

Both Autosub6000 and Delphin2 are designed as bositively buoyant, torpedo shaped, flight style vehicles (see Figure 3.1), propelled by an aft propeller and controlled in the vertical plane mainly by horizontal sternplanes inducing a pitching moment. Figure 3.2 illustrates and compares the moments and forces induced by the vertical plane actuators on both vehicles.

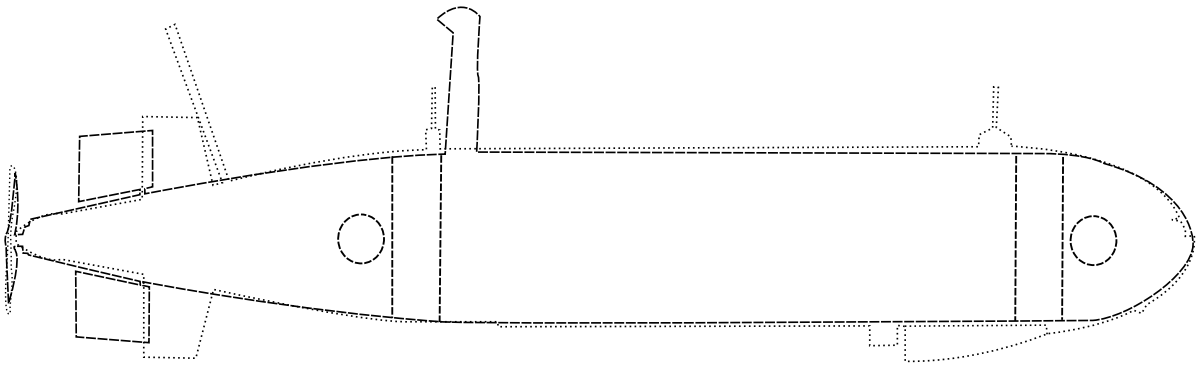

Figure 3.1: A shape comparison illustrating the similar hull design of Autosub6000 (dotted line, sledge included) and Delphin2 (dashed line).

When moving at speed, the foil shape of the sternplanes results in a force at the attachment point of the sternplanes. Since the leaver arm of the sternplanes is very long, the effect of the pitch inducing moment is significantly larger than the effect of the opposing force. A change in depth is achieved by changing the pitch angle of the vehicle, resulting in the vehicle de- or ascending.Whilst not technically an actuator, it is worth mentioning that Autosub6000 has a second pair of sternplanes positioned at a fixed angle and a more central position. For those sternplanes, the effect is the reverse, they apply a constant downwards force, opposing the constant upwards force of the buoyancy whilst exerting a relatively small upwards pitching moment.

Delphin2 is over-actuated in the vertical plane, with a pair of vertical thrusters. Unlike sternplanes, the thrusters do not require a forwards speed to generate force. They can either be used to apply a force in the same direction, generating opposing moments, as a result translating the vehicle, or they can apply opposing forces, generating a pitching moment around the centre of rotation. By controlling the difference between the two forces, translation and pitching moment can be combined.

The speed of both vehicle is not actively controlled. On Autosub6000, a constant power for the propeller is set; on Delphin2 a constant Rotations Per Minute (RPM) demand is set. The power and RPM settings are selected based on surge speed estimates from previous experiments. Since Autosub6000 is always reliant on forwards speed for controllability, the typical speeds range from 1 m/s to 2 m/s whilst Delphin2 can be operated from hovering at 0 m/s to 1 m/s.

3.4 Sensors

On AUVs, typically two types of sensors are distinguished: operational sensors and science payload. The data from the scientific sensors is usually logged for post-processing at a later time and not considered during operation. The operational sensors are used

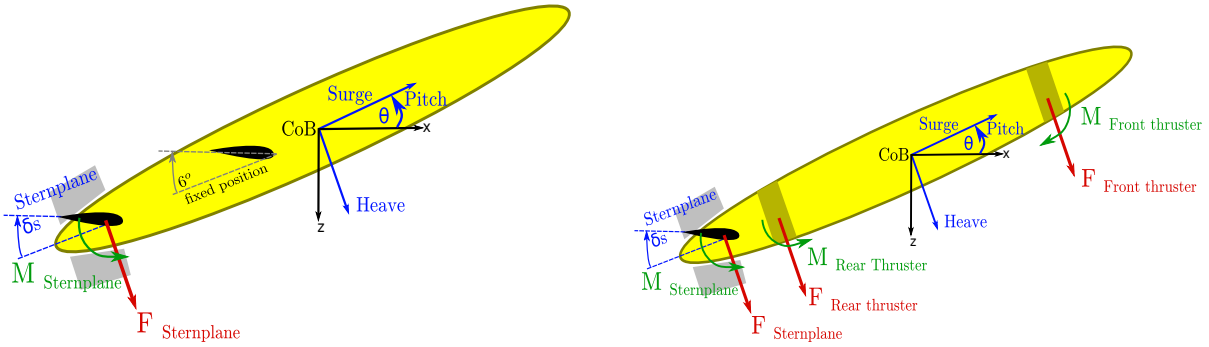

Flight style actuation of Autosub6000. Flight style, hover capable actuation of Delphin2.

Figure 3.2: Comparison of the actuators available on Autosub6000 and Delphin2.

in real time control. Since this work focuses on the vertical plane control, a further separation is introduced, between sensors used for the control in the vertical plane, and operational sensors that are used in the analysis of the altitude tracking after completion of the experiment. The sensors further described in this section and table 3.1 are science payload for photography collection, sensors used in the altitude tracking control, and the operational sensors used for post-mission analysis of the altitude tracking. It is assumed that the control systems for maintaining the correct heading are functioning independently.

	Autosub6000		Delphin2
Cameras			
	downwards and forwards		downwards, unused due to turbidity
Navigation sensors			
ADCP	Teledyne RDI Workhorse Navigator 300 kHz	IMU	MTi-30 4^{th} generation
	velocity over ground, v_{east}, v_{north}		heading, roll, pitch, yaw
	4 altitudes, average altitude, minimum altitude	compass	Oceanserver OS5500
INS	Oceano Ixsea PHINS FOG		reference heading
	Latitude, Longitude	pressure sensor	CTE9010GY7
	depth		depth
	v_x, v_y, v_z	altimeter	Tritech Micron Echosounder
	roll, pitch , yaw		altitude
Mechanical scanning sonar OAS			
	Tritech Seaking		Tritech Micron
	325 kHz		700 kHz
	vertical opening angle 3^o		vertical opening angle 3^o
	horizontal opening angle 20^o		horizontal opening angle 35^o
Key mission parameters			
goal altitudes	2.7m, 3m, 3.2m, ...	goal altitudes	0.6 m, 1 m
speed	1 m/s - 1.3 m/s	speed	0.3 m/s, 0.6 m/s, 1.0 m/s

Table 3.1: Comparison of altitude tracking with the two AUV platforms Delphin2 and Autosub6000.

For photographic surveys, Autosub6000 is fitted with a forwards facing (oblique) camera and a downwards facing (vertical) camera. Both are Grasshopper 2 models by Point Gray Research, with a resolution of 2448x2048 pixels, and opening angles of 26.7^ox22.65^o. The cameras are aligned with their wider side orthogonal to the direction of movement [Morris et al., 2014], their positions on the vehicle are indicated in Figure 3.3. The maximum frame rate of the camera is 15 Herz, the repetition rate of the strobe light system is $2Hz$; at 3.2 m altitude, one image is approximately $1.3m$ long.

When altitude tracking, both vehicles rely on the same measurands, but acquire the measurements using a different combination of sensor suites. The altitude, depth, and pitch angle are measured, and combined with the obstacle detection from the forwards OAS. On Autosub6000, the altitude is provided by the Acoustic Doppler Current Profiler (ADCP), which measures the altitude of the vehicle with four beams at a 20° angle; projected in the vertical plane, two beams are measuring at ±14° from the z-axis (see Figure 3.3). The pitch angle and depth are provided by the intertial navigation system. The navigation errors accumulated during diving are compensated trough a pre-defined manoeuvre in communication with the surface vessel.
On Delphin2 the altitude is measured by a dedicated altimeter measuring parallel to the z-axis, positioned in the front section of the vehicle. The altimeter is a Tritech Micron Echosounder; the sonar frequency is 500 kHz, the beam shape is a 6° conical beam. The altimeter has a minimum range of 0.5 m and a digital resolution of 1 mm [Tritech International Ltd]. The update frequency achieved with the software framework on Delphin2 is 2.5 Hz. If the altitude is less than the minimum sensor range, the altimeter returns larger readings, resulting in a terrain estimate below the actual terrain. When using only the altimeter, this increases the vehicle risk significantly, in the worst case the vehicle will try to reduce its altitude further, based on the high altimeter readings. The depth is provided by a pressure sensor and the pitch angle comes from an inertial measurement unit. Since Delphin2 is only used for short missions close to surface, no error compensation procedures are implemented, however a drift in the heading angle has been noticed over the passage of a day, so a less accurate compass without inbuilt sensor fusion is kept running for reference. A full list of sensor makes and measurands is given in table 3.1, the sensor positions for the two vehicles are indicated in Figures 3.3 and 3.4.

3.5 Vehicle Command and Control

For both vehicles, the control software is structured in a node structure where nodes can be considered as independent units, exchanging information through a well defined message system. The organisation in nodes makes it easy to modify and exchange one node without changing the rest of the system: as long as the same information is still made available by a node, the rest of the system does not need to adapt. Thanks to this structure, the obstacle detection and depth/altitude control nodes can be considered in-

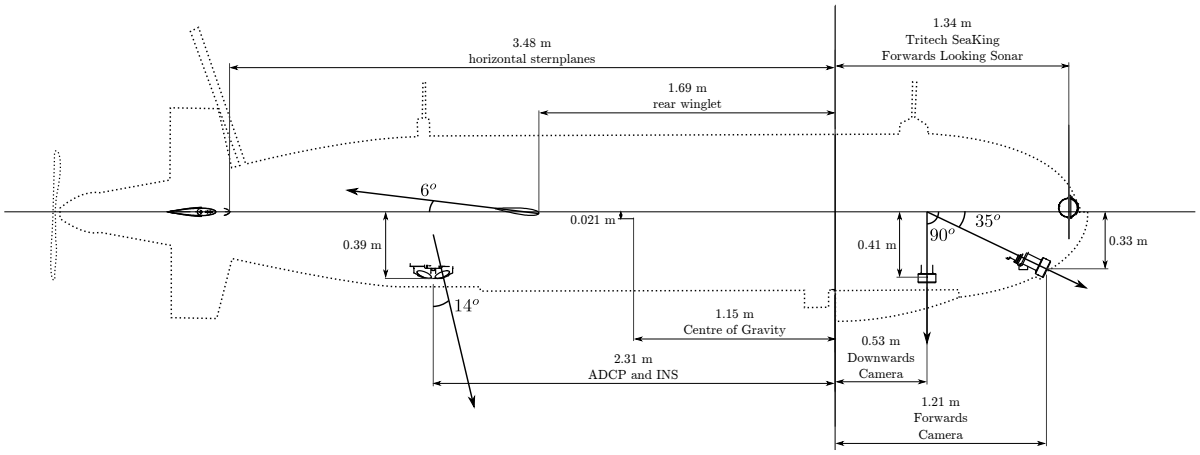

Figure 3.3: Side-view drawing of Autosub6000, indicating key sensor positions.

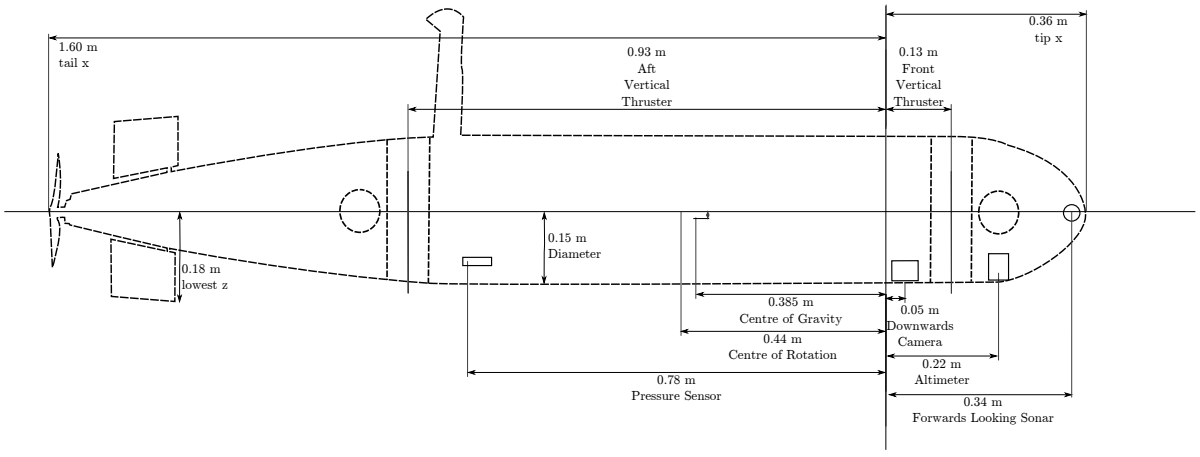

Figure 3.4: Side-view drawing of Delphin2, indicating key sensor positions.

dependently. In the case of Autosub6000, this distributed networked control architecture is implemented using LonWorks [1] [McPhail and Pebody, 1998]. In a similar manner to Delphin2 it is organised in sensor analysis, lowlevel-, and highlevel control, with several safety flags that can be raised by nodes and lead to changes in the behaviour of the vehicle. With the independent nature of the node structure, an analysis of the firmware beyond the depth control and obstacle detection nodes was not required for this thesis.

The firmware of Delphin2 is based on the Robot Operating System (ROS), a free and open source framework for robots that provides a communication structure for different sub-units (nodes) and a wide range of tools for processing, analysing, and visualising data [Quigley et al., 2009]. As a consequence of the availability and popularity of Robot Operating System (ROS) a large choice of library has been developed. Many other tools for robot development, like simulators or Simulink, have an interface for ROS. The ROS nodes that form the firmware of Delphin2 are structured in higher and lower level functionality (see Figure 3.5). At the highest level are the mission scripts and the fault response. The mission scripts describe the various actions that are to be performed during a mission. The actions are structured as states of a state machine. In the default configuration each action can exit as 'succeeded', 'preempted' or 'aborted' and each state can define the transition for each of those cases. In addition to the mission, the fault response is running in every mission. This node monitors properties that are key for the functionality of the AUV. If any of the sensor values leaves a defined safe range, it raises an error flag that will then lead to a state transition in the mission. In current missions this usually means the vehicle will switch off and as a consequence return to the surface, during lake experiments the vehicle will then make several attempts to return to its home position. The lower level nodes are the surge speed, depth, and heading control. To track an altitude demand, a depth demand is calculated based on the sensor data and the altitude demand. Below the lower level nodes are the actuator and sensor drivers. The actuators drivers translate the human readable actuator demand into output demands using the protocol of the actuators. The sensor analysis node adjusts the sensor settings based on parameters configured at the beginning of the mission; it analyses and filters the sonar data, and if the mechanical scanning sonar is used for horizon tracking it also re-configures the sonar scan angle.

On both vehicles, the altitude tracking control is implemented as a depth control, where the altitude error is added to the depth demand. When the obstacle avoidance is active, a pseudo altitude is calculated from the angle of the horizon and the current pitch of the vehicle (see Figure 3.10); the minimum of the altitude from the altimeter and the pseudo altitude are used to calculate the altitude error and thus the depth error. Figure 3.7 shows how the obstacle detection and depth control come together for altitude tracking on the two flight style vehicles.

Previous studies into the depth tracking performance of Delphin2 have utilised model predictive control [Steenson et al., 2014] and a cascaded PID controller [Tanakitkorn et al., 2016]. For this study the cascaded PID depth controller was utilised due to its

[1] LonWorks is the registered trademark of the Echelong Coropration

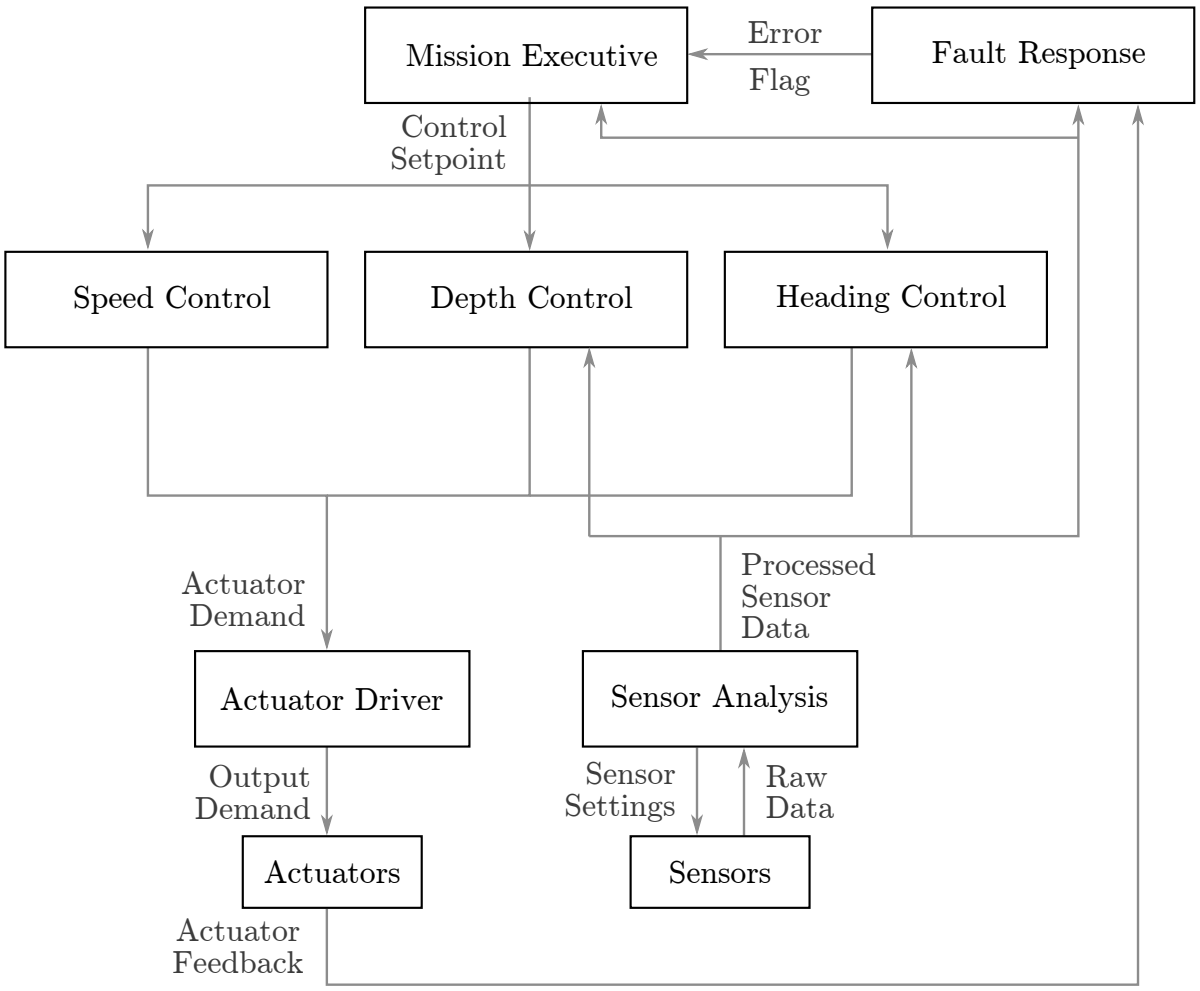

Figure 3.5: Diagram of the Delphin2 software structure.

similarities to the control on Autosub6000. Unlike on Autosub6000, the existing PID control scheme on Delphin2 is a combination of hover capable and flight style control, unified to work over a range of operation speeds. The contribution of the thrusters and horizontal sternplanes is allocated by applying a weighting function based on the forwards speed. The full control design is shown in Figure 3.6, with the split of flight style control (top) and hover capable control marked.

The weight functions w_{th} for the thrusters and w_{sp} for the horizontal sternplanes are given in (1) and (2) below. For both actuator sets, a transition speed is determined. The center of the transition between full thruster use at no thruster use is at the surge velocity u^*_{th}, the center of the transition to full sternplane use is at the surge velocity u^*_{sp}. The width of the thruster transition zone is σ^*_{th}, the width of the sternplane transition zone is σ^*_{sp}. Examples of weight functions are shown in Figure 4.15.

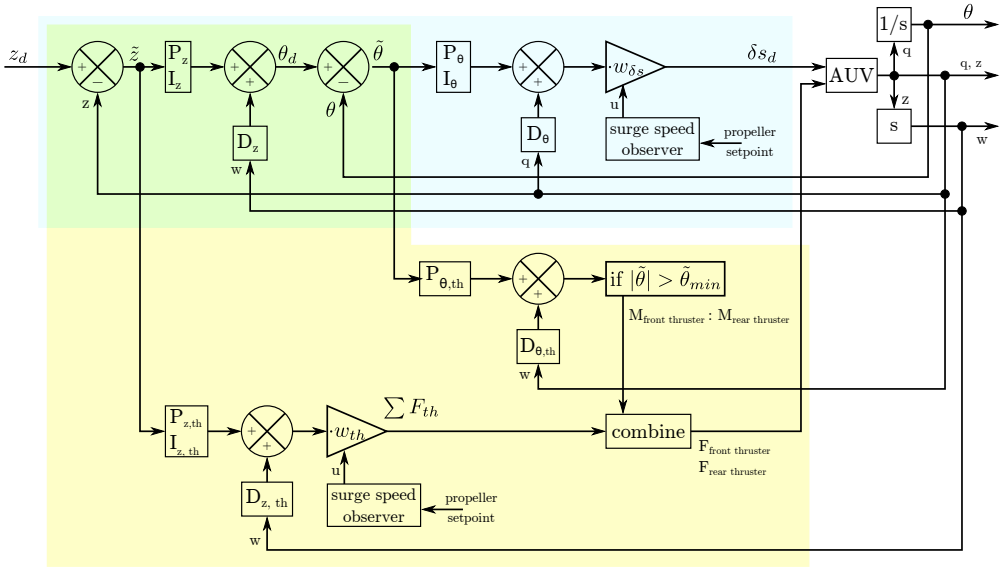

Figure 3.6: PID control scheme unifying flight style and hover capable actuation of Delphin2. The flight style (top) and hover style (top left, bottom) components are indicated.

$$w_{th} = 1 - \frac{1}{2}\left(tanh\left(\frac{u - u^*_{th}}{\sigma^*_{th}}\right) + 1\right) \tag{3.1}$$

$$w_{sp} = \frac{1}{2}\left(tanh\left(\frac{u - u^*_{sp}}{\sigma^*_{sp}}\right) + 1\right) \tag{3.2}$$

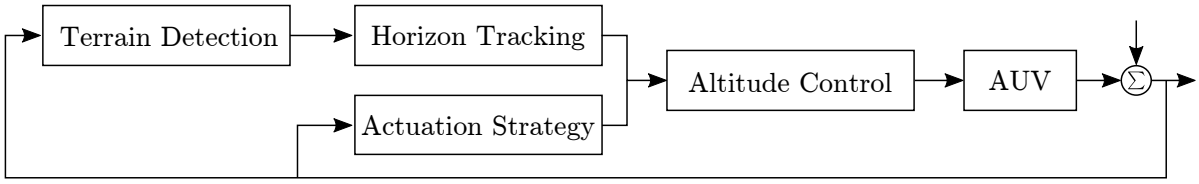

Figure 3.7: Block diagram illustrating the components of altitude tracking on Delphin2 and Autosub6000.

When using flight style acutation, the depth-pitch control on both vehicles is a cascaded PID-PD depth-pitch control shown in Figure 3.8. The equations for generating a pitch demand θ_d to reduce the depth error $\tilde{z}$ in the PID depth control loop, and a sternplane demand δs_d to reduce the pitch error $\tilde{\theta}$ in the PD pitch control loop, are given in 3.5. To avoid integral windup, the integral term I_z, calculated over the integration time TC_z in the depth control is limited to a maximum and minimum value. The proportional gains P_z and P_θ, the derrivative gains D_z and D_θ, the integration time TC_z, and the limits of the integral term I_z used during the Autosub6000 missions that are further analysed here are given in 3.3.

$$Pitch_{demand} = \theta_d = P_z \cdot \tilde{z} + I_z + D_z \cdot Rate_z \tag{3.3}$$

$$= P_z \cdot \tilde{z} + \frac{\sum_{TC_z} P_z \cdot \tilde{z} \cdot \delta t}{TC_z} + D_z \cdot Rate_z \tag{3.4}$$

$$Sternplane_{demand} = \delta s_d = P_\theta \cdot \tilde{\theta} + D_\theta \cdot Rate_\theta \tag{3.5}$$

For Delphin2, the control scheme was extended to work over a range of speed, using the vertical thrusters by adding a hover capable depth-pitch PID scheme, and applying a weighting function dependant on the forwards speed [Tanakitkorn et al., 2016]. The control scheme that is active for surge speeds between 0.3 m/s and 1.0 m/s surge speed is shown in Figure 3.6. The weight factors w_{th} for the thrusters and w_{sp} for the horizontal sternplanes are given in equations 3.7. Figure 4.15 illustrate the effect of changes in the transition speed u_{th} and the width of the transition zone σ_{th}.

$$w_{th} = 1 - \frac{1}{2}\left(tanh\left(\frac{u - u^*_{th}}{\sigma^*_{th}}\right) + 1\right) \tag{3.6}$$

$$w_{sp} = \frac{1}{2}\left(tanh\left(\frac{u - u^*_{sp}}{\sigma^*_{sp}}\right) + 1\right) \tag{3.7}$$

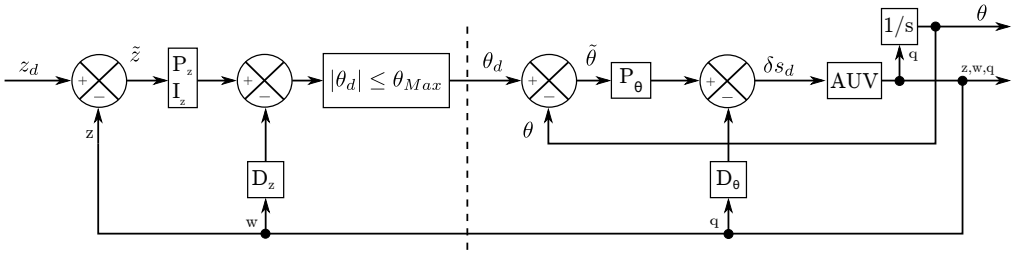

Figure 3.8: Cascaded depth-pitch PID control of Autosub6000 based on [McPhail and Pebody, 1998, Pebody, 2008] and code extracts.

Due to the ongoing development on Autosub6000, the depth control coefficients of Autosub6000 varied between missions during the cruises D343 and D377. A re-construction what coefficients were likely used during the missions is given in table reftab:asubMissions. On Delphin2 the P, I, and D terms were not changed since [Tanakitkorn et al., 2016], but the weight function of the thrusters was varied in some of the experiments.

3.6 Terrain Detection

The forwards looking sensor providing situational awareness for obstacle avoidance measures on both platforms is a mechanical scanning sonar. When making a sonar measurement with a mechanical scanning sonar, an acoustic pulse of approximately conic

beam shape, described by a vertical and horizontal opening angle, is sent. The direction of the beam in the rotational plane of the mechanical scanning sonar is given by the transducer angle.
As the sonar beam travels through the water, it is reflected by the terrain; some of those reflection return to the transducer and are magnified. The distance these returns travelled is estimated based on the time since the acoustic pulse was sent, up to a maximum time, corresponding to a maximum range. The measuring time since sending the pulse is split into discrete time steps, the so-called 'bins' (adumbrated in Figure 3.10). The intensity of the sonar signal returning to the transducer is then measured per bin, using an Analog to Digital Converter (ADC) after applying a configurable initial gain. These measurement results are then returned as a list representing the measured intensity for each bin with one value. Within the sonar transducer, pre-processing may already happen, from amplification to compensation for spreading and attenuation losses [Ltd, 2004]. The post processing for terrain detection is then applied to this list of bin returns. For a mechanical scanning sonar, the key parameters that can typically be configured in order to obtain a set of bins for analysis are:

- maximum and minimum scan angle
- angle step between two scans
- maximum range (or time interval per bin)
- number of bins
- initial gain applied to the received signal

Through the choice of maximum and minimum scan angle, a specific transducer angle can be selected as well.

On both vehicles, the mechanical scanning sonar is mounted so it scans in the vertical plane ahead of the vehicle (see Figure 3.10). The sonar returns are then analysed to detect if, and at which distance, a reflection from the terrain ahead occurred. Whilst the actual transducer angle may be different due to mounting details, the angles considered here are converted to be relative to the surge direction of the vehicle. A positive transducer angle α is pointing upwards towards the surface (see Figure 3.10).

The scanning sonar can change the angle at which a sonar ping is transmitted and received by a small angle step between measurements, which can be configured within the sonar limitations and is typically a fraction of a degree up to a small number of degrees. Using this step angle, the mechanical scanning sonar can then be configured to scan continuously over a sector, going through angle steps between the two angles limiting the sector. Instead, the angle can also be either increased or decreased by one step between individual measurements. On Autosub6000 the latter individual step control is used to track the highest angle ahead, at which a reflection from the terrain can still be detected. The scan angle is increased if a return from the terrain was detected until either no return is detected or a pre-defined highest scan angle is reached. If no terrain returns are detected, the sonar angle is decreased until a return is detected or a

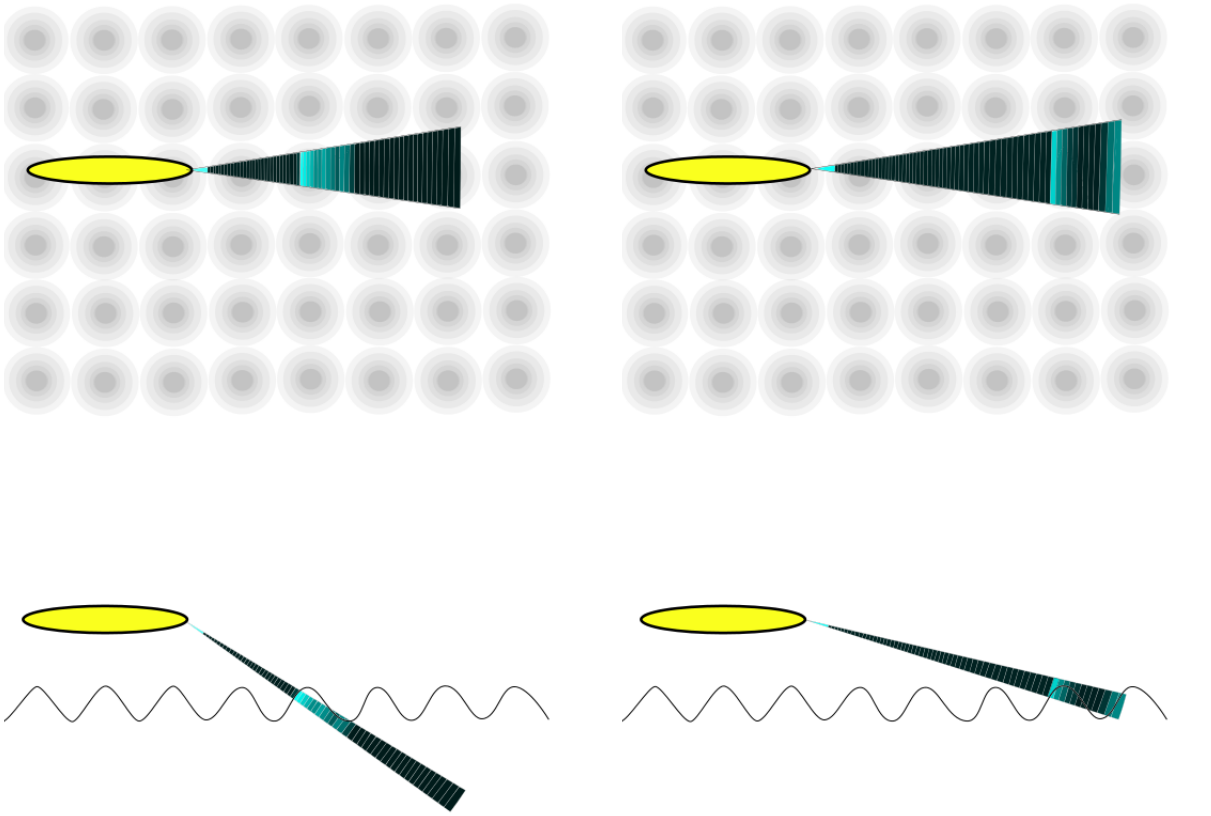

Sonar angle set for closer seafloor section

Sonar angle set for further away seafloor section

Figure 3.9: Example of resulting reflections. For a better impression what is represented in the sonar, a seafloor with a regular hill pattern is indicated. Brighter colours represent higher returns.

pre-defined lowest scan angle is reached. If the lowest angle is reached without a terrain detection, the sonar performs a continuous scan over the lower half of the scan sector ($\alpha \leq 0$), until a detection occurs.
Attempts were made to implement the same scanning method on Delphin2, however with a shorter detection range, the time to update the sonar angle between each scan is too long. It was found that faster terrain detection results were achieved by carefully selecting an angle sector for continuous scanning. The results of a detailed investigation in the scanning pattern and the achieved ranges are given in section 5.4.
For detecting the terrain ahead, Autosub6000 uses an impulse response digital filter. To ensure the vehicle would use the maximum pitch angle when passing over steep cliffs, a 'panic mode' is implemented. The 'panic mode' further reduces the pseudo altitude when an obstacle is detected closer than a minimum range. Furthermore a filter us applied to remove side lobes at a $-40°$ offset to the main sonar angle [McPhail et al., 2010a].

For Delphin2, the impulse respnse digital filter was tested and compared to other methods; for the Testwood lake experiments a fixed threshold was chosen. A detailed analysis

and comparison of the detection methods, as well as improvement suggestions, that were developed based on the data recorded at Testwood lake, can be found in section 5.4.

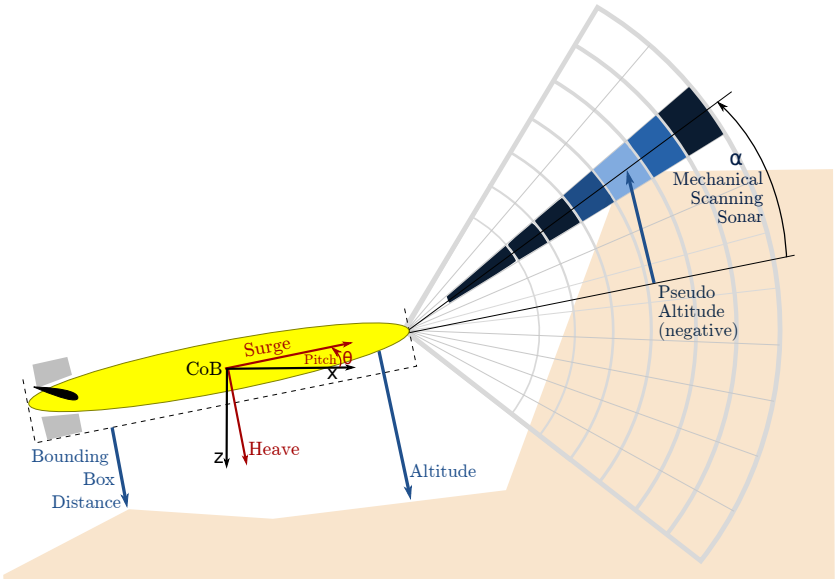

Figure 3.10: Illustration how the pseudo altitude is generated from the detected terrain ahead (altitude sensor as on Delphin2).

Both vehicles maintain a table with entries for each of the possible scan angles, indicating if terrain was detected in the last measurement at this angle. If terrain was detected, the table contains the range at which this detection was made as well as the pitch angle of the vehicle when the last measurement at this angle was made. The angle conventions used for the pitch angle θ and the sonar transducer angle α are given in Figure 3.10.

After each new measurement the highest angle $\alpha_{horizon}$ with a valid measurement is determined from this table. The table entries for the range and pitch at the angle $\alpha_{horizon}$ then yield the horizon range $Range_{horizon}$ and the pitch angle $\theta_{horizon}$ at the moment of the horizon detection. Combined with the current pitch angle θ_{now} they are used to calculate the pseudo altitude using Equation 3.8:

$$a_{pseudo} = -Range_{horizon} \times \sin\left(\alpha_{horizon} + \theta_{horizon} - \theta_{now}\right) \tag{3.8}$$

Horizon following is not yet full terrain following, since it does not consider all the details of the terrain, it only reacts to the highest angle at which the seafloor can be detected.

The key data of the mechanical scanning sonar on Autosub6000, a TritechSeaking scanning sonar, and that on Delphin2, a Tritech Micron scanning sonar, are included in the sensor comparison in table 3.1. Besides the depth rating, the most noteworthy difference is the different horizontal beam angle. As a consequence, the width of the area that is

scanned for obstacle avoidance is larger than for Autosub6000. Figure 3.9 visualises the beam spreading over a wider angle, how obstacles outside of the actual vehicle path impact it, and how this can lead to neglecting complex terrain structures.

3.7 Available Experiment Data

For Autosub6000, datasets from the four research cruises D343, D377, JC136, and JC142 were used for this research. Cruises are counted continuously for each research vessel, beginning with a letter indicating the research ship, 'D' for the RRS Discovery and 'JC' for the RRS James Cook. Each cruise includes several missions of Autosub6000; the different science missions per cruise are counted up continuously with the cruise number as a prefix, but the missions of Autosub6000 are also counted up over all cruises, with the prefix 'M'. As this work focuses on Autosub6000, the Autosub6000 mission index is used. Table 3.7 gives an overview of the cruises and lists the Autosub6000 missions that were selected for further used. Figure 3.11 indicates the location of the research missions. A full list of all available missions and details on the data sources can be found in appendix D.

Cruise no.	D343	D377	JC136	JC142
Cruise title	Deepwater trials of the Autosub6000 AUV, HyBIS, and telemetry systems	Autonomous ecological surveying of the abyss: understanding mesoscale spatial heterogeneity at the Porcupine Abyssal Plain	DEEPLINKS: Influence of population connectivity on depth-dependent diversity of deep-sea marine benthic biota	-
Cruise report	[McPhail, 2010]	[Ruhl, 2013]	[Howell et al., 2016]	-
Date Altitude tracking missions	sep/oct 2009 M23, M25	jul 2012 M50, M51, M53, M54, M55, M56, M57, M58	may/jun 2016 M115, M116, M120, M122	oct-dec 2016 M133, M134, M138, M139, M140
Existing papers	[McPhail et al., 2010a, Brito, 2015, Schillai et al., 2016]	[Wynn et al., 2014, Morris et al., 2014, Brito, 2015, Schillai et al., 2016, Durden et al., 2015b]	-	-

Table 3.2: Overview of cruises for which Autosub6000 altitude tracking data was analysed.

During each mission considered, Autosub6000 repeatedly follows a goal altitude whilst keeping a constant goal altitude. For the following work, each of the paths between which a constant altitude is kept, is called a section. Cruise and mission documents were used to re-construct the vehicle settings at the time; for mission analysis MATLAB files with post-processed mission logs were used.

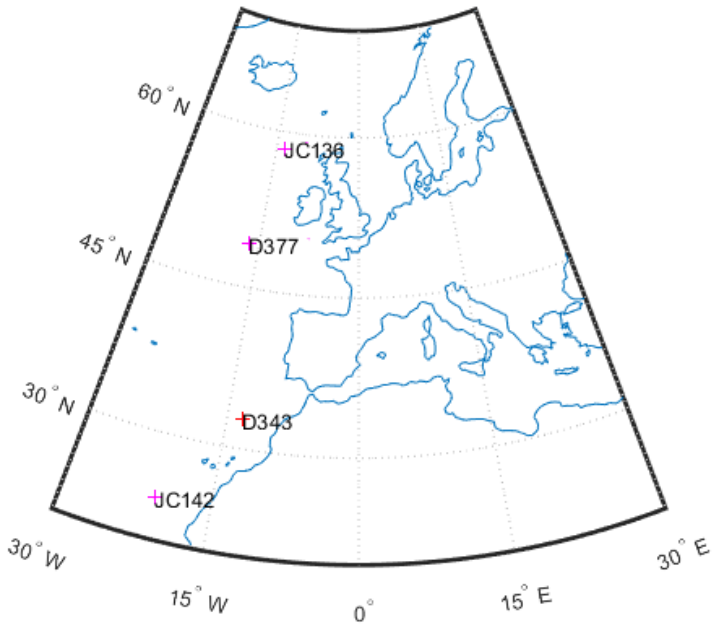

Figure 3.11: Map of the research cruise locations D343, D377, JC136, and JC142.

So far, a detailed analysis of the photographic results is only available for the photos from research cruise D377 for the downwards facing camera, in [Morris et al., 2014].

	altitude demands	OAS output used	collision noted	avg. speed over ground	surface buoyancy (positive)	P_z	D_z	TC_z	Max. I_z	Min. I_z	P_θ	D_θ	Max. θ	Min. θ	scale factor	motor power
M23	3-200m	True	-	-	16.6 kg	0.06	0.1	60	0.4	-0.1	2.2	6.0	0.6	-0.5	1.05	300 W
M25	3-50m	True	-	-	16.6 kg	0.06	0.1	60	0.4	-0.1	2.2	6.0	0.6	-0.5	1.05	270 W
M50	2.7-10m	False	-	1.18 m/s	9.6 kg	0.05	0.1	60	?	-0.1	2.2	6.0	0.3	-0.3	1.5	230 W
M51	2.7-10m	False	-	1.28 m/s	9.6 kg	0.05	0.1	60	0.03	-0.03	2.2	6.0	0.3	-0.3	1.5	250 W
M53	3m	False	1	1.15 m/s	9.6 kg	0.035	0.1	60	0.3	-0.05	2.2	6.0	1.0	-0.25	1.5	180 W
M54	3m	False	-	1.13 m/s	14.2 kg	0.03	0.1	60	0.4	-0.05	2.2	6.0	1.0	-0.25	1.5	180 W
M55	3.2-100m	False	-	1.12 m/s	14.2 kg	0.04	0.1	90	0.05	-0.05	2.2	6.0	0.6	-0.3	1.5	180 W
M56	3.2-100m	False	-	-	14.2 kg	0.04	0.1	90	0.05	-0.05	2.2	6.0	0.6	-0.3	1.5	180 W
M57	3.5-20m	True	3	1.09 m/s	14.2 kg	0.04	0.1	70	0.4	-0.15	2.2	6.0	1.2	-0.3	1.0	180 W
M58	3.2-50m	True	-	1.29 m/s	14.2 kg	0.04	0.1	90	0.1	-0.1	2.2	6.0	0.4	-0.3	1.0	230 W
M115	3m	True	-	0.97 m/s	13.5 kg	0.04	0.1	90	0.1	-0.1	2.2	6.0	0.4	-0.3	1.0	220 W
M116	3-110m	True	1	1.0 m/s	13.5 kg	0.04	0.1	90	0.1	-0.1	2.2	6.0	0.4	-0.3	1.0	220 W
M120	3m	True	-	0.96 m/s	13.5 kg	0.04	0.1	90	0.1	-0.1	2.2	6.0	0.4	-0.3	1.0	220 W
M122	3-90m	True	-	0.96 m/s	13.5 kg	0.04	0.1	90	0.1	-0.1	2.2	6.0	0.4	-0.3	1.333	220 W
M133	3-25m	True	-	0.88 m/s	17 kg	0.04	0.1	90	0.1	-0.1	2.2	6.0	0.4	-0.3	1.333	220 W
M134	3m	True	-	0.69 m/s	17 kg	0.04	0.1	90	0.1	-0.1	2.2	6.0	0.4	-0.3	2.0	220 W
M138	4-10m	True	-	0.94 m/s	17 kg	0.04	0.1	90	0.1	-0.1	2.2	6.0	0.4	-0.3	2.333	220 W
M139	3-25m	True	-	1.01 m/s	17 kg	0.04	0.1	90	0.1	-0.1	2.2	6.0	0.4	-0.3	2.333	220 W
M140	3-30m	True	-	0.86 m/s	17 kg	0.04	0.1	90	0.1	-0.1	2.2	6.0	0.4	-0.3	2.333	220 W

Table 3.3: Overview of Autosub6000 altitude tracking missions selected for further use.

For Delphin2 several experiments and tests were performed in the University of Southampton towing tanks and Testwood lake, a nearby lake with several hundred metres cross section and a depth up to ca. 4 m. Details on the test locations are given in section 4.9. A repeated set of altitude tracking experiments was performed at Testwood lakes between August 2017 and February 2018. For this dataset, Delphin2 repeatedly dived from two start positions, tracking a constant heading and altitude over a terrain ca. 0.6 m high step in the terrain. Between the repeated experiments over the same terrain, altitude tracking parameters were modified as given in table 3.7

Case No.	Altitude		Speed			Thrusters		Detection		Repeats	
	$0.6m$	$1.0m$	$0.3\frac{m}{s}$	$0.6\frac{m}{s}$	$1.0\frac{m}{s}$	original	varied	S_{th}	S_r	$A \triangleright B$	$B \triangleright A$
1)		■	■			■				2	1
2)		■		■		■				2	2
3)		■			■	■				2	2
4)		■			■		half			1	1
5)		■			■		full			1	1
6)		■	■			■		95		2	3
7)		■		■		■		95		3	2
8)		■			■	■		95		10	11
9)		■			■	■		85		2	2
10)		■			■	■		75		2	1
11)		■			■	■		95	1	1	1
12)	■		■			■		95		3	2
13)	■			■		■		95		2	2
14)	■				■	■		95		4	4
15)	■				■	■		75		1	1
16)	■				■	■		95	1	1	1

Table 3.4: Experiment Matrix for Testwood Lake experiments. An empty detection threshold S_{th} in the obstacle detection indicates that only the altimeter was used for obstacle avoidance. Repeats vary due to time limitations at the lake not allowing for all missions with a mission abort to be re-run.

Chapter 4

Methods

The quality of a photographic survey can directly be quantified through a range of criteria like area covered, resolution, and contrast. The parameters impacting these results are determined by the survey environment, the onboard camera system, and vehicle control components. The relationship between the quality factors and system parameters is discussed in detail in Section 2.2, and illustrated in Figure 2.1.

To simplify this complex relationship, it was decided early on that this work would focus on the altitude tracking and manoeuvrability components, with the altitude as an intermediate measure of the photo quality. The ability to keep a desired altitude has a direct impact on all factors required for good photo quality, and replaces a large set of parameters with a single value. At the same time, the altitude is also a good representation of the vehicle safety, a key contrary of the aim of keeping a low altitude. This simplification also reduces the amount of vehicle information required to compare vehicles, and is inclusive of vehicles that have not feedback of photographic data back into the control loop (e.g. due to collecting the camera data with a separate system).

As illustrated in Figure 4.1, a control system capable of tracking an altitude demand can be extended further, by generating an altitude demand (or an altitude change demand) based on beforehand plans or in-situ photo analysis. Using previously determined photo quality requirements and estimates of the water quality, an altitude goal may be determined, e.g. as a range of suitable altitudes. If the loop is closed by directly analysing the acquired photos to analyse the photo quality, or if an area should be surveyed with a different set of requirements, the goal altitude may be adapted during the mission. After this outer control loop, the survey goal altitude may be compared to vehicle safety requirements to obtain an altitude demand. In control systems similar to Autosub6000, this altitude demand is then transformed into a depth/pitch demand. In the inner control loop, the required actions of the available actuators are determined.

This analysis of terrain following with flight style AUVs focuses on the two vehicles Autosub6000 and Delphin2. According to fluid dynamic theory, results on the vehicle dynamics are transferrable to vehicles operating in a similar flow regime. To show com-

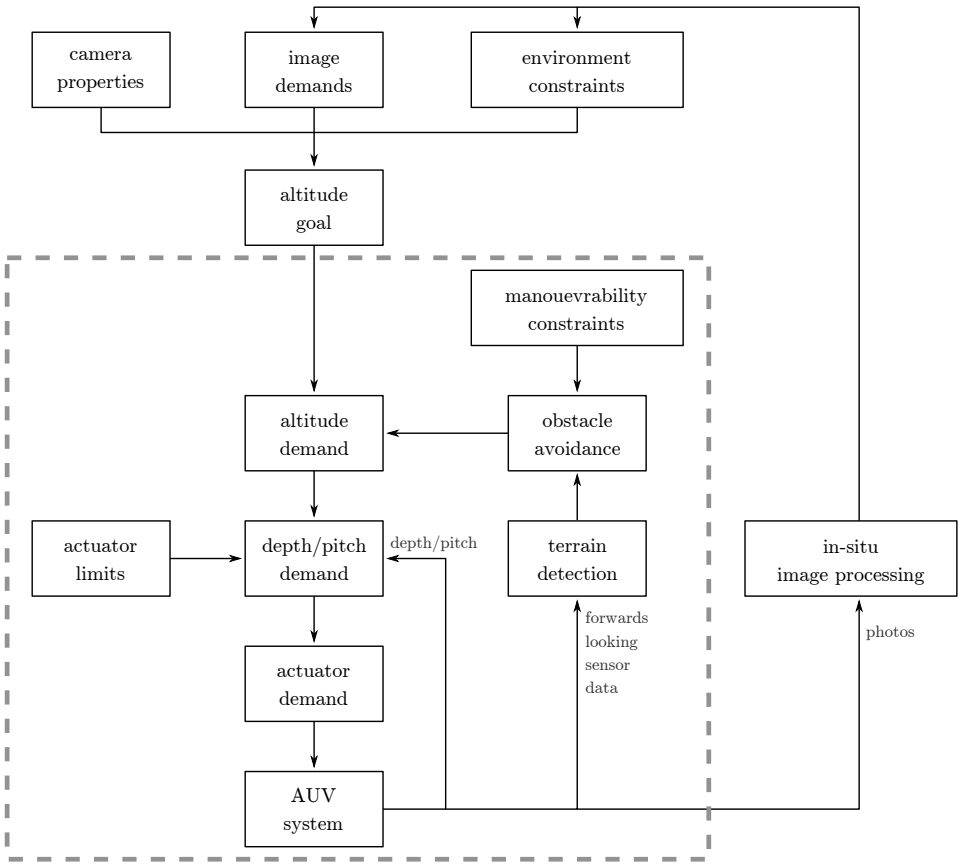

Figure 4.1: Diagram of the full photographic survey altitude control system. The area of focus of this work, tracking a given goal altitude in unknown terrain, is marked by the dashed line.

parability, the Froude and Reynolds numbers based on the vehicle length are included both in the overview of photographic survey vehicles (Table 2.1) and in the overview of the vehicles analysed in experiment and simulation (Table 4.2). The vehicles are operated with Reynolds numbers between $0.59 \cdot 10^6$ and $8.33 \cdot 10^6$. This is at the transition between laminar and turbulent flow regime ($0.5 \cdot 10^6$ to $1 \cdot 10^6$) and slightly above. The flow is subcritical with Froude numbers ranging from 0.1 to 0.4. The Reynolds numbers for the sternplanes are all below $4 \cdot 10^5$ and thus operating in the laminar flow regime, assuming that there is no disturbance e.g. from thrusters.

The terrain following analysis is performed using three complementary approaches:

- Analysis of existing Autosub6000 mission data
- Vertical plane simulation of Autosub6000
- Small scale experiments with Delphin2

The goal of the analysis of existing Autosub6000 data is to understand what the capabilities and limits of the current altitude tracking implementation are. Based on this,

a simulation is implemented to better understand small changes in key parameters. Finally, an altitude tracking system similar to that on Autosub6000 is implemented on Delphin2 to test changes in experiment, validate if the key problems identified for Autosub6000 apply to Delphin2, and to establish Delphin2 as a small scale platform for testing altitude tracking for a wide range of flight style and hover capable AUVs.

Before describing the three analysis approaches, the methods shared amongst all three are introduced: the reference system and sign convention that was used for all systems, the vehicle motion simplifications and the consequences thereof, how the mission risk and success are quantified, and the software tools that were used.

4.1 Reference System and Sign Conventions

Typically, AUV motion of a scale of a few kilometres or less is described using global and body fixed reference frames as described in [Fossen, 2011, section 2.1]. This applies to the scales of the Autosub6000 and Delphin2 experiments considered here. All reference frames used are right handed frames; the global reference frame usually uses the North-East-Down (North-East-Down (axis conventions for global reference frame) (NED)) convention, pointing the x, y and z axes in north, east and down direction respectively. The body fixed frame axes coincide with the longitudinal, transversal, and normal axis of the vehicle. This vehicle attached frame system is used for considerations of velocities (surge u, sway v, and heave w), as well as rotations (roll p, pitch q. and yaw r).

During photographic missions, the vehicle typically moves along a linear path that is pre-defined by the waypoints selected for the mission (see mission paths in Figure 4.11). It is not expected to accelerate or rotate in a direction outside the vertical plane. Whilst in reality the path has a grid shape, it can be split into linear sections and the reference frame can be simplified to the vertical plane only. The consequences of this are discussed in the next section. For the reference frames used here this means the y-axis is omitted, and the global fixed frame is aligned with the vertical plane of motion of the vehicle. The global reference frame is therefore not aligned with cardinal directions. The global frame axes are reduced to the x-Axis, which is positive in the direction of movement of the vehicle, and the z-Axis, which gives the depth, pointing from the water surface downwards. This is illustrated in Figure 4.2.

Assuming positive surge velocity $u > 0$, a positive pitch angle $\theta > 0$ leads to the AUV's surfacing. Moments that contribute to a positive pitch angle can be obtained by setting a positive sternplane angle δ_s or, if available, using the leaver arms l_{aft} and l_{front} of the aft and front thrusters, to generate a pitching moment. A positive, upwards pitching moment is achieved by configuring the thruster forces so the difference between the aft thruster force F_{aft} and front thruster force F_{front}, and thus the sum of aft moment M_{aft} and the front moment M_{front} is larger than zero.

$$0 \leq M_{aft} + M_{front} = F_{aft} \cdot l_{aft} - F_{front} \cdot l_{front} \tag{4.1}$$

The vehicle is moving along a linear path, over a terrain that is given as a two dimensional profile. The points of the profile are given as depth values, taken as positive distances from the water surface (or, in case of simulations, any reference zero depth). The vehicle position in the global frame is given as a z position (depth) from the reference zero depth, and a progress from the start position in the x-direction.

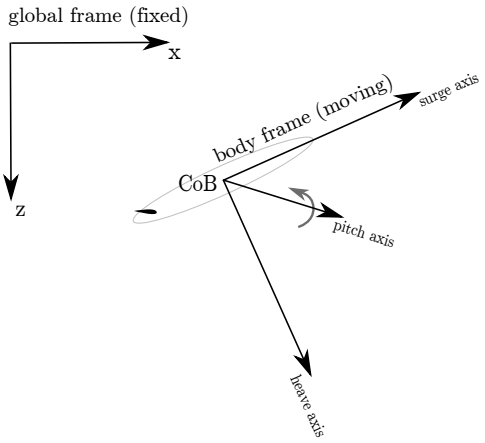

Figure 4.2: Illustration of the reference frames used in in simulation and analysis. The vehicle surge axis is assumed to always be in the global frame x-z plane.

The altitude is the vertical distance measured from the vehicle to the terrain. It is measured from the bottom of the hull, at the x-position of the altitude sensor (altimeter on Delphin2 and ADCP on Autosub6000), pointing in the positive heave direction (downwards), parallel to the heave axis. The sonar beam transducer angle gives the position of the scanning sonar beam in the vertical plane. Zero degrees are aligned with the forwards heave direction. At a positive scanning angle, the beam points towards the surface (see Figure 3.10). Both the altimeter and the scanning sonar beam are simulated as ideal beams, without opening angle.

4.2 Simplifications

Both the simulation and the observation of AUV experiments are limited by computational power, available sensor data, and simplifications made in the analysis to reduce the complexity of the problem. This section discusses key simplifications and their impact on the obtained results.

4.2.1 Vertical Plane

The vertical plane simplification is a motion, sensory, and obstacle avoidance strategy simplification. Regarding the vehicle dynamics, the assumption that the motions in the vertical and horizontal plane are independent is regularly made. The statistical analysis and plots of Autosub6000 missions in the Appendix support this simplification with small average roll values and very small heading change rates outside of the turning areas of the lawn mower pattern. The horizontal sternplanes are considered as a pair that is moving synchronously, whilst the vertical sternplanes are neglected for analysis and simulation.

For the sonar detection, a number of sources for false detections are neglected as a result of the vertical plane simplification. These are discussed separately in the next section. It is assumed that the difference between the vehicle heading and its direction of motion in the horizontal plane is small, so its terrain detection overlaps with its path. From the perspective of improving the obstacle avoidance, a range of options that include an obstacle avoidance strategy to the side are dismissed before considering them. However, it can be argued that the current limitations of the forwards looking sensors make it difficult to plan such manoeuvres anyway.

4.2.2 Sonar Sensors

As illustrated in Figure 3.9, the opening angle of sonar beams results in an increasing amount of returns from terrain features outside of the vehicle path as the sonar range increases. On Delphin2 and Autosub6000, the sonar beams in question are the altimeter and DVL beams respectively, as well as the forwards looking mechanical scanning sonars. These in particular have a very wide horizontal opening angle (see Table 3.1). For the analysis of Delphin2 and Autosub6000 experiments, the non-ideal beams are nonetheless represented by a single measurement. The altimeter beams are assumed to be pointing downwards in the heave direction. In case of the four ADCP beams of Autosub6000, it is unclear if the beam ranges and their average value have already been compensated for the angle of the beams relative to the heave direction. Since the error is small (less than 3%), the average ADCP value as recorded is used without further compensation.

Whilst in reality, the mechanical scanning sonar beams are described by an opening angle in both the horizontal and vertical direction, for this work the sensors are simplified to only open in the vertical plane. This simplifies the simulation, where otherwise choices about additional terrain features would need to be made. This removes the impact of complex terrain features in the horizontal plane, which may cause a detection and avoidance of features that are not in the direct vehicle path, and as a consequence reduce survey success, but would not compomise mission safety. Homogenous features, like the step features used at Testwood lake, are well represented as long as they are approached without a heading or roll error. When the vehicle is operating with a non-zero roll angle or a heading error, the sonar beam is tilted with the vehicle, and as a result

misaligned to the terrain compared to the expected scanning pattern. This particularly impacts of repeated studies, since the assumption of a comparable terrain needs to be questioned. The impact of roll and heading errors on the terrain detection are analysed for the example of the conditions in the testwood lake experiments (see Section 4.9.1 for a detailed description of the terrain feature).

The overestimate of the terrain height due to vehicle roll is analysed in B. Inserting the 0.6 m step height at the experiment site (see 4.9.1), and the observed sonar detection range of 3 m (see 6.4), the upper limit for the terrain overestimate is calculated from B.5. The resulting error, split into the two error components described in B, the resulting Error for the step in Testwook Lake is shown in Figure 4.3. Whilst tracking a constant heading, the roll stays close to zero. The combination of maximum roll during heading tracking, roll offset, and the mounting offset are estimated to remain below 5°. The terrain overestimate due to roll thus remains below 0.1 m.

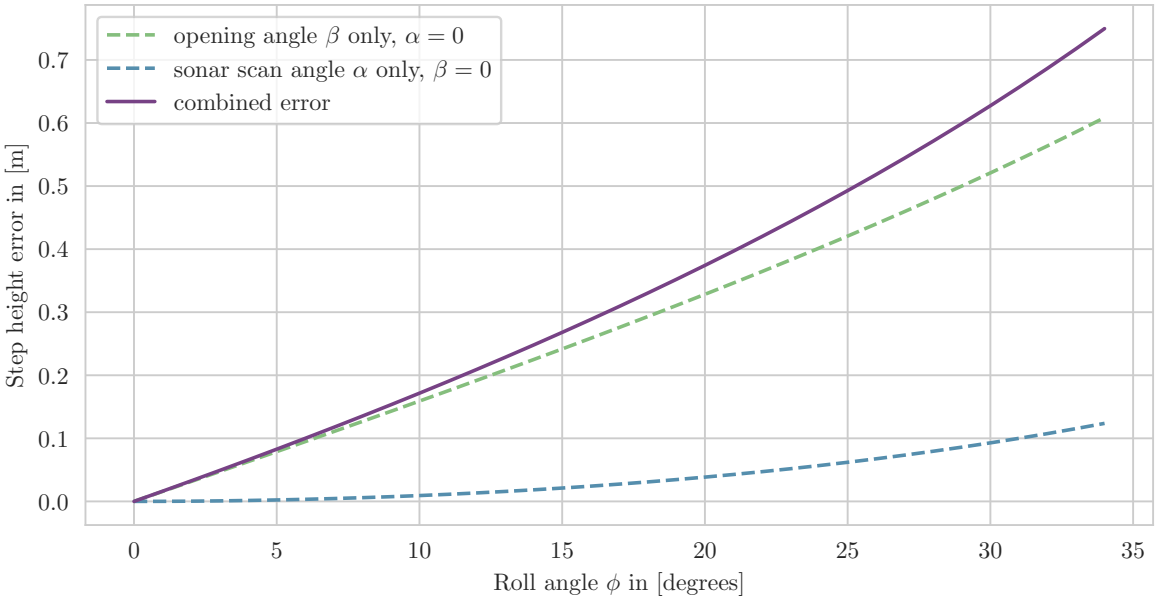

Figure 4.3: Upper limit of the terrain over-estimate due to roll error for the Testwood Lake experiments with Delphin2.

Approaching the terrain step with a heading error results in an underestimate of the distance to the terrain. A geometric analysis of this error is given in A. This assumes that the reflections from the terrain can still be distinguished from the noise levels when spread over a larger number of bins. Figure 4.4 shows the upper limit of the terrain distance underestimate due to heading error for the Testwood Lake experiment. After dismissing some of the worst heading errors from the experiment data (since the experiments goal was not heading reliability, but repeated passing of a comparable terrain), the heading error of the analysed data is below 10°, and thus the expected terrain distance underestimate below 0.05 m.

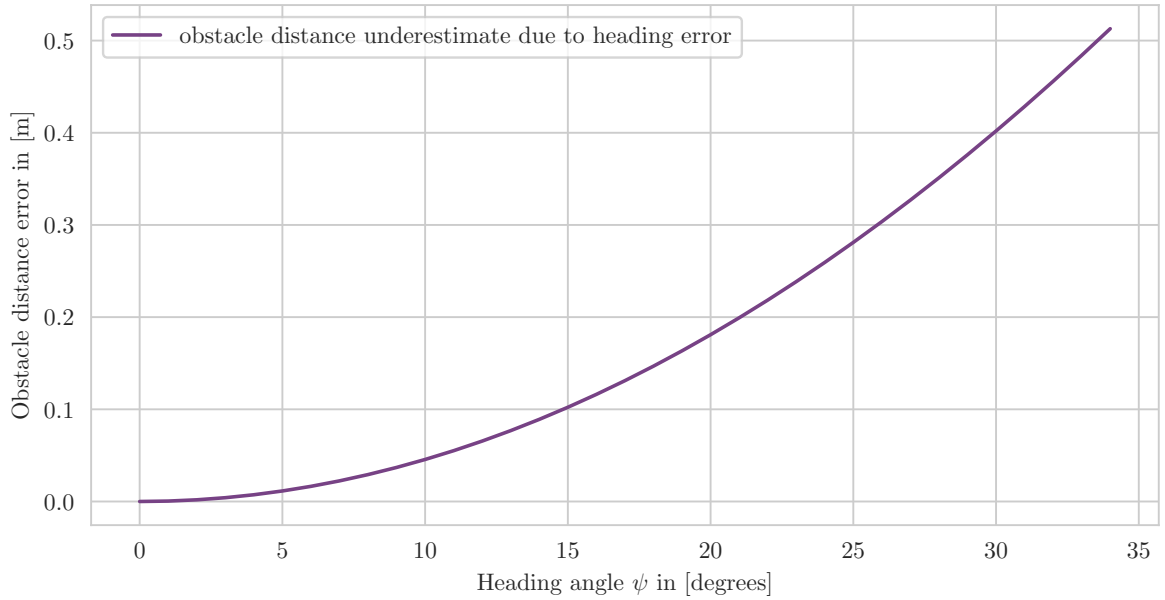

Figure 4.4: Upper limit of the terrain step distance under-estimate due to heading error for the Testwood Lake experiments with Delphin2.

Both of these errors reduce the photo success, as the vehicle reduces its depth in reaction to both a terrain overestimate and an early obstacle detection. In addition to these false estimates, the sonar reflection from the terrain also looses its clarity when it is distributed over several scan angles, or when additional terrain features add high levels of noise. This effect is more difficult to simulate, whilst also presenting a vehicle risk. However, the analysis of the lake test sonar data showed that with the current sonar analysis, other causes of error have a more significant impact on the detection range.

4.2.3 Deeply Submerged in Still Water

It is assumed that the operating conditions for both Autosub6000 and Delphin2 are close to those of operating deeply submerged in still water. Autosub6000 is operated at sufficient depth to be certain that the wave disturbance at the water surface can be neglected. Whilst Delphin2 is diving at much smaller depths, the lake surface was barely disturbed during all test days, with occasional small ripples from a gust. Whilst operating close to the seabed/lakefloor, it is assumed the distance at most times is sufficient so suction forces or increase of added mass occur [Burcher and Rydill, 1994, p. 155], and thruster efficiency reductions can be neglected. As can be seen in the results for Delphin2 with thruster actuation, this last assumption needs reconsideration for more complex flight style and thruster actuation combinations.

Whilst it is assumed that the vehicles operate in still water without currents or eddies,

constant currents with small components orthogonal to the direction of movement effectively stretch or expand the terrain. The vehicle will maintain a constant surge velocity relative to the water stream, so the hydrodynamic derrivatives remain applicable. The distance of terrain features to the vehicle needs to be compensated accordingly in the obstacle detection step though. Depending on whether the vehicle tries to compensate for the sidewards current (and thus approaching the terrain at an angle) or keeps a constant heading angle whilst drifting sidewards, different additional terrain detection errors are introduced, similar to those due to a heading error. As long as angle between the direction of movement and the goal heading is smaller than half the horizontal opening angle, the vehicle still gets information about the terrain it is moving in. In more complex terrain, eddies may form and contribute additional disturbance both to the dynamic behaviour of the vehicle and the terrain reconstruction.

4.2.4 Fixed Surge Velocity

Furthermore, to focus on the vertical plane control it is assumed that a constant surge velocity is maintained by a separate control loop, rather than being propelled with constant power. This simplifies the simulation significantly, since no separate controller is needed and surge and pitch dependand drag forces can be neglected. However, this leads to an overestimate of the manouvrability, since the loss of speed when changing pitch is neglected. Whilst in the simulation used here, the largest pitch angle indeed provides the best possible pitch change rate, after consideration of surge velocity reduction due to drag a better pitch change rate may be achieved with smaller pitch angles In citep[p. 154]burcher1994concepts this case is made for the heading change, the equivalent manoeuvre in the horizontal plane. As a result, the depth change rates are optimistic, or, if the vehicle is slowed down by a too fast pitch angle change, controllability may reduce. With conservative pitch angle limits in place, the latter case is unlikely.

4.2.5 Small Variations around Operation State

Finally it is assumed that all operating conditions are close enough to the state for which the hydrodynamic coefficients were determined. Whilst many effects, such as added mass, or Munk Moment, are already captured in the hydrodynamic coefficients from the towing tank test, the assumption is that the operational states are not far outside the states considered in the tests, so the linearizations are valid and no additional effects, e.g. stall on the control surfaces need to be considered. This assumption is made since the sternplane angles are limited below 25° and the Reynolds number for all considered vehicles is in the laminar flow regime (see 4.1).

4.2.6 Terrain Reconstruction From Mission Data

To be able to understand the complexity of the terrain, and later on to simulate the terrain, the terrain needs to be re-constructed from the in-situ data collected during the mission.

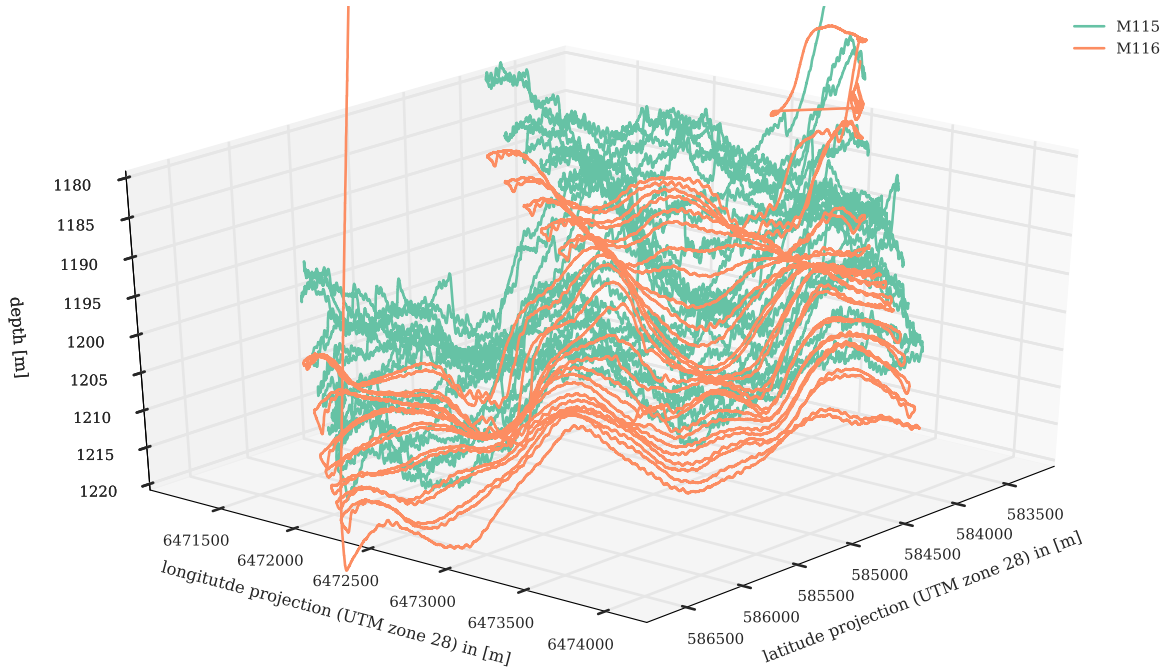

Figure 4.5: Missions M115 and M116 were run using the exact same waypoints. After bad altitude tracking results for M115, the sonar head on the AUV was aligned for M116.

Whilst at a first glance, this seems like a simple enough task, adding the altitude and depth measurements, missions M115 and M116 demonstrate that the motion of the vehicle itself can result in terrain estimate variations of over one metre. Both missions were run using the exact same waypoints, however during the first mission the altitude tracking did not perform well, the altitude remained well above the goal altitude and the vehicle performed an oscillating motion in the vertical plane. The rotation at which the mechanical scanning sonar was mounted was then adjusted and the mission was re-run with successful altitude tracking in M116. Whilst due to navigation inaccuracies the exact vehicle path over the terrain is not the same, the mission paths can be aligned well enough to compare the terrain reconstruction over a similar area of the terrain. A 2.5 km long section of such a matched terrain area is shown in Figure 4.6. The simplest reconstruction method of adding the depth and altitude was chosen for the terrain estimates in this figure.

In an attempt to improve the terrain estimation, the problem was further analysed. Since the INS, where the depth data is collected, and the ADCP are almost in the same position, there is no requirement to compensate for any changes of the relative positions

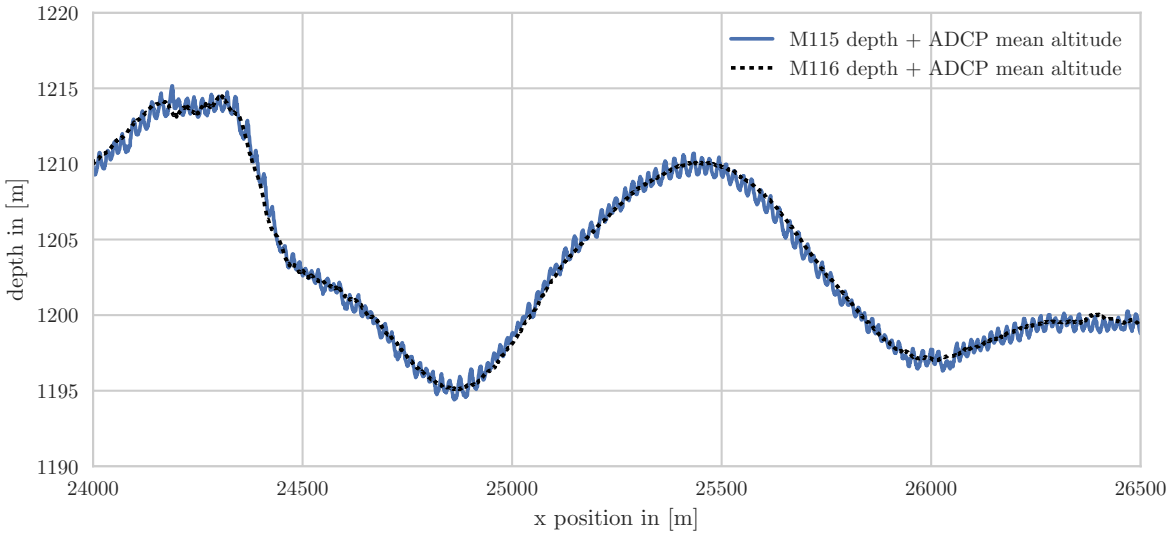

Figure 4.6: Comparison of a similar terrain area, reconstructed from in-situ data of M115 and M116.

of the sensors due to the vehicle motion.
The four individual beams from which the average altitude is calculated can be further processed, e.g. by choosing for each measurement the beam that measured the minimum altitude, or selecting one single beam for the re-construction. The altitude can also be compensated for the pitch angle. For a maximum altitude of 10 m, and a pitch angle variation of $\pm 10^o$ this still only accounts for a variation of less than ± 20 cm. Examples of these different variations are shown in Figure 4.7. Whilst the resulting terrain estimate changes slightly, the overall variability remains. A plot of the depth only, with the average altitude added to offset it closer tot the terrain estimate, shows that the oscillation pattern can be found in the vehicle depth. The length of one oscillation is around 25 m, consistent with the pitch angle change, and thus realistic for the motion range of a flight style AUV. With the information available, it is unclear if the depth measurement is accurate and there is an unaccounted error in the altitude measurement, or if there is an error (e.g. an exaggeration of the oscillation motion) in the depth measurement.

It must also be noted, that without having the second data set over the same terrain, as is the case for most available data, it is more difficult to determine if the terrain estimate is realistic. Whilst a regular oscillation over an entire mission may arouse suspicion, sandwaves with a relief of 1.5 m to 25 m, a wavelength of 30 m to 500 m and an extent up to tens of kilometres can occur naturally [Allan, 2000], thus making it difficult to determine which oscillation is due to the terrain, and which due to sensor and reconstruction method errors.

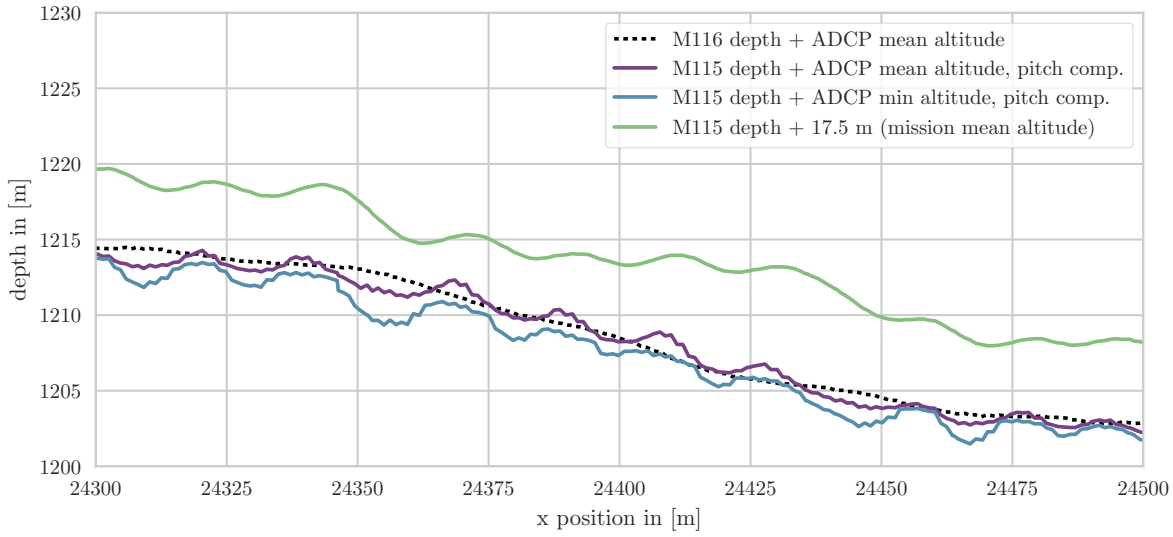

Figure 4.7: Comparison of different (unsuccessful) compensation methods in an attempt to reduce the oscillation in the terrain reconstruction.

4.3 Quantification

To be able to compare results, and apply the information learned from simulations and experiments to different vehicles, quantification methods have to be found. Whilst it is interesting to see a real or simulated vehicle path and different data about the vehicle under given conditions and a given terrain, a quantifiable way of describing vehicle risk and success is more desirable. Furthermore, measures that may be understandable to the operator of the vehicle are less meaningful to the user of the vehicle data. To empower scientist choosing vehicles for their purposes, the measures that describe the expected results to them need to be adapted to their needs.

4.3.1 Photographic Survey Quality

For vehicle operation purposes, a fixed goal altitude is usually set. The distance from which a photo can be used for scientific purposes is less clearly specified. Often photos within a certain range of distances are included for further analysis, and inquiries with scientists if a specific distance would be their ideal distance remained without a clear answer. In the further analysis, the range of altitudes within which photos are considered useful is called the photo success zone. It is indicated in Figure 4.8. The mission success quantifies the photo quality by giving the percentage of the total mission where the altitude remained within this area.

For mission success evaluation in the simulation, where the simulation terrain is available in full detail, the photographic mission success is calculated as the distance between the

camera and the centre of the recorded frame, also called the 'photo centre altitude' (see Figure 4.8). For experimental data, the altitude is considered a sufficient representation of the camera distance, since larger variations are expected from the terrain variability, which is difficult to quantify even when using all available data at the end of a mission (see section 4.2.6). For evaluation of Autosub6000 missions and simulations the photo success range of 1.9 m to 4.2 m, as specified in [Morris et al., 2014], is used. On Delphin2, the altimeter is positioned next to the camera (though in Testwood lake no photos were recorded due to algae). Since the altimeter minimum range on Delphin2 can cause an over-estimate of the altitude, a second altitude estimate was calculated by subtracting the depth measurement from the water depth at the estimated position. Unlike the altitude measurement from the altimeter, which is parallel to the vehicle-fixed z-axis, this altitude measurement is parallel to the global z-axis. The measurement zero is also at the bottom of the hull, and its x-position is that of the Centre of Buoyancy (CoB).

Future analysis, particularly for determining altitude tracking missions and strategies with a scientific goal in mind, may also look at gaps and overlaps between photos, minimum resolution, and a success function that varies with the altitude, scoring photos less binary between useful and not useful. For now these measures were neglected since they vary largely based on camera type and mission goals.

4.3.2 Vehicle Risk

Similar to the vehicle success, the risk quota is also given as a percentage of the full mission length. Due to the low goal altitude, at the same order of magnitude as the vehicle dimensions, the vehicle can not be simplified to a point for evaluating the risk to the vehicle: Whilst the altimeter may measure a safe distance to the terrain, other parts of the vehicle might already be in contact with the terrain. In addition, a faulty sensor measurement might lead to a sudden wrong altitude demand, causing an unexpected motion of the vehicle.
To reflect the full vehicle size, in the simulation analysis a bounding box is fit around the vehicle (see Figure 4.8). The y-direction is limited by the front and aft of the vehicle, in the z-direction the lowest point of all vehicle components yields the limit.

For each measurement or simulation step, the shortest distance between the terrain and the bounding box is determined as the collision distance. A collision distance of zero or less represents a terrain collision. To consider potential movement of the vehicle, further risk zones are defined. Since the maximum/minimum pitch angle defines the demand limits of controller and thus the range of motion of the AUV, it is used to calculate further risk zones: The distance by which the tip and tail of the vehicle move when one of the extrema of the pitch angles is reached is estimated as the 'lowest tail' and 'lowest tip', and subtracted from the collision distance. For Autosub6000 this gives $lowest\_tip \approx 1.3m$ and $lowest\_tail \approx 2.9m$. The collision distance is therefore split into four regions:

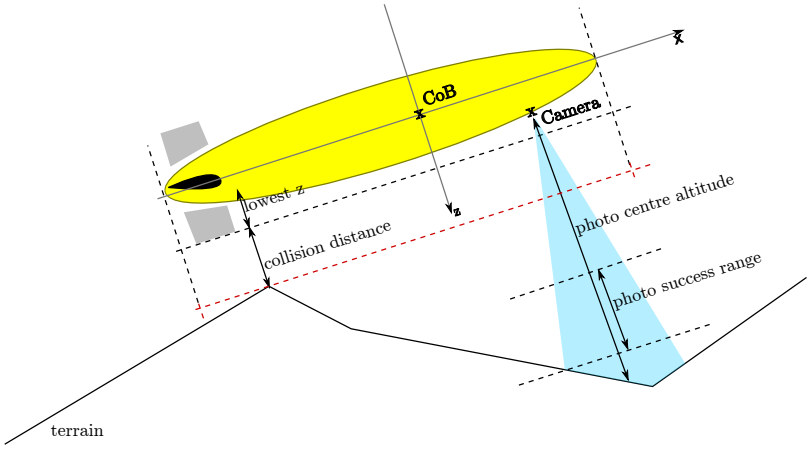

Figure 4.8: Illustration of bounding box, collision distance and photo centre altitude.

1. $collision\_distance < 0$: collision.
2. $collision\_distance < lowest\_tip$: tip collision possible.
3. $collision\_distance < lowest\_tail$: tail collision possible.
4. $lowest\_tail < collision\_distance, lowest\_tip < collision\_distance$: collision unlikely

A nose collision is considered more severe, since it has a higher risk of damage that can change the buoyancy of the vehicle, whilst a tail collision may have a severe impact on the manoeuvrability but is unlikely to change buoyancy. For the remainder of this work, the risk quota uses the 'tip collision possible' risk zone. Since much of the information needed to calculate a detailed risk analysis is not available for experimental data, the 'lowest tip' distance is used as a minimum altitude for estimating the risk quota.

Whilst on Autosub6000 the terrain information is not accurate enough for a detailed risk calculation, the surface map available at Testwood allows for the introduction of a third

measure for the terrain distance of Delphin2. It is implemented by fitting a bounding box around the Delphin2 vehicle (see Figure 4.8 for illustration and Figure 4.14 for the length and lowest z-coordinate of Delphin2). Using the estimate of the x-position and the terrain estimate, and considering the current pitch angle, the shortest distance of the bounding box to the terrain was used to better describe the collision risk of the entire vehicle rather than that of just a selected point. The zone limits used for estimating vehicle risk are indicated in Figure 5.33. With the altimeter failing to detect correct values below 0.4 m altitude, the risk zone was set at this altitude.

4.3.3 Cost of Transport

On Delphin2, the power consumption can be estimated based on measurements of the battery voltage and currents to various devices. However, statistics on power consumption on the vehicle miss one key information for understanding mission performance: they do not take the distance covered into consideration. A normalised measure that considers the energy required to move a vehicle by a unit distance is the Cost Of Transport (COT) [Murphy and Haroutunian, 2011].

$$COT\left[\frac{J}{m \cdot kg}\right] = \frac{\text{Energy}[J]}{\text{Distance}[m] \cdot \text{Mass}[kg]} \tag{4.2}$$

This evaluation was only performed for Delphin2, since no detailed information on the power supply system on Autosub6000 was easily accessible.

4.3.4 Extrapolation to Battery Charge

Whilst the cost of transport is very useful for comparing vehicles as well as different configurations of the same vehicle, it is not necessarily meaningful to mission planners. With increasing vehicle endurance, most vehicles are limited by the available battery charge rather than mission time. Once the cost of transport and the available battery capacity are known, estimates of total mission length, photo success length and mission length at risk can help choose the vehicle configuration best suited for achieving the survey goals. Once the available camera equipment is known, the expected image frame width can also be used to calculate a total area covered.

4.3.5 Dimensionless Generalisation

In vehicle dynamics tests with scaled models, a transfer to the full scaled model is made via a dimensionless generalisation. To be able to understand and transfer what can be learned from the altitude tracking experiments on Delphin2 for Autosub6000 and other

	Autosub6000	Autosub6000 non-dimensional	Delphin2	Delphin2 non-dimensional
Vehicle length L	5.5 m	1 L	1.96 m	1 L
Sonar				
Update rate r	$0.8\,s^{-1}$	1 r	$0.6\,s^{-1}$	1 r
Lower sector scan period	$16\,s^{-1}$	20 r	$2.8\,s^{-1}$	2 r
Step size	3°	3°	3.6°	3.6°
Vertical beam opening angle	3°	3°	3°	3°
Horizontal beam opening angle	20°	20°	35°	35°
Low Altitude Detection Range	150 m	27.3 L	4 m	2 L
Blanking distance	5 m	0.9 L	0.6 m	0.3 L
Mission parameters				
Min. goal altitude	3 m	0.5 L	0.6 m	0.3 L
Max. goal altitude	10 m	1.8 L	1.0 m	0.5 L
Surge velocity	1.2 m/s	0.22L/s=0.17Lr	1.0 m/s	0.51L/s=0.31Lr

Table 4.1: Dimensional and non-dimensional key scales of the experiments with Autosub6000 and Delphin2

flight style vehicles, a similar scaling method is needed. This section identifies the key parameters of the obstacle avoidance system, and derives dimensionless sizes for them.

Following the standard in vehicle dynamics parametrisation, all vehicle sizes are expressed as multiples of the vehicle length L, assuming an operation in the same Reynolds number regime. The vehicle length is a dominant factor for scaling the manoeuvrability of the vehicle, and since Autosub6000 and Delphin2 are scaled versions of the same shape, the ratio of the lengths represents the scale factor between the two vehicles.

To parametrise the movement of the vehicle over the terrain, the vehicle speed and update rate of the obstacle detection were chosen. With vehicle pitch for Autosub6000 and delphin2 limited below 30°, is assumed that the vehicle mostly moves horizontally over the terrain, at surge velocity. The surge velocity is expressed in terms of how far the vehicle moves during one update of the information on the terrain ahead. Depending on how the sonar is analysed, the definition of the update rate for the terrain ahead may vary, a timespan is chosen within which the highest point in the detection range is seen at least once. Table 4.1 gives an overview of key parameters and their dimensionless representation.

4.4 Sonar Scan Visualisation

The interpretation of a sonar scan image is not immediately intuitive, being used to interpret images that were recorded using light waves rather than acoustic waves. Rather than the flat projection, a 2D projected sonar image shows a slice of a 3D space. Where a photographic image resolves an image in an x and y direction, the sonar beam resolves how far away a reflection was made and at what angle this data was recorded. Since small objects do not reflect the full sonar beam, often multiple patterns can be distinguished. However, within the beam width no further resolution can be achieved.

Figure 4.9 shows examples of such sonar images, recorded in the Lamont towing tank with the Tritech mechanical scanning sonar. In the left image, two metal rods were held into the sonar beam so they are at different distances from the sonar device, but behind each other from the perspective of the sonar. Since this results in reflections at different ranges, the two rods can clearly be distinguished in the sonar image. In the image on the right, the same rods were placed at the same range. Since the sonar beam does not resolve in any direction but the range, and both rods were placed within the width of the sonar beam, they show up as a single line in the sonar image.

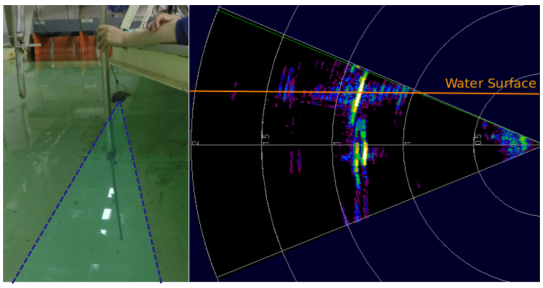

Metal object in line with the direction of propagation of the sonar.

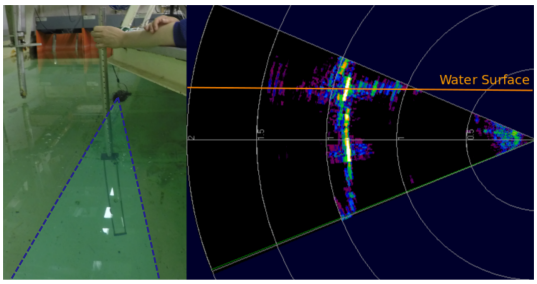

Metal object orthogonal to the direction of propagation of the sonar.

Figure 4.9: Photograph of a metal object being held into the sonar beam (marked in blue: approximation of the horizontal beam width) and the resulting image from the Tritech Software (marked in orange: water surface).

This typical visualisation of the mechanical scanning sonar data as a two dimensional image, recorded from a fixed position, is not possible for performing sector scans whilst moving at the surge velocities typical for flight style missions. By the time the last angle of the scan is complete, the vehicle has already moved so far that first scan angle from the sector scan has moved significantly, distorting the scan image and introducing gaps in what would normally be displayed as a sector of a circle. To give a meaningful two-dimensional representation, further processing is needed. The processing and assumptions made for the reconstruction already add a processing layer, which makes this visualisation unsuitable for understanding the raw data. When the mechanical scanning sonar is used for horizon tracking, only a small set of angles is regularly scanned by the sonar, making a re-construction of a two dimensional image even more complex.

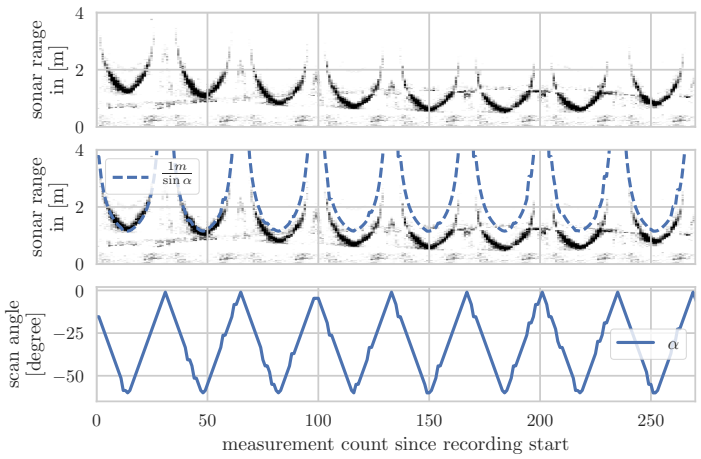

Figure 4.10: Example visualisation of sonar scan data. The colour darkness in the sonar image indicates the intensity of the scan return. With some practice, the first plot alone suffices to recognise the scan angle from the shape of the main terrain returns.

For further investigating the scan returns, and what effects might impact the processing of the sonar data, additional processing steps was avoided by choosing a different visualisation. To give an initial view of the sonar data, applying as little processing as possible, one scan result is plotted as a vertical line, without any further scaling. Along the x-axis, the measurement time (or the scan number) increases continuously, whilst the y-axis represents the distance from the sonar head (or the bin number). A sector scan as shown in Figure 4.9 is thus visualised as a square image. For a scan at angle α, over a flat terrain at an altitude a, the range at which the terrain reflection is seen is $r = \frac{a}{\sin\alpha}$. Since the angle at which this data is recorded changes, a flat horizon appears curved, and interrupts where the sonar scan angle becomes too shallow or points away from the terrain.
For better readability of the scan returns, the scan angle is often included in the same figure or in a plot sharing the same x-axis. However, for continuous sector scans the angle indication is often neglected, since the scan angle can usually be inferred from the distortion of the horizon: the lowest scan angle is at the bottom of the $1/\sin\alpha$ shaped curve. If the scan angle continues over the surge direction of the vehicle ($\alpha > 0$), a second $1/\sin\alpha$ curve may appear due to reflections from the water surface. An example of the typical shape of the sonar returns in the chosen visualisation of the scan lines is given in Figure 4.10. In the mission part that is shown, the vehicle approaches the terrain, starting from an altitude of 1 m. Since the lowest scan angle is 60°, the 1 m altitude shows up at a larger range even at the bottom of the curve. Since the sonar scan data has already undergone some filtering steps, to ease visual recognition of the terrain reflection, only artefacts remain of other reflections. The chosen filtering steps as well as the reflections that can be observed besides the terrain reflections are discussed in the results in section 5.4.

4.5 Software Tools

All mission analysis and programming of Delphin2 and the Autosub6000 simulation were implemented using Python and various toolboxes thereof. The Autosub6000 simulation and Delphin2 both rely on the ROS framework. This allows the dual use of nodes both in simulation, on Delphin2, and combined with a playback of recorded data.
One of the key ROS tools for analysing missions is rosbag, a package for recording and replaying ROS messages. Not only does it make it easy to record data during experiments and simulation, the data can also be read either as a pandas dataframe or replayed in ROS. If a new node or an analysis method is developed long after an experiment, it can be tested and applied to older experiments by simply running the node for the analysis whilst also playing back the rosbag from the experiment. This includes the selective replay of only some of the available data. Both for configuration and logging, rosparam is another vital ROS tool. The parameters are given in files written according to the YAML Ain't Markup Language (originally Yet Another Markup Language) (YAML) standard, "a human friendly data serialization standard for all programming languages" [Evans, 2016]. They can also be loaded from ROS scripts (less human readable) or the command line. The command line loading is particularly useful for changing individual parameters between two launches of the same mission. The parameters used for a mission can also be saved to file via a command line expression, making it easy to log the configuration of every single simulation and experiment, so the full mission configuration is available for verification at a later time.
Since the capabilities of the ROS internal launch scripts are limited, for lakeside operation as well as simulation instead a bash script is used to launch the different missions. This allows making small changes between re-runs of the same mission design, as well as logging of the ROS parameters to file (which is not possible from a ROS script due to timing issues). Furthermore, at the end of a lake mission several attempts at returning to a home coordinate can be launched from the shell script with a generic home return ROS launch script without the requirement for making a wireless connection to the vehicle.
For the sake of the operators nerves, as well as to improve debugging after the experiment, during experiments the shell output is logged as well both locally on the vehicle and, until the wireless connection is lost, also on the operator Personal Computer (PC). Furthermore, CPU and memory usage are logged to file to detect if problems with the vehicle occur due to system limitations that would not be recorded through the ROS framework or shell output.

4.6 Autosub6000 Mission Analysis

The available Autosub mission data records range from initial tests to large scale pho-

tographic surveys. Figure 4.11 gives an overview of the different mission paths, showing the variation between the different missions patterns and an increasing size of the survey area after the initial tests. The survey areas during the JC136 research cruise are spread so far apart that the actual pattern is not visible; they were all lawnmower patterns, as shown in Figure 4.5. It can be seen that independent of the exact mission pattern, all missions are composed of very long linear paths, defined by a list of turn points.

For each mission, the data is recorded continuously from start to finish of the mission. Both raw sensor data and processed data are recorded with a timestamp. Before starting the analysis, the data before and after an altitude below 20 m is reached, representing the diving and surfacing components of the dive, was removed by manually selecting a suitable timestamp from an altitude plot.

Two plots give a good initial overview of the different missions: a map of the vehicle path, to inform about the mission purpose, and a plot of the vehicle depth, altitude and heading change. To be able to gauge the altitude tracking performance of all missions, the depth and altitude tracks are plotted at the same scale for all missions. This gives a clear comparison of the length of the vehicle path and the complexity of the terrain. The heading change rate gives an indication when a waypoint is reached, and can be used to match the map view of a mission path to the linear plot of the mission data. Appendix E gives the overview plots for all missions. In addition to the overview plots, a statistical analysis of various measurands, like altitude, sonar range or pitch angle, was performed. The results are given in section 5.1.

Since an in depth analysis of all 18 missions would be too time consuming, missions were selected for futher analysis and simulation validaton. Based on the overview plots and the statistical analysis, the following missions were selected:

- M53: altitude tracking without the use of obstacle avoidance
- M57: early mission with complex terrain and high risk
- M115/116: repeated mission using the same waypoints after scanning sonar adjustment, possible collision in the second attempt.

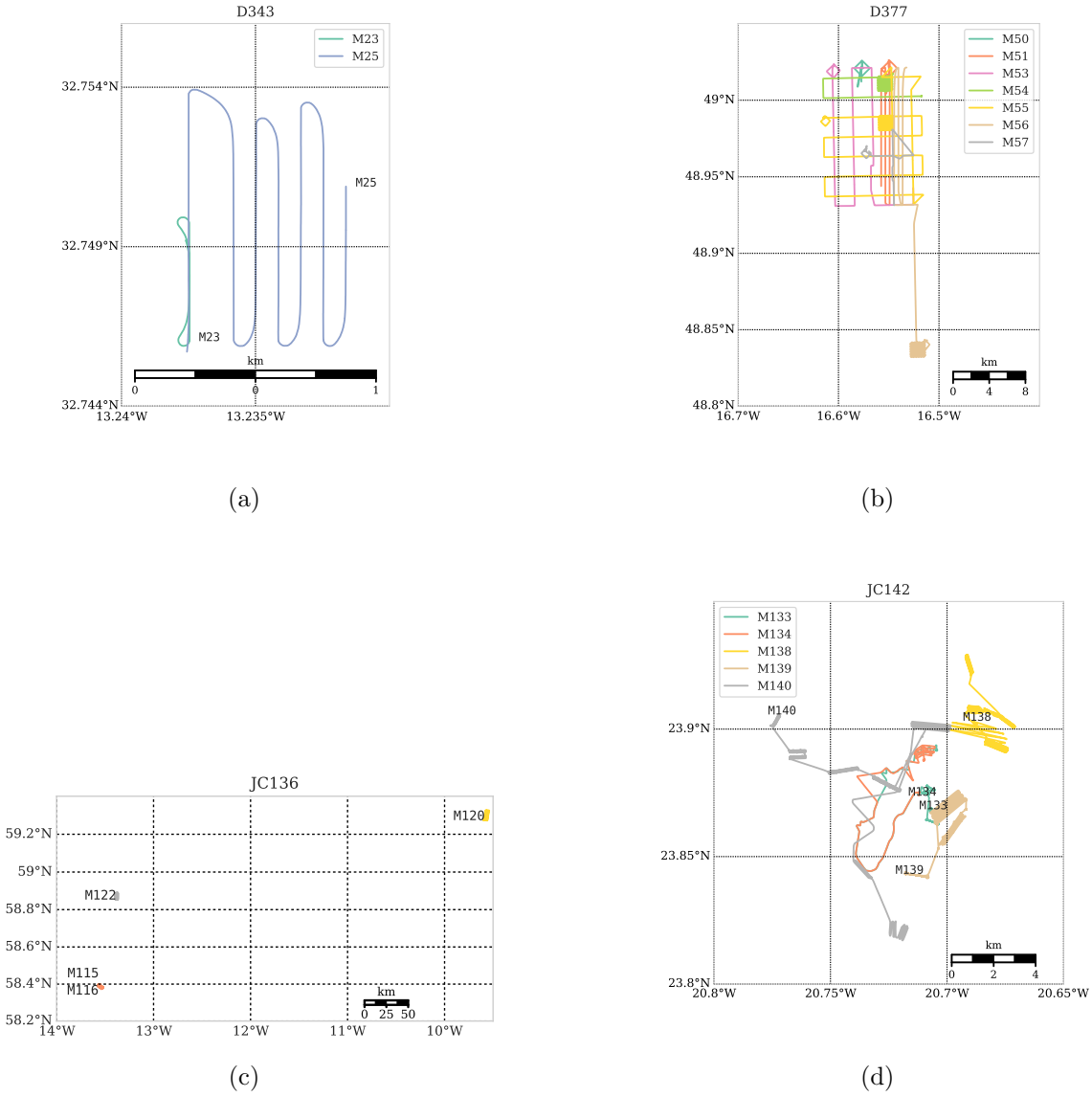

Figure 4.11: Overview maps of the available Autosub6000 missions.

4.7 Simulation

The main purpose of the Autosub6000 vertical plane simulation is to better understand the flight style altitude tracking problem, by simulating the vehicle dynamics and the mechanical scanning sonar returns in the vertical plane, applying the same controller and data processing as on Autosub6000, and then varying different vehicle and mission parameters. It was also used to inform Delphin2 experiment design.

The simulation uses the reference frame outlined in section 4.1, and the simplifications discussed in 4.2.

For compatibility with the Delphin2 firmware and existing work, the terrain following simulation was implemented as a set of ROS nodes, clearly separating the different components and allowing the exchange of some nodes with data from towing tank tests or Hardware In the Loop (HIL) simulation. Just like the nodes on an actual robot, the nodes exchange information via ROS messages. Whilst MATLAB now allows publishing for ROS via the Robotics System Toolbox [MathWorks, 2016], at the time the simulator was started this did not exist yet, so the simulation was implemented using Python instead. However with the ROS node system, any components of the simulation could be replaced by MATLAB nodes in the future.

Parameters that stay constant during one simulation run are set in the launch file and distributed via the ROS parameter server. Such parameters are for example the goal altitude of the vehicle or model parameters for the chosen vehicle. Vehicles and mission demands can quickly be exchanged by using a different set of parameter files in the launch file, or re-configuring them from the command line or a shell script launching multiple missions, without modifying the nodes.

4.7.1 Structure

The complete terrain following simulation is composed of four main simulation components: the *Altitude Control*, the *Actuator Update*, the *Vehicle Dynamics*, and the *Sensor Model*. Figure 4.12 shows an overview of the structure of the basic terrain following simulation.

Currently, the altitude demand and pseudo altitude as implemented on Autosub6000 are the available inputs for the *Altitude Control*. The *Alititude Control* section is where either the reconstructed current control of Autosub6000, real current control nodes from Delphin2 or newly developed altitude control nodes can be used. It outputs the demand for the sternplanes. Since real actuators come with constraints in speed, maximum output and stepsize, the *Actuator Update* sections makes sure that the model keeps within these constraints, determining the actual actuator state. This actuator state is then used in the *Vehicle Dynamics* to estimate the next vehicle state. The *Sensor Model* section keeps track of the position of the vehicle over the terrain based on the

information from the *Vehicle Dynamics*, and the terrain provided before the start of the simulation. With improvements to the control, the *Sensor Model* will have to provide data closer to the actual sonar measurement, since it will need considering for the newly added mapping process. Figure 4.12 shows how the current structure will change to comprise this.

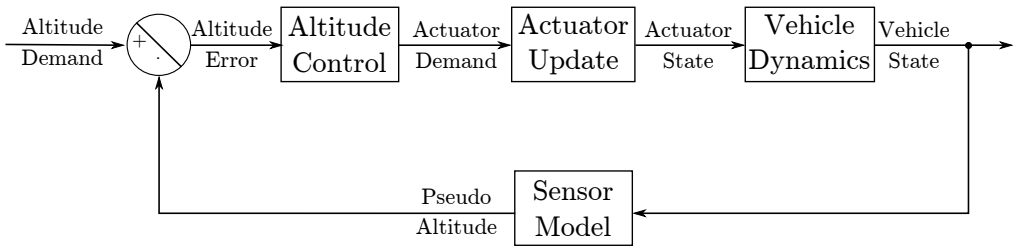

Figure 4.12: Overview of the structure of the terrain following simulation.

The simulation can be sped up via the */simulation/speedup*, this factor leads to an increase in the frequency at which the nodes function; for systems that have a frequency limit applied, the maximum frequency is increased according to the speedup factor. The other timings of the nodes are based on the results of the model node. In this node, the speedup factor is considered, and due to their reliance on messages from that node, the other nodes need no further modifications.

4.7.2 Notation and Units

To achieve flexibility in the simulation, all simulations are kept generic, using parameters for all vehicle specific measures. Whilst focused on Autosub6000, the simulation is based on a dynamic model of Autosub1, so some of the validation steps were performed using Autosub1 measurements. For both vehicles a separate configuration file collates all model values, and is loaded at the beginning of the simulation. Individual changes between missions or simulation variations are also applied through ROS parameters. As a convention in the simulation, all units are strictly SI or SI derived units only. For human readability, angles in the YAML files are sometimes given in degrees, but contained a YAML function that converts their value to radians, so the parameter server only publishes angles in radians.

Where possible, software nodes that are run on the real physical Delphin2 system are used in simulation as well. At the transition to the actuators, a consideration of the actuator limits is added before the actuator settings are used in the model. Based on each actuator demand from the control node, the actuator simulation node then publishes the closest real actuator value that is achievable in the next time step. Errors in setting the actuators are not considered.

4.7.3 Vehicle Dynamics

In the vehicle dynamics component of the simulation, the reaction of the vehicle to the applied control forces is calculated. It takes the current vehicle state and the actuator states as an input and publishes all parameters describing the next vehicle state. The publishing frequency of the model node is the maximum rate used in the terrain following simulation. In addition to the vehicle model, a second message type for publishing the forces and moments can be published for debugging and validation purposes. Originally it was planned to implement the model in MATLAB and using the MATLAB Robotic Systems Toolbox for publishing the model state with ROS. However, for convenience and portability it was decided to instead implement the model equations in python.

The model currently considers only surge, heave and pitch motion. Depth and x-position are considered in a global coordinate system, the pitch angle θ is relative to the direction of the x-axis in the global coordinate system. Surge and heave are considered in the AUV centred coordinate system, with its origin at the volumetric centre of the vehicle, which is also assumed to be the Centre of Gravity. The angle of the sternplane is relative to the vehicle based x-axis.

The model reads the vehicle measurements, the time resolution of the model calculations and the initial speeds and actuator settings from the parameter server.

For every time step at the ROS system frequency, the input state for the integration is initialised with the results from the previous integration step. For integration the scipy odeint function [Community, 2016] is used. As an input it needs a set of timesteps

within the time over which it is integrated. In the model, these timesteps are calculated over the period time of the ROS frequency. The resolution within one ROS timestep can not be set directly, but the integration allows an input of demanded sample points, the density of which can be varied through the model resolution parameter.

The surge velocity is currently assumed to stay constant, regulated by an external control system not considered in this simulation. To stay flexible for the future, the surge velocity is used as an input for the integration but no forces that may change the surge velocity are considered.

The current values for the forces and moments are calculated using a separate set of functions that can be switched via a ROS parameter. This allows fast switches between models of different complexity, a clear definition of each set of model forces and moments in a separate file and an easy comparison between models. Using the assumptions that the surge velocity and heading angle are constant, and the sway velocity and roll angle are zero, the vehicle model is based on [Gertler and Hagen, 1967], considering hydrodynamic coefficients for viscous damping, added mass and radiation damping. All model descriptions first calculate individual forces and moments from the hydrodynamic derrivatives and the vehicle model state. Equations 4.3 and 4.4 summarize the moments M_i and forces Z_i that are considered. The hydrodynamic derrivatives are listed in Table 4.3, they are dimensionalised using the vehicle lenght L and water density ρ given in Table 4.2. This table also contains the additional data needed to calculate the force and torque equilibrium equations for each of the vehicles: the mass m, the z-distance between the Centre of Buoyancy and the Centre of Gravity BG, and the difference between the absolute sum of the gravitational forces and the absolute sum of the buoyant forces $W - B$. The model parameters are discussed in more detail in Section 4.7.4. Since most velocities are assumed to be fixed or zero, only the derrivatives using the heave and pitch velocities w and q, their accelerations $\dot{w}$ and $\dot{q}$ as well as the constant surge velocity u are included.

$$\begin{aligned} m\left(\dot{w} - uq\right) &= \sum_i Z_i \\ &= Z_{\dot{q}} \cdot \dot{q} + Z_{\dot{w}} \cdot \dot{w} \\ &+ Z_{qu} \cdot qu + Z_{wu} \cdot wu \\ &+ Z_{|q|w} \cdot |q|w + Z_{|w|w} \cdot |w|w \\ &+ Z_{\delta_s uu} \cdot \delta_s uu \\ &+ (W - B) \cdot \cos\theta \end{aligned} \tag{4.3}$$

$$
\begin{aligned}
I_{yy} \cdot \dot{q} &= \sum_i M_i \\
&= M_{\dot{q}} \cdot \dot{q} + M_{\dot{w}} \cdot \dot{w} \\
&+ M_{qu} \cdot qu + M_{wu} \cdot wu \\
&+ M_{|w|q} \cdot |w|q + M_{|q|q} \cdot |q|q \\
&+ M_{\delta_s uu} \cdot \delta_s uu \\
&+ BG \sin\theta
\end{aligned}
\tag{4.4}
$$

All forces and moments calculated are published under the ROS topic "auv_model_forces_moments", so their influence during a manoeuvre can be looked at individually.

4.7.4 Model Parameters

The Hydrodynamic coefficients for the Autosub6000 AUV are based on hydrodynamic coefficients that were experimentally obtained for Autosub1, an older vehicle of the Autosub AUV class. The coefficients were obtained experimentally in a towing tank, using a 3/4 scale model of Autosub1, under consideration of scaling effects [Kimber and Marshfield, 1993]. The model tests were performed with the sternplanes attached, recording the effect of a change relative to the zero position of the sternplanes in the sternplane derivative $M_{uu\delta'}$. As a result, effects such as added mass [Fossen, 2011], the Munck Moment [Faltinsen, 1999, p. 197], the Chinese Effect [Burcher and Rydill, 1994, p. 49], or transverse rudder forces [Fossen, 2011, p. 356] are included in the coefficients and will be reproduced in simulations of operational states close to the operational point around which the hydrodynamic coefficients were derived.

The sternplanes are considered to be moving synchronously, using a single sternplane derrivative $M_{uu\delta'}$ to describe the effect of both sternplates being deflected by an angle of δ. Since the sign convention in the model experiments was reversed to the sign convention used here (positive sternplane angle induces a surfacing motion), the sign of $M_{uu\delta'}$ is reversed. All coefficients are given in non-dimensional form, multiplied by 1000 (see Table 4.3. They are then dimensionalised using the vehicle length, average surge and the density of the water they are used in. These parameters are summarised for Autosub1 (the original study subject), 3/4 scale Autosub1 (the model used in [Kimber and Marshfield, 1993]), Autosub6000, and Delphin2 in Table 4.2.

Different to Autosub1 and Delphin2, on Autosub6000 a set of rear winglets was added. It is positioned closer to the vehicle centre of rotation, to apply a downwards force with a smaller rotational momentum, reducing the pitch angle required to keep a constant depth with a positively buoyant vehicle. These fixed winglets are mounted pointing downwards at a fixed angle of $\beta = 6°$. Their position on Autosub6000 is shown in

Figure 3.3. It is assumed that the force is applied to Autosub6000 at the centre of pressure of the foil, at $\frac{1}{4}$ chord. The profile of the foils is NACA0015. The Reynolds number Re for the winglet with chord length $L = 0.25\,\mathrm{m}$ moving at a surge velocity of $u = 1.2\,\mathrm{m/s}$ in water with a kinematic viscosity of $\nu = 1.8 \cdot 10^{-6}\frac{m^2}{s}$ is:

$$Re = \frac{u \cdot L}{\nu} = \frac{1.2\frac{m}{s} \cdot 0.25m}{1.8 \cdot 10^{-6}\frac{m^2}{s}} = 1.6 \cdot 10^5 \tag{4.5}$$

The lift coefficient Cl and the drag coefficient Cd for a NACA0015 foil at a six degree angle of attack is taken from the publicly available airfoil database airfoiltools.com [air] as $Cl = 0.7659$ and $Cd = 0.01544$ in the flow regime around $Re = 2 \cdot 10^5$.

From [Molland and Turnock, 2011, p. 71] the equations for the lift and drag coefficient are used to calculate the lift force F_L and the drag force F_D:

$$\begin{aligned} Cl &= \frac{F_L}{0.5 \cdot \rho \cdot A \cdot U_0^2} \\ F_L &= 0.5 \cdot \rho \cdot A \cdot U_0^2 \cdot Cl \end{aligned} \tag{4.6}$$

$$\begin{aligned} Cd &= \frac{F_D}{0.5 \cdot \rho \cdot A \cdot U_0^2} \\ F_D &= 0.5 \cdot \rho \cdot A \cdot U_0^2 \cdot Cd \end{aligned} \tag{4.7}$$

A is the plan area of the wing, calculated as the product of the wing span and the chord, ρ the density of the liquid, and U_0 is the speed of the foil in the liquid. With a chord of $0.25\,\mathrm{m}$ and a span of $0.27\,\mathrm{m}$, the resulting plan area is $A = 0.0675m^2$.

The winglets are mounted at a small angle of 6° only, so the drag mainly contributes a force parallel to the surge direction of the vehicle. With the surge assumed to be constant, this force needs no further consideration. With increasing surge velocity, the lift contributes a downwards force counteracting the positive buoyancy of the vehicle and reducing the required pitch angle to keep a constant depth. Since two wingles are mounted symmetrically, the winglet force $Z_{winglet} = 2 \cdot F_L$ acts at the longitudinal centreline of the vehicle.

To correct for the fact that the span of the winglets is finite, an aspect ratio correction is applied. The body of the AUV is considered as a reflection plane effectively doubling the span of the winglets [Molland and Turnock, 2011, p.182]. For easier readability of the equation, the correction factor C_{ai} is introduced:

$$Correction_{aspect} = \frac{1}{1 + \frac{\frac{Cl}{\beta}}{\pi \cdot \left(2\frac{span}{chord}\right)}} \cdot \beta = C_{ai} \cdot \beta \tag{4.8}$$

Finally, whilst the winglet itself is at a fixed position relative to the AUV, the angle of attack varies with the heave velocity. To correct for this, a small angle approximation

is made. The ratio of heave to surge velocity is considered to correct the winglet angle (in radians). The simulation assumes the surge velocity u to be constant, so the winglet angle of attack α_w only needs to be corrected for the heave velocity w:

$$\alpha_w = \beta \cdot \frac{w}{u} \tag{4.9}$$

The resulting force (and derrived from it, the momentum caused by this force) with all corrections is calculated as follows:

$$Z_{winglet} = 2 \cdot 0.5 \cdot \rho \cdot A \cdot Cl \cdot u^2 \cdot C_{ai} \cdot \alpha_w \tag{4.10}$$

The effects of the added winglets on the simulation were analysed by consecutively adding the correction terms, whilst reaching a steady state keeping a constant depth. The results of this analysis are presented in 5.2.3.

4.7.5 Sonar Scanning

The sonar scanning speed is simulated at a rate of 1 Hz. The sonar range is a fixed parameter. For each measurement, a line with the sum of the pitch angle and the sonar scan angle is drawn though the position of the sonar. If the line meets the terrain at a distance below the sonar range, this distance is returned as the detection range. Otherwise no valid detection is recorded.

Since a misalignment of the sonar device was recorded, a scanning angle offset was added to the simulation. To separate the effect of a scan angle offset from the effect of choosing different maximum and minimum limits for the sonar scan angle, it was implemented differently to a real offset in the mounting position. The scan angle offset is applied only in the terrain altitude calculation, so it is not considered when checking the scan angle limits for determining the next sonar scan angle. The sign convention for the direction of the sonar scan angle offset is shown in Figure 4.13.

4.7.6 Validation and Variation

The validation of the simulation is performed in separate steps, testing scenarios of increasing complexity. During many of the validation steps, it becomes clearer which parameter variations on Autosub6000 impact the performance results, so a variation step is often integrated in a validation case. This variation step provides further understanding of the impact of one particular parameter variation and informs the parameter choices for the next validation step. The validation was split into the following steps:

1. Test simulation stability for change in simulation frequency
2. Compare to simulation from Autosub1 design study [Kimber and Marshfield, 1993]

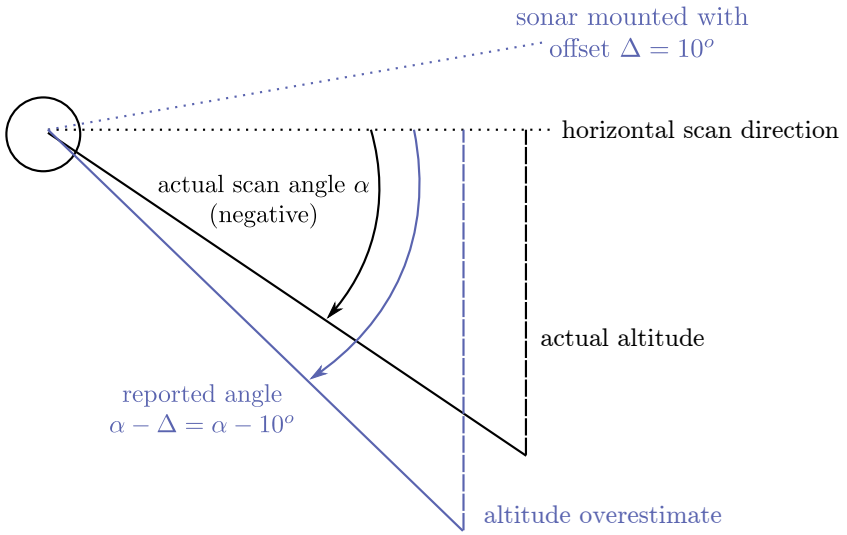

Figure 4.13: Sign convention for the direction of the of the sonar scan angle offset, describing the angle by which the device mount position is offset from the assumed mount position.

3. Simulate vehicle path for Autosub6000 mission that did not use obstacle avoidance

4. Simulate vehicle path for Autosub6000 mission that used obstacle avoidance

4.8 Terrain Following with Delphin2

To further understand the horizon tracking challenges, terrain following was added to the existing AUV control system on Delphin2 using a similar structure as developed for Autosub6000. The added system consists of three components already existing on Autosub6000: terrain detection with the mechanical scanning sonar, horizon tracking based on the terrain detection data, and use of this data for altitude control. The choice of actuation method available on Delphin2 adds an additional component of the altitude tracking which allows comparing hover- to flight style actuation as well as evaluating if thrusters at higher speeds, albeit less efficient, can improve the survey success. The actuation force allocation is based on the surge velocity estimate. The surge dependent weight function for the actuators (further described in Section 4.8.2) is then applied to the actuator demands of the controller (Section 4.8.1). An overview of the system components is shown in Figure 3.7. This section describes the implementation on Delphin2, detailing the changes made relative to the Autosub6000 system due to sensor and actuation differences between the two vehicles, as well as variations in the experiment conditions.

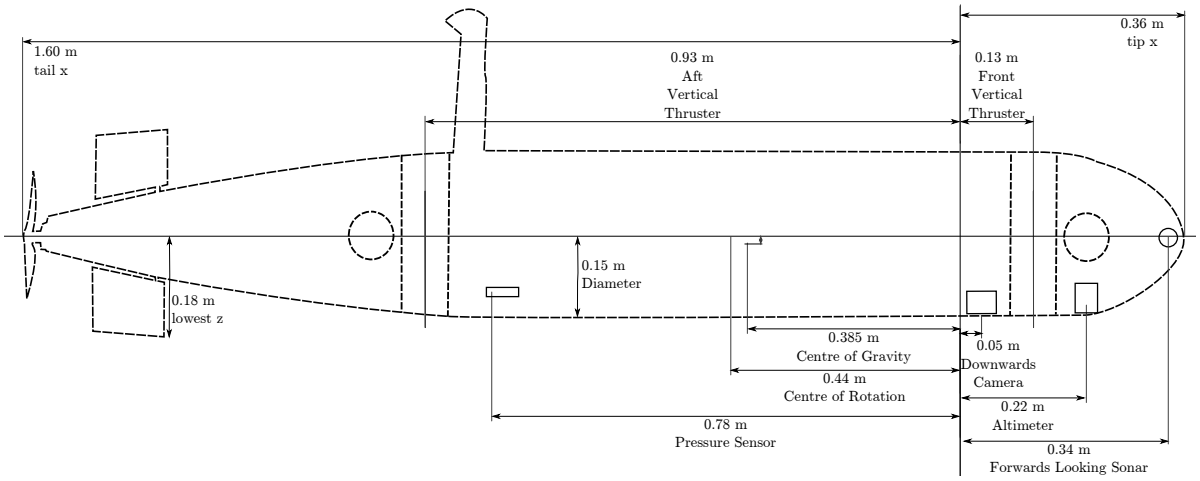

Figure 4.14: Sensor and actuator positions on the Delphin2 AUV.

4.8.1 Altitude Controller

For the altitude tracking experiments, the altimeter was used as the only input of the depth controller. The depth demand was calculated from the current depth, the current pitch, the current altitude and the altitude demand. During the horizon tracking experiments, the altitude from the altimeter was compared to the pseudo altitude calculated from the forwards looking sonar, and the lowest of the two values was used to calculate the depth demand.

4.8.2 Actuation Strategy

The weight function for the thrusters was modified for the fastest speed, to test if the altitude tracking performance could be improved by using thrusters outside their optimal speed. The used parameters for the mid-transition speeds u^*_{th} and u^*_{sp}, and the width of the transition zone are given in Figure 4.15, which also shows the resulting weight functions.

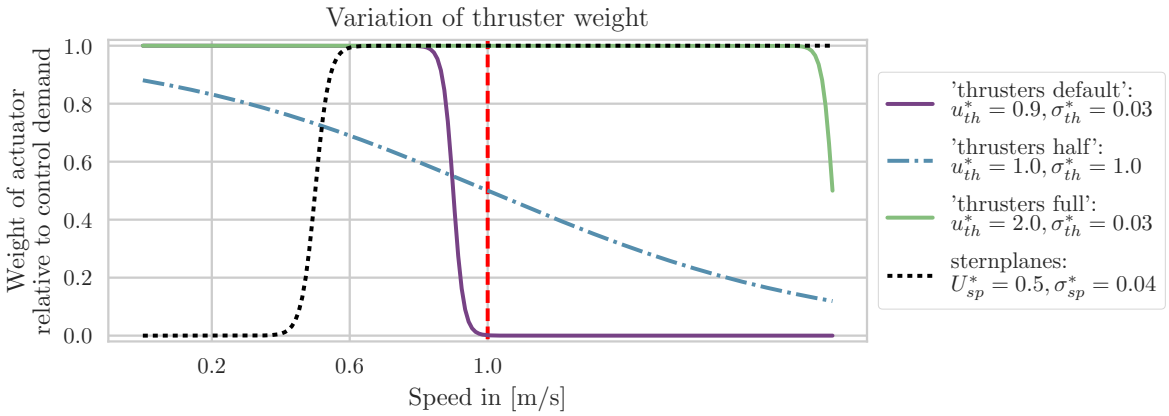

Figure 4.15: Thruster and sternplane weight functions: the sternplane weight function remains unchanged. The transition centre surge speed u^*_{th} anf the transition width σ^*_{th} are varied to add additional thruster force at higher speeds. The default thruster weight function is used for all three surge speeds, and the 'thrusters half' and 'thrusters full' variation is tested in cases (4) and (5), at 1 m/s surge speed.

Vehicle	Autosub1	3/4 scale Autosub1	Autosub6000		Delphin2		
							Unit
Length	7	5.2	5.5		1.96		m
Diameter	0.9	0.67	0.9		0.26		m
L/D	7.7	7.7	6.1		7.5		
W-B	unknown	0	100 to 150		6		N
m	3600	1476	1434.3		79.4		kg
BG	0.02	0.015	0.021		0.06		m
I_{yy}	8304	1879	4950		35		$kg \cdot m^2$
mean chord	0.32	0.23	0.25		0.1		m
ρ	1025 (Seawater)	1025 (Seawater)	1025 (Seawater)		1000 (Freshwater)		$kg \cdot m^{-3}$
ν	$1.68 \cdot 10^6$ (Seawater $4°C$)	$1.68 \cdot 10^6$ (Seawater $4°C$)	$1.68 \cdot 10^6$ (Seawater $4°C$)		$1.31 \cdot 10^6$ (Freshwater $10°C$)		m^2/s
Min. flight style surge velocity	-	-	0.8		0.6 (est.)		m/s
Max. flight style surge velocity	-	-	1.8		1 (est.)		m/s
simulated surge velocity	2	2.69	1	2	0.6	1	m/s
Reynolds number based on sternplane mean chord	$3.8 \cdot 10^5$	$3.8 \cdot 10^5$	$1.5 \cdot 10^5$	$3.0 \cdot 10^5$	$0.5 \cdot 10^5$	$0.8 \cdot 10^5$	
Reynolds number based on vehicle length	$8.33 \cdot 10^6$	$8.33 \cdot 10^6$	$3.27 \cdot 10^6$	$6.55 \cdot 10^6$	$0.90 \cdot 10^6$	$1.50 \cdot 10^6$	
Froude number based on vehicle length	0.24	0.38	0.14	0.27	0.14	0.23	

Table 4.2: Overview of vehicles relevant for simulation and validation. Dynamic viscosity ν is read from [26th ITTC Specialist Committee on Uncertainty Analysis, 2011] for the given conditions. Water density ρ is chosen for the water type the vehicle operates in. L/D: ratio of length to diameter. $W - B$: difference between the absolute sum of the gravitational forces and the absolute sum of the buoyant forces. m: vehicle mass. BG: z-distance between the Centre of Buoyancy and the Centre of Gravity. I_{yy}: moment of intertia.

Coefficient	3/4 scale Autosub1	Delphin2	Dimensionalisation
Z'_{wu}	-28.45	-28.5	$1/2\rho \cdot l^2$
$Z'_{\dot{w}}$	-17.39	-17.40	$1/2\rho \cdot l^3$
$Z'_{\|w\|w}$	-27.05	-95.27	$1/2\rho \cdot l^2$
Z'_{qu}	-12.64	-12.6	$1/2\rho \cdot l^3$
$Z'_{\dot{q}}$	-0.169	$---$	$1/2\rho \cdot l^4$
$Z'_{\|q\|q}$	$---$	0	$1/2\rho \cdot l^2$
$Z'_{\|q\|w}$	-6.87	$---$	$1/2\rho \cdot l^3$
$Z'_{\delta_s uu}$	5.31	0.169	$1/2\rho \cdot l^2$
M'_{wu}	4.54	4.5	$1/2\rho \cdot l^3$
$M'_{\dot{w}}$	-0.17	0	$1/2\rho \cdot l^4$
$M'_{\|w\|w}$	$---$	-0.0157	$1/2\rho \cdot l^3$
M'_{qu}	-5.35	-5.3	$1/2\rho \cdot l^4$
$M'_{\dot{q}}$	-0.98	-0.98	$1/2\rho \cdot l^5$
$M'_{\|q\|q}$	$---$	-11.1	$1/2\rho \cdot l^4$
$M'_{\|w\|q}$	-2.57	$---$	$1/2\rho \cdot l^3$
$M'_{\delta_s uu}$	2.11	4.95	$1/2\rho \cdot l^3$
Source	[Kimber and Marshfield, 1993]	based on [Tanakitkorn et al., 2016]	[Gertler and Hagen, 1967]

Table 4.3: Overview of non-dimensional hydrodynamic coefficients used for simulation, all values multiplied by 1000. Values unavailable for a vehicle are set to zero. Coefficients are dimensionalized using the water density ρ and the vehicle characteristic length l.

4.9 Lake Experiments

To experimentally evaluate altitude tracking using flight style actuation, a body of water that allows a long enough path for the vehicle to reach a steady state is required. To test the altitude tracking performance, interesting terrain features are required. Two test locations were considered: the Boldrewood Towing Tank at Boldrewood Campus Southampton, and Testwood lake, a reservoir north-west of Southampton. Both locations are easy to access, so within one day several hours of experiments can be performed and both bodies of water are large enough so the order of magnitude of a vehicle path length is 100 m. Both bodies of water are sufficiently deep so obstacles in the order of 1 m height can be crossed at 1 m altitude without surfacing. However the narrow width of the Boldrewood Towing Tank results in sonar detection problems due to reflections from the side walls (see Appendix C). Testwood Lake is particularly suited for terrain trackin experiments, since it has a very even step feature, which shows up well on a sonar scan when approached orthogonally to the step, so this location was chosen the repeated Delphin2 experiments.

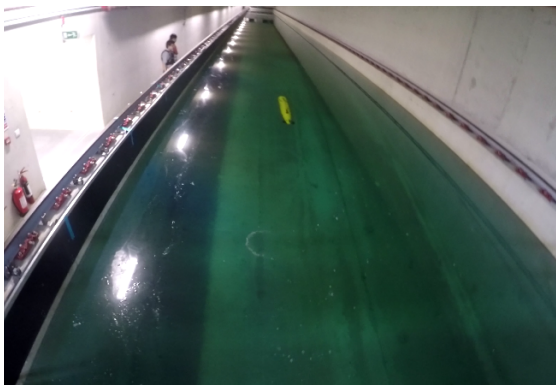

Delphin2 in the new
Boldrewood Towing Tank.
3m depth, 148 m length,
6 m width.

Delphin2 in
Testwood Lake.
Depth up to 4 m,
200 m by 500 m area.

Figure 4.16: Key data and photos of the available water bodies for testing.

Using a specific test location with a well understood or human constructed terrain to assess the performance of terrain following systems on AUVs has several advantages: the terrain is well known and does not have to be reconstructed based on mission data; specific test cases can be defined, repeated and compared; a set of algorithms and parameters can be tested and compared to previous data.
During each experiment, the AUV continue along a constant heading and constant goal altitude, passing over a step-like obstacle. The experiment path is composed of three section. First a steady state at speed is reached over an initial distance. Then the obstacle comes within the forwards looking detection range and an obstacle performance manoeuvre is performed. On the last section the vehicle returns to the goal altitude

after passing the obstacle.

In the following sections the Boldrewood location, a detailed experiment plan for the test site, and the problems and advantages of the location are discussed.

4.9.1 Testwood Lake

Testwood Lake has a suitable, evenly shaped, 300 m wide, and 0.6 m high step feature (see Figures 4.17 and 4.17). When heading towards it at a 90° angle, or even with a small heading error, it can be well detected without reflections from other terrain features. Furthermore the lake environment has less magnetic field disturbance, making it easier to achieve the correct heading.
Before tests began, a depth map of the entire lake was acquired from the water surface using Global Positioning System (GPS) positioning and altimeter readings. A transect for crossing the step feature at a 90 degree angle was chosen, and a distance of 25 metres was added before and after the step, to ensure the vehicle was operating in a steady state when reaching the step (see Fig. 4.17). Surveys were executed both in the direction from point A to point B ($A \triangleright B$) and in the reverse direction ($B \triangleright A$). This area of interest was crossed twice, once from each direction. Based on the GPS position, the distance to the start point A was calculated. Both depth maps show spikes which stem from altimeter noise. A running average was used to combine the two terrains into an estimate of the real terrain. Figure 4.17 shows the depth measurement from the two crossings, and the interpolated terrain estimate.
All experiments were then executed by reaching the start position at the surface with GPS fix, diving to the goal altitude with the thrusters, and then moving forwards whilst maintaining a constant heading and the chosen altitude tracking method for the selected case. To be able to compare the experiments in both directions, and to remove initial stabilising behaviour, a fixed length of 15 m was included symmetrically before and after the step, resulting in a 81.5 m long path (E to F in Figure 4.17). The recorded data was restricted to the area between the points E and F by matching the terrain estimate, obtained from the depth, pitch, and altitude during the mission, to the terrain profile obtained from the surface. This method was chosen since it was more reliable compared to acceleration based positioning. The x-position gives the distance from the start point, along the goal heading (see Figure 4.17).

Unlike the towing tank, an external accurate recording the vehicle position over the step is impossible. The vehicle internal position estimate is reliant on integrating accelerations. To get a more accurate position estimate, the terrain is used for estimating position. The terrain as seen during a mission is combined from the depth of the vehicle, the altitude, compensating the altitude based on the vehicle pitch angle. To better align the missions, the time of crossing the upwards and downwards step were read manually from a plot of the terrain as seen during the mission, over time. The error of this reading is estimated at $\pm$ 0.5 s.

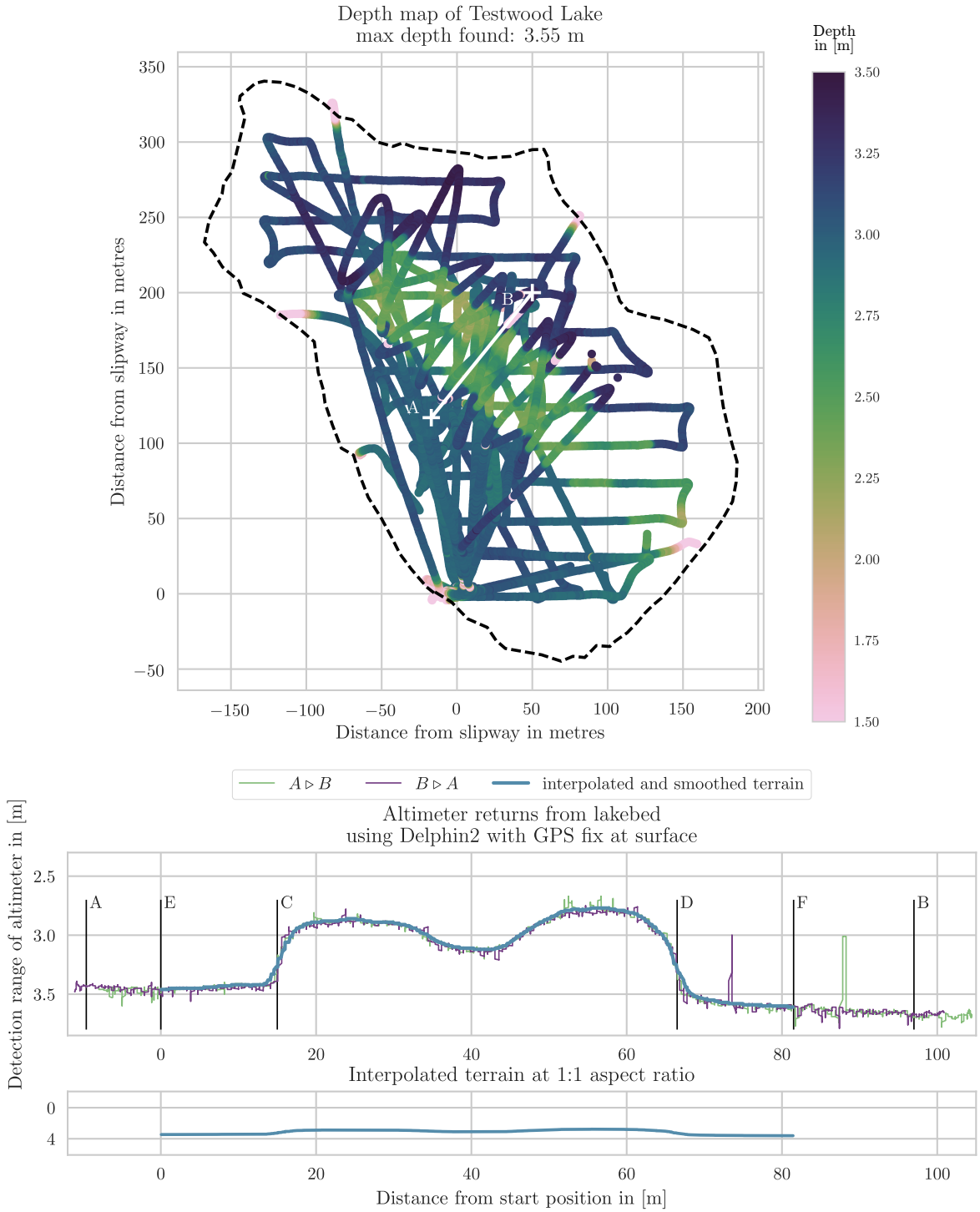

Figure 4.17: Testwood lake depth map and profile of the experiment path, obtained from altimeter measurements made with GPS fix at the water surface. The end points of the experiment path are A and B. It was structured with further points for analysis purposes.

4.9.2 Experiment Setup

Attempts were made at taking actual photos, but the algae growth in the lake was too bad to take photos of anything but shades of green. 1.0 m and 0.6 m were chosen as goal altitudes for the experiments. The 1.0 m altitude is of a similar geometric scale to those used by Autosub6000 (see 4.1), whilst keeping the vehicle submerged throughout the path. The lower altitude of 0.6 m was chosen to make the step a real obstacle in the path, that required avoidance. The success zone was chosen to contain the space between both goal altitudes plus 0.1 m around the altitudes, resulting in a mission success zone from 0.5 m to 1.1 m. This is to compare two strategies: using a low value within the limit, or keeping the vehicle safe, but at the upper limit of the goal altitude. Diving deeper into the vehicle configuration, the thruster weight and the terrain detection threshold were used to modify the altitude tracking behaviour.

The experiment paths were crossed at 0.3 m/s, 0.6 m/s, and 1.0 m/s surge velocity. They represent low, medium, and high speeds for Delphin2 and are well understood from previous experiments on diving control [Tanakitkorn et al., 2016] and heading control at the surface [Tanakitkorn et al., 2017]. During the horizon tracking experiments, the control allocation at 1 m/s speed was varied, to increase the use of thrusters from the default thruster weight of 0 to a factor of 0.5 ("half") and 1.0 ("full") (see Figure 4.15). All combinations of actuator settings, goal altitude, and obstacle detection settings are given in the experiment matrix (table 4.9.2).
Two cases were identified as reference cases. To ensure repeatability, they were repeated several times, on separate days. All other experiments were only repeated twice, though sometimes these numbers vary since missions with indications of a sensor failure or an early mission abort at the lakeside were repeated as a precaution.

Case No.	Altitude		Speed			Thrusters		Detection		Repeats	
	$0.6m$	$1.0m$	$0.3\frac{m}{s}$	$0.6\frac{m}{s}$	$1.0\frac{m}{s}$	original	varied	S_{th}	S_r	$A \triangleright B$	$B \triangleright A$
1)		■	■			■				2	1
2)		■		■		■				2	2
3)		■			■	■				2	2
4)		■			■		half			1	1
5)		■			■		full			1	1
6)		■	■			■		95		2	3
7)		■		■		■		95		3	2
8)		■			■	■		95		10	11
9)		■			■	■		85		2	2
10)		■			■	■		75		2	1
11)		■			■	■		95	1	1	1
12)	■		■			■		95		3	2
13)	■			■		■		95		2	2
14)	■				■	■		95		4	4
15)	■				■	■		75		1	1
16)	■				■	■		95	1	1	1

Table 4.4: Experiment Matrix for Testwood Lake experiments. An empty detection threshold S_{th} in the obstacle detection indicates that only the altimeter was used for obstacle avoidance. Repeats vary due to time limitations at the lake not allowing for all missions with a mission abort to be re-run.

4.10 Delphin2 Data Analysis

The various sensors on Delphin2 record data asynchronously at rates between 5 Hz and 20 Hz. To combine data for calculating values derived from the sensor data, the recorded measurements were first interpolated based on the time between subsequent measurements. With a constant propeller setting and the maximum pitch angle at $-20°$, the speed along the experiment path x-axis is assumed constant. With the step length read as 51.5 m, and the time between crossing the beginning and end of the step, the speed of Delphin2 along the global x-direction was estimated, cross referenced with existing speeds estimates for Delphin2 and used to estimate the x-position along the experiment path, so experiments at different speeds could be compared based on the x-position. It was found that despite attempts of normalising the depth sensor at the water surface, it had a constant error that varied by several centimetres on the same day. To compensate this offset, the mean water depth of the first section of each experiment was calculated and compared to that of the re-constructed terrain. For comparison between different experiments, all datasets were finally interpolated and re-sampled at a resolution of 1 cm, starting at x-position $x = 0$ m. All data post-processing relies on the python pandas library [McKinney, 2010], specifically for interpolation, re-sampling, combination and plotting of data.

4.11 Summary

The methods chapter showed how using the altitude as the key parameter for optimization, the terrain following capabilities of flight style AUVs are analysed in the vertical plane. The effect of the simplifications made was analysed in detail, showing which details can be neglected due to their small impact, and which simplifications may need further analysis in the future. It was shown how inaccuracy of vehicle position and terrain detection combined with the low resolution of surface based maps add a further challenge to simulating vehicle behaviour over realistic terrain.
The toolset of analysis was continued with the introduction of the measures used, from the direct photographic survey evaluation with mission success and vehicle risk, to an energy and thus cost efficiency analysis through cost of transport and battery charge extrapolation, and finally thoughts how the dimensionless generalisation based on the vehicle length may be extended for comparing key parameters for altitude tracking.
Then the uncommon properties of data collected with a mechanical scanning sonar that is moving over terrain and the chosen visulalization were explained.
The next section focused on the Autosub6000 simulation, its structure, notation and units beyond the general conventions introduced earlier, the simulated vertical plane vehicle dynamics, as well as the model parameters, sonar scan simulation and finally the validation and variation strategy used throughout the simulated experiments.
Finally the methods of the practical experiments with Delphin2 were introduced, from the terrain following implementations that were developed and tested, to the experiment site and setup, and the data analysis performed over the datasets obtained through a repeated crossing of the same terrain feature.

Chapter 5

Results

This chapter describes the results of the Autosub6000 mission data analysis, it shows which key parameters were identified in the validation and variation steps of the Autosub6000 simulation, and the results of the lake experiments with Delphin2. All datasets are analysed for mission success and vehicle risk. Selected experiments are then studied further, using altitude, pitch, detection range, actuator demands, and, in case of Delphin2, power consumption. The cases selected for simulation and experiment are targeted at determining how the simulation can be used as a general tool for understanding the altitude tracking performance of AUVs, determining what parameters (and lack of information about parameters) causes inaccuracies in the simulation and have significant impact on the terrain tracking performance. The repeated experiments with Delphin2 compare different combinations of thruster and sternplane actuation, show the general repeatability of the AUV performance, and how this repeatability diminshes with failures to reliably detect the terrain. Based on the problems identified with sonar terrain detection on both Autosub6000 and Delphin2, the results chapter ends with a section focusing on the mechanical scanning sonar, where its limitations lie and how better use can be made of this - widely used - type of sonar for flight style altitude tracking in the unusual situation of scanning whilst moving over a significant distance while a scan is completed.

5.1 Autosub Mission Analysis

To get an initial overview, a statistical analysis was run over all recorded mission data, after restricting the data only to those parts of the mission that mostly remained at an altitude below 20 m.

Figure 5.3 gives an initial view showing that, after initial tests, a full photographic survey length of over 80 km can be achieved with Autosub6000 in a single mission. Most missions achieve a success of over 50%, 9 of the 19 missions achieved over 80% mission

success. It must be noted that during the most recent available research cruise, JC142, the performance is significantly worse than in previous missions. At the same time, due to the bad results of each mission, the configuration of the obstacle avoidance was varied more than usually between missions, changing at least a scaling factor for the pseudo altitude significantly. It is surprising that during M134 a larger speed over ground is achieved with the same logged motor power request as for M116, a mission that kept a much more even pitch angle. This raises the question if any further changes were made, the information on which is unavailable for this work. This variation, and the uncertainty thereof, increases the difficulty in re-creating and analysing these missions in simulation. Several of the successful missions also got too close to the terrain at least once, with in the worst case over 60 m spent in the risk zone during M57. Neither the mission success nor the vehicle risk could be read as clearly from the statistical altitude analysis alone, or even from the detailed altitude plot (see appendix E), demonstrating the usefulness of the newly introduced measures.

The surge velocity was estimated from the north- and south- velocity recorded by the Inertial Navigation System (INS), neglecting the vertical surge component due to moving at a pitch angle. Over time, the operational velocity reduced from around 1.5 m/s in early missions to 1 m/s in the most recent (JC142) missions, with most missions run at around 1.2 m/s. 1.2 m/s was selected as a surge velocity for most studies.

Looking into the statistical data for the obstacle avoidance (Figure 5.4, it can be noted that on average the pseudo altitude used in the less successful missions is not notably larger, and the standard deviations do not stand out either, compared to the more successful missions. In reality, of course, the pseudo altitude was indeed larger and varied more, however this is only visible after removing the scaling factors that were introduced in an unsuccessful attempt to keep Autosub6000 closer to the terrain.

Whilst the theoretical detection range of the obstacle avoidance is 150 m and above, the statistical analysis shows that this range is hardly ever achieved. Even the maximum range of most missions stays in the range of 50 m. It is noteworthy that the detection range of the less successful missions is on average larger (note M115), however it cannot be determined if the larger range caused an over-estimate of the terrain, or more likely if the larger altitude resulted in a steeper angle between the sonar beam and the terrain, increasing the terrain returns.

Figure 5.1 shows the average detection range taken from the available Autosub6000 missions, plotted against the median altitude at which the horizon was detected. Before applying this analysis, all ranges indicating no detection were removed from the data. Since it is unclear at what processing step in the software the scale factor is applied, the horizon detection range might already include the scale factor; for these plots the values remain unchanged from the recorded data. To investigate what altitudes would have to be achieved on Delphin2, a non-dimensional plot was made. To achieve a comparable range to the data from the D377, on the 2 m long Delphin2, a range of 8 m would need to be achieved.

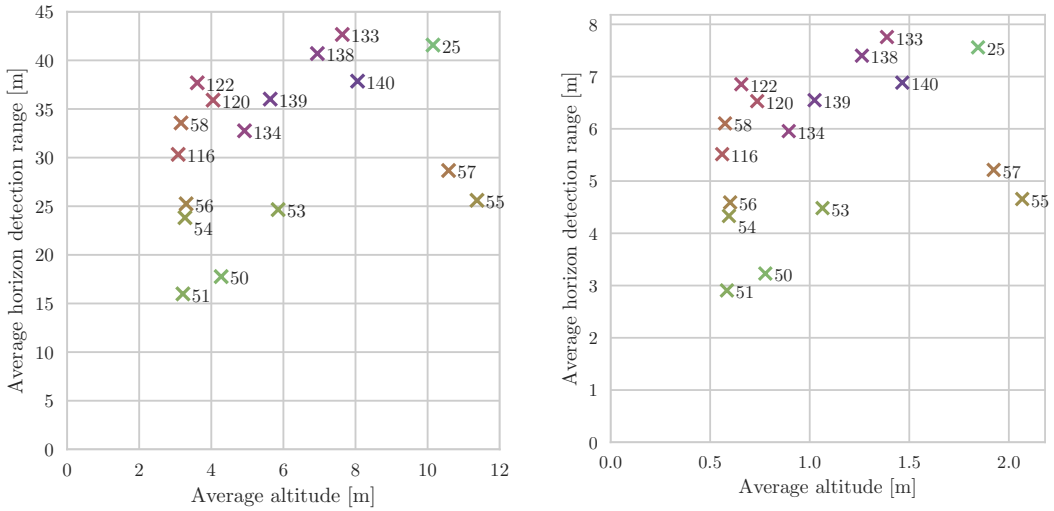

(a) At Autosub scale. (b) Non-dimensionalised (L=5.5 m).

Figure 5.1: Comparison of altitude and horizon detection range.

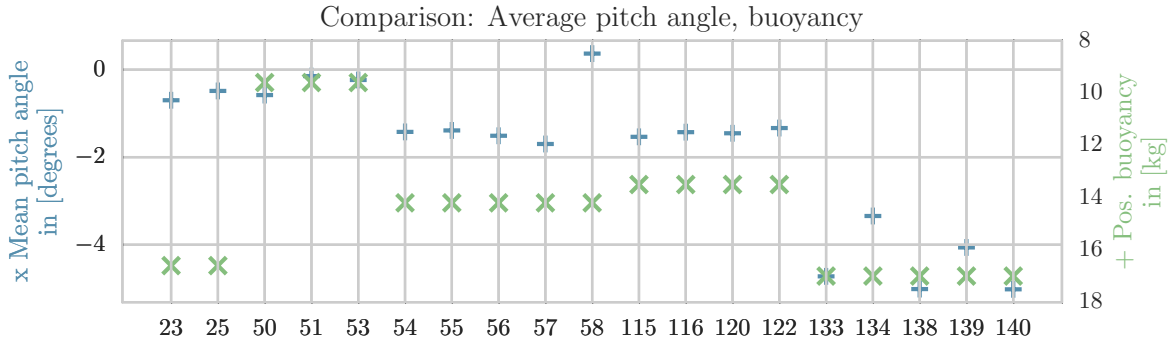

Figure 5.2: Correspondence of average pitch angle and Autosub6000 buoyancy.

A comparison of the pitch angle (Figure 5.2 shows that overall the pitch angle goes inversely with the positive buoyancy of the vehicle. This is expected: a stronger force towards the surface due to the increased positive buoyancy needs to be counteracted by a stronger downwards force. Small variations in the pitch angle are likely due to differences in the terrain, but also variations in the AUV's buoyancy due to changes in water pressure and water density. At a first glance, missions M23, M25 and M58 seem to badly match this expectation, maybe due to errors in the recorded buoyancy. A look at the average mission depth reveals that all three have in common that their average depth is less than 1000 m. This allows an alternative explanation that the mean pitch changes due to buoyancy changes as the vehicle dives. This would mean that during missions of less than 1000 m depth, the vehicle is around 4 kg less positively buoyant thus requiring a smaller pitch angle to compensate the positive buoyancy.

The full data set of the statistical analysis is given in table F.2.

Figure 5.3: Overview statistics of all available Autosub6000 missions. Missions where the obstacle avoidance, was not used for the complete low altitude tracking section are marked with a star (*).

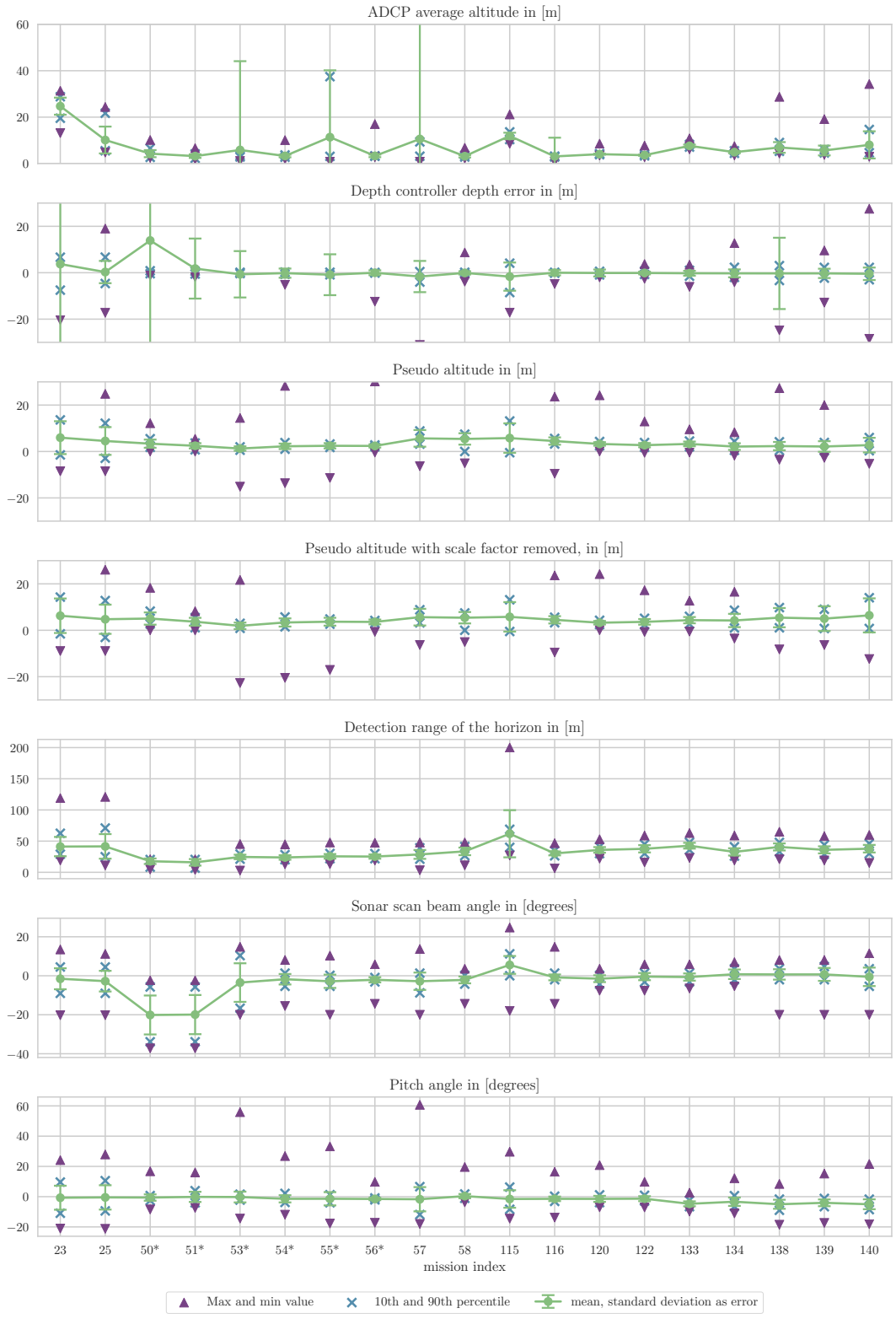

Figure 5.4: Statistical analysis of obstacle avoidance data for all Autosub6000 missions. Missions where the obstacle avoidance, and thus the horizon tracking with the sonar beam, was not used for the complete low altitude tracking section are marked with a star (*).

5.2 Autosub Simulation

The following section presents the validation steps that were performed for the Autosub6000 simulation. Often a set of key parameters became clear during a validation step, which was then selected for future simulation based on a study of the variation of this parameter. As a result, evaluations of different parameters are presented interwoven with the validation cases, showing how parameters of later validation cases were chosen, but also demonstrating the impact of a selected parameter.

The initial validation looks at the stability, convergence, and repeatability of the simulation. It uses a test case that was already simulated in [Kimber and Marshfield, 1993], the design study of Autosub1, on which the dynamic model of Autosub6000 is based. As a second case, these simulation results are then also compared to the original results from 1993. After this validation case, the Autosub1 model is replaced by Autosub6000. A main change in the design between the two vehicles is the addition of winglets close to the centre of rotation. The addition of the winglets in simulation is studied on the test case of tracking a constant depth.

These initial validation steps are followed by two parameter studies, first analysing the vehicle depth and pitch while the sternplane angle is varied between its maximum and minimum angle, to achieve the maximum pitch angle. Then the tallest step change that can be navigated is determined through simulation, and the passage over a small terrain step with and without use of the obstacle avoidance is analysed in detail.

Finally, Autosub missions M53 (without obstacle avoidance) and M57 (with obstacle avoidance) are used to compare the simulation results with real mission data and to study how the simulation implementation and parameters may differ from those during the actual mission.

5.2.1 Stability Analysis

For the stability analysis, the same test case was chosen as for the comparison to the Kimber report for Autosub1. The vehicle dynamics parameters given in the report were used for the simulation at full scale Autosub1 length (7 m), with zero buoyancy and 2 m/s surge velocity (target speed given in the report). A constant sternplane demand between zero and twenty degrees is applied for ten seconds. The simulated model uses parameters for Autosub1 and zero buoyancy. Simulation frequencies between 1 Hz and 30 Hz were tested. It was found that the simulation frequency has both an upper and a lower limit. As expected, with an increase in frequency the results converge from inaccurate results at 1 Hz to consistent results between 10 Hz and 20 Hz. At above 20 Hz it was found that the ROS messaging system on the local machine slows down and several nodes work with a lower frequency than required. The same effect happens if a simulation frequency of 10 Hz is chosen and the simulation is sped up. As soon as the effective ROS frequency passes above 20 Hz the simulation results become unreliable.

However, after tests on other machines, it appears this limit is due to the available Random-Access Memory (RAM) on the machine. Based on these results the speed-up factor was varied depending on the machine used for simulation. A factor two speed-up was used with 4 GB, a factor five with 12 GB (both machines have four CPUs).

5.2.2 Kimber Report Validation

As a second validation step of the simulation, the ten second sternplane action results were compared to the simulation results from [Kimber and Marshfield, 1993](section 12.2.1).

Overall the dynamic behaviour is very similar, though with increasing sternplane angle it becomes visible that in the ROS simulation the pitch angle has a higher change rate than in the original simulation. As a result a larger depth is reached. The percentage difference of the maximum pitch angle and maximum depth reached is given in table 5.1. Comparing to the typical pitch angles during Autosub missions (see Figure 5.4 and Appendix E), most of the time the absolute pitch angle is below 10°, and the downwards pitch is limited to 30°. The vehicle (and the simulation thereof) are thus mostly operating in a pitch angle range where the simulation results match well.

δ_s	5	10	15	20
pitch error	11 %	12 %	15%	17%
depth error	1 %	2%	6%	11%

Table 5.1: Error of the ROS simulation compared to the [Kimber and Marshfield, 1993] simulation.

5.2.3 Autosub6000 Rear Winglets

To account for the added winglets on Autosub6000, additional terms were introduced as described in Section 4.7.4. To better understand the impact of the different corrections, a depth keeping simulation was repeated with an increasingly complex correction term. For the simulation, the AUV was simulated using the depth PID control with a constant depth demand until a steady state pitch angle was reached. The following cases were simulated (see Section 4.7.4 for the introduction of the correction factors):

1. Sternplane only, no winglets
2. Winglets without correction:
   $Z_{winglet} = 2 \cdot 0.5 \cdot \rho \cdot A \cdot Cl \cdot u^2$
3. Winglets with aspect ratio correction:
   $Z_{winglet} = 2 \cdot 0.5 \cdot \rho \cdot A \cdot Cl \cdot u^2 \cdot C_{ai} \cdot \beta$

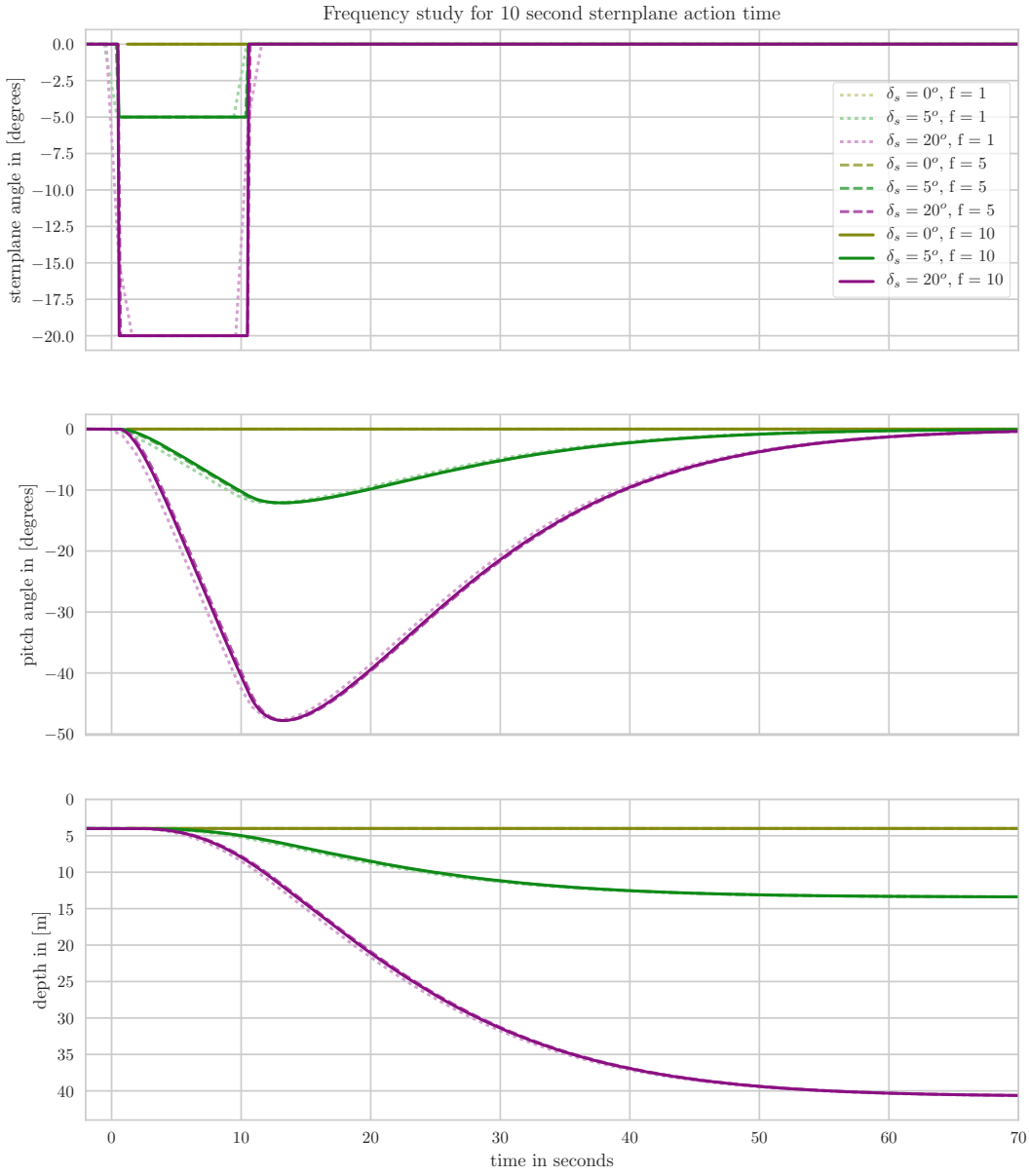

Figure 5.5: Convergence of the simulation results with increasing simulation frequency, simulated at three sternplane angles δ_s over a range of frequencies f.

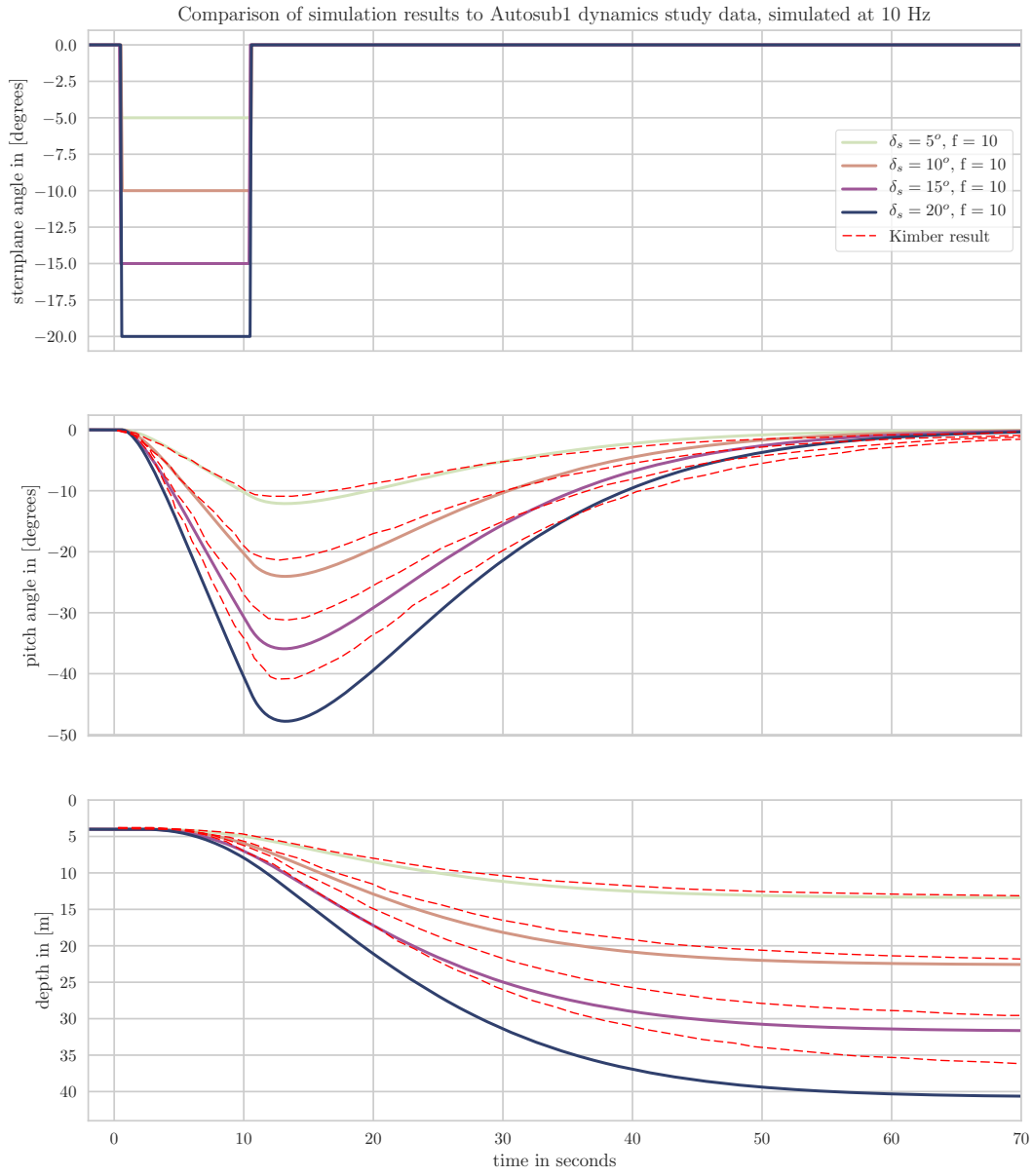

Figure 5.6: Comparison of simulation results from the implemented ROS simulation and [Kimber and Marshfield, 1993], simulating the Autosub1 vehicle with zero buoyancy, applying different sternplane angles δ_s at a simulation frequency $f = 10Hz$.

4. Winglets with aspect ratio and angle of attack correction:
   $Z_{winglet} = 2 \cdot 0.5 \cdot \rho \cdot A \cdot Cl \cdot u^2 \cdot C_{ai} \cdot \alpha_w$

The simulation results are shown in Figure 5.7. The simulation without correction terms requires a pitch angle of almost five degrees for steady state, whilst all correction terms move the required pitch angle closer to the typical range of 1° to 2° downwards pitch of Autosub6000 with a similar buoyancy. Cases two and four come closest to this range. Since the consideration of the heave velocity was deemed important, the full correction with aspect ratio and angle of attack terms was chosen.

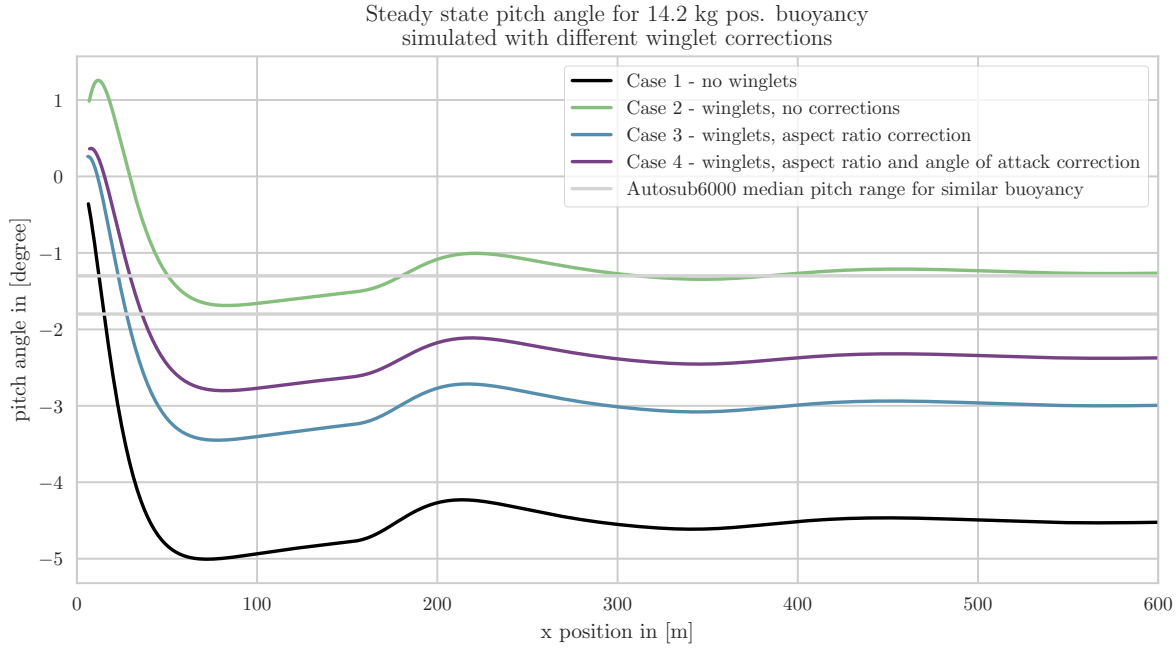

Figure 5.7: Reaching a steady state pitch for keeping a constant depth, simulated with different winglet correction terms.

Whilst going over the corrections for the winglets, the changes in the control surfaces were also considered. The size and position of the control surfaces on Autosub6000 has slightly changed, however based on simulation results it was decided that the changes were small enough to not warrant further scaling factors.

It should also be noted that with the used controller it takes over 100 m for the variation of the pitch angle to reach a value within 0.5° of the steady state.

5.2.4 Sternplane Response

To evaluate the manoeuvrability of Autosub6000 in the vertical plane, the sternplane response was further tested. For a combination of buoyacies and surge velocities, a sternplance change procedure was repeated. The sternplane procedure was executed starting

both with the maximum and minimum sternplane angle. It is described for the case of starting with the minimum angle, the other case simly has all maximum/minimum attributes swapped. The maximum and minimum sternplane is ±20°, the maximum and minimum pitch angle is ±23°. Both limits are based on typical configurations of Autosub6000 (see Appendix D). First, a depth controller was used to achieve a stable depth, and thus a realistic initial condition for all buoyancies. Then the experiment was started by applying the maximum sternplane angle until the maximum pitch angle is reached. At this point, the sternplane angle is switched to the minimum sternplane angle, which is kept until the minimum pitch angle limit is reached. Then the maximum sternplane angle is applied again. This time on reaching the maximum pitch angle the sternplane is set to zero. The buoyancy, speed, and use of winglets was varied.

Figures 5.9 and 5.10 show the resulting vehicle path, and pitch angle, and the sternplane angles that were applied. The values are plotted over x-progress rather than time, to analyse the manoeuvrability relative to the terrain. The initial stable depth is taken as zero depth and the moment of first applying a maximum or minimum sternplane angle is the zero x-position.

Independent of the type of variation, all simulations barely change their depth over the first ten metres after the initial sternplane action. The depth change stays below 0.7 m. At this point experiments with a significant buoyancy counteracting the direction of motion already reach the pitch angle limit. For the 1 m/s experiments, most of the non-zero buoyancy cases fail to reach one of the pitch angle limits, since the restoring moment is larger than the moment from the sternplane at this speed. After reaching the pitch angle limit and changing the sternplane setpoint, all vehicles overshoot the pitch angle limit before changing the pitch direction. On a pitch controlled vessel, a well tuned controller would approach the maximum angle slower, since the error would become smaller as it is approached. As a result, the maximum surfacing rate is reached slower, but this overshoot would be reduced and a considerable sternplane action in the opposite direction may also lead to a faster change.

The fastest simulation at 2 m/s has the strongest curvature and the steepest ascend rate in the depth plots. The vehicle path and initial pitch are also influenced significantly less by the vehicle buoyancy and the initial pitch angles are all close to zero. Not only the manouvrability, but also the predictability of the manouvrability is better at higher speeds. This also results in a larger overshoot, which increases the time between reaching the pitch limits. Whilst one would expect that the increase in speed means a disadvantage for avoiding obstacles, the faster speed clearly achieves the best manouvrability. Only the limit in detection speed of the forwards scanning sonar makes operation at high surge velocity less attractive compared to slower speeds. Whilst not reaching the same manouvrability and similarity at different buoyancies as at 2 m/s, the added winglets at 1 m/s slightly improve the manoeuvrability of the AUV, particularly when opposing the forces and moments due to buoyancy. The vehicle reaches a stable state faster at 1 m/s than at 2 m/s after the sternplanes are set to zero. The advantage of moving at slower speed is the additional time for obstacle detection.

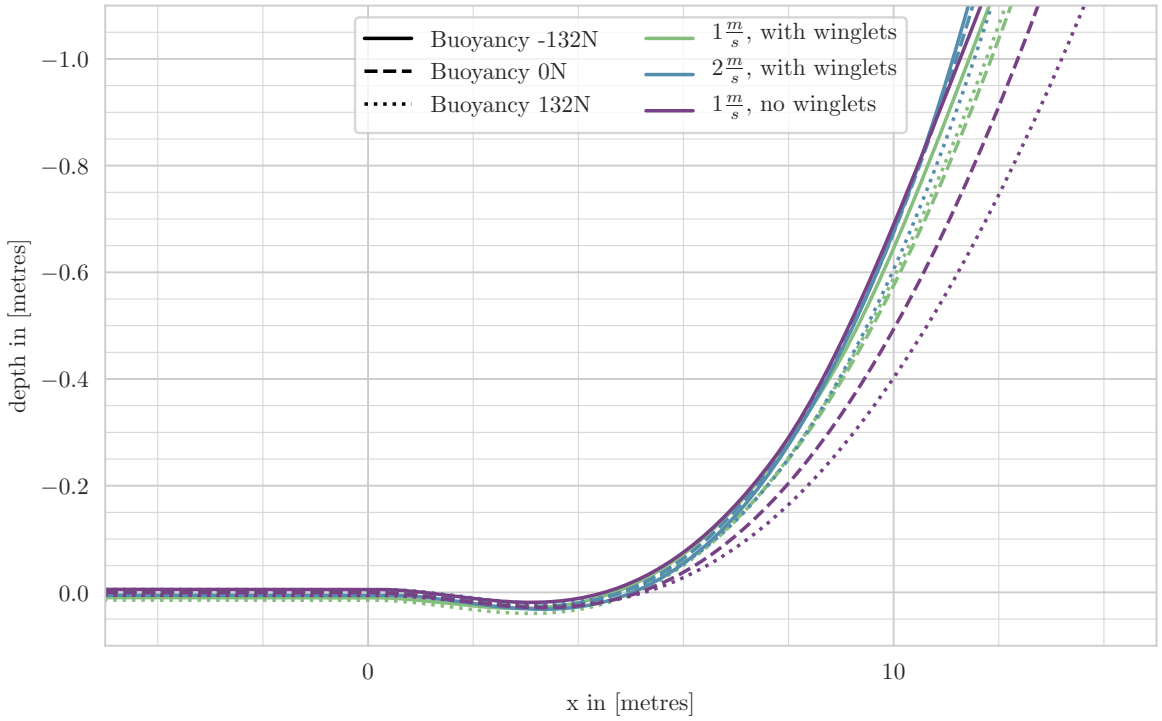

Figure 5.8: Detail view of the sternplane variation: Autosub6000 reaction to a maximum sternplane demand from keeping a stable depth. A small increase in depth is observed before surfacing, due to rudder forces acting before the pitch change causes the expected upwards motion. The depth is measured relative to the Centre of Gravity (CoG).

The figures also show the delay between pitch angle and depth change rate, illustrating that that the pitch angle itself is not an indication of the depth change rate. Comparing for example one of the cases where the pitch limit is never reached to the depth change rate of any other case at the point when the maximum pitch angle is reached, it is barely different.

Depth change rates around 60% are achieved. To achieve a depth change of 100 m (the order of magniture of the variations expected around the depth data at the 5 km pixel resolution of most seafloor maps), approximately 150 m detection range are required. Since a constant surge velocity is assumed, the turning rates and surfacing rates observed in simulation are optimistic.

A close look at the first 15 m in Figure 5.8 show that initially the vehicle actually moves in the opposite direction of the intended direction. A similar effect can be observed in the advance phase of the turning circle manoeuvre (see [Molland and Turnock, 2011, p.61]). Before the vehicle reaches a pitch angle, pointing it in the intended direction, forces due to the rudder position push it in the opposite direction. This effect was expected from discussion with vehicle operators, and it showing up in simulation affirms the validity of the simulation. Compared to the goal altitude range, the variation of less than 0.05 m is small. A larger impact on vehicle safety comes from the vehicle changing its pitch angle and thus its bounding box distance to the terrain. At the point of reaching the maximum pitch angle, after around 10 m, the depth change is still less than 1 m, whilst its bounding box distance has reduced by the same order of magnitude.
The simulation also showns that unlike the horizontal plane, where constant sidewards forces are usually not expected, calculating a turning radius in the vertical plane for a non-zero buoyant vehicle is a complex, buoycany and surge dependant endeavour.

5.2.5 Tall Step Simulation

So far, none of the simulations used the altitude controller beyond reaching a stable depth state. Now the altitude control is integrated in the simulation. First, an estimate of the largest step that can be avoided with Autosub6000 is made by simulating the vehicle response to a steep step. Shown here are simulation results for a 150 m sonar range, at 1.6 m/s surge velocity, with 14.2 kg positive buoyancy. The maximum pitch limit is 23 degrees. Figure 5.11 shows the step heights between which the vehicle is no longer able to avoid crashing. For such a steep step change of course the photo survey success is very small, since the vehicle spends most of the time avoiding the step. Nonetheless for vehicle safety considerations the simulation of a specific vehicle configuration including simulating the obstacle avoidance is vital. It helps determining the maximum step size than can safely be navigated and what unexpected effects may occur. With increasing sonar range the distance until the maximum surfacing velocity is reached looses significance. At x-position zero, the step is first within the 150 m range of the sonar. It then takes over 10 m progress in x-direction before the vehicle reaches an altitude outside of the photo distance. At this point, the vehicle is reaching its

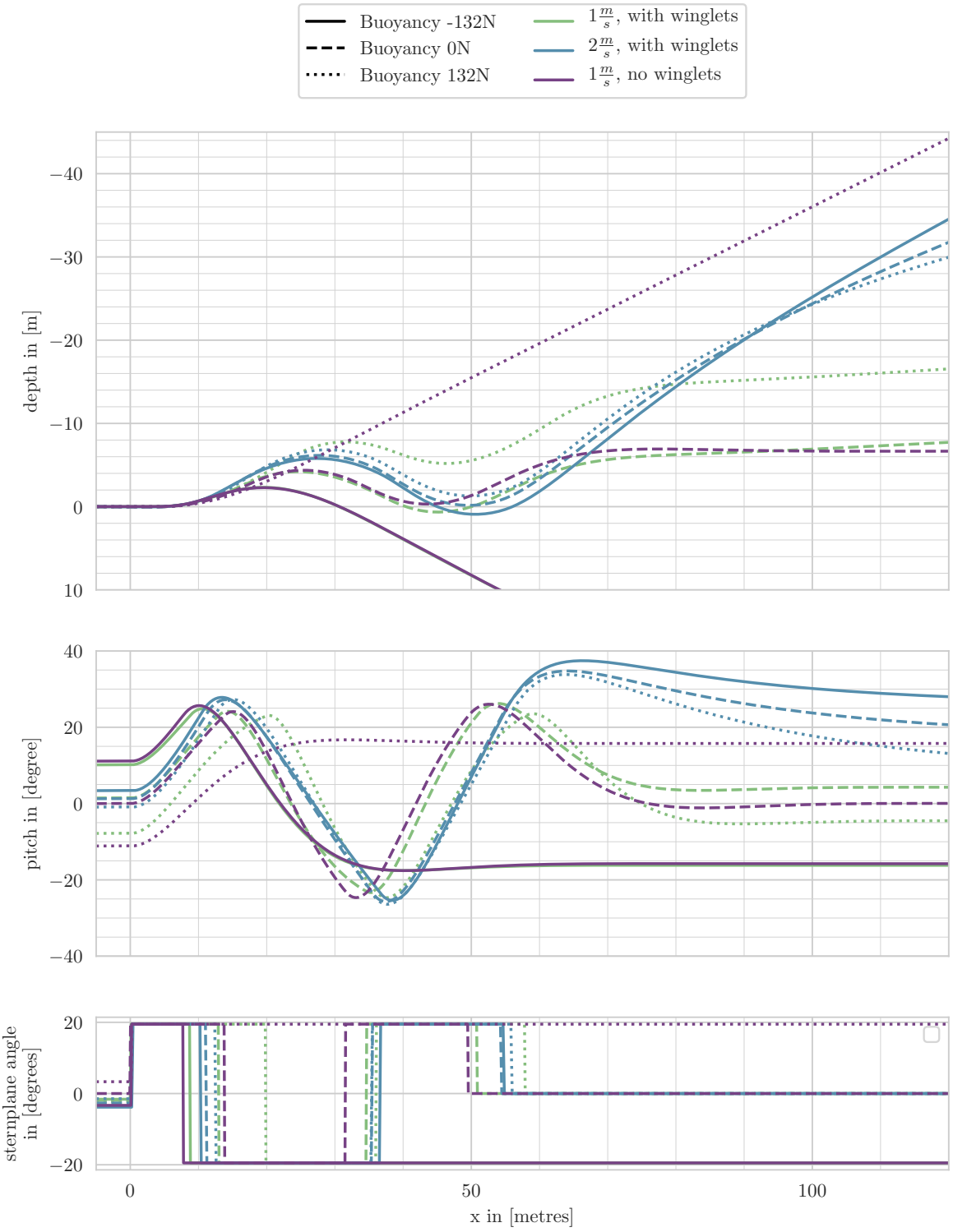

Figure 5.9: Autosub6000 reaction to maximum and minimum sternplane demands, starting with a maximum demand first. The sternplane variation is explained in detail in 5.2.4.

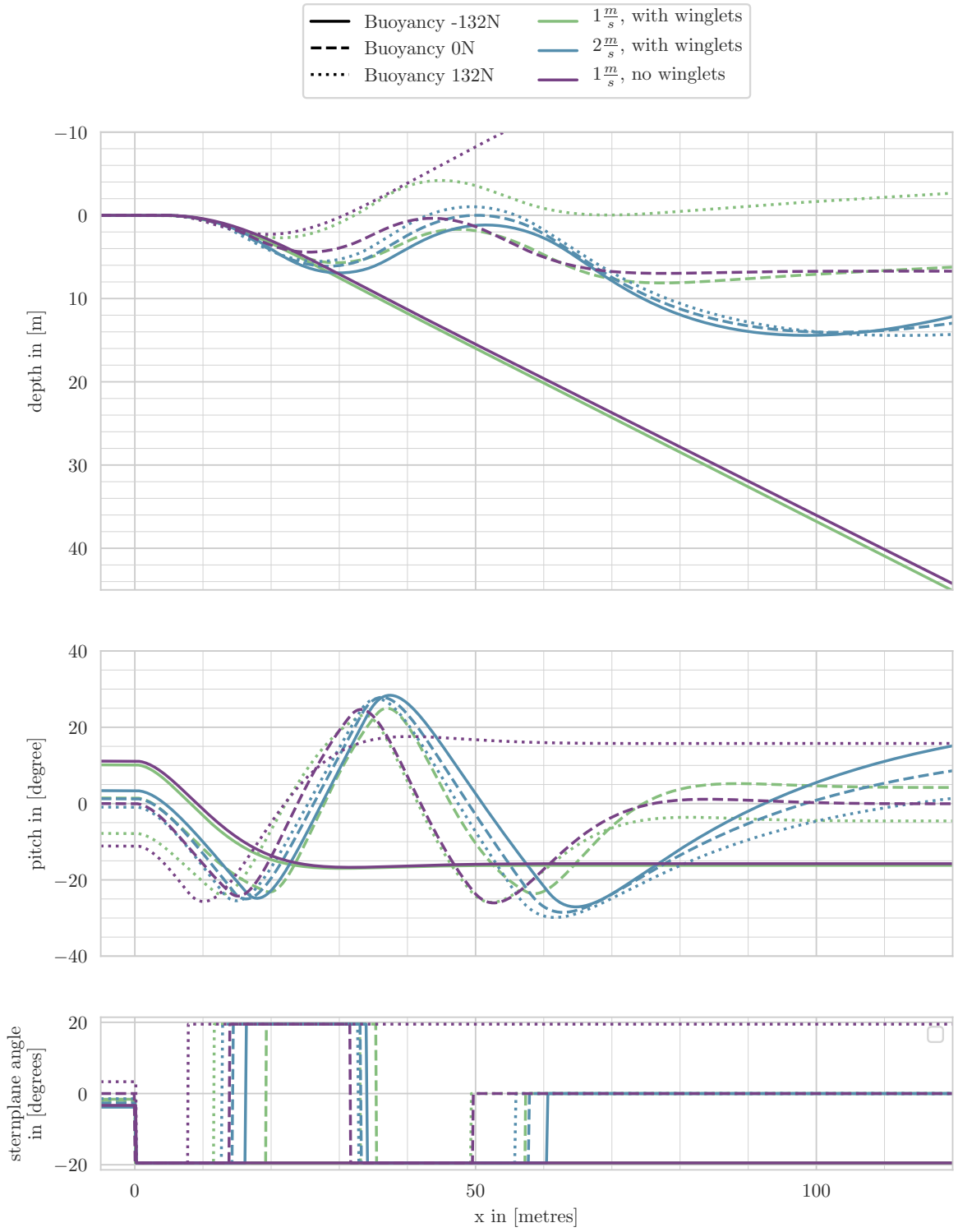

Figure 5.10: Autosub6000 reaction to maximum and minimum sternplane demands, starting with a minimum demand first. The sternplane variation is explained in detail in 5.2.4.

maximum surfacing velocity. In the simulated case, the slope of the surfacing motion is less than the maximum allowed pitch angle. Relative to the detection range of 150 m, the maximum slope that can be navigated for this vehicle, control, and sonar detection configuration is between 33% and 40%. This is less than what would be expected from the sternplane response simulation, since the depth controller did not apply as extreme sternplane demands as in the stenplane response study. The detailed simulation of the obstacle detection also shows that when approaching the top of the step, the pitch demand reduces once the obstacle is no longer detected at the maximum scan angle. This may cause cause the vehicle to crash in the terrain, even if the terrain step is slightly lower than the height at which the simulated vehicle collides with the 60 m step. It also shows that whilst a steep step response is a further improvement towards gauging the vehicle risk for a given flight style AUV and control configuration, the vehicle response depends on more details of the terrain structure. With the asymmetry in vehicle response due to buoyancy, not only the variability of the terrain, the maximum step, the ascend rate and the curvature of the terrain need consideration, but also the sign for each of these parametrizations.

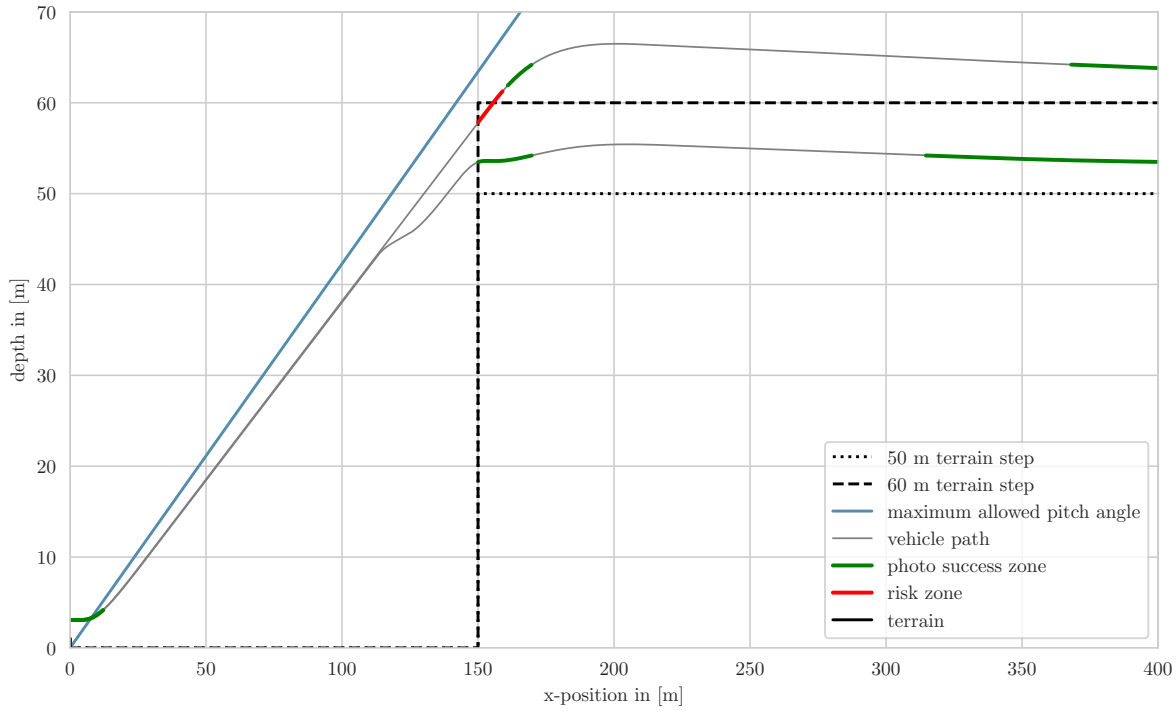

Figure 5.11: Vehicle paths over steep steps at the limit of the Autosub6000 manoeuvrability.

5.2.6 Small Step Simulation

Moving from the basic need of recognising the maximum step that can safely be navigated, towards increasing the photo survey success over complex terrain, smaller terrain steps are simulated. A 3 m altitude over a small step of 2 m is chosen for varying numerous parameters of the vehicle, control and obstacle detection.

The scaled equivalent of this altitude and step, using the length of Autosub6000 and Delphin2 as the scaling factors, would be tracking a 1 m altitude over a 0.7 m terrain step, similar to the experiments in Testwood Lake.

First the impact of buoyancy, integral term, and surge velocity is tested without forwards looking obstacle avoidance, then the obstacle avoidance is applied. Before the start of the plot, 300 m of constant altitude demand are skipped, during which the vehicle can reach a steady state. The variations shown in this section were chosen based on variations that were noticed in the configuration of Autosub6000, and based on variations that are made for terrain following simulations of real experiments over more complex terrains in the next sections.

When not being varied, the surge velocity is 1.2 m/s, the minimum depth integral term is -0.3, and the buoyancy is 14.2 kg, based on the configuration used in most of the Autosub6000 missions analysed. The vehicle success and risk zones of this configuration is shown in Figure 5.12(A) and simulation results for this configuration are included in all variation studies.

A mission risk analysis for selected variation configurations is shown in Figures 5.12 (withouth forwards looking detection) and 5.13 (with forwards looking detection). Figure 5.12 illustrates the need for a forwards detection, with all vehicles at risk when first crossing the step. A comparison of Subfigures (A) and (C) also shows the significant impact of the surge velocity on manoeuvrability. When crossing the step ad a higher speed, the vehicle risk barely increases, whilst the photo success improves slightly. A comparison with the results using forwards looking obstacle avoidance shows that whilst removing the vehicle risk, the forwards looking obstacle avoidance also significantly reduces mission success. The best result of all step response simulations is achieved with a sonar that is mounted with an offset. In this case, the step is detected, so the vehicle can adapt its altitude, but the height of the terrain is underestimated so the vehicle still keeps at a close distance to the terrain.

Going into more detail, the altitude, the sternplane angle applied to achieve this altitude, the pitch demand and feedback in the cascaded PID contrl loop and the depth integral term I_z are compared. Figure 5.14 shows the results of the buoyancy variation. Since the altitude measurement is simulated as a beam that moves with the vehicle, the vehicle path over the terrain varies whilst for all three buoyancies the altitude is kept accurately, and there is no noticeable variation between the goal achieved by the controller. As expected, the sternplane angle, pitch angle and depth integral term vary with the buoyancy.

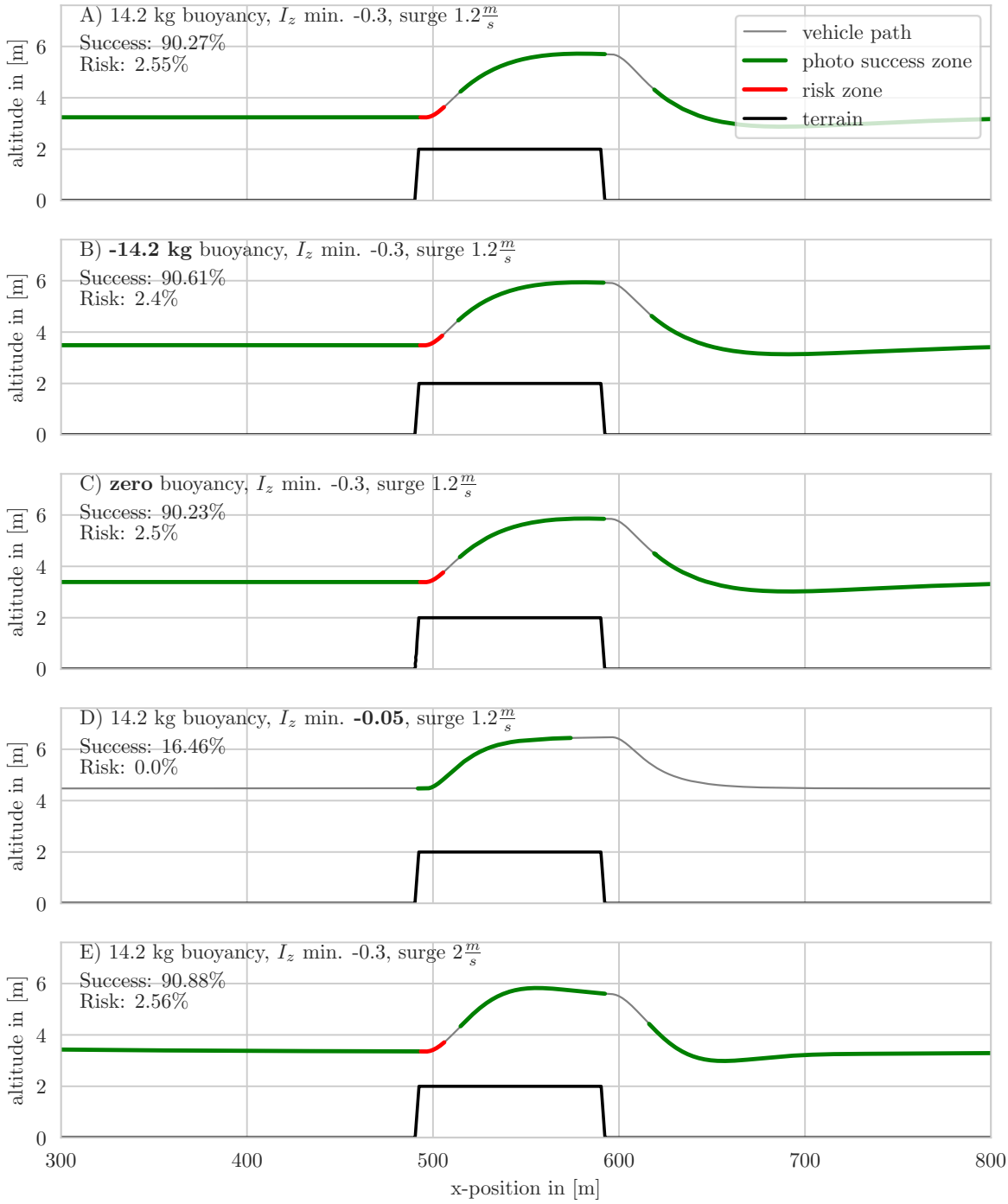

Figure 5.12: Vehicle paths of step simulation without forwards looking obstacle avoidance. The results are analysed in detail in Figures 5.14 (A, B, C), 5.15(A, D), and 5.16(A, E).

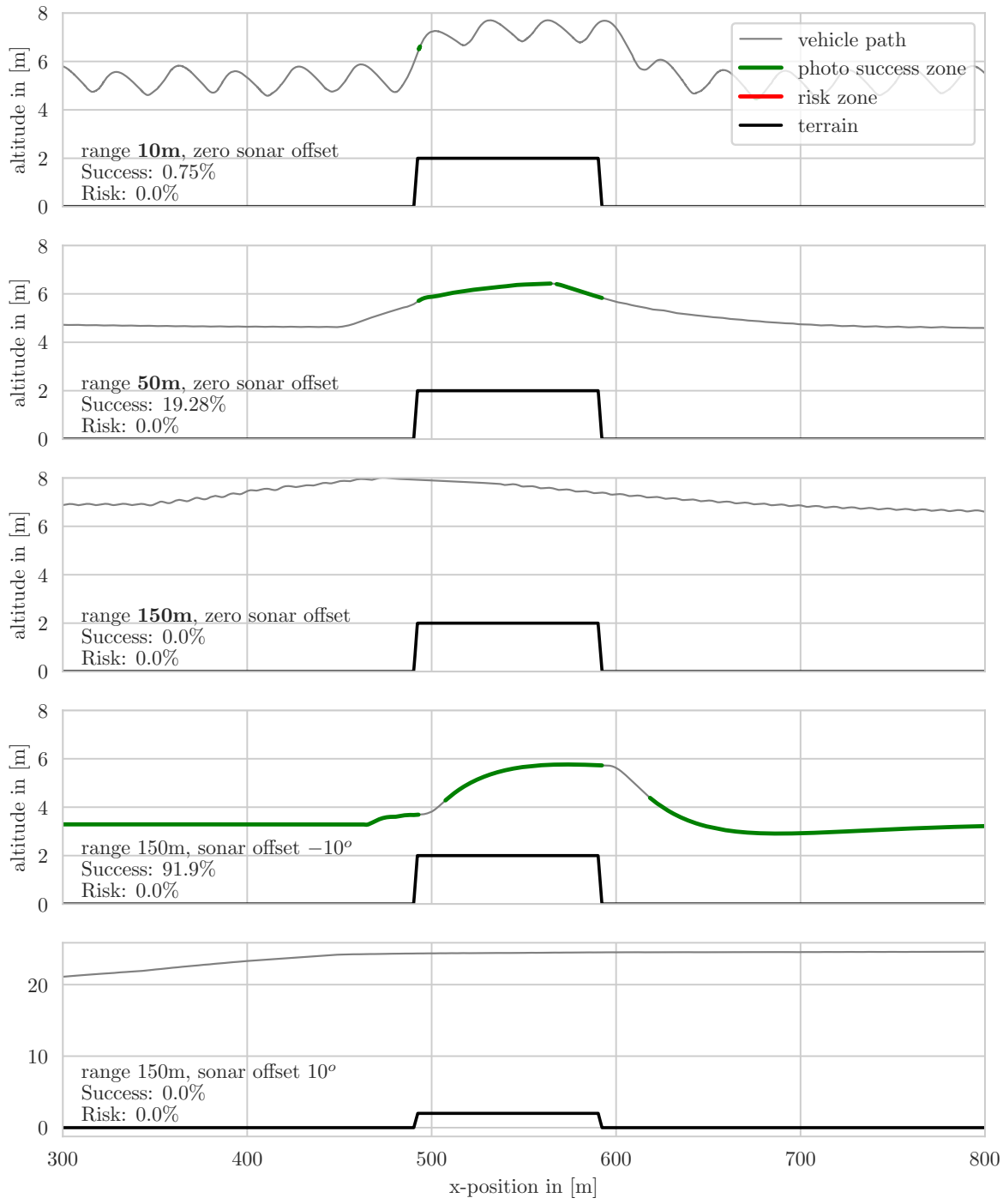

Figure 5.13: Vehicle paths of step simulation with forwards looking obstacle avoidance. The results are analysed in detail in Figures 5.17 (A, B, C), 5.18(A, B, C), and 5.19(A, D, E).

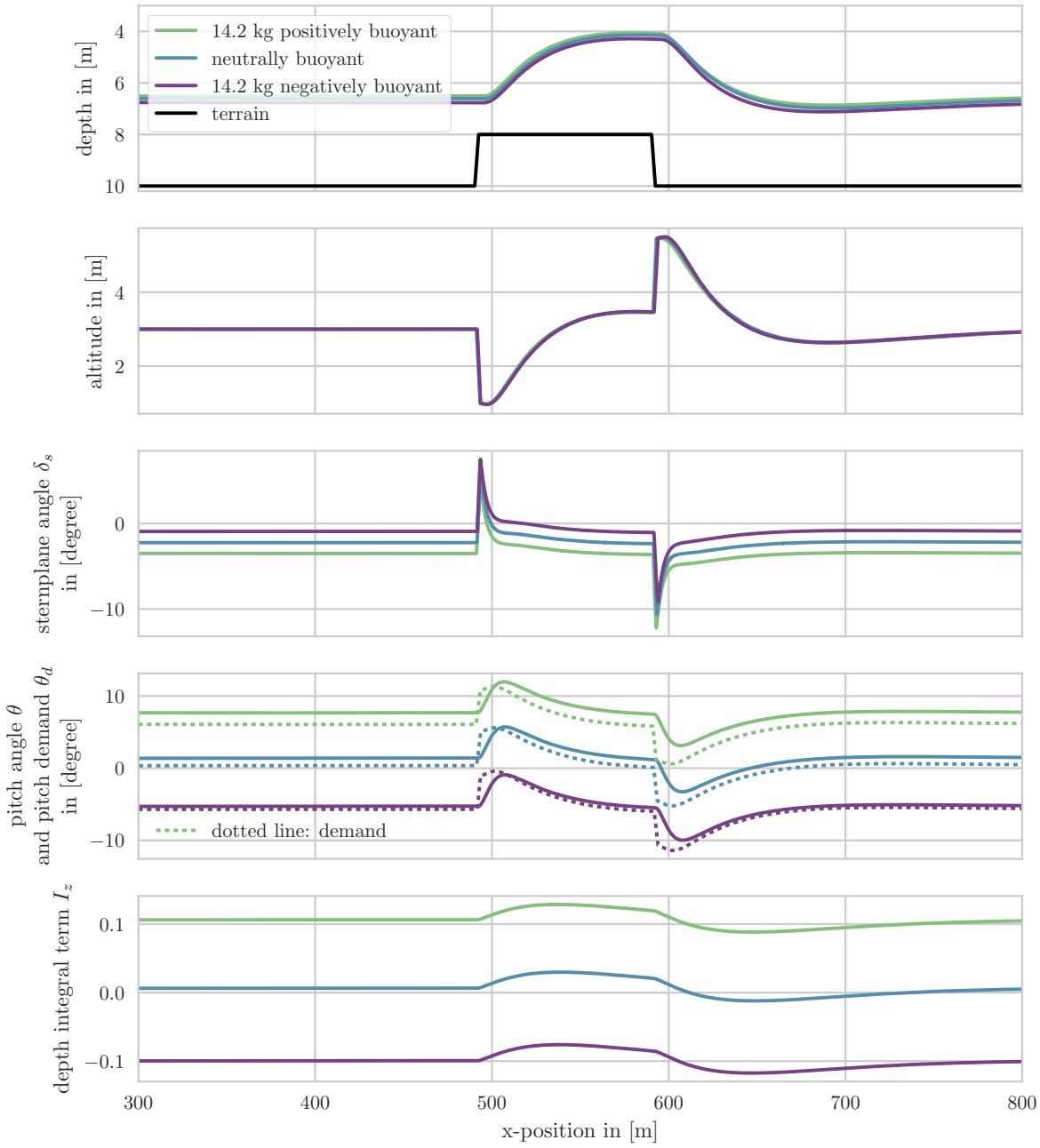

Figure 5.14: Altitude tracking at 3 m altitude over a 2 m high step without obstacle avoidance, with buoyancy variation.

Next, the integral term is varied. This variation of the integral term was chosen since in later simulations a consistent positive altitude error was observed. Since with increasing buoyancy the required altitude term changes (see Figure 5.14, this points towards a variation in the buoyancy. The simulation shows that a too small limit for the depth integral term on a positively buoyant vehicle means that the vehicle will remain at a too large altitude, with the controller incapable of compensating for the constant upwards force of the positive buoyancy. However, increasing the integral term by too much will lead to the controller increasing the integral term whilst the vehicle is returning to its goal altitude after a downwards step, causing an overshoot and increasing the vehicle risk.

In the last simulation without obstacle avoidance, again the surge velocity is varied between 1.0 m/s and 2 m/s. Again the fastest surge velocity results in the best results, returning to the correct altitude first even when plotted against the x-position rather than time. This further supports operations at faster speeds, putting the pressure on the detection range.

Next, the forwards looking obstacle avoidance using the horizon tracking algorithm from Autosub6000 is introduced. Whilst usually the detection range is varied due to the terrain properties and grazing angle of the sonar, in the simulation it is set to a fixed value. Figure 5.17 shows that depending on the scan range a significant oscillation can occur. A closer inspection in Figure 5.18 shows a detailed view of the two causes of this oscillation: for very long ranges, it is due to the detection angle increasing or decreasing by one angle step. Due to the sonar beam opening angle the altitude estimate changes by several metres. This low resolution, of a magnitude larger than the goal altitude itself, also causes the vehicle to generally stay above the goal altitude. For shorter ranges, the oscillation starts if the vehicle reaches a combination of too large altitude and upwards pitch, so the lowest detection angle no longer detects the terrain. The horizon scanning angle then increases to zero and then starts decreasing again. In the meantime the vehicle descends towards the terrain based on the altimeter measurement. With the vehicle pitched towards the terrain, the flat terrain appears as an upwards slope, leading to a high pseudo altitude, which in turn causes the vehicle to ascend steeply, loosing the detection again.

Both oscillation would be significantly reduced by increasing the scan rate, or even receiving an instantaneous scan result for all scan angles, as can be achieved with a multibeam sonar.
The bad resolution of the terrain at large ranges can only be resolved by increasing the complexity of the altitude tracking, e.g. by implementing a mapping algorithm and using the long range detections only for large changes in the altitude demand.

Since during M115 an angle offset was reported, an offset of the scan angle was also simulated. Unlike on the real vehicle, the scanned sector on the simulated vehicle remained the same, and the scan angle offset was applied in the evaluation. Figure 4.13 indicates the sign conventions of the applied offset. The simulation was performed with an 150 m detection range, and to remove the effect of the scan rate, the sonar was simulated at a

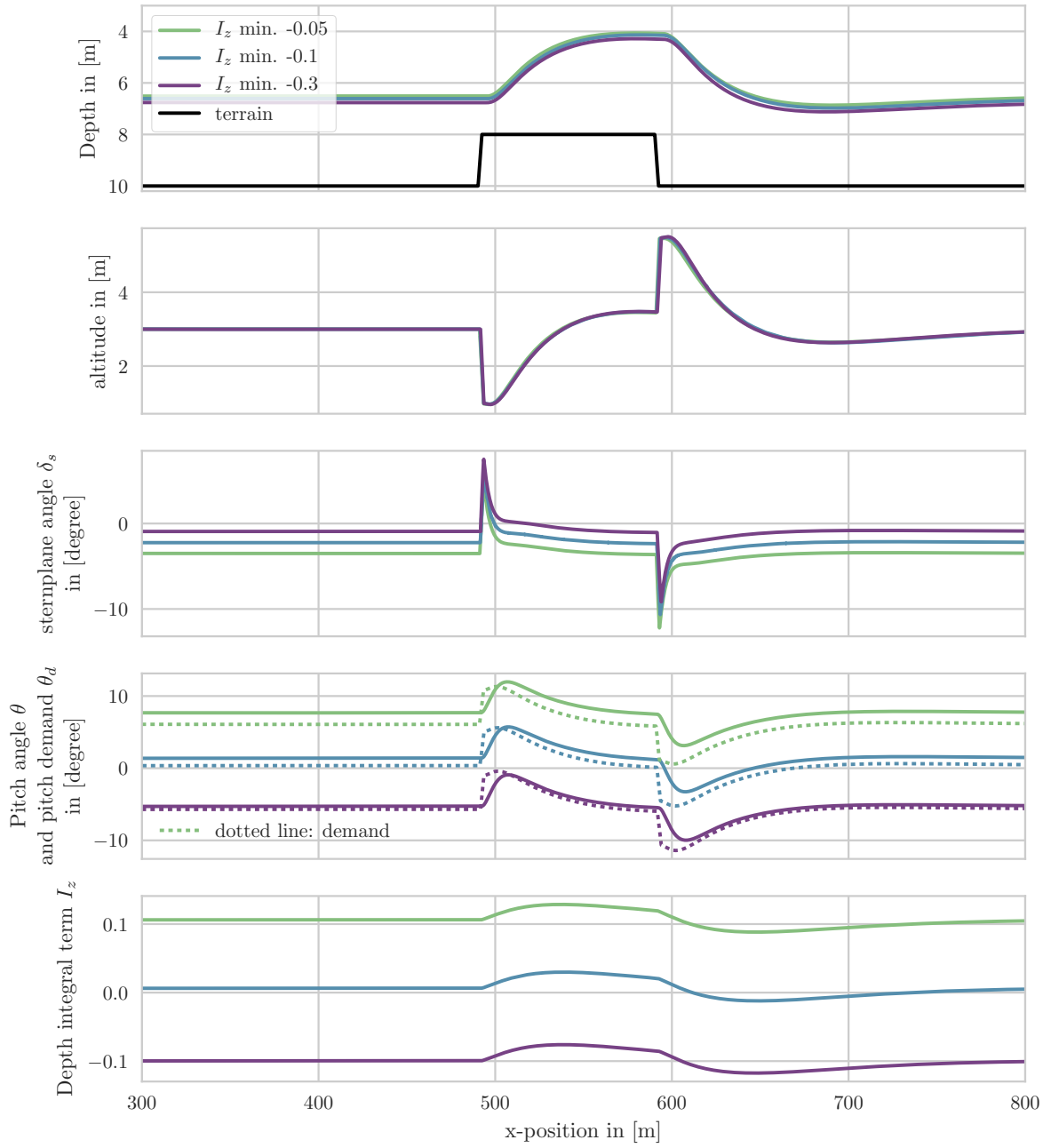

Figure 5.15: Altitude tracking at 3 m altitude over a 2 m high step without obstacle avoidance, varying the minimum limit of the depth integral term.

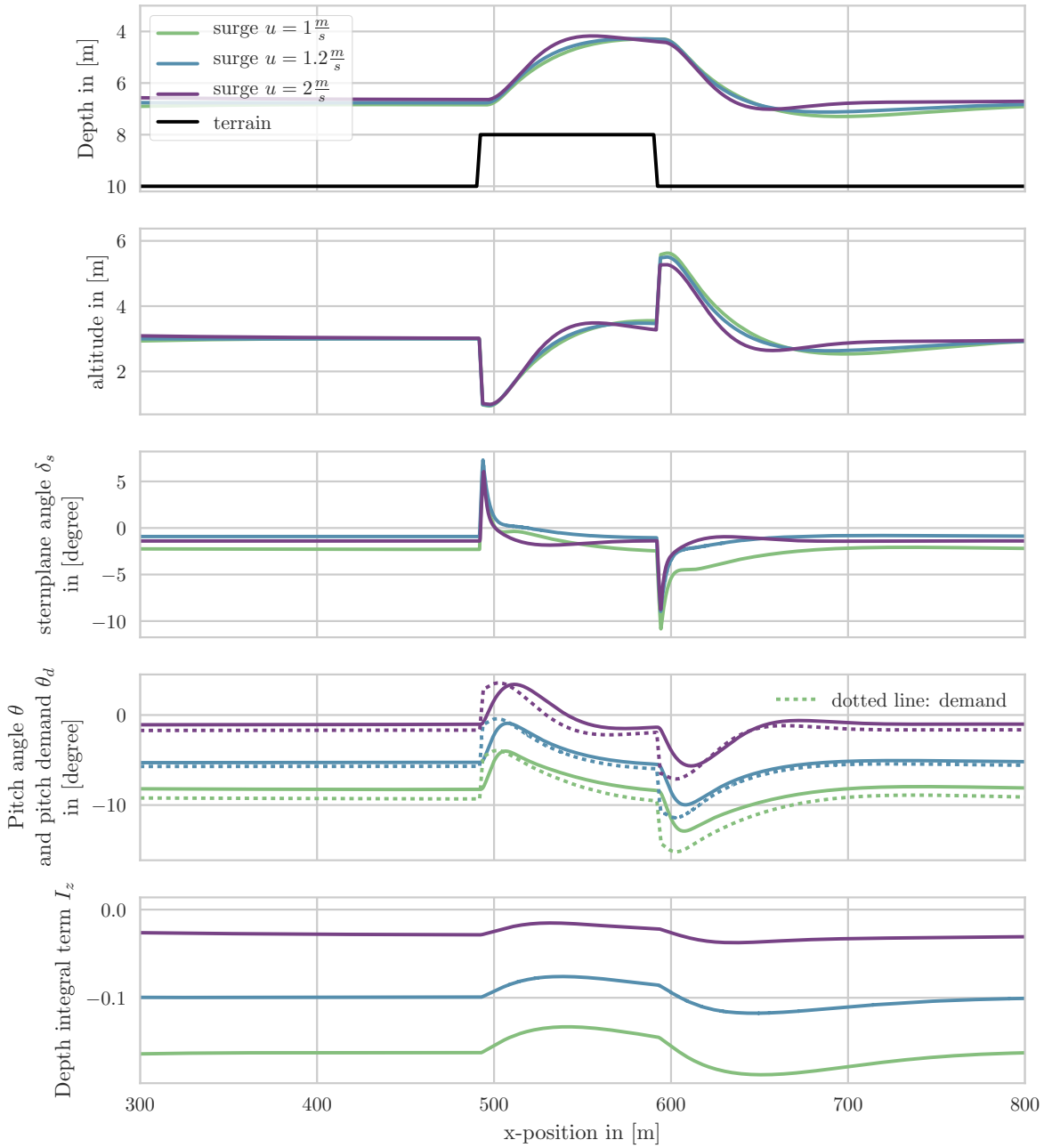

Figure 5.16: Altitude tracking at 3 m altitude over a 2 m high step without obstacle avoidance, varying the surge velocity.

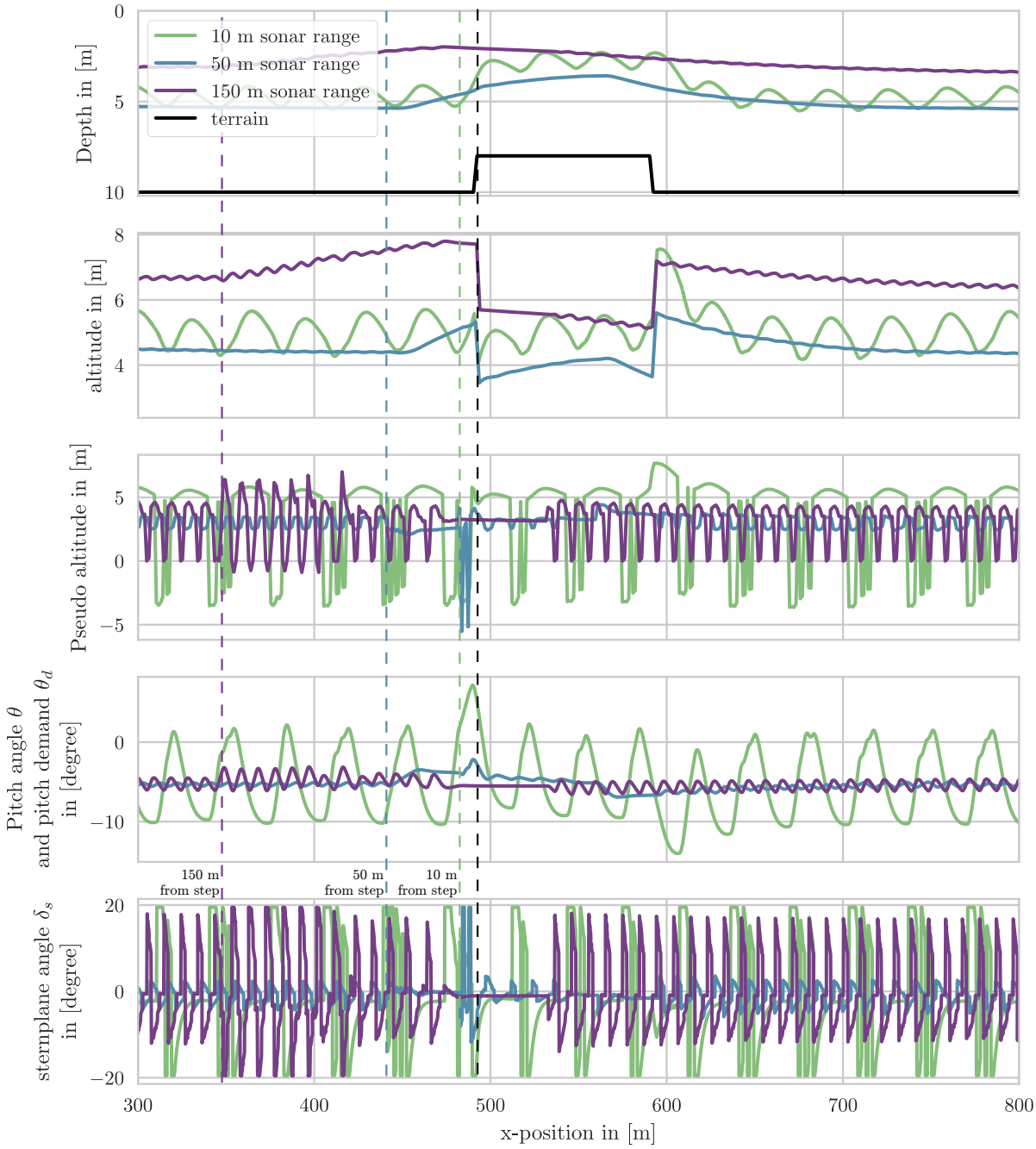

Figure 5.17: Altitude tracking at 3 m altitude with forwards looking obstacle avoidance, horizon tracking between $\alpha = \pm 30^o$, varying the detection range. The position before the step, where the first detection for each of the simulation occurs is indicated by a vertical dashed line.

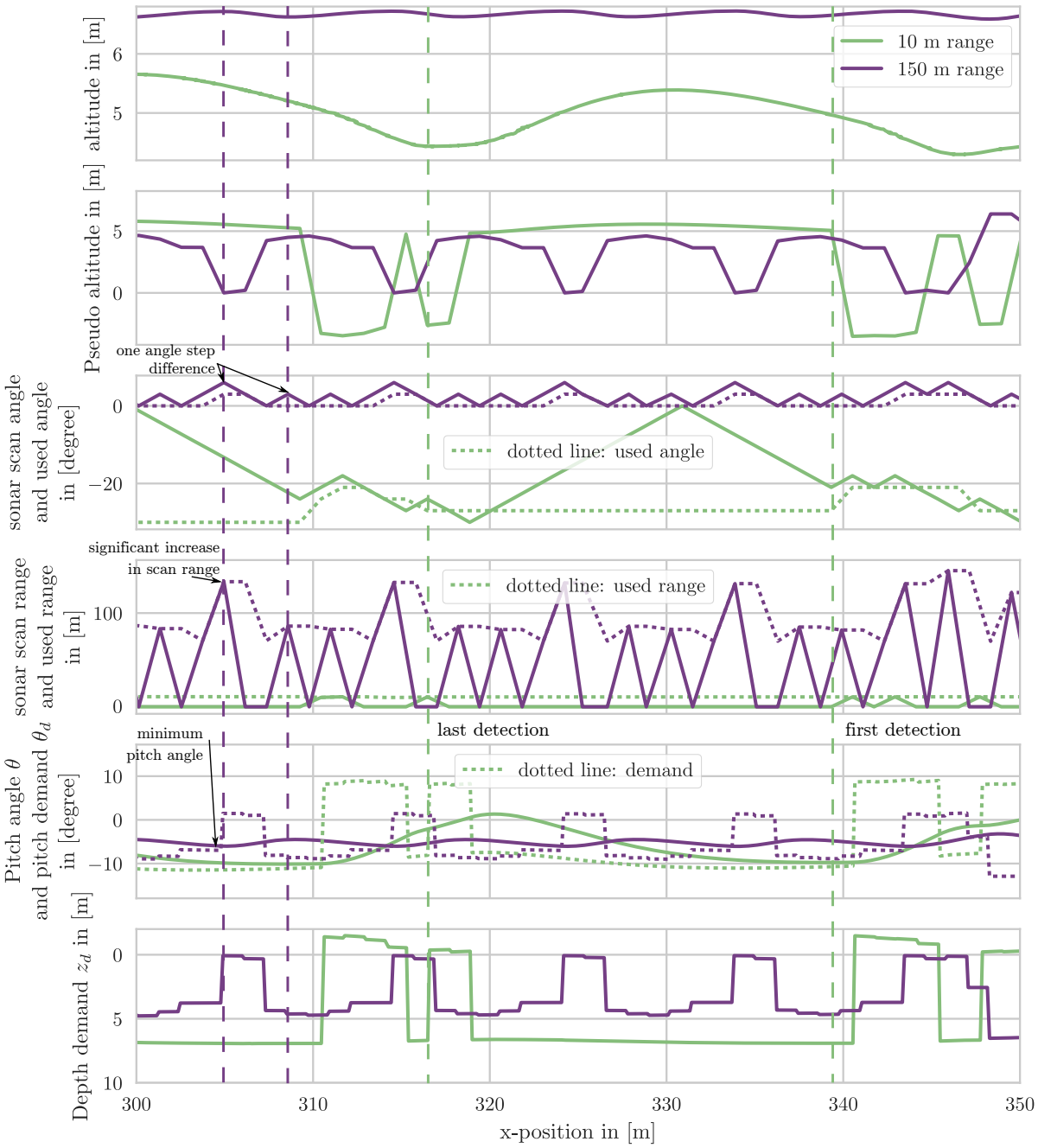

Figure 5.18: Detailed view of oscillation for altitude tracking at 3 m altitude with forwards looking obstacle avoidance, horizon tracking between $\alpha = \pm 30^o$, varying the detection range.

tenfold increase of the scan rate (10 Hz). Removing the effects of the sonar scan speed, and keeping the same sector over which scans are performed, no oscillation occurs. This indicates that the oscillation observed during M115 is most likely due to the offset in the mounting position changing the lowest scan angle and thus causing the vehicle to loose detection. An offset in the reported scan angle alone only causes a change in the vehicle altitude error by increasing or decreasing the overestimate of the terrain. The underestimate of the terrain has a similar effect to a shorter detection range, causing the vehicle to initiate obstacle avoidance at a shorter distance to the obstacle.

Based on these simulation results, the Autosub6000 data for M115 was re-visited and analysed for the sonar scan angle. As predicted by the detection range variation, it was found that the vehicle looses detection of the terrain as it is pitching upwards by around 10° to avoid the terrain detected ahead. Once the detection is lost, the pseudo altitude is calculated based on the altitude and previously recorded detections at each sonar angle, which are overwritten by empty returns as the vehicle continues making measurements at decreasing sonar angles. This reduces the altitude demand, causing the vehicle to pitch downwards until terrain is detected again. Since at this point the vehicle continues pitching downwards, the terrain horizon seems to increase in front of the vehicle, again causing a steep increase in the pitch angle. Due to the pitch angle changing faster than the sonar can follow it, this oscillation continues. This shows that the offset of the sonar angle did not cause the oscillation per se, but the step change between pseudo altitude and altitude based terrain tracking. In hindsight it is difficult to tell if the terrain estimate is indeed incorrect. The correction of an offset, or the addition of an offset that causes a horizon underestimate both would have the same effect: reducing the step between altitude and pseudo altitude and thus reducing the change rate of the pitch angle. Following the same idea, during this cruise also further factors to reduce the pseudo altitude were applied. A more consistent method for avoiding such oscillation would be a steadier control input, using a map or sonar data collected at a faster rate.

Without knowing from the simulation where to look, this analysis would have been more difficult to make. Due to the slow nature of the system, the altitude and pitch angle are offset, from the altitude alone it is unintuitive that the vehicle looses terrain detection whilst at a lower altitude.

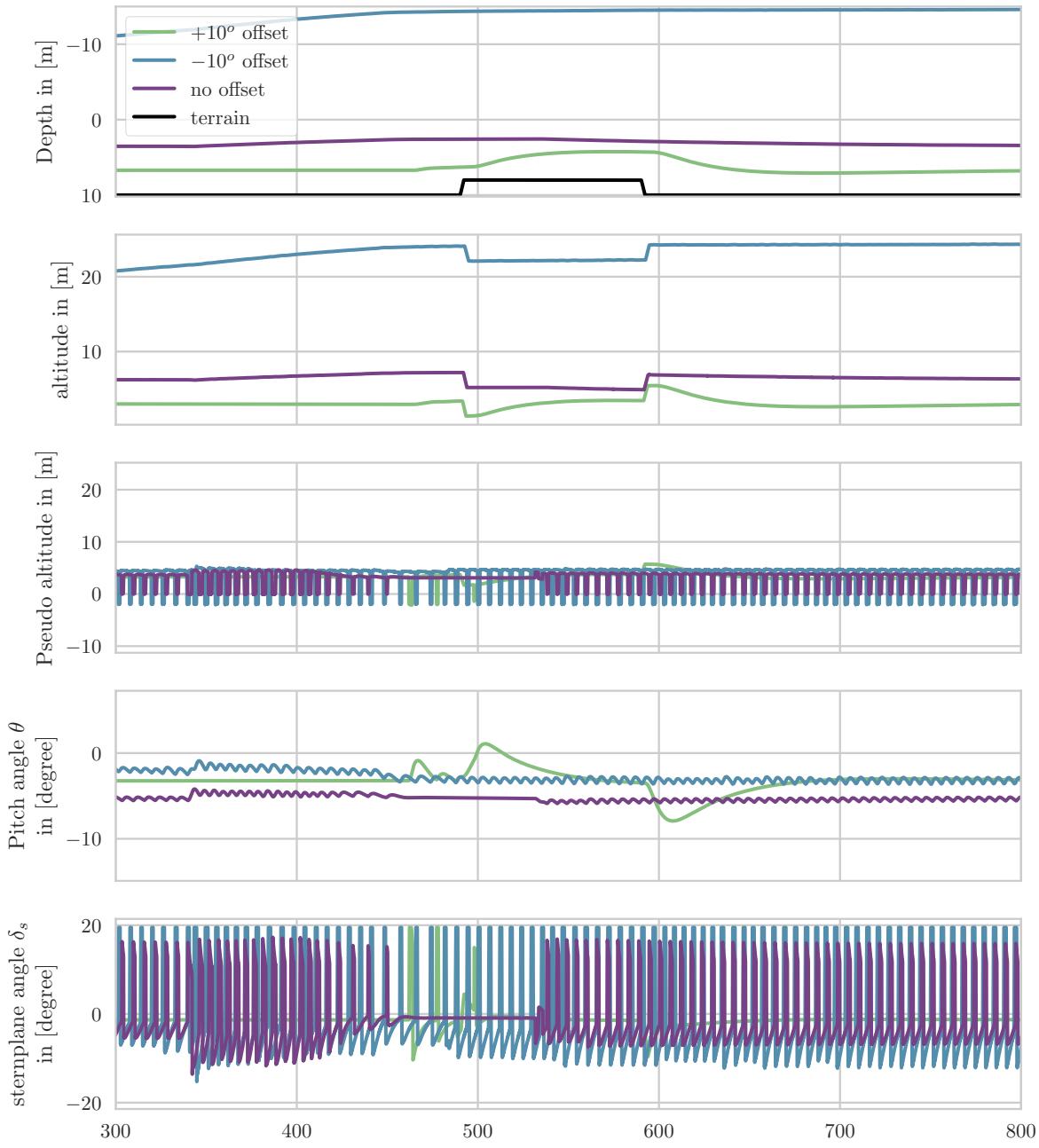

Figure 5.19: Simulation of different sonar position offsets. A $+10^o$ offset, where the sonar is aligned pointing upwards rather than horizontally, causes a terrain underestimate of the pseudo altitude, and results similar to a shorter detection range.

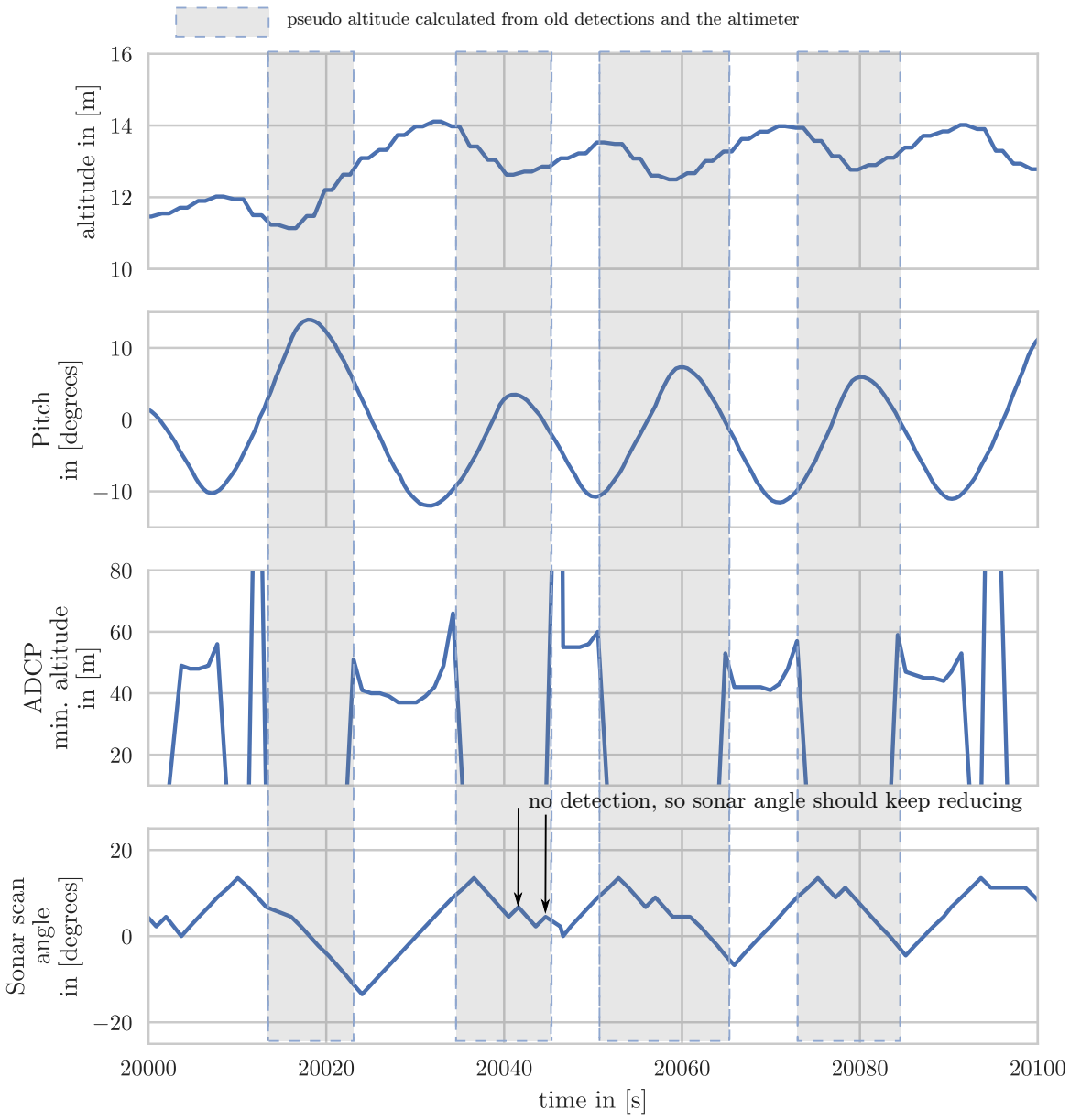

Figure 5.20: Guided by simulation results, a detailed look at the sonar detection and pitch angle reveals that the loss of terrain detection causes an oscillation that maintains itself.

5.2.7 M53: Validation and Variation Without Obstacle Avoidance

After evaluating the simulation, and the impact of separate parameters, the simulation is compared to real Autosub6000 missions. M53 is selected as the first test case, since this mission did not use the forwards looking obstacle avoidance. It is thus well suited to compare the vehicle system and the altitude tracking controller before adding the obstacle avoidance. Figure 5.21 shows a view of the entire mission. For a better comparison, noise was removed from the plot by applying a 100 m long running average to the data.

In the vertically exaggerated depth plot, the vehicle paths match well. A look at the vehicle success (see Figure 5.22 and the altitude plot (Figure 5.21) reveals that the initial simulation with the PID control terms taken from the original mission documents has a consistent altitude error. With the results from the variation of the I_z term limit in Figure 5.15 in mind, the mission analysis focused on the depth integral term, which was at its limit for most of the mission. The simulation was repeated with a larger absolute value of the integral term limit. The increased integral term gives results more similar to those of the real mission. However, a comparison of the vehicle risk shows that the chosen limit for I_z might be too large (see Figure 5.22), since the large integral term can cause a too low altitude at the end of a downwards slope. The simulation could be further improved by tuning this limit further. Since the simulation is intended for pre-mission analysis, the use of further optimising this value without understanding the cause for the required change is questionable. It remains unclear if this change was needed due to inaccuracies in the simulation, a different I-term limit than the recorded being used, or a change in the vehicle buoyancy.

Next the pitch and sternplane angles were compared. The overall trends are very similar for the simulation and the real experiment data. The angles of the simulation are offset compared to the simulation and match closer to each other than to the data recorded on the vehicle, despite the very different altitude outcome. However this offset is small and the winglet study in Figure 5.7 shows that this variation is within the inaccuracies of the estimate of the control surface and winglet forces. It may also be caused by variations in buoyancy compared to the value recorded at the surface.

Furthermore, it must be noted that the actual sternplane position recorded on Autosub6000 does not match the demand well. It is unclear if this is due to the recoding method, or due to the sternplanes not moving with the demand. This further complicated the comparison of simulation and experiment.

Closer scrutiny of the altitude tracking, without the running average, gives a more detailed view of the failure to track the goal altitude due to the integral term limit. It also shows a similar oscillation in the altitude for the simulation and the experiment. The oscillations in the simulated data are most likely due to the oscillation being present in the terrain (see Figure 5.24), however it is unclear if this oscillation was indeed present in the terrain or if it is an artefact of the terrain reconstruction.

Both the sternplane position demand, sternplane position, and pitch angle have a much stronger variation than during the simulation (see Figure 5.23). The pitch variation is likely an effect following the variation in sternplane demand from the controller. With the controller using only the depth and altitude as inputs, and both signals looking smooth, it is unclear what causes this variation in the controller demand.

Overall, the simulation is a very close match for the altitude tracking. Small unexplained oscillations occur, but their magnitude is in the centimetre range, at least one magnitude smaller than the altitude goal. The change of the integral term limit is applied to all further simulation.

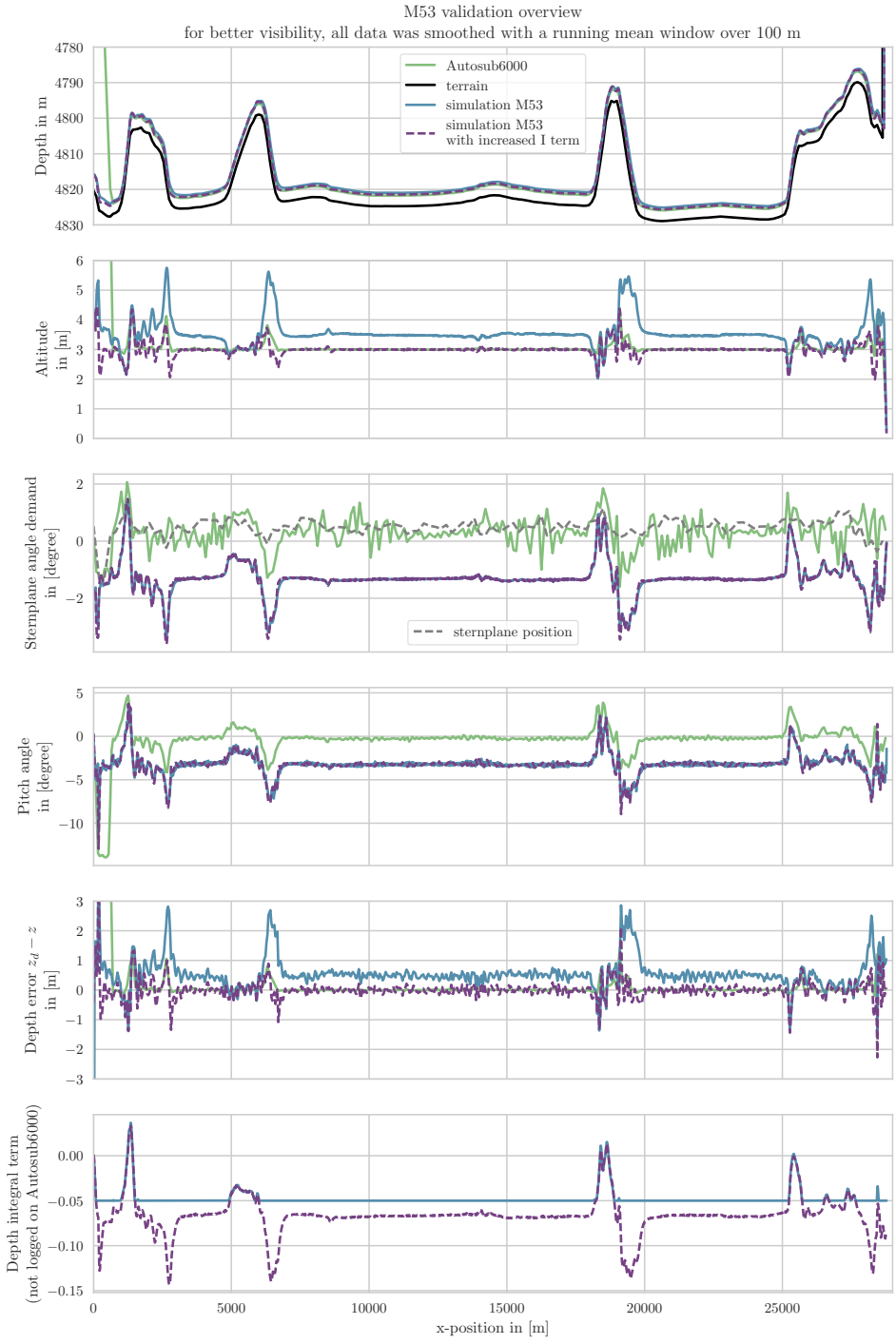

Figure 5.21: Comparison of data logged onboard Autosub6000 during the M53 mission, and simulation data. M53 was performed without obstacle avoidance. After an increase of the integral term, the simulation of Autosub6000 altitude tracking is very accurate. For more visibility, this plot used a running average window of 100 m to reduce small scale oscillations.

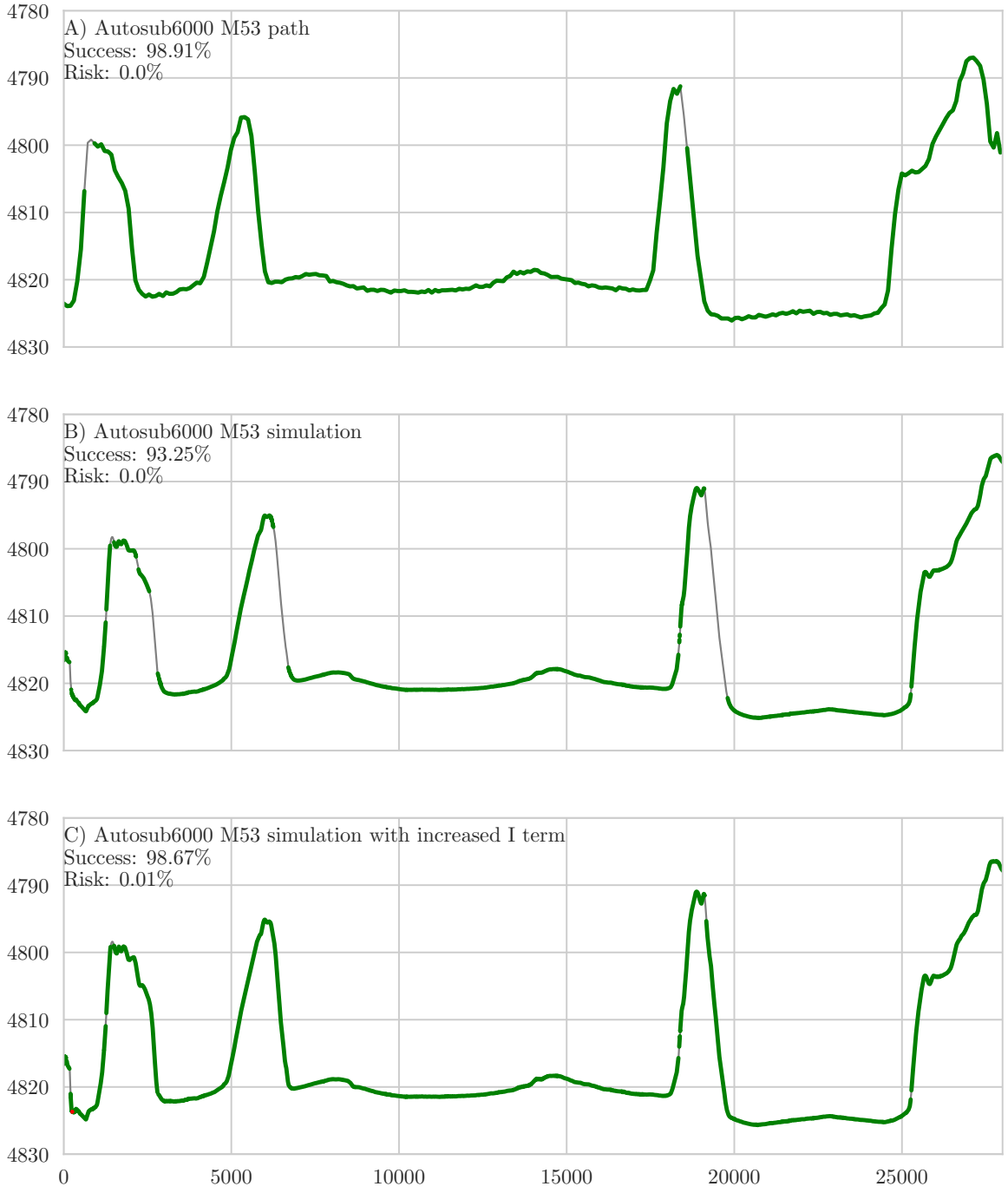

Figure 5.22: Risk and mission success analysis of Autosub6000 mission path during M53 and vehicle paths from the M53 vertical plane simulation.Due to vertical exaggeration, the terrain and vehicle path can barely distinguished when the the terrain is not flat, so the terrain was not included in the plots. The results are analysed in detail in Figures 5.21, 5.23, and 5.24, which also include the terrain outline.

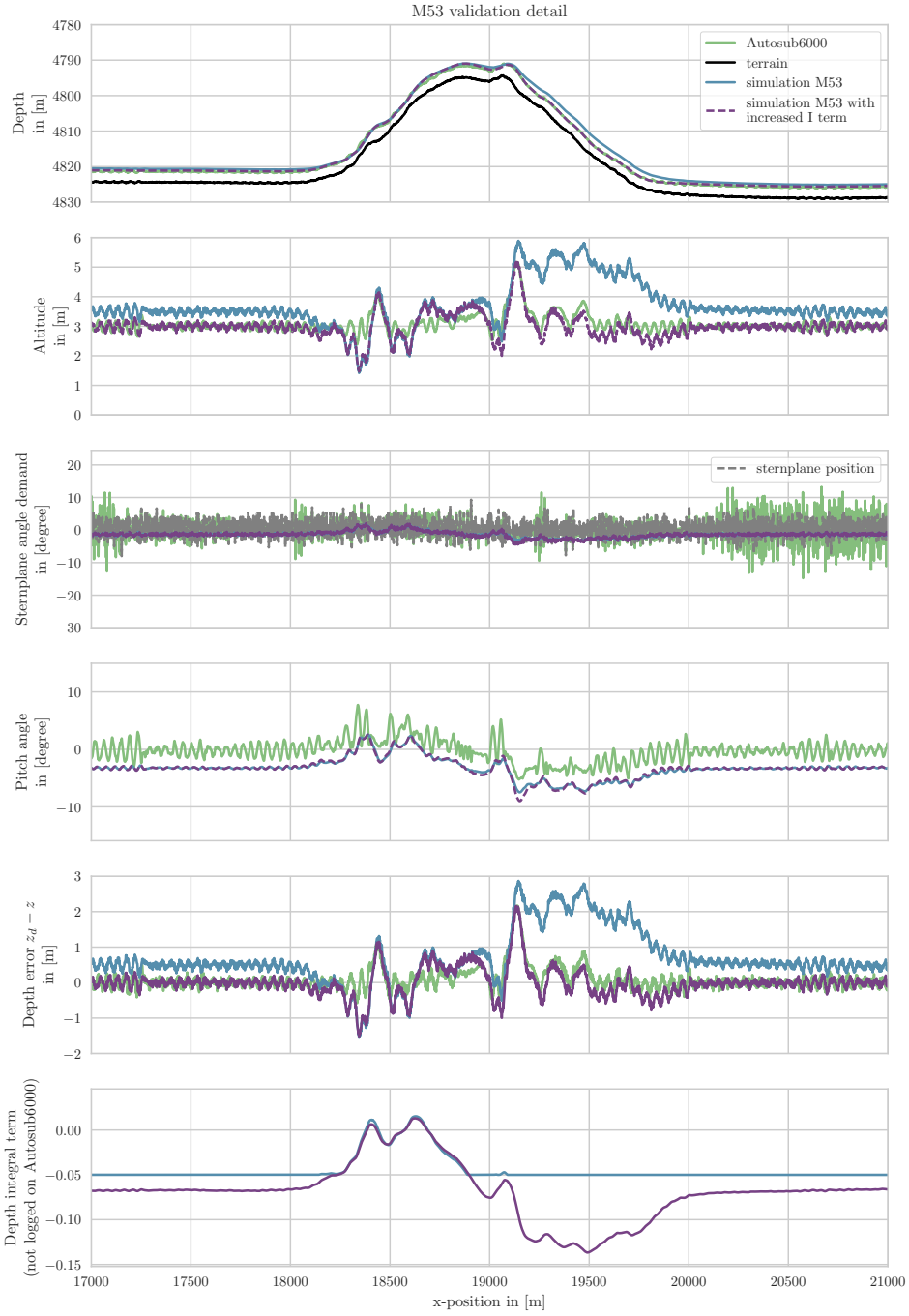

Figure 5.23: Detail view of M53 recorded data and simulation. A small oscillation is observed in pitch, altitude and depth error. Due to the large step it is invisible, but the same oscillation is present in the terrain as well.

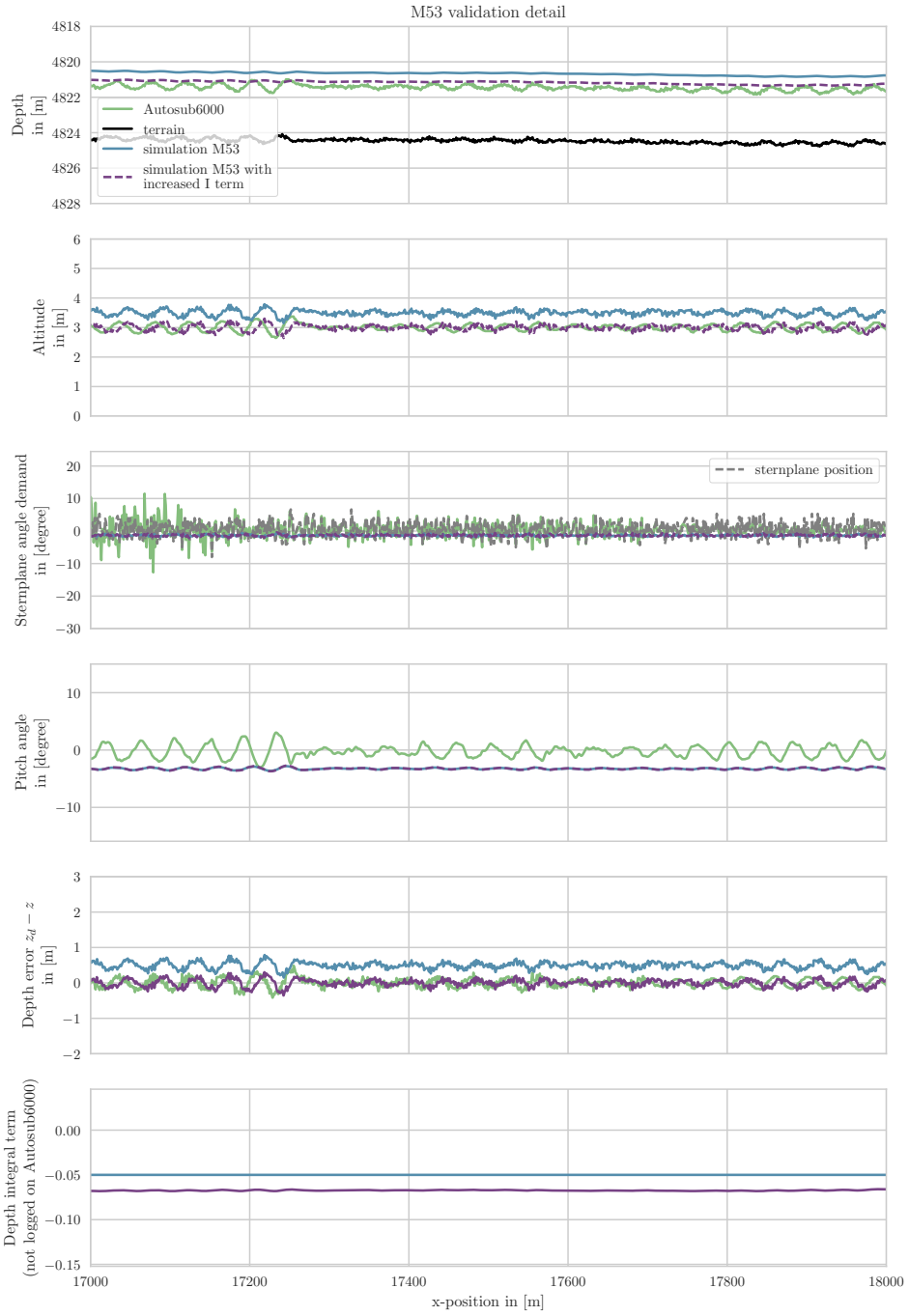

Figure 5.24: Detail view of M53 recorded data and simulation, showing the oscillation in terrain. The simulated vehicle path is smoother than the actual path, it is difficult to determine if this is due to the simulation or the terrain that was reconstructed from the recorded data.

5.2.8 M57 Validation and Variation With Obstacle Avoidance

Once the suitability of the simulation for altitude tracking without forwards looking detection was established, simulations with forwards looking obstacle avoidance were performed. The surge velocity is chosen at 1.2 m/s, the average speed from the statistical analysis of the Autosub6000 mission data. The detection range was varied between using no obstacle avoidance and the average detection range of 29 m; buoyancies between zero buoyancy and 14.2 kg positive buoyancy were used.

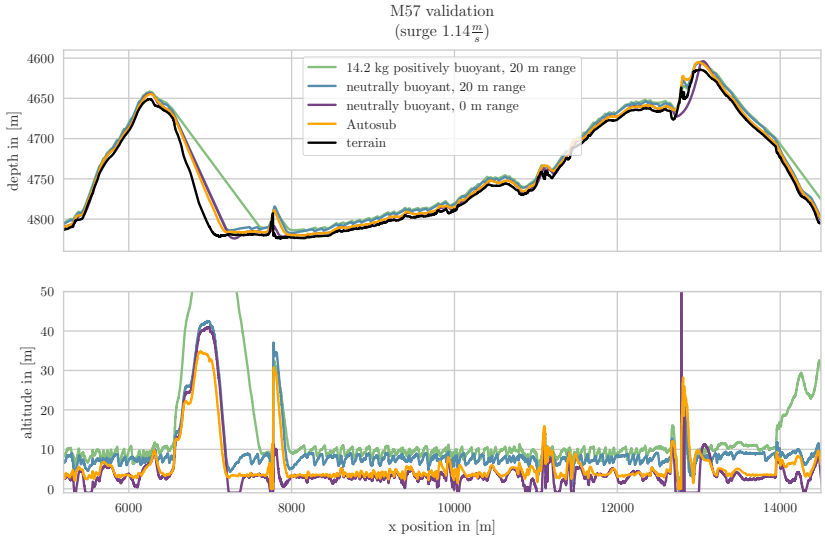

Figure 5.25: Comparison of Autosub6000 mission M57 with simulation results. Based on previous studies, the detection range and buoyancy were varied to better understand the causes behind the differences of simulation and experimental data.

Figure 5.25 shows the depth and altitude of selected simulations and the real mission data. The risk and success analysis for each of the cases is shown in Figure 5.26. With the addition of obstacle avoidance, the similarity of simulated mission and real vehicle data reduces significantly. All simulation resolts have in common that the vehicle incurs a terrain collision at x-positions around 7700 m and 12 750 m. In both areas the terrain slope over a ca. 40 km long slope is over 60%, well above the safe limit of 30% slope estimated in the tall step analysis. On downwards slopes the positively buoyant vehicle cannot match the descend rate of the neutrally buoyant vehicles, and that of Autosub6000. Both simulations with a forwards looking detection range stay several metres above the altitude of the actual mission and the simulation without obstacle detection. During steep ascends the both the Autosub6000 path and the simulation without obstacle detection get very close to the terrain, with likely collisions. The simulation without obstacle avoidance has more collisions than the Autosub6000 data, indicating some forwards looking capability. Based on the simulation of the sonar angle offset, and the fact that the recorded detection ranges are larger than the simulation results, it is likely that the sonar on Autosub6000 was mounted with a negative offset

and the pseudo altitude estimated from the sonar data is too small. With inaccuracies in buoyancy, sonar detection range, and sonar mount position it was determined that further variations to better approximate the results would be complex, and meaningless without a way of verifying which combination of error corrections best described the actual vehicle during mission. Nonetheless, a closer look at the simulation results yields a better understanding of the parameters involved in altitude tracking.

A more detailed view of one upwards and downwards slope is given in Figure 5.27. On the downwards slope, none of the simulated vehicles achieves a descent rate as fast as the recorded rate. During the descent, all vehicles reach a constant downwards pitch, the maximum downwards pitch that can be achieved with the integral term limit. Of all vehicles, Autosub6000 reaches the steepest downwards pitch, getting close to the limit of 23°. It is noteworthy that this is achieved with a sternplane angle of almost zero degrees, whilst the simulated vehicles have a constant downwards sternplane angle of at least 10°. Such a small sternplane angle is unexpected for a positively buoyant vehicle pitching downwards and descending. The offset is also larger than what can be explained by inaccuracies in the sternplane and winglet force estimate and raises the question if the vehicle was in fact negatively buoyant (see Figure 5.14), or if the zero degree position of the sternplanes is offset, thus not representing a horizontal sternplane.
During the altitude tracking on the upwards slope, the pitch angle and pitch demand of the simulation without altitude tracking has the lowest variation. The 20 m detection range has a larger variation than the Autosub6000 simulation. Despite the horizon range being above 20 m on the upwards slope, the altitude and pitch angle, indicate that the terrain is either not detected at a long range, or underestimated.

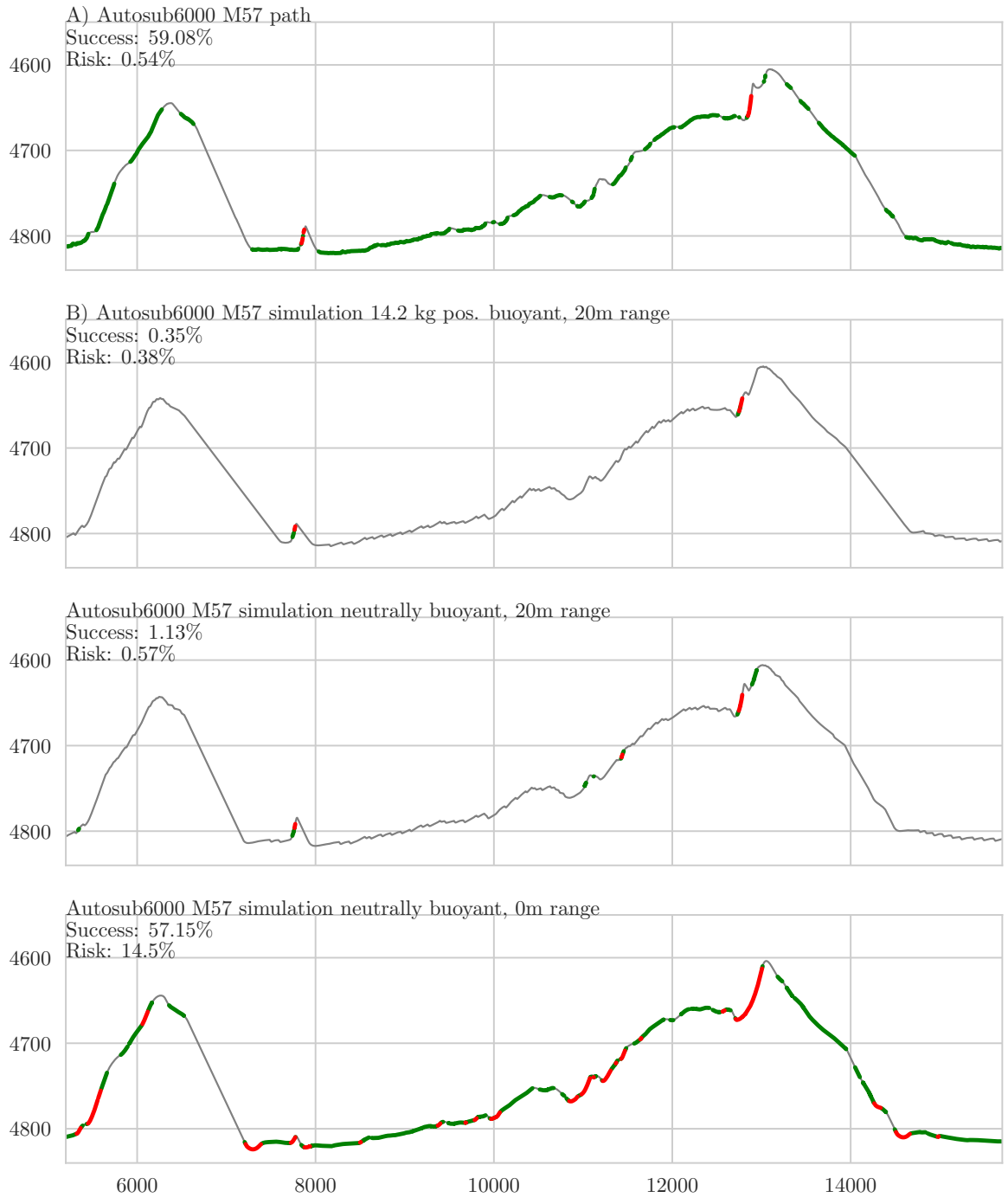

Figure 5.26: Risk and mission success analysis of Autosub6000 mission path during M57 and vehicle paths from the M57 vertical plane simulation. The results are analysed in detail in Figures 5.25 and 5.27.

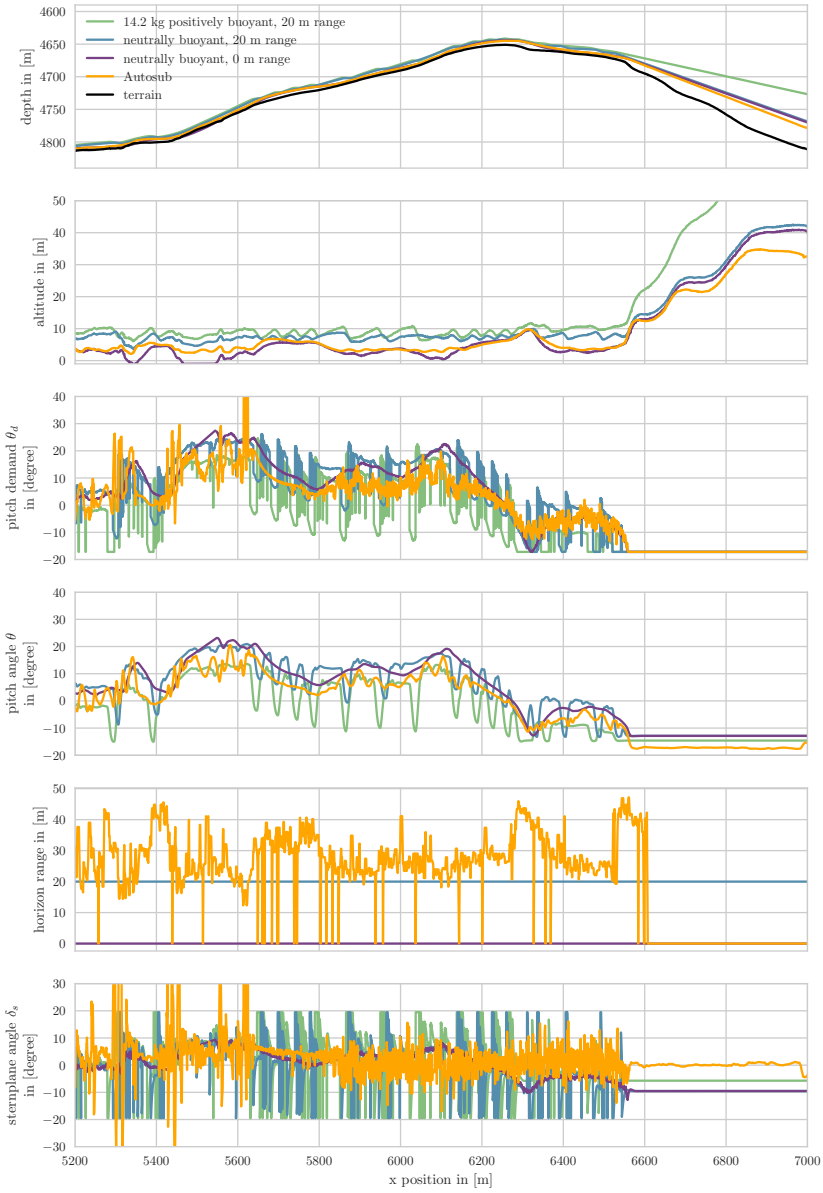

Figure 5.27: A smaller section of the M57 mission, showing details of altitude tracking along an upwards slope and a downwards slope.

5.3 Delphin2 Lake Experiments

The breadth of experiments overall was found as expected, with almost perfect altitude tracking for a hover capable, and less accurate results when pushing to higher speeds in flight style control. For all cases, the return to the goal altitude after the downwards step takes between 1.5 to 2 times longer than when navigating the step in the reverse direction. This is due to the positive buoyancy of Delphin2, and when using the forwards looking avoidance the effect is further increased due to overestimating the horizon ahead.

Closer scrutiny of the sensor measurements shows that the terrain step and false detections propagate through the measured values as the AUV passes over terrain. Whilst the vehicle path looks smooth for all cases, and the altitude line only shows sensor noise of the altimeter, the impacts of sensor noise, false detections, and controller oscillation can be recognised in the altitude results after a closer look at the terrain detection sensors, the pitch angle, and the sternplane setpoints. Figure 5.28 is annotated to highlight this for the slowest case with hover actuation at 0.3 m/s, using the forwards looking obstacle avoidance (case 6), as well as the fastest 1.0 m/s case with flight style actuation both using the altimeter only (case 3) and using altimeter as well as forwards looking obstacle avoidance (case 8).

The next sections present a discussion of altitude tracking quality, repeatability, obstacle detection range and reliability, and impact of the actuation method. Selected cases give a more detailed insight in the factors for successful altitude tracking. Finally implications for mission planning are analysed.

5.3.1 Repeatability and Obstacle Detection

Globally, the results of the experiments are very similar within repeats of one case, whilst showing distinction between the different test cases, indicating a good repeatability and clear separation between different configurations. To further test for the repeatability of the results, the cases 8 and 14 were selected as reference cases. For each reference case, all repeats of one heading ($A \triangleright B$ or $B \triangleright A$) of that case were combined in a median line. To determine a median line for a measurement, the median of the value from each individual repeat was calculated for each point along the x-direction, at a resolution $\Delta x < 0.1\,\text{m}$. The median lines are used as a reference when comparing experiments of the same case, or to compare the reference cases amongst themselves.

To compare the different altitude outcomes, and see if the different sonar and control configurations were distinguishable, whilst being repeatable within one case, the mean absolute difference was calculated. Every experiment case was compared to the reference case by calculating the absolute difference of the altitude $a(x)$ to the altitude $a_r(x)$ of the reference case, for each of the x-positions x_i of the reference cases. Then, for easier comparison, the mean value is taken.

$$\text{Mean absolute difference} = \frac{\sum_{i=0}^{N} |a_r(x_i) - a(x_i)|}{N} \tag{5.1}$$

The clear clustering of the results of each individual case and the close similarity of the individual experiments of the reference case to the reference case itself indicate that the experiments overall are very repeatable. The different position of the clusters show that there is a clear distinction between the different experiments, and particularly that the two different goal altitudes give distinctly different results. Cases 10 and 15 stand out with the largest variations compared to the reference case, and a large variation of the mean absolute difference result for individual experiments. Finally, for reference case 8, in the $B \triangleright A$ direction, one experiment has a comparably large mean absolute difference of almost 0.2 m. This case is further investigated in Figure 5.29, with the special case highlighted. The large difference of this case is due to false altimeter measurements. Whilst in most experiments only individual false measurements occur, this case has a significant number of repeated false measurements, which lead to the vehicle increasing its altitude significantly and thus differing greatly from the other vehicle paths.

The impact of the obstacle detection parameters on the repeatability can be seen in the altitude, photographic success and risk analysis of cases 10, 11, 15, and 16, which all only differ from one of the reference cases in their sonar setting, but have a greater variation in altitude, mission success, and vehicle risk. Other experiment cases vary in their difference to the median line of the reference cases, however for most cases the repeat of the same case leads to similar results. This supports the assumption that as long as the terrain detections are correct, the experiments are very repeatable, and that a single experiment is representative of the expected performance, despite timing variation in terrain detection and unsteady control.

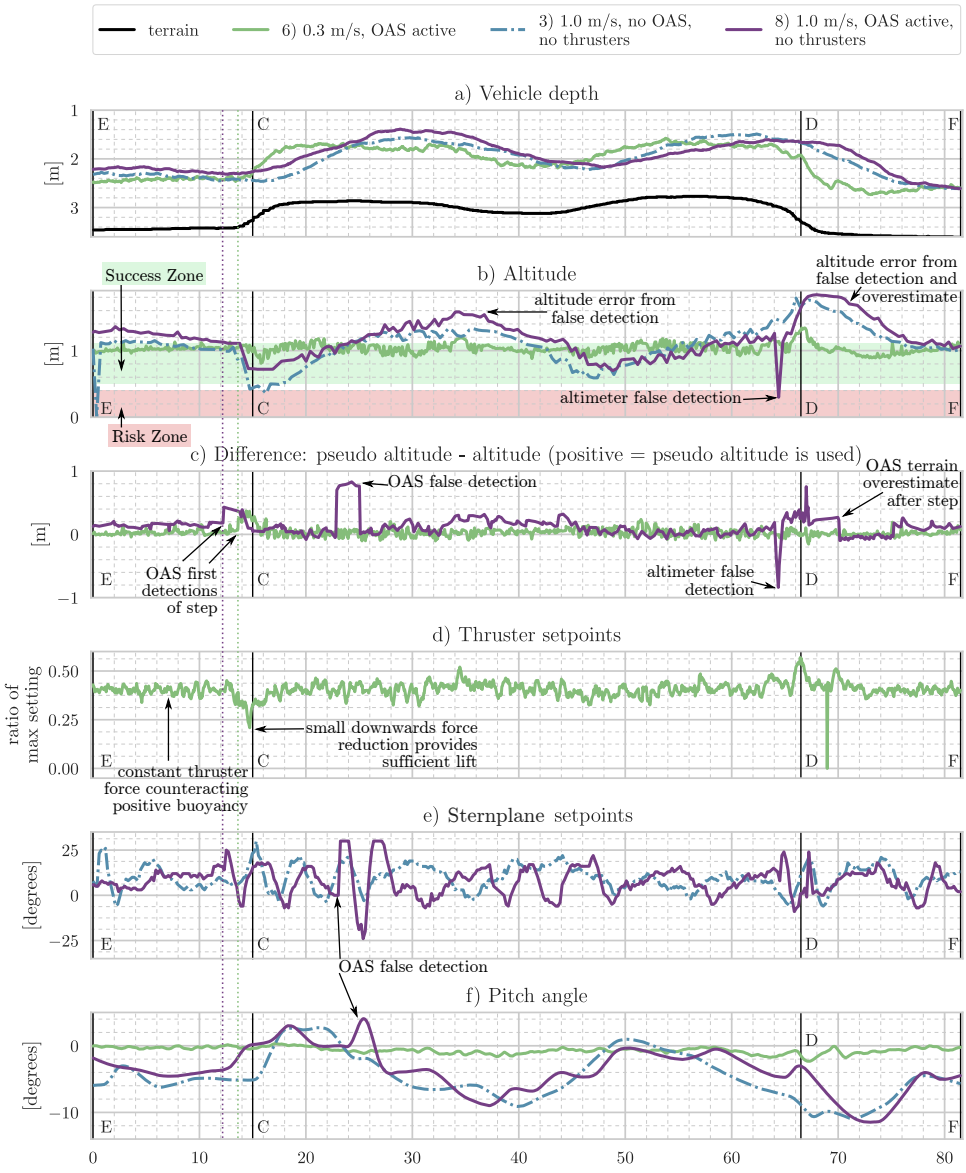

Figure 5.28: Comparison of terrain following performance over full terrain section for key cases, in the direction $A \triangleright B$: at slowest speed with forwards looking obstacle avoidance (case 6), and at highest speed with- and without forwards looking obstacle avoidance (cases 8 and 3).

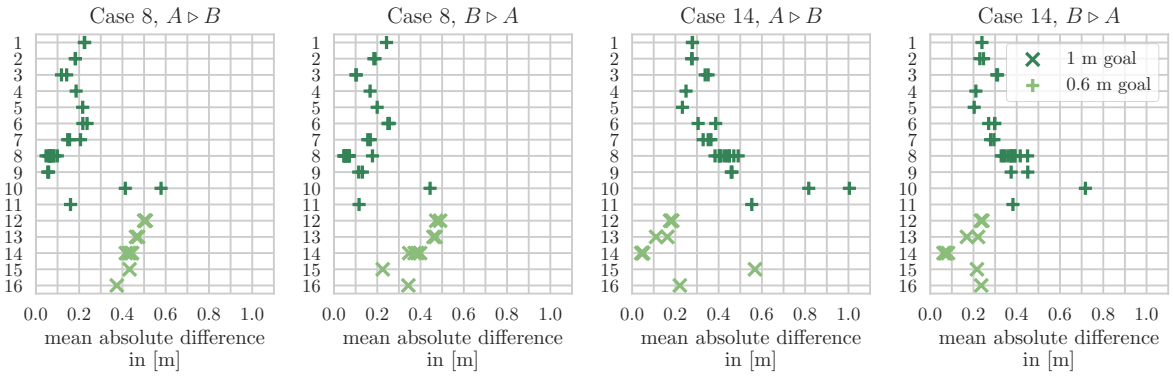

Figure 5.29: Comparison of the mean absolute difference between the vehicle altitudes. The calculation for the absolute difference between the altitudes is given in equation 5.1.

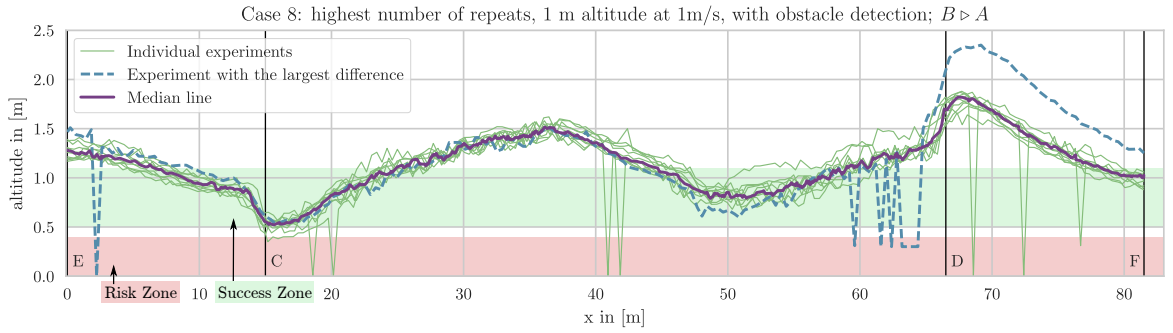

Figure 5.30: Comparison of the altitude median line of reference case 8, to the actual experiments of case 8.

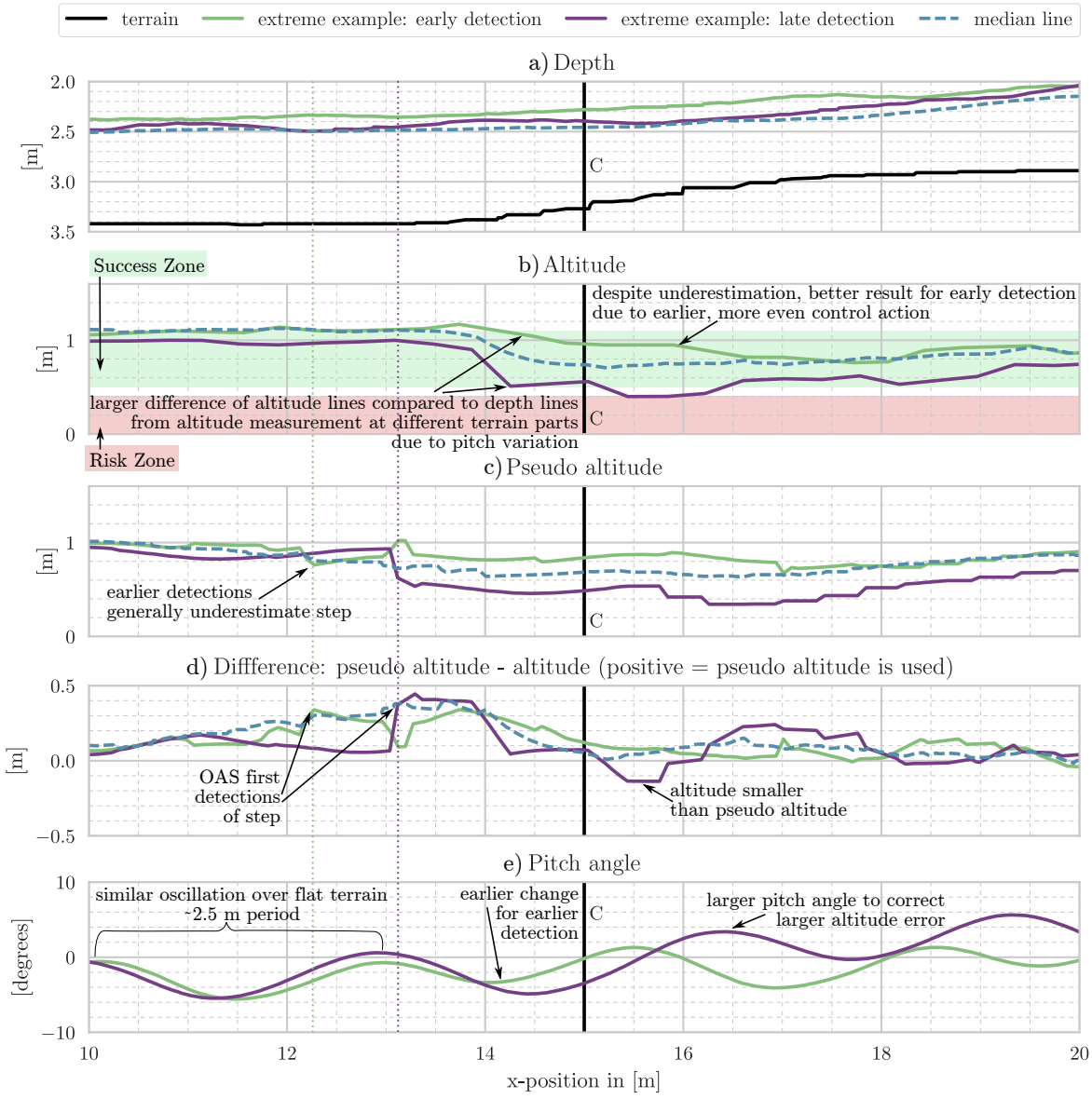

Figure 5.31: Extreme examples of detection variation compared to median line of reference case 8, direction $A \triangleright B$, at 1 m/s. The section show includes 5 m before and after the upwards step at C.

To estimate the overall obstacle detection success, the detection of each experiment was manually compared to the sonar scan, and categorised into three groups: no false detection, occasional false detections, and significant false detections. No false detections were found for most of the experiments with a fixed threshold S_{th} set at 95. Reducing the threshold to 85 or varying it proportionally to the distance resulted in occasional false detections for each of the experiments, and further reducing the threshold to $S_{th} = 75$ resulted in significant false detections for all experiments. Whilst it was expected that the detection would be less impacted by the surface reflections at lower altitude, due to the larger depth, the improvement was not significant.

At 1 m altitude, the detection range of the first step was on average 3 m. This distance varied by up to ± 1.4 m, as expected a 2.8 s sector scan time. The sonar settings from case 10 and 11 increased this distance to over 4 m. For a 0.6 m altitude goal, the average range is drastically reduced to between 1.5 m and 2 m. With the variation over the scan period this lead to detection ranges as low as 0.1 m. However this still presents a significant safety improvement, compensating false altimeter readings. Figure 5.31 compares examples of both very late and very early detection to the median line of case 8. Whilst the experiment with a late detection measures a significantly higher terrain altitude, the detection range of just above 1 m does not leave enough time for the vehicle to achieve a sufficient depth change rate, resulting in one of the highest risk results for case 8. This illustrates the importance of considering repeatability and variation in sensor performance for understanding the vehicle risk.

5.3.2 Actuation Strategy

The impact of the transition between flight style and hover capable actuation is measurable in the distance made good until the goal altitude is reached again (without obstacle detection). It is below 3 m for 0.3 m/s hover capable control and increases to over 7 m for flight style control. Using flight style actuation only, at 1 m/s speed a significant portion of the experiments show an oscillation in the pitch angle (see Figures 5.28, 5.31) that is not observed when tracking a depth with the same controller (see [Tanakitkorn et al., 2016]). Due to the dynamics of the AUV acting as a low pass filter this oscillation is barely noticeable in the altitude and depth measurements.

Whilst the standard control for Delphin2 phases out the use of the thrusters between surge velocities of 0.8 m/s and 1.0 m/s (see Figure 4.15), the thruster weight was varied at maximum speed to see if the thrusters can support the flight style control for obstacle avoidance. Figure 5.32 compares the three 1 m/s cases with sternplane only actuation and variations of the thruster usage. The selected cases use only the altimeter for obstacle avoidance to remove timing effects from the obstacle detection. The flight style control with added thruster actuation overall maintains the goal altitude better (see Figure 5.33), however an impact of the thrusters on the efficiency on the pitch control can clearly be seen: despite sternplanes set for pitching the vehicle upwards, and the expected thruster moment supporting this, the vehicle error indicates that the vehicle tends to

pitch downwards more than demanded. A fast pitch change rate is still achieved at the upwards step (see altitude and pitch error plots in Figure 5.32), but the goal altitude is approached much slower since the vehicle soon acquires a downwards pitching error again. This contributes to a lower overshoot for the current control parameters, and reduces the time it takes to return to the goal height after a downwards step. Thus the overall results are still better for these actuation strategies, but the loss of pitch control makes them unsuitable.

The reasons behind the difficulties tracking a given pitch angle when combining the thrusters at high speed are likely a combination of the sternplanes being less efficient due to the turbulence cause by the thrusters, the thruster performance degrading with surge speed at different rates as observed in [Palmer et al., 2009]. Furthermore ground effects from operating at low distances to the terrain, similar to those observed at the free surface, may play a role, though the thruster tests at up to 0.8 m/s altitude only show variations in differential pressure at larger depths (lower altitudes) for the highest thruster speeds [Steenson et al., 2011].

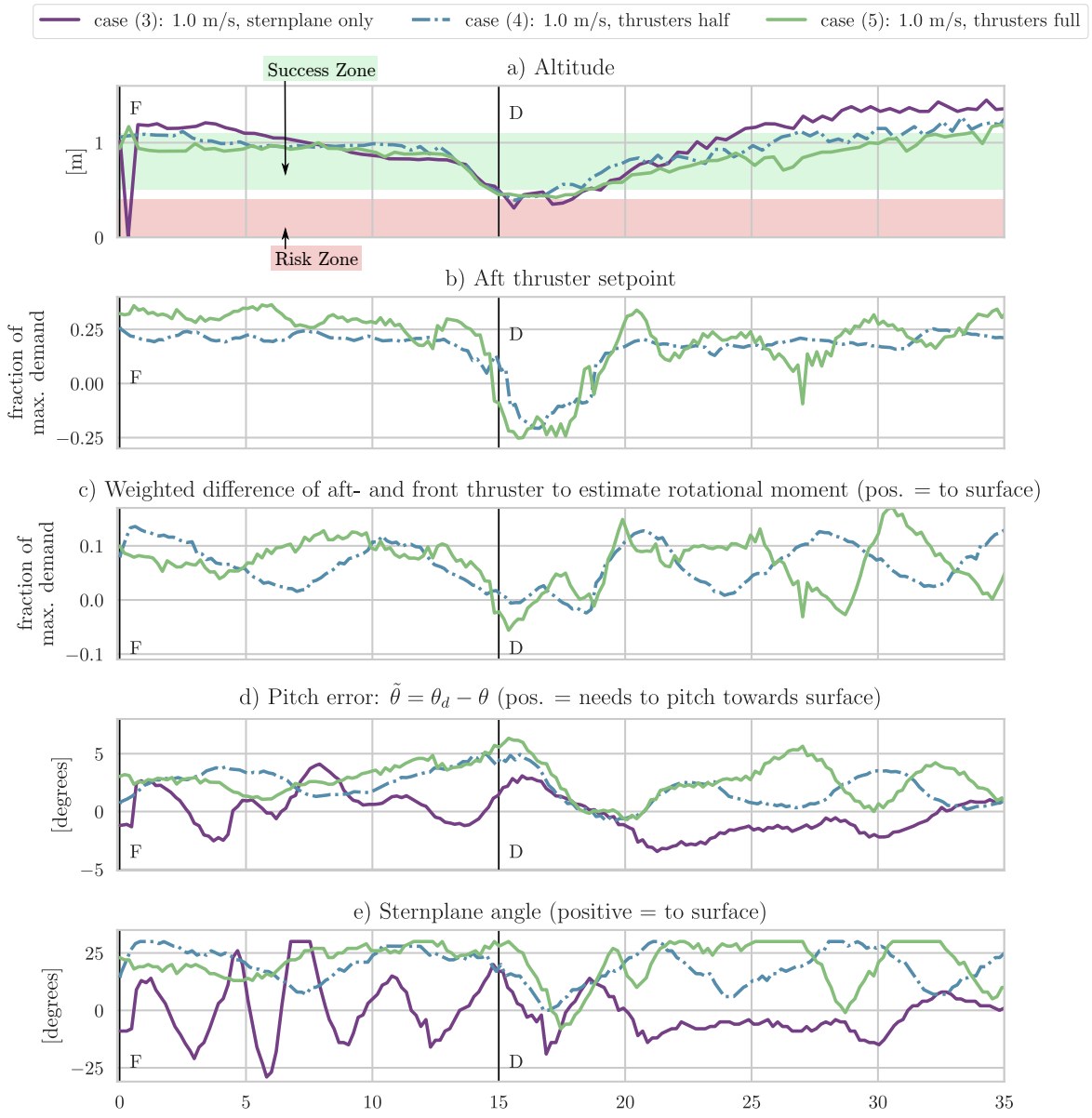

Figure 5.32: Using the altimeter only for tracking, and a constant surge velocity of 1 m/s, the thruster weight is varied (cases 3, 4, 5, variation as in 4.15). The $B \triangleright A$ direction is shown, since for this direction none of the three cases had altimeter spike measurements. To estimate the pitching moment generated by the thrusters, the thruster setpoints are weighted to consider their distance to the centre of rotation and subtracted to get the differential forces that contribute to the pitching moment.

5.3.3 Altitude Tracking Performance

The altitude tracking performance was analysed using both the altimeter measurement directly and the altitude estimated from the depth and position over the terrain. Whilst the altitude estimate is only available through post-processing, the altimeter measurement errors due to the sensor minimum altitude limit are expected to give false results particularly for experiments where a collision with the terrain was likely. To measure the ability of Delphin2 to keep a constant altitude over complex terrain, the mean and standard deviation of the altitude was calculated over all experiments of each case.
The two altitude estimation methods agree well overall; when the altitude estimate is used, the average altitude reduces and the vehicle risk increases in the $B \triangleright A$ direction. With this more accurate altitude estimate, several experiments in the $B \triangleright A$ direction can be identified where a collision at point D is likely due to the altitude estimate falling below 0.1 m. Once the distance of the bounding box was considered, the vehicle risk was further increased, resulting in several likely collisions for the 0.6 m altitude tracking experiments. Whilst this method of altitude estimation is unavailable for the typical terrain tracking applications, it not only illustrates the impact of the altimeter accuracy for understanding the performance, but also highlights the advantage of performing repeatable experiments over an easy to access and well mapped terrain.

Figure 5.33 shows that for most cases, the resulting altitude was above the goal altitude. Only the over-actuated cases 4 and 5 resulted in a mean altitude below the goal altitude. The 0.3 m/s altitude tracking without obstacle avoidance (case 1) comes closest to achieving the goal altitude. The lowest standard deviation can be found for the slower speed cases, with a standard deviation below 0.2 m. For most cases the standard deviation is smaller for the direction $A \triangleright B$. Using a fixed sonar threshold of $S_{th} = 85$ or above results in an altitude deviation below 0.5 m, whilst the remaining sonar settings (cases 10, 11, 15, and 16) clearly stand out with an altitude standard deviation above 0.5 m, and often also with the standard deviation larger for the $A \triangleright B$ direction, indicating a failure to detect the terrain ahead.

Figures 5.34 and 5.35 show the success and risk results for the individual experiments, since for most cases the number of repeats is not sufficient to make statistical assessments. Considering only the risk and photo success numbers, the best performance is found for cases 1, 2, and 4, with a mission risk of less than 5% and a success rate above 60%. All cases use thruster actuation, but the success of case 4 has been shown to be due to control problems rather than effective altitude tracking. The tendency to stay above the goal altitude when using flight style actuation is clearly indicated in the mission success as well. All attempts at tracking the 1 m goal altitude with flight style actuation and forwards looking capabilities result in a mission success below 50% (Cases 8, 9, 10, 11) , conforming with their mean altitude above the mission success zone. Whilst using the direct altitude measurement, comes as a surprise that the added forwards looking capability increases the vehicle risk for the 0.3 m/s at 1 m altitude experiments (cases 1 and 6), however with a reduced risk for the bounding box analysis this is

likely due to sensor errors. The majority of the forwards scanning experiments at 1 m/s have a very low mission risk. In the reverse direction, the reference case 8 still shows several experiments with a similar risk factor to that of the 1 m/s altitude tracking without forwards looking obstacle avoidance. Based on the obstacle detection analysis, these are cases where the timing of the scanning sonar lead to a late detection of the step. Considering the total number of experiments of the reference case, the risk is still significantly reduced by using forwards looking obstacle avoidance, whilst accepting a reduction in mission success.

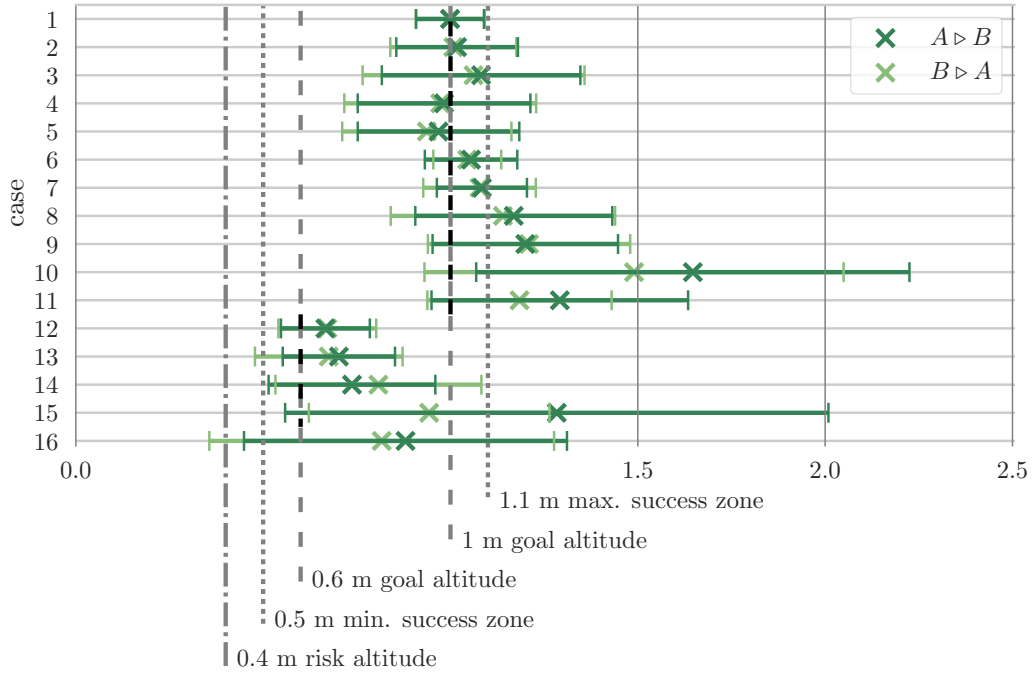

(a) Using direct altimeter measurements.

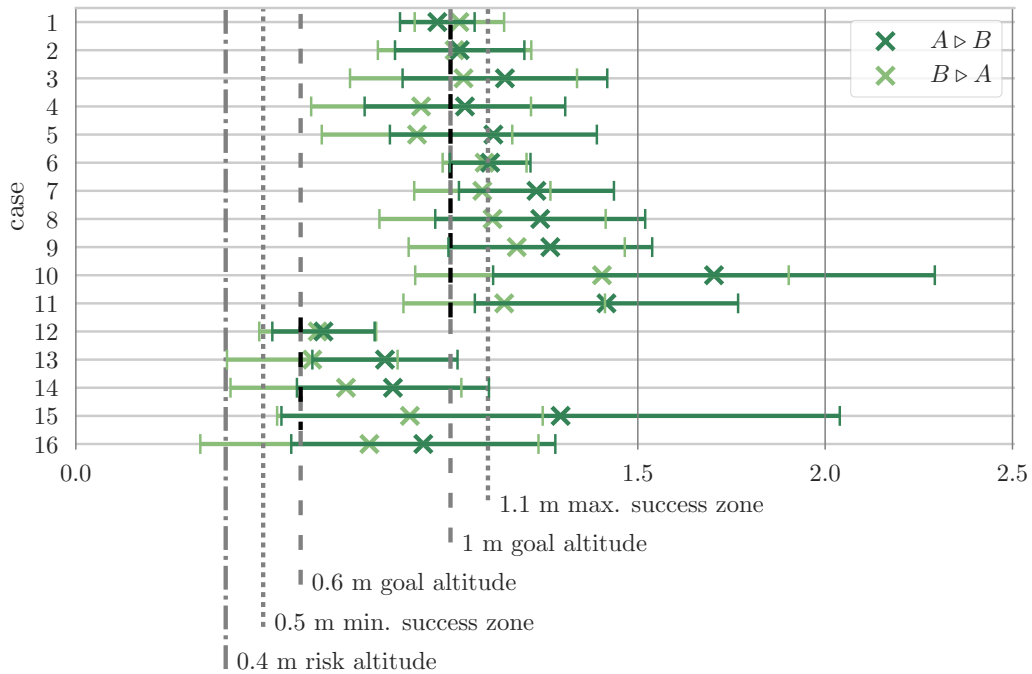

(b) Using altitude estimate from depth and terrain reconstruction.

Figure 5.33: Mean altitude and standard deviation of that altitude for all configurations.

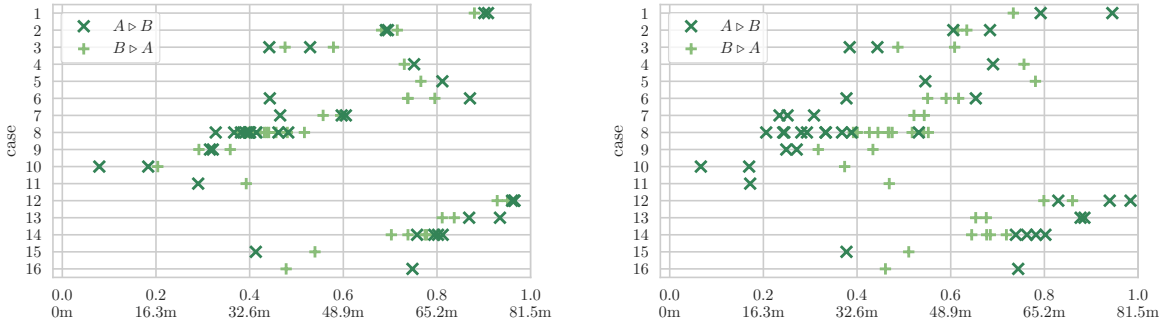

(a) Using direct altimeter measurements.

(b) Using altitude estimate from depth and terrain reconstruction.

Figure 5.34: Comparison of the mission success results for all experiment cases.

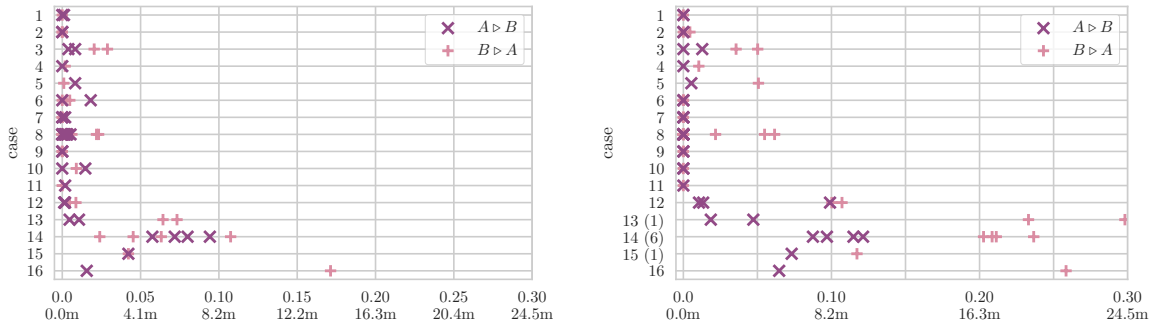

(a) Using direct altimeter measurements.

(b) Using altitude estimate from depth and terrain reconstruction combined with bounding box. Number of missions where a collision was likely is marked in brackets.

Figure 5.35: Comparison of the vehicle risk and the impact of the altimeter limits.

5.3.4 Energy Considerations

When designing long term mission plans, not only vehicle safety and mission success need consideration. Further factors are the distance made good, the time spent, and the energy consumed. Depending on the operational practices, the goals may differ. While operating Delphin2 at the lake, the energy consumed may be secondary to the time consumed, since the time is a stricter limit. Only around 5 hours of operation are feasible within the opening hours of Testwood lake.

Extrapolating the altitude tracking results for a full battery charge and estimating the total path length that was successfully photographed, it becomes clear how much the false terrain detection can impact the photographic success, reducing the expected photographed area even below that of hover capable operation at 0.3 m/s speed for the obstacle configurations of the cases 10 and 11, rather than doubling the covered length in the case of correct detection at 1 m/s, case 8.

5.3.5 Cost of Transport

For any mission plan, the power consumption is a major factor that needs consideration. This section compares the average power use of the different terrain tracking cases, the resulting successfully covered study area and the impact of the terrain complexity on the energy consumption by the actuators.

The total energy used during one experiment is calculated by integrating the product of the supply voltage and the current drawn over each time step. The average power consumption is the total energy used divided by the total time. The battery voltage as well as the current drawn by the individual thrusters, the control surfaces, and the propeller are logged at rate of 0.5 Hz. The hotel load is estimated at 30 W [Tanakitkorn et al., 2016], based on the current drawn when running Delphin2 directly from a power supply. Based on the style of propulsion a variation in power usage can be observed but it is less than expected since the power use mostly shifts between the propeller and the thrusters (see Figure 5.37), with a variation of less that 15% around the average value of 71.7 W. The minimal average power is consumed during 1 m/s flight style propulsion, the maximum average power during thruster enhanced flight style control and during 0.6 m/s hover capable control. Figure 5.37(a) shows the average power usage of one experiment, the 81.5 m distance between E and F, for examples of cases with low (8), medium (6) and high (3, 7) average power consumption.

Delphin2 has a mass of 79.40 kg, the energy available is estimated as:

$$\begin{aligned} E_{battery} &= \text{Number of cells} \cdot \text{Nominal Voltage} \cdot \text{Battery capacity} \\ &= 3 \cdot 21.6V \cdot 10Ah \\ &= 2333kJ \end{aligned} \tag{5.2}$$

Case No.	Altitude [m]	Speed $\frac{m}{s}$	Thruster weight	Detection s_{th}	Detection s_r	[km] per hour Distance	[km] per hour Success	[km] per hour Risk	[km] per Battery charge Distance	[km] per Battery charge Success	[km] per Battery charge Risk
1)	1.0	0.3	original			1.1	1.0	0.0	7.9	7.0	0.0
2)	1.0	0.6	original			2.2	1.6	0.0	14.6	10.3	0.0
3)	1.0	1.0	original			3.6	1.7	0.2	27.3	12.9	1.2
4)	1.0	1.0	half			3.6	2.7	0.0	25.1	19.0	0.3
5)	1.0	1.0	full			3.6	2.2	0.2	25.3	15.7	1.3
6)	1.0	0.3	original	95		1.1	0.7	0.0	7.7	4.6	0.0
7)	1.0	0.6	original	95		2.2	0.7	0.0	15.8	5.1	0.0
8)	1.0	1.0	original	95		3.6	1.3	0.0	27.1	10.1	0.4
9)	1.0	1.0	original	85		3.6	1.1	0.0	29.5	9.3	0.0
10)	1.0	1.0	original	75		3.6	0.4	0.0	29.0	3.4	0.0
11)	1.0	1.0	original	95	1	3.6	0.7	0.0	28.4	5.7	0.0
12)	0.6	0.3	original	95		1.1	1.0	0.1	7.4	6.7	0.8
13)	0.6	0.6	original	95		2.2	2.0	0.6	15.8	14.3	4.2
14)	0.6	1.0	original	95		3.6	2.9	0.8	28.6	23.4	6.1
15)	0.6	1.0	original	75		3.6	1.3	0.4	26.0	9.2	3.0
16)	0.6	1.0	original	95	1	3.6	2.8	0.9	27.5	21.1	7.1

Table 5.2: Estimated performance for a day long mission and for one battery charge.

Compared to cost of transport of depth tracking at different speeds in [Tanakitkorn et al., 2016], the cost of transport for altitude tracking increases around 10% for flight style actuation, 20% for hover capable actuation, and 20% for flight style actuation with thruster use.

For hover capable control, the thrusters are both used for generating a pitching moment and vertical translation. The variation due to generating a pitching moment is differential between the two thrusters, whilst that for vertical translation is additive. Depending on which of the two is dominant, either the change rate of the slope (= correction of pitch angle), or the slope (= altitude correction) will have a larger impact on the variation power consumption. In terms of power, an altitude correction will always lead to an according change in power consumption; a pitch angle correction may be a zero change by varying the thrusters differentially, but an upper limit can be estimated by taking the difference between the thruster demands and assuming that only one of the thrusters changes its setting. To analyse which of the two is dominant in the current control scheme for Delphin2, the standard deviation of the sum and difference of the actuator power consumption was analysed. Overall, the translation was always found dominant, with varying extent between the cases. Figure 5.36 demonstrates that the variation in the sum of both thrusters is indeed well aligned with the altitude error. For a positively buoyant vehicle like Delphin2 this means a reduced power demand for a negative altitude error and vice versa. As a result the average power demand increases for a downwards sloping terrain and reduces on an upwards slope. A difference in power consumption between the different altitude tracking methods or the two directions could not be distinguished.

Since the sternplane actuation on Delphin2 is not proportional to the required force, the direction of the slope has no influence and the 10% increase is only due to the increased length of the vehicle path relative to the progress made in x-direction.

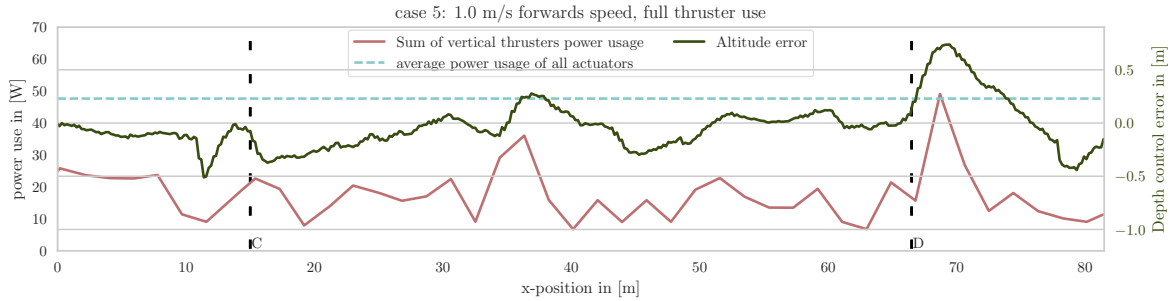

Figure 5.36: Correspondance between altitude error and thruster power consumption.

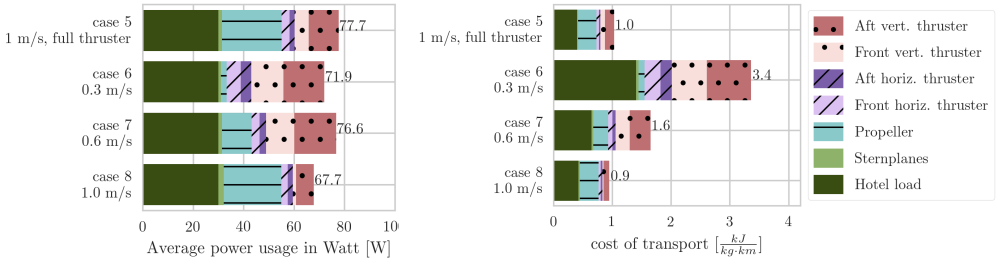

(a) Power

(b) Cost of transport

(c) Side view of Delphin2 with energy consuming components colored in.

Figure 5.37: Comparison of the average power consumption and cost of transport for 0.3 m/s, 0.6 m/s, and 1 m/s with default configuration and 'full thruster' configuration, using experiment cases 5, 6, 7, and 8.

To see if the current terrain following algorithm would perform better with a faster mechanical scanning sonar or a multibeam sonar, the sonar was run at a frequency of $10Hz$ rather than $1Hz$ and without delay. For some artificial terrains small gains where observed, as the sonar would find the horizon again more quickly. Over the real and artificial terrains, a marginal reduction in the risk was found, but at the same time the vehicle altitude is forced to be more conservative, which has a slight negative impact on the photo success rate.

During the validation of the simulation it was noticed that the use of previous sonar values for generating the pseudo altitude sometimes lead to very outdated values being used. The pseudo altitude calculation was then modified. If no terrain has been detected, the last pseudo altitude generated from a terrain detection is used until the sonar scanned its minimum angle or terrain is detected again. This slightly improved the mission

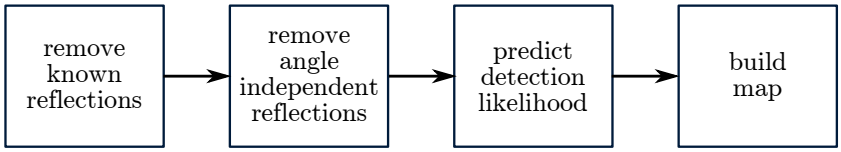

Figure 5.38: Block diagram of the sonar processing method introduced for increasing the sonar detection range at Testwood lake.

success rate, whilst only varying the vehicle risk between zones 4 and 5.

5.4 Forwards Scanning Sonar Analysis

Since both the Autosub6000 and Delphin2 experiment analysis showed that the mechanical scanning sonar detection range was significantly lower than expected, this key sensor was analysed in more detail. For Delphin2, the mechanical scanning sonar was analysed in two steps. First before the Testwood lake experiments, the scan angle and scan pattern choices were analysed, and existing methods for sonar analysis were tested on sample data from the lake to determine the terrain detection method to be used for the lake experiments. Then the larger dataset collected at the lake was used to suggest methods for improving the obstacle detection for similar test environments and to make Delphin2 a more suitable platform for testing altitude tracking in complex terrain with flight style and hover capable AUVs.

With the variable scan angle of the horizon tracking sonar scans used on Autosub6000, it is very difficult to analyse the sonar data further to understand the cause of the range limitations and to test a better detection mechanism. Thus the development of an improved detection mechanism is focused on the sector scanning method, using the data obtained with Delphin2. The improvements were applied in two steps: Improving the post-processing of the sonar data, followed by an analysis aiming to dismiss invalid data. The development aim was to keep the tuning process simple, and applicable for a wide range of mission parameter variations.

5.4.1 Scan Rate and Pattern

The mechanical scanning sonar can be operated in two modes: scanning continuously, stepping with a fixed angle step between two angle limits, or choosing to increase or decrease the current angle by a fixed angle step between each measurement. Both on Delphin2 and Autosub6000 it can be observed that the scan rate becomes less regular if the scan angle is updated between each measurement. Figure 5.40 compares the update rate of the sonar during an Autosub6000 mission that used both sector scanning and horizon tracking. The variation in the measurement rate is larger for the horizon tracking, but stays around the same average. On Delphin2 update rates between 1.2 Hz

and 1.3 Hz, or a time between measurements of 0.8 s, were achieved for horizon tracking. When scanning in continuous mode, the time per scan reduces significantly, taking less than a tenth of the time (see Figure 5.39.

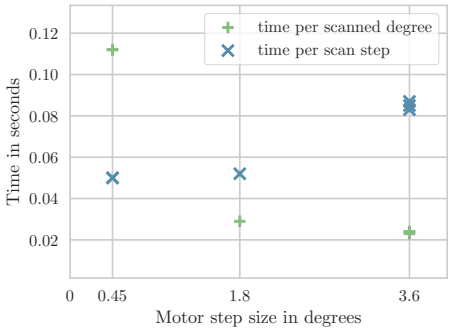

Figure 5.39: Scanning speed of the Tritech Micron mechanical scanning sonar at different angle steps.

With a high likelihood of false detections, a limited detection range, and a scan speed variation between the different scanning modes, the choice of scan pattern needs further investigation.

The horizon tracking scan pattern is very sensitive to false detections. If a false detection of the water surface overlaps with the horizon, the scan angle will not only generate a too large altitude (as for any scan pattern), it will also keep tracking the water surface until no surface detections are made below the maximum scan angle. Since the vehicle will react to a large pseudo altitude by pitching upwards, the most likely reaction is the vehicle surfacing once the water surface was falsely detected.
If a false return is detected above the horizon, the long time between measurements also means a longer time until the offset in the sonar scan angle is corrected back to the horizon.
In addition to reducing the impact of false detections, the sector scan pattern also has the advantage that it is easier to visually inspect after the experiment, and that all scan angle measurements are updated regularly, so if the horizon angle reduces no old measurements need discarding.
To be able to still emulated a similar behaviour to that of Autosub6000 on Delphin2, a horizon tracking algorithm over a sector scan was developed as an alternative to the direct tracking of the horizon with the sonar beam. For each angle position of the scanning sonar, two values are stored: the detection range when the angle was last visited (-1 for no detection) and the pitch angle of the vehicle at the point of detection. For every new measurement, the highest angle with a valid detection in this table is used for estimating the height of the horizon ahead.
Similar to the original horizon tracking, a selection of the angle range for the best detection of the terrain ahead needs to be made. Figures 5.41 and 5.42 illustrate the impact of scanning speed, vehicle speed, sonar range, vehicle altitude and step height

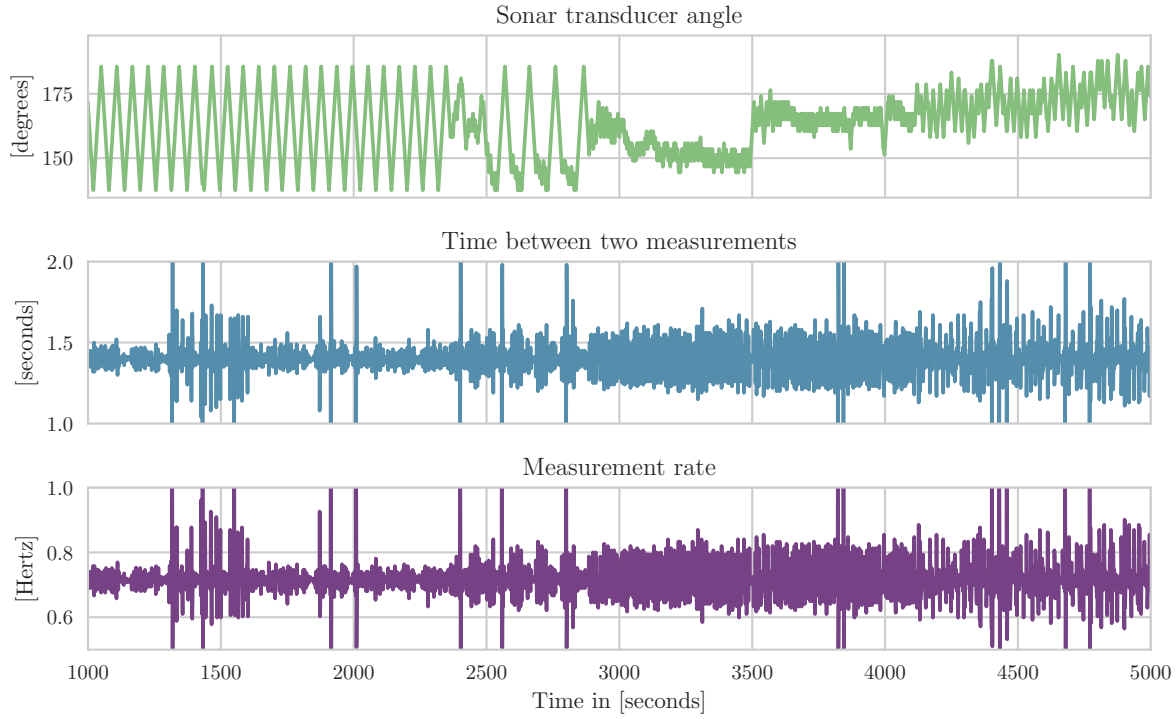

Figure 5.40: Scanning speed of the Tritech Seaking 325 kHz mechanical scanning sonar performing sector scanning and horizon tracking with a 2.5° angle step (D343, M25).

when using a fixed sonar beam or a continuous sector scan. A step of given height is positioned at $x = 2\,\text{m}$, and the plots show the AUV's horizon estimate at each position. Figure 5.41 illustrates that the scanning angle limits determine how well the size of an obstacle can be determined, and how especially obstacles higher than the vehicle altitude tend to be underestimated. Expressing the obstacle height h as a pseudo altitude $a_{pseudo} = a - h$, the range Δx_d at which an obstacle can first be detected by a scanning sonar with range R is $\Delta x_d = \sqrt{R^2 - (a-h)^2}$. This assumes that the full height can actually be detected by the lowest (for small obstacles) or highest (for high obstacles) beam angle α. The detection limits for obstacle heights are $h_{min} = R \cdot \sin(\alpha_{min}) + a$ and $h_{max} = R \cdot \sin(\alpha_{max}) + a$. As the vehicle approaches, all obstacles that are not exactly the same height as the vehicle will not be detectable at full height any more. The range at which obstacles with $a - h > 0$ will be overlooked, and obstacles with $a - h < 0$ will be underestimated, is $\frac{|a-h|}{\sin(\alpha_{min/max})}$. If neither mapping nor a panic range is implemented, this will reduce the vehicle altitude error and thus its actions to avoid the obstacle.
Transitioning from a fixed sonar to a slow scanning sonar, Figure 5.42 illustrates that it is detrimental for the obstacle detection that the scan period is shorter than the obstacle detection range. As the scan period reduces further (increased speed of a complete sector scan, or reduced vehicle speed), the offset in terrain detection moves closer together and it is more likely that the terrain step height is detected correctly.

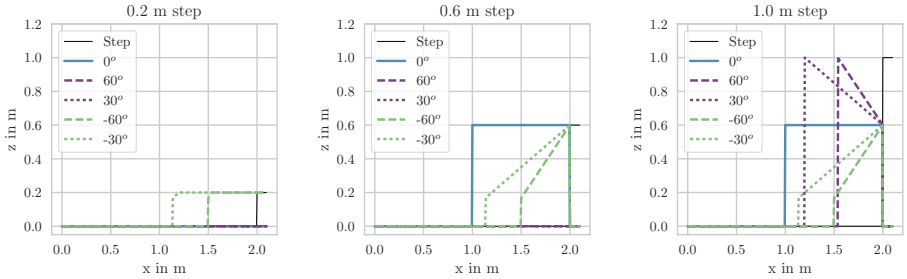

(a) Detection only by 60 degree downwards facing beam.

(b) Detection by downwards and forwards facing beam

(c) Detection by all beams, reduced height estimate with increasing proximity

Figure 5.41: Detection height and range of a terrain step using fixed sonar angles. Parameters used for the simulation: AUV altitude 0.6 , detection range 1 m.

After investigating the detection likelihood of a step, the density of the scanned area was investigated. When moving in the surge direction, a large portion of the scans overlaps in the same region, when the vehicle moves forwards while the scan angle moves towards a vertical scan direction (towards $\alpha = \pm 90^o$), see Figures 5.43, 5.44. Assuming a mostly flat terrain, the scanlines for a vehicle moving parallel to the terrain, pitched at the same angle as the terrain were visualised for a better understanding where scanlines overlap, how evenly the terrain ahead is scanned, and where gaps in the terrain detection may occur.

To ensure that a flat terrain is evenly scanned, the detection area before loosing the terrain detection at the shallowest angle, the horizon angle α_{hz}, and the detection area of the next steepest downwards detection at the steepest scanning angle α_{max} need to overlap (see Figure 5.44). The area $\Delta x_{scanned}$ that is scanned during one full sector scan can be calculated from the progress made by the vehicle Δx_u whilst moving between the shallowest and the steepest detection, the x-component of the furthest detection of the terrain $\Delta x_{\alpha_{hz}}$ (relative to the vehicle position at the time), at the horizon detection angle α_{hz}, and the x-component of the closest detection of the terrain $\Delta x_{\alpha_{max}}$ (relative to the vehicle position at the time) at the steepest scanning angle α_{max}. The progress made between the steepest and the shallowes detection is a function of the time per scan, t_{scan}, the angle step size $\Delta\alpha$, the horizon detection angle α_{hz} and the scan angle limits α_{max} and α_{min}. The x-distance of the shallowest and steepest detection are determined geometrically from the scan angle and the vehicle altitude a (see Figure 5.45).

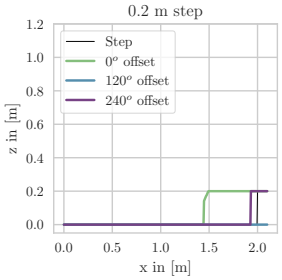

(a) With the correct offset, a shallow step can be missed completely.

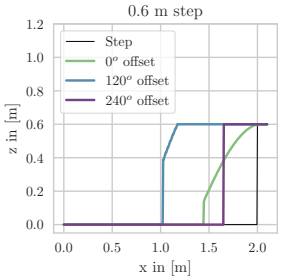

(b) With increasing step height, the chances of missing the step reduce. The correct step height is approached.

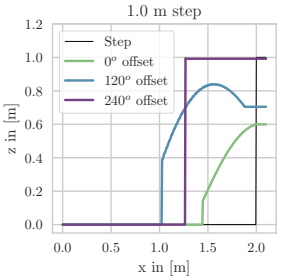

(c) Step is detected reliably, detected height and distance varies.

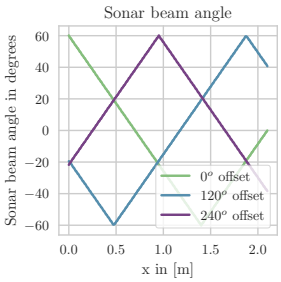

(d) Sonar scan angle vs. x-position

Figure 5.42: Detection height and range of a terrain step using a scanning sonar, scanning a sector between $-60°$ and $60°$, with a scan period of 2.8 s at 1 m/s surge speed and varied offsets of the initial scan angle. AUV altitude 0.6 m, detection range 1 m.

$$\begin{aligned}\Delta x_{scanned} =& \Delta x_u + \Delta x_{\alpha_{hz}} - \Delta x_{\alpha_{min}} \\ =& t_{scan} \cdot \frac{(\alpha_{hz} - \alpha_{min})}{\Delta\alpha} \cdot u \\ &+ \frac{a}{\tan|\alpha_{hz}|} \\ &- \frac{a}{\tan|\alpha_{min}|}\end{aligned} \tag{5.3}$$

Thus the length of the gap area Δx_{gap} calculated from the progress Δx, made by the vehicle during one full scan from α_{max} to α_{min} and back again, and the area scanned $\Delta x_{scanned}$ is:

$$\begin{aligned}\Delta x_{gap} =& \Delta x - \Delta x_{scanned} \\ =& t_{scan} \cdot \frac{2 \cdot (\alpha_{max} - \alpha_{min})}{\Delta\alpha} \cdot u \\ & - t_{scan} \cdot \frac{(\alpha_{hz} - \alpha_{min})}{\Delta\alpha} \cdot u \\ & - \frac{a}{\tan|\alpha_{hz}|} + \frac{a}{\tan|\alpha_{min}|} \\ =& t_{scan} \cdot u \cdot \frac{2\alpha_{max} - \alpha_{min} - \alpha_{hz}}{\Delta\alpha} \\ & + a \cdot \left(\frac{1}{\tan|\alpha_{min}|} - \frac{1}{\tan|\alpha_{hz}|} \right)\end{aligned} \tag{5.4}$$

Assuming flat terrain, the horizon detection range can be expressed as a function of the altitude a and the sonar detection range R:

$$\alpha_{hz} = -\arcsin\frac{R}{a} \tag{5.5}$$

Based on the assumption that the goal altitude is mostly kept, the expected gap size can be expressed as:

$$\begin{aligned}\Delta x_{gap} =& t_{scan} \cdot u \cdot \frac{2\alpha_{max} - \alpha_{min} + \arcsin\frac{R}{a}}{2\alpha_{max} - 2\alpha_{min}} \\ & + a \cdot \left(\frac{1}{\tan|\alpha_{min}|} - \frac{1}{\tan|\arcsin\frac{R}{a}|} \right)\end{aligned} \tag{5.6}$$

Figure 5.43 shows the resulting estimated for the expected scan gaps for the sonar scan sectors considered for the Testwood lake experiments. A negative gap estimate means that the scans will overlap. The figure shows that increasing the absolute value of the downwards scanning limit $|\alpha_{min}|$ will improve the scan coverage for a flat terrain.

Whilst in real missions the vehicle rarely moves at the exact goal altitude over a flat, horizontal terrain with a zero pitch, this estimate can be extended by considering offsets for the terrain slope γ, and the steady state pitch θ_{steady} the vehicle needs to maintain a constant altitude over this slope in the maximum and minimum limits of the sonar scan angle limits α_{max} (5.7 and α_{min} 5.8. Furthermore, the altitude a (orthogonal to the x-axis) may be compensated to be orthogonal to the terrain instead, however the impact of this factor is very small.

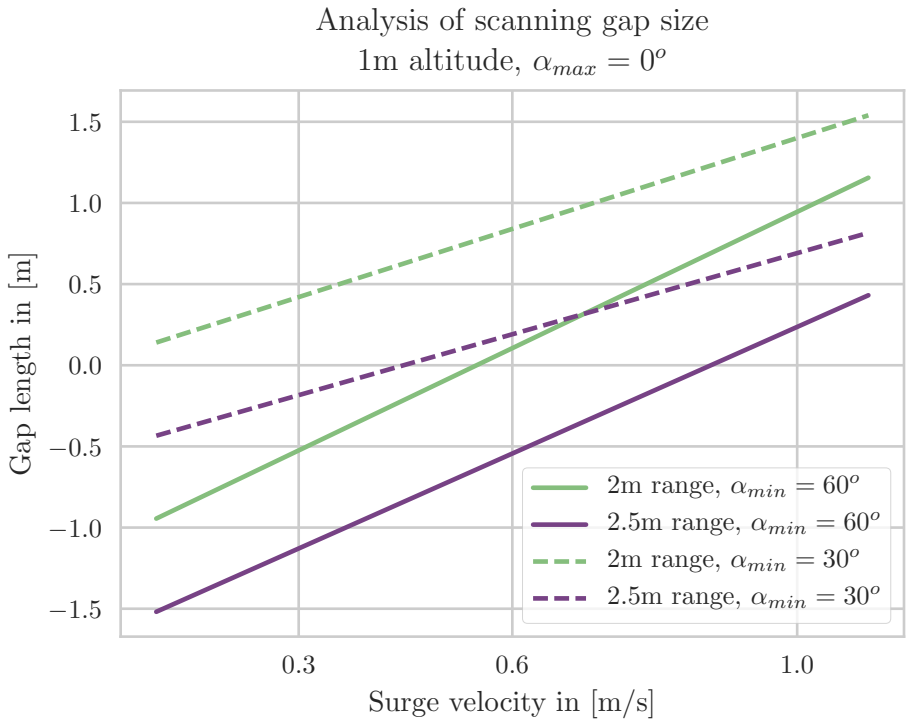

Figure 5.43: Estimate of the scanning gap for different sonar scan sector limits that were considered for altitude tracking at Testwood Lake.

$$\alpha_{max} \rightarrow \alpha_{max} + \theta_{steady} - \gamma \tag{5.7}$$
$$\alpha_{min} \rightarrow \alpha_{min} + \theta_{steady} - \gamma \tag{5.8}$$
$$\tag{5.9}$$

Based on this evaluation a scanning sector of $\alpha_{min} = -60°$ to $\alpha_{max} = 0°$ and an angle step size $\Delta\alpha = 3.6°$ were selected for the Testwood Lake experiments. The selected range was used to illustrate the detection offset in Figure 5.42. The upper limit of 0° was chosen to reduce the risk of falsely detecting the water surface as terrain, whilst still detecting all steps of a similar hight to the goal altitude. A downwards scan angle of 45°, as on Autosub, would have sufficed, since a pseudo altitude below the altimeter altitude does not improve the altitude tracking. However, to improve the terrain coverage at high speed and the detection of the downwards step for future investigations and to make visual inspection easier, a lower limit of −60° was used.
The step angle of 3.6°, above the recommended maximum angle step size of 1.8°, minimises the scan time. At this step size, the speed per degree is $0.023\frac{s}{1°}$ (4.1 s for a 90° sector scan period), see Figure 5.39. The resulting time for a full scan with 3.6° steps is 2.8 s. In the same time, a horizon scanning beam pattern would complete 3.5 measurements, covering a maximum angle change of 12°.

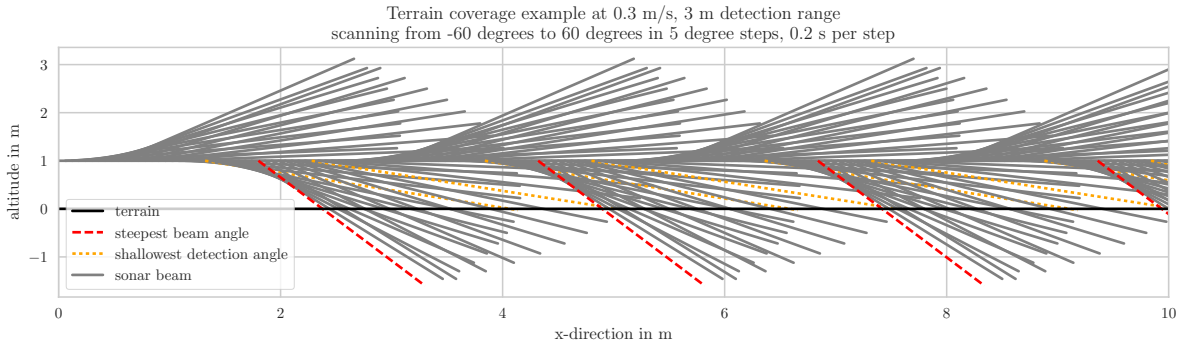

(a)

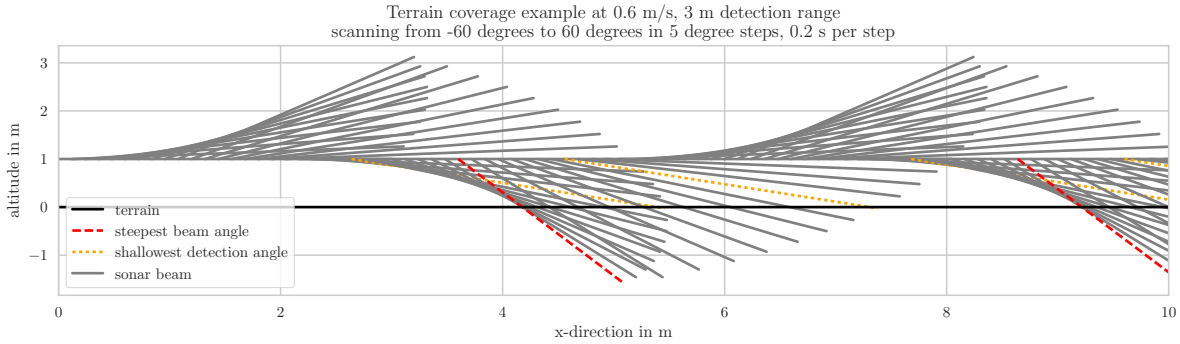

(b)

Figure 5.44: Example overlaps of sonar scan patterns which scan positive and negative sonar scan angles. The shallowest detection angle α_{hz} and the steepest detection angle α_{min} are highlighted.

The irregular scan pattern that is recorded when using a mechanical scanning sonar at flight style speeds also shows why it is challenging to verify map data through repeated scans of an area. Whilst in some areas scans overlap repeatedly, with the scan ranges achieved, several sections are only scanned once before the vehicle passes over them. One might think that a longer detection range could simply be achieved by entering all returns in a map and calculating a probability for each cell to be empty or filled. However the irregular scan pattern combined with strong false returns (see section 5.4.2) make the correct tuning of the cell size and limits for the probability map difficult. For applicability over a range of missions a better understanding of the parameter selection process and a better pre-processing method are required.

5.4.2 Detection Reliability

Besides determining a suitable scan pattern and horizon tracking algorithm, a suitable terrain detection method for the lake tests needed to be found. For the Testwood experiments, the aim was to evaluate the data on a per-scan basis, determining a range

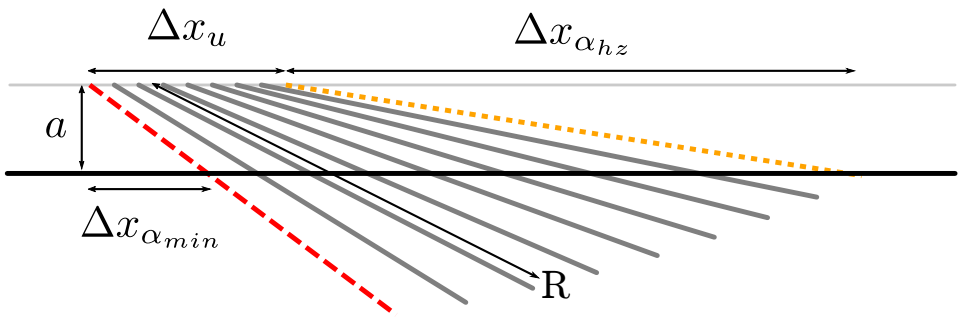

Figure 5.45: Nomenclature of the angles used for estimating the area covered by forwards looking detection and the gaps in detection.

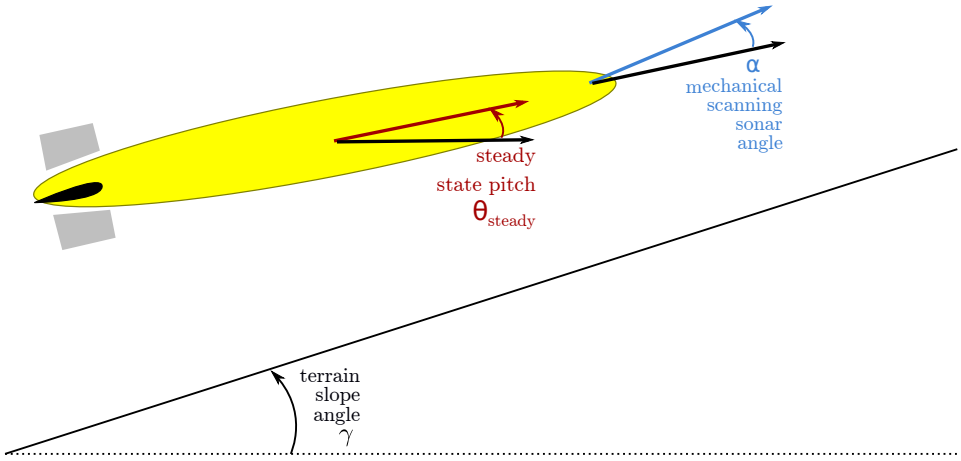

Figure 5.46: Pitch and terrain slope considerations for generalising sonar scan coverage estimations to non-horizontal terrains and a steady state AUV pitch.

to the terrain at the scan angle. Further analysis based on the data recorded in the experiments also took a small set of previous scans into account for post processing of the sonar data and scan range determination. The main challenge for both terrain range estimation strategies was the correct dismissal of false detections.
Such false detections of the terrain can come from a variety of sources. The impacts of those different sources of false returns vary with the sonar device, the test location and the scan pattern. Figure 5.47 illustrates the three types of false reflections that were observed on Autosub6000 and Delphin2. Figure 5.48 shows what the different false returns look like in the sonar scan visualisation chosen for this work.

Side lobe returns are due to a non-ideal shape of the sonar beam. Besides the signal in the main beam direction, another strong sonar beam is emitted into a different direction, and the returns from this beam are also detected by the sonar device. When looking at the return data, it can be difficult to distinguish the two sets of returns which are detected additively. On a scan image combining multiple sonar beams from a fixed position, they look like a second terrain line at a different slope angle than the main

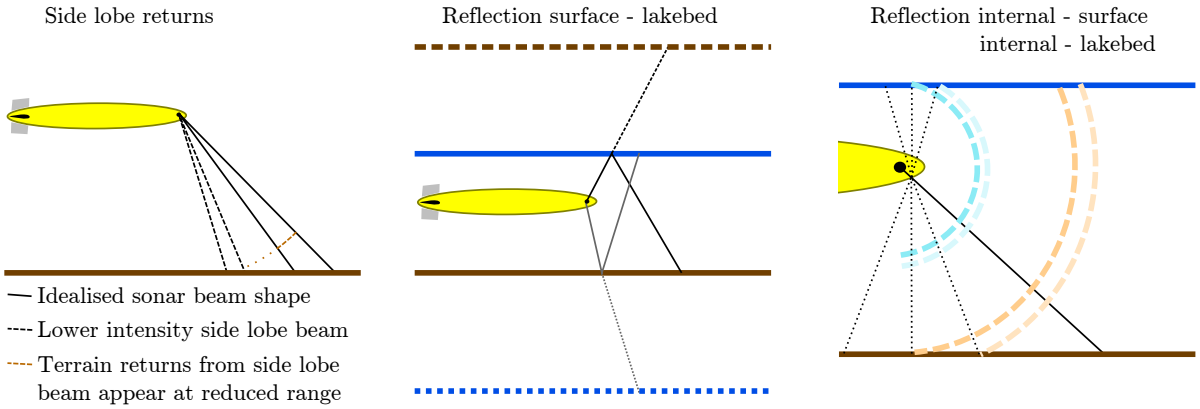

Figure 5.47: Types of sonar reflections that do not come from the target and may lead to false detections.

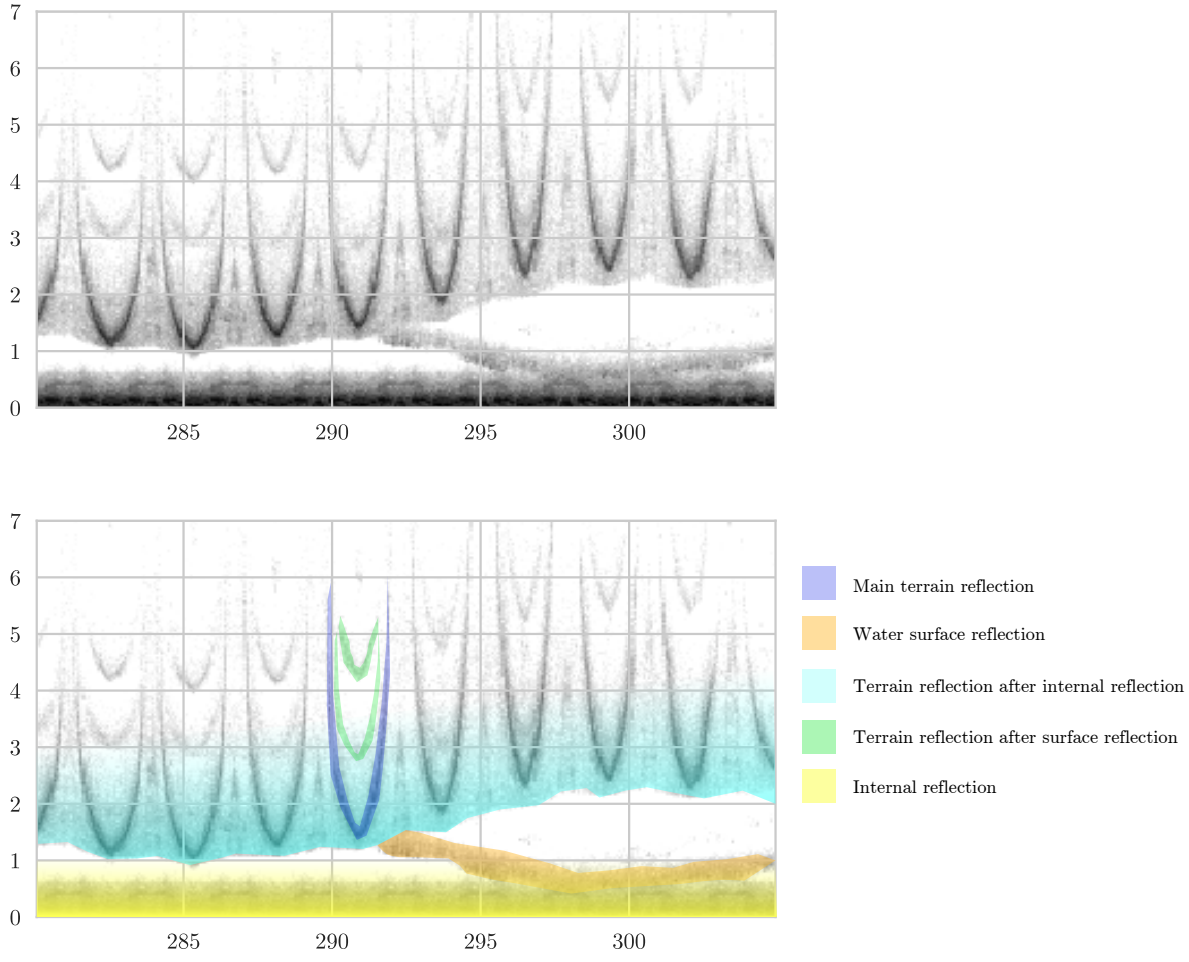

Figure 5.48: Examples of different types of false returns that can occur, highlighted in different colours to indicate the cause of the return pattern. Example sonar data collected at Testwood Lake.

terrain.
Besides the terrain, the water surface reflects sonar beams well. When operating in shallow water, it can be detected directly if the sonar beam is pointing at the water surface. It can also be detected indirectly, if a portion of the sonar beam reflecting from the terrain may also travel to the water surface, reflect back, and then back to the sonar device. On sonar scan images, these multiple reflection paths show up as repetitive patterns, at ranges larger the main reflections and smaller intensities. However, with unsuitable detection methods they can end up being falsely recognised as the main terrain returns.
Finally, portions of the sonar beam, whether from the main beam or from smaller side patterns, are reflected on the vehicle itself. This direct returns from the vehicle register at a very small detection range and are typically dealt with by ignoring the return bins closest to the vehicle, the so-called blanking distance. However, again some of the reflected sonar pulse then makes its way to the surface or the terrain, and back again to the sonar device. On a scan image combining multiple sonar beams from a fixed position, these returns form a ring-like pattern at a range of approximately the vehicle depth and the vehicle altitude. Depending on how the sonar is mounted, these returns can be of an intensity similar to that of a valid terrain return.

In the Testwood data no sidelobe returns as on Autosub6000 were observed. With the overall low reflectivity of the lakebed at Testwood, however, problems with water surface reflections emerged which had been less pronounced in the more reflective towing tanks: Since the sonar device is mounted inside the hull of Delphin2, to better protect it from collisions and keep a smooth hull shape, internal strong reflections on the hull occur, causing strong return signals from the water surface. Combined with low reflectivity of the lakebed, and the shallow grazing angle when operating at low altitudes, the reflections corresponding to the depth and altitude are barely distinguishable in the returns of one measurement. In the experiment setup the typical detection range for the terrain and the required vehicle depth are very similar, and the range of returns around the depth and altitude is fairly wide. Due to this, the option of filtering a band around the current depth was dismissed due to the high risk of removing valid terrain returns and thus tracking the wrong horizon.

Besides sonar reflections, on the tritech mechanical scanning sonar a mechanical problem may also impact the terrain detection reliability. On several occasions a drift of the head angle was observed repeatedly within the same day. An example of this drift is shown in Figure 5.49, where the vehicle is operated in the towing tank, at the surface. The returns from the bottom of the towing tank are marked with a dashed line. Based on the reported transducer angle, the returns from the bottom of the towing tank are detected above the vehicle. Similar observations were also noted on the Sirius AUV [personal communication, Stefan B. Williams, NOC 2018].
After several observations, an additional feedback analysis for the sonar was introduced on Delphin2, analysing the `mtAlive` messages for the `centred` information. This message is normally not logged on Delphin2, so it was impossible to analyse older recordings for the occurrence. Problems with the transducer angle have not been observed since, how-

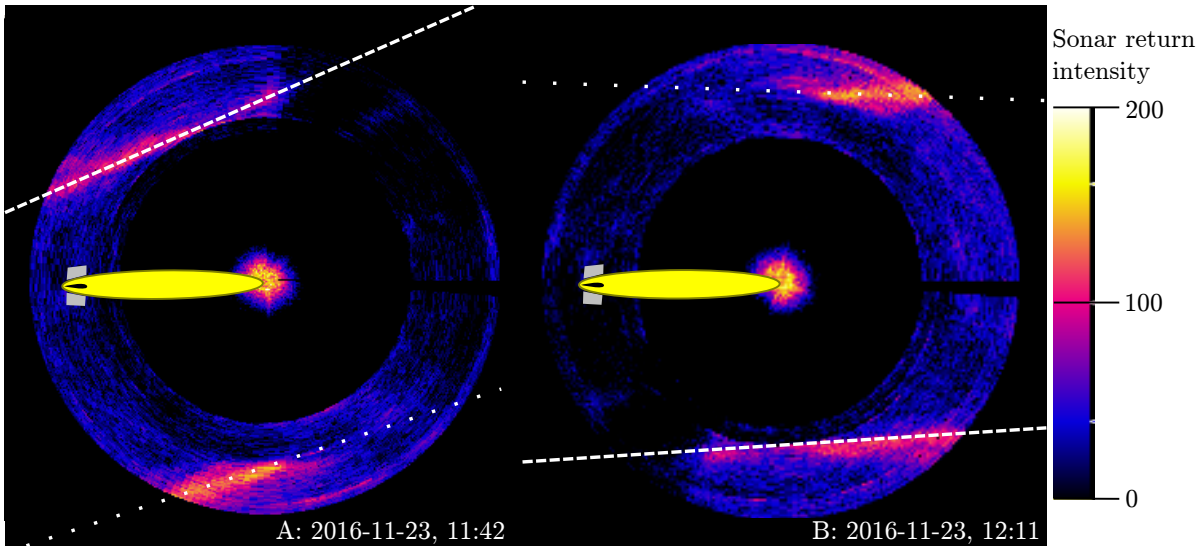

Figure 5.49: Sonar measurements from the same day, in similar position, showing the effect of the sonar head drift. The terrain is marked with a dashed line, the water surface with a dotted line.

ever this further encouraged a continuous scan pattern over regular scan angle changes to make it easier to detect such issues after the end of a mission through visual inspection.

5.4.3 Evaluation of Existing Detection Methods

Several detection methods for single-beam based detections were compared to establish the most suitable method for the Testwood lake experiments: As on Autosub6000, an impulse response filter was applied to determine a threshold function for each measurement. A variety of methods for automatically determining a threshold by treating a plot of several measurements as an image was applied. Finally, a single threshold was selected manually to be applied for all measurements. Furthermore, image analysis methods for line recognition were tested over the continuous scan images.

The obstacle detection on Autosub operates on a per-scanline basis, determining a threshold value for each bin. However, over the Testwood data it was found difficult to tune for a reliable terrain detection. The terrain returns due to internal reflections are very well defined and may be detected instead of the main returns, but they can also 'mask' the main returns, and the detection of a steep bin value change instead occurs on a terrain reflection after a surface reflection (green in Figure 5.48, middle Figure in 5.47). Figure 5.50 (b) shows an example of this threshold method where both occur. Whilst the chosen example is extreme, to demonstrate both effects, the results that can be achieved are not as good as the manually chosen fixed threshold which is included in the same figure.

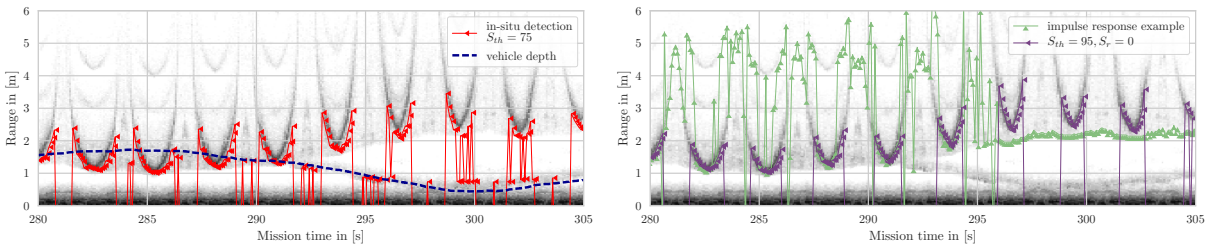

(a) Terrain detection and false detection due to surface reflections during the mission, resulting in the vehicle surfacing.

(b) Variation of the terrain detection method over the recorded sonar data.

Figure 5.50: Terrain detection example: the sonar is continuously scanning the angle sector over time, as the vehicle moves forwards over the terrain, each individual vertical line represents return intensity at a new scan angle. During the mission, a constant threshold of 75 was used, and returns from the water surface were mis-detected as an obstacle, resulting in the vehicle surfacing. Detection results using a higher threshold and an impulse response filter over the same sonar returns are shown in (b).

Different automated thresholding methods that are typically used for image analysis were used over a varying window size, from individual scanlines to images combined from several sector scans (see Figure 5.51). Again, none of the thresholding methods were found to deal well with the false returns and improve the overall detection results over a manually chosen, fixed threshold for all experiments.

The manually selected constant sonar threshold S_{th} was tested, and found to be most reliable around $S_{th} = 95 \approx 30\,dB$, with a detection range of 2 m to 4 m. To increase the range further, instead of a constant threshold a threshold linearly decreasing with the range was used for each measurement. A reduction of S_r per metre was applied until a minimum threshold was reached.

Through visual inspection of several scans, and comparison of the results of the different tested methods, it became clear that the method that achieved the best results was manually selecting a fixed threshold. Whilst this method can only be used if reference data is available, achieving a large detection range for the small scale experiments was prioritised over choosing a generally applicable detection method. Several fixed and range dependent thresholds were selected for testing during the Testwood Lake experiments.

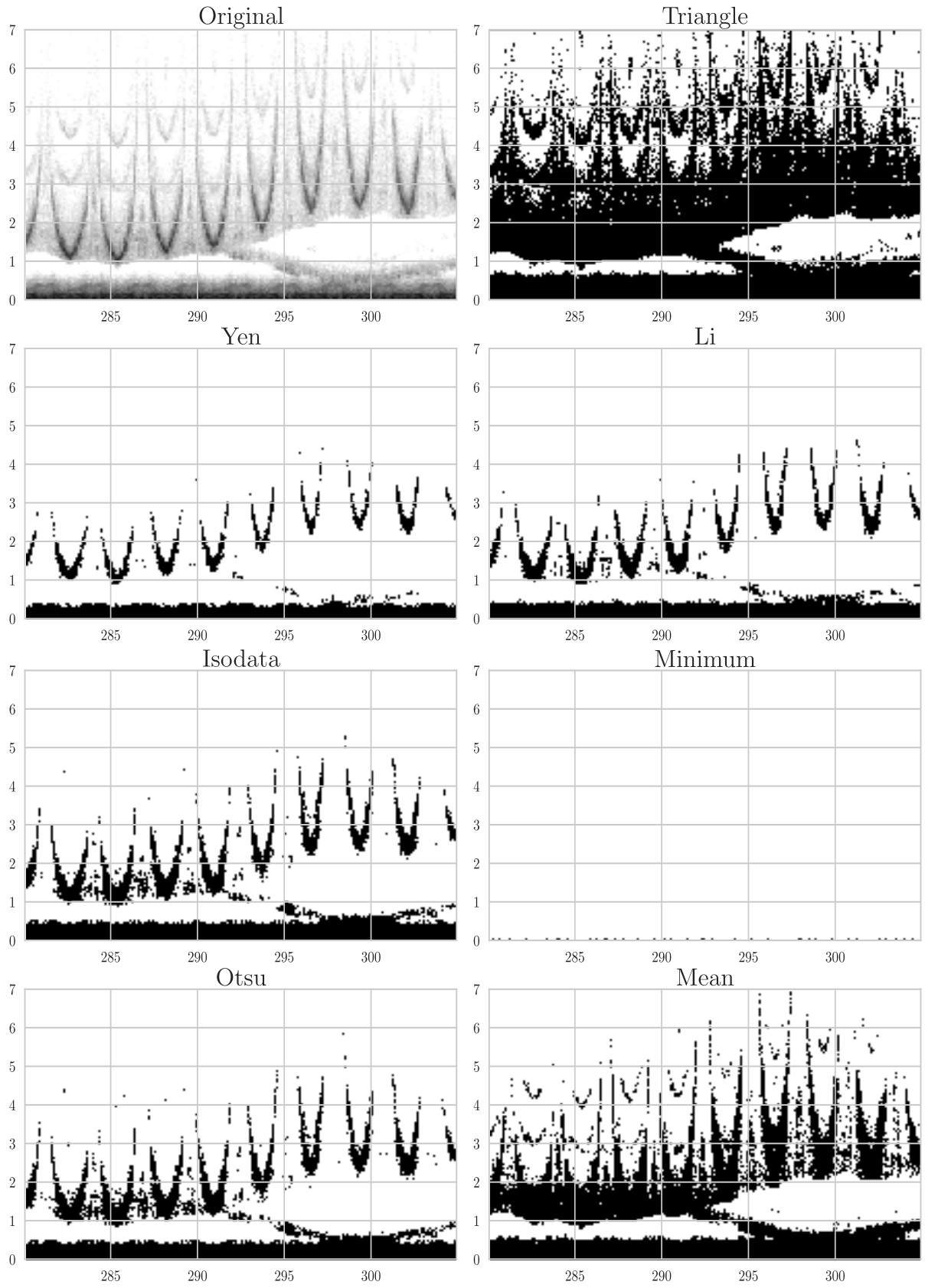

Figure 5.51: Examples of threshold determination methods applied over an entire set of sonar scans, using [van der Walt et al., 2014].

5.4.4 Signal Filtering

To improve the terrain detection, several methods were tested for filtering the signal better, to remove as much of the false detections (see Figures 5.47 and 5.48) as possible before applying a threshold for terrain detection.

First the noise that can be determined before an experiment is removed: the reflections that occur directly on the vehicle. Normally, the range where these reflections are detected is ignored completely, however by removing it, the proximity at which detections are made can be slightly improved.
It was observed that that the blanking pattern on Delphin2 is very regular, but dependant on the sonar scan angle (note the pattern around 0 m range in Figure 5.52). The pattern permeates to ranges up to 0.7 m. Since this is in the range of altitudes at which the vehicle was operated, the pattern impacts the clear detection of the terrain. To remove it, several repeated scans of the sonar sector were taken, and the median $Med(m_{\alpha_{min},n})$ for each bin b in the N_b bins per scan was calculated for each individual angle α of the N_α in the scan over a set of individual measurements $m_{\alpha_{min},n}$. The median was chosen over the average value, to avoid peak datapoints skewing the results and instead determining the typical value for each bin. This typical value is what is caused by reflections, whilst the rare, high value peak datapoints stem from terrain reflections. The calculation of these lookup values from a reference set of measurements is given in matrix form $M_L^{(N_\alpha \times N_b)}$ in equation 5.10.

$$M_L^{(N_\alpha \times N_b)} = \begin{bmatrix} Med(m_{\alpha_{min},1}) & \dots & Med(m_{\alpha_{min},N_b}) \\ \vdots & Med(m_{\alpha,b}) & \vdots \\ Med(m_{\alpha_{max},1}) & \dots & Med(m_{\alpha_{max},N_b}) \end{bmatrix} \tag{5.10}$$

For each scan angle α the according row of N_b lookup values for individual bins b is then subtracted from each new measurement $m_{\alpha,b}(t)$ at that angle. In practice, the lookup value for bins b at ranges larger than the visual pattern are assumed to be zero: $Med(m_{\alpha,b>b_{pattern}}) \approx 0$.

Figure 5.53 shows the result after such filtering. The pattern is not visible any more, and terrain detections that were very close to the blanking distance can be clearly distinguished (e.g. around measurement count 350 to 400).

After clearing this known pattern, the less even patterns from internal reflections that bounce off the hull and then reflect from the water surface or the terrain are removed. They could be filtered by measuring the depth and altitude, and applying a filter around the expected bin range. However, this method will not work if there are floating objects at the surface (ice, pontoons, ...), and as is visible in the measurements around count 400, the intensity of the reflection from the terrain varies with the terrain (Figure 5.53, or more clearly visible in Figure 5.55. To account for this, a different method was chosen. A sliding window median filter was applied, subtracting the median for each

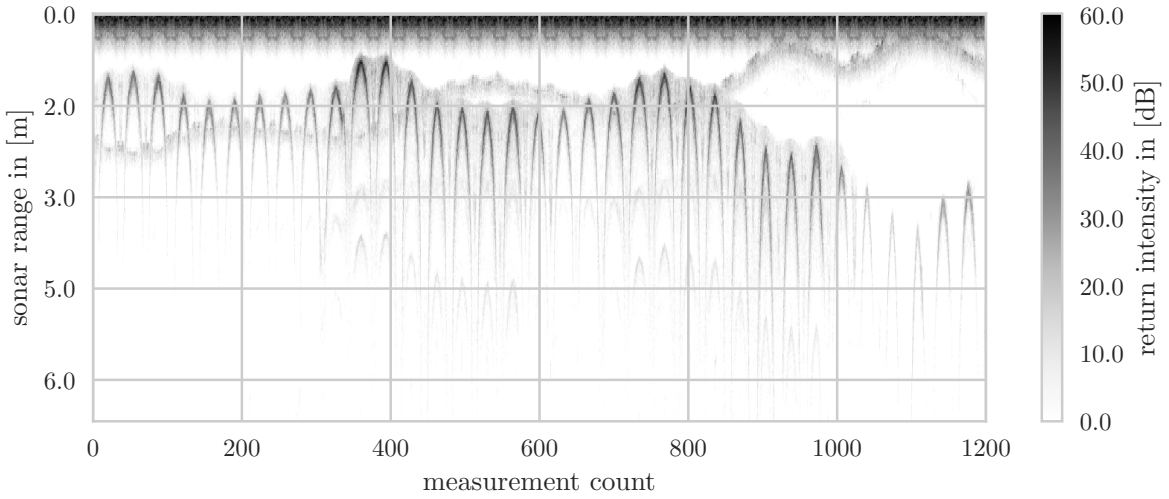

Figure 5.52: Raw sonar data from performing a continuous sector scan, before any filters are applied. In the original experiment, the vehicle surfaced due to false detections of surface reflections around measurement 800.

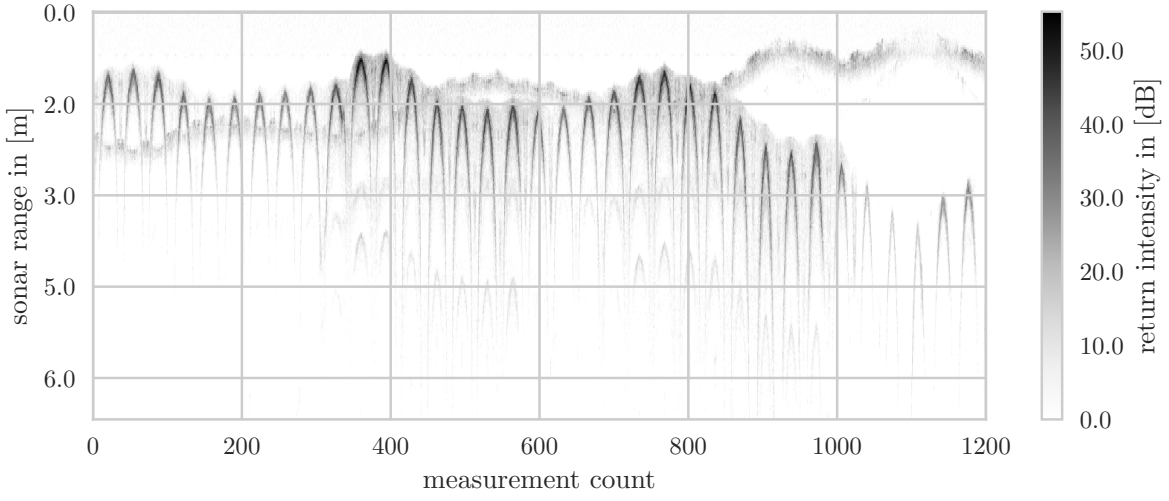

Figure 5.53: After removing the repetitive pattern from internal reflections the scanlines at low altitudes are clearer.

bin calculated over the previous $2N_\alpha$ measurements $\vec{m}(t-i)$ at times $t-i$ before the current measurement $\vec{m}(t-i)$ at time t (one sector scan). The vector of the scan angle independent noise estimate for a measurement $\vec{m}(t)$ containing the compensations for all bins of one scan at time t is:

$$\vec{m}_I(t) = \sum_{i=1}^{2N_\alpha} \vec{m}(t-i) = \sum_{i=1}^{2N_\alpha} \left(\begin{bmatrix} m_1(t-i) \\ \vdots \\ m_b(t-i) \\ \vdots \\ m_{N_b}(t-i) \end{bmatrix} \right) \tag{5.11}$$

This uses the fact that the reflections causing this pattern are present for every scan angle, and always return a similar range, dependant on the surface and terrain distance but not the sonar scan angle. As a result, the typical value calculated by the median stems from the terrain and surface reflections, whilst even reflections that are small deviations from this typical value show up after removing the median This holds, as long as the depth change of the vehicle and the terrain variation are small over one sector scan time. In cases where not all angle independent reflections can be removed, due to steep depth or terrain changes, the level of noise in the data is still reduced significantly, making it easier to remove it in further post-processing steps.

The filtered measurement $\vec{m}^f(t)$ for a measurement $\vec{m}(t)$ at a scan angle α_t is thus calculated as:

$$\vec{m}^f(t) = \vec{m}(t) - \begin{pmatrix} 0 & \dots & \overset{\alpha=\alpha_t}{1} & \dots & 0 \end{pmatrix} \times M_L^{(N_\alpha \times N_b)} - \vec{m}_I(t) \tag{5.12}$$

The results after applying the averaging window are showing in Figure 5.54. It can be seen that around the very fast depth changes some noise remains, but the continuous lines are broken up and the terrain reflections are much clearer. Furthermore, the removed data (Figure 5.55) gives a clear depiction of the altitude line and the depth line, which may be useful for further analysis, e.g. as a cost efficient method to detect if the path to the water surface is free, or if the AUV is trapped underneath something. Further processing for mapping purposes may include the angle independent pattern to derive information for more directions than just the main beam angle, or to infer details about the terrain from the reflectivity recorded in the angle-independent data.

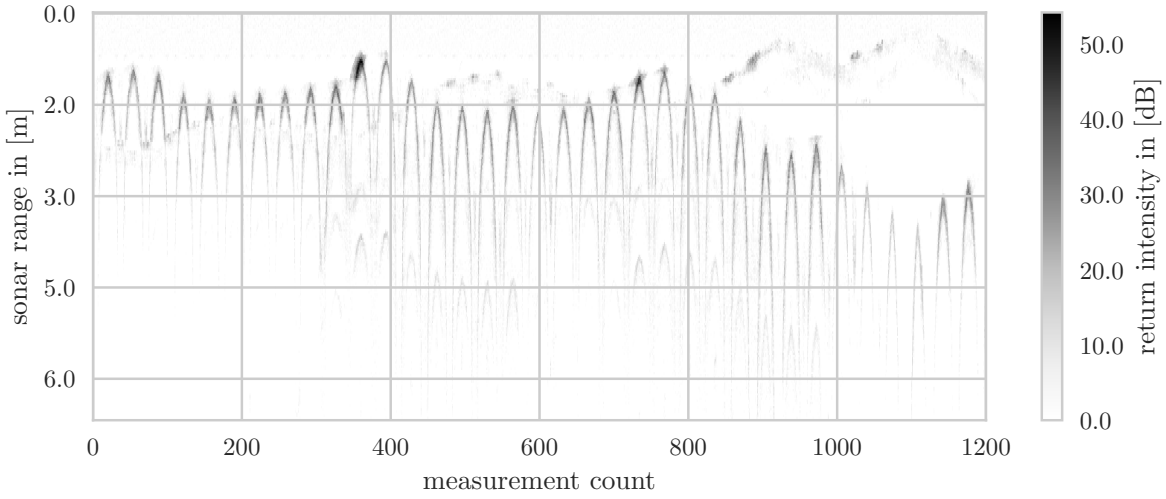

Figure 5.54: After removing the repetitive pattern from internal reflections and applying a sliding window median filter, the terrain reflections are easily distinguished from other noise by visual inspection.

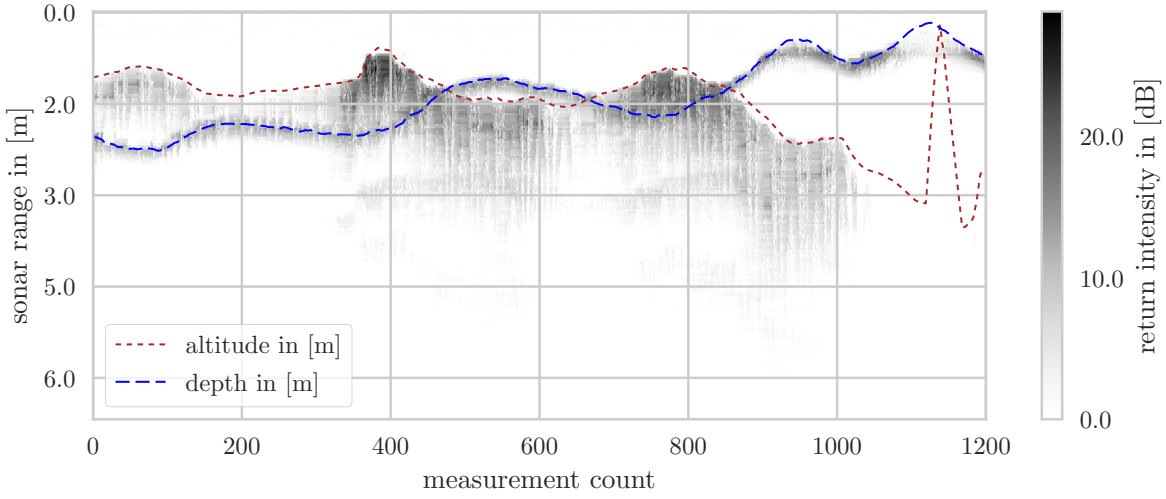

Figure 5.55: The data that was removed by the sliding window median filter matches the altitude and depth of the vehicle well, but also shows variations in terrain reflectivity.

5.4.5 Gaussian Tracking of Terrain Detections

Once the data has been cleared of reflections based on beforehand knowledge and data from the previous $2N_\alpha$ scans, the processing for detection of the terrain starts. The goal is to apply a weight over the returned scanline, based on the likelihood of a terrain return at that range. To avoid distorting the location of the detection, first peaks in the scanline are detected, then the peak values are weighted based on the likely position of the next detection. An example of the detection process is given in Figure 5.56.

The most recent altimeter measurement is used to perform a prediction where the detection at the lowest angle sonar scan angle can be expected, and weighting the detected peaks with a Gaussian distribution around the predicted range $r_{predicted}$, with a standard deviation $\sigma_{predicted}$.

Two strategies for the prediction were compared, a simple method relying only on the last altimeter measurement a, and a more complex method using the last valid detection r_{last}. For both, the user only has to configure a constant standard deviation base value σ_{base} and a threshold T. Initially, applying a low pass filter over the terrain was considered before running the peak detection, to get fewer, clearer peaks. However, this, too distorts the peak position, so the approach was dismissed (see Figure 5.56).

For the prediction method relying only on the altimeter measurement $a(t)$, the predicted range $r_{predicted}(t)$ and the standard deviation $\sigma_{predicted}(t)$ used at time t are calculated from the sonar scan angle $\alpha(t)$ as:

$$r_{predicted}(t) = \frac{a(t)}{\sin \alpha(t)} \quad \text{for} \quad \alpha < 0^o \tag{5.13}$$

and

$$\sigma_{predicted}(t) = \frac{\sigma_{base}}{\sin \alpha(t)} \quad \text{for} \quad \alpha < 0^o \tag{5.14}$$

The prediction range $r_{predicted}$ is limited by the maximum allowed range r_{max} to limit the prediction for a zero degree sonar scan angle α and to account for detection inaccuracy at long detection ranges.

To be able to predict steeper steps, a different prediction method was developed. For the more complex detection prediction method, the range r_{last} and sonar scan angle α_{last} of the last successful detection are taken into consideration for all but the lowest scan angle. To avoid tracking a false detection for too long, the prediction for the lowest scan angle α_{min} is calculated based on the altitude as in equations 5.13 and 5.14. Note that the last detection is not necessarily the detection at $(t-1)$; this was chosen to avoid loosing valid detections due to a single bad measurement.

The predicted range is calculated similar to previously, but the altitude is replaced by the orthogonal component of the last prediction. If the predicted range is larger than the maximum range r_{max}, or the scan angle is zero, it is replaced by the maximum range.

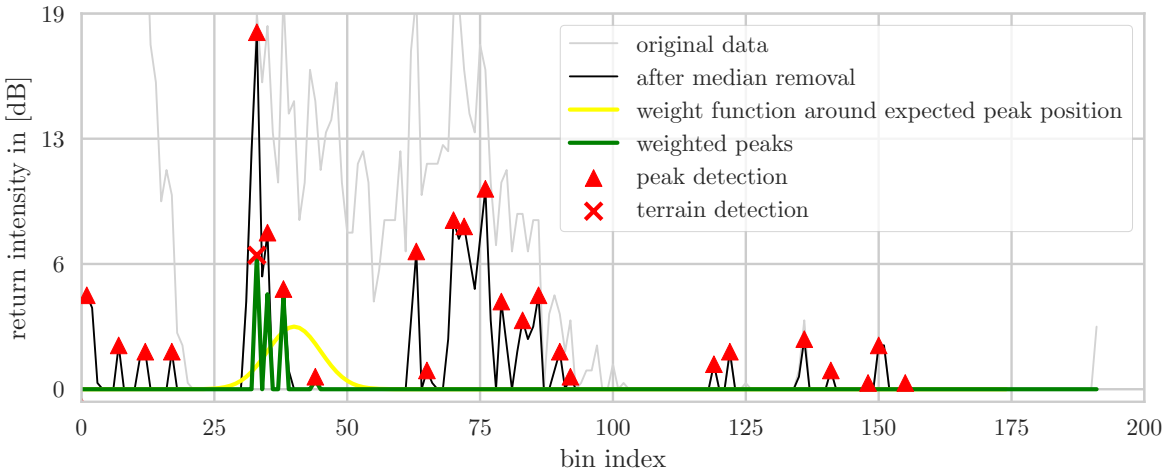

Figure 5.56: Steps of the terrain detection illustrated on one single measurement.

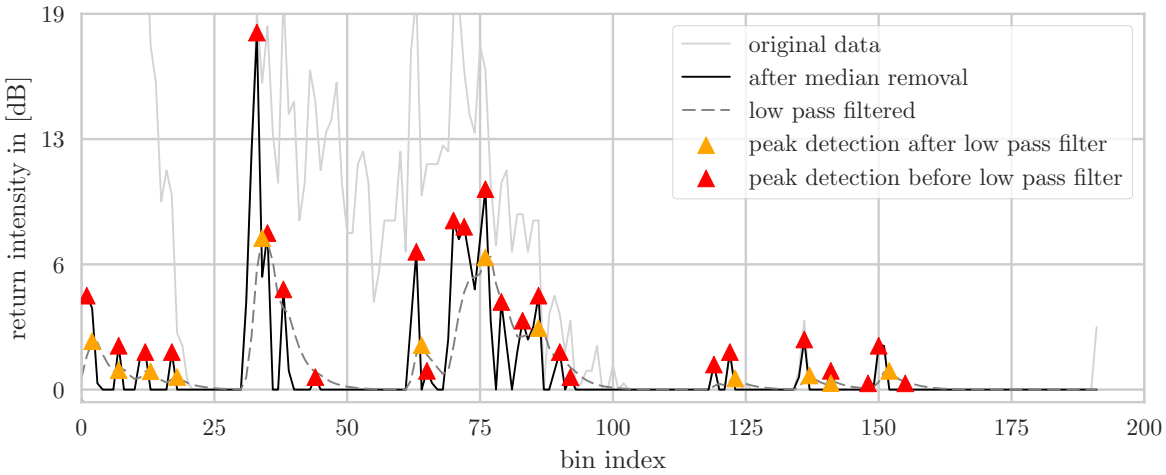

Figure 5.57: Peaks are detected at a slightly larger range if the data is first passed through a low pass filter. Whilst the resulting scanline is cleaner, terrain reconstruction becomes more difficult.

$$r^*_{predicted} = \begin{cases} r_{max} & \text{if } \alpha = 0 \\ r_{predicted} & \text{if } \alpha = \alpha_{min} \\ Min\left(r(t-1) \cdot \frac{\sin\alpha(t-1)}{\sin\alpha(t)},\, r_{max}\right) & \text{else} \end{cases} \tag{5.15}$$

The standard deviation around the predicted range is now calculated based on the goal to include a vertical step, so it is calculated to be the distance between the predicted range and the vertical continuation of the previous detection. It is generally assumed that $|\alpha|$ is less than 90°; if the vertical continuation of the last detection is larger than the maximum range, or if $\sigma^*_{predicted}$ becomes too small, the base standard deviation σ_{base} is used instead.

$$\sigma^*_{predicted} = \begin{cases} \sigma_{predicted} & \text{if } \alpha = \alpha_{min} \\ Max\left(r^*_{predicted} - |r(t-1) \cdot \frac{\cos\alpha(t-1)}{\cos\alpha(t)}|,\, \sigma_{base}\right) & \text{else} \end{cases} \tag{5.16}$$

It was expected that using the actual detection to calculate the next most likely detection would be the more successful strategy, however it was found that this strategy is still likely to attach to a false detection and miss the actual terrain. Using the measured altitude to predict all future detections on the other hand is not only simpler in the implementation, over several different experiments taken from the Testwood data it proofed to be more reliable. With the base standard deviation and the threshold as the only parameters it was easily tuned to work over the full range of vehicle paths over the terrain, and an original concern that deviations from a flat terrain would not be detected well was not a problem for the tested terrain.

Figure 5.58 shows how the terrain detection works on the example of a smaller section selected from the terrain used as an example in this section. The terrain prediction (orange cross marker) moves along a $1/\sin$ line as the sonar angle changes. The detected peaks of this measurement are then weighed with a Gaussian distribution, the standard deviation thereof is indicated in blue around each of the predicts points. If any of the peaks detected in this area remains above the chosen threshold, causing a valid detection, it is marked with a red 'x'. As can be seen for the measurement counts 890 to 920, this approach sometimes leads to several missed detections as well as an underestimate of the detection range, however without such weighting the detection of measurements 880 to 895 would have likely occurred at the water surface reflection (indicated by the depth line). Whilst a more adaptive method of tracking reflections was attempted, so far no suitable prediction and weight functions have been found that avoid following the wrong detection whilst also achieving good detection ranges.

The full set of valid detections over the example terrain is shown in Figure 5.59. With the exception of the false altimeter measurement, the detection of false returns is mostly avoided, whilst also achieving a significant range increase with detection ranges up to 6 m.

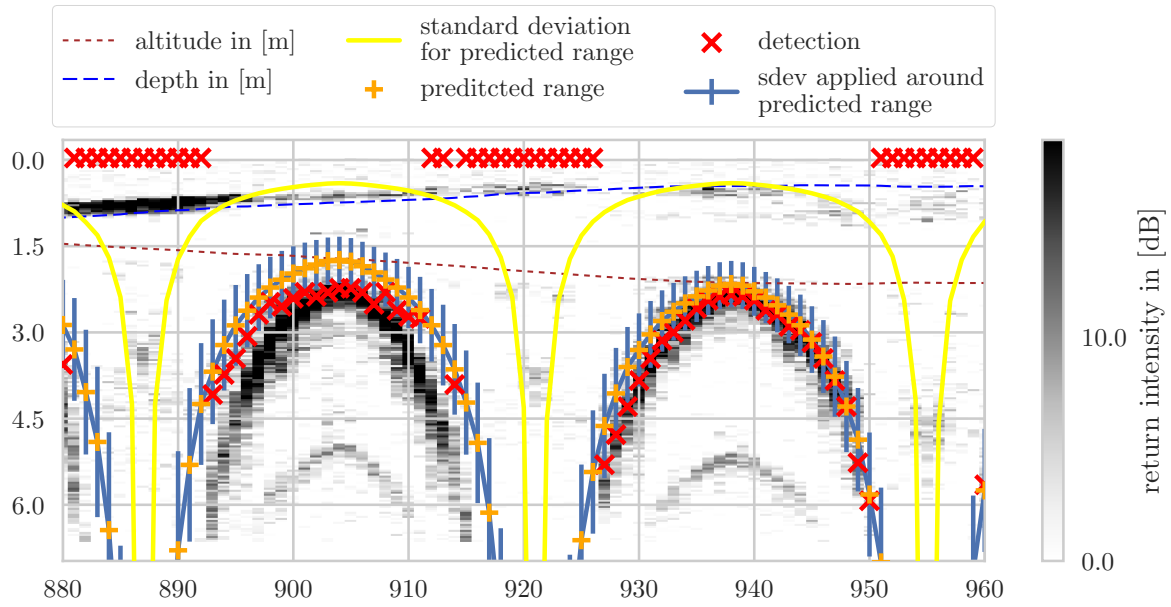

Figure 5.58: Section illustrating the components of the sonar detection.

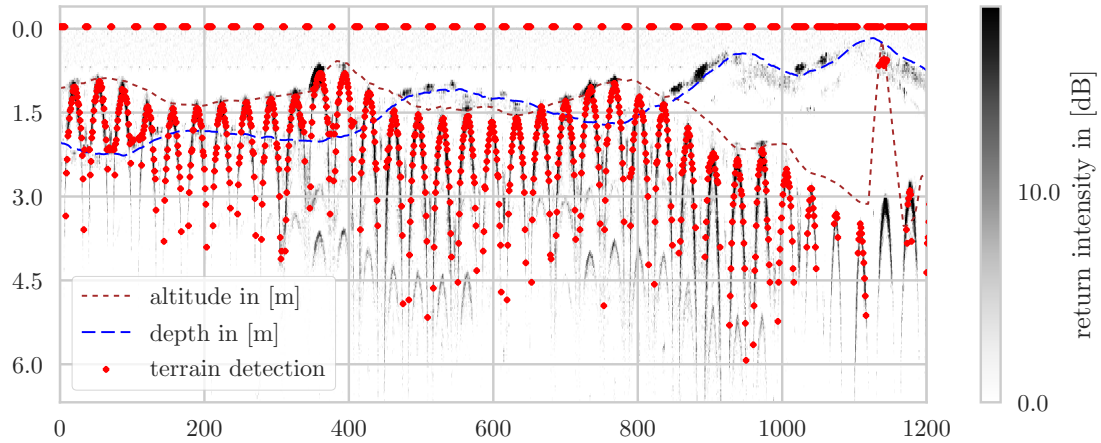

Figure 5.59: Final detection results for the example data. Note the false detections around measurement count 1100, due to the wrong altitude measurement.

The gaussian terrain tracking method still leaves room for further work, e.g. for better tracking of successful detections, or to allow for steps going above a maximum height at around the altitude of the vehicle. However, it shows promise as a fast, simple standalone detection method. The range extension achieved already increases the detection range for Testwood Lake sufficiently to improve the performance of Delphin2 as a test platform for Autosub6000. The map in Figure 5.62 below especially highlights the terrain detections above a range of 3 m - all detections that would have been missed with the detection methods considered before the experiments. The terrain information available now is sufficient and reliable enough to use it for long term planning. The achieved ranges compare in scale to those of Autosub6000 experiments.

5.4.6 Mapping

First attempts at mapping the sonar range detections were already made with the thresholding method used for the Testwood lake experiments, using the ROS package octomap [Hornung et al., 2013]. Using the ROS framework, specifically the transfer functions for pose information, maps can easily be obtained and transformed relative to the vehicle fixed or the global coordinate system. However where typical mapping systems usually eliminate false detections, the scan time and detection range compared to the surge velocity mean that most coordinates in the map are only measured once. Thus very little could be gained from generating a map with the achieved scan ranges at the time. With the new improvements in the detection range, meaningful maps can now be built from the sonar data.

Figure 5.62 shows a terrain map generated from the data of the sonar scan that was used in the previous sections. Taking the vehicle in-situ depth and pitch measurement, and assuming a constant x-velocity, the terrain can be estimated accurately and correctly from these detections. Figure 5.61 shows the resulting terrain detections and where on a global map they would be positioned. An error bar is placed around each detection, indicating the maximum estimate error in the z-direction. The same maximum error applies in the x-direction, however due to the vertical exaggeration of the plots it is barely visible and thus neglected in the plot. Since the error is calculated as a radius around the centre of the detection area (see Figure 5.60), it is independent of the vehicle pitch.

$$\text{max error} = \sqrt{\left(\frac{1}{2}l_{bin}\right)^2 + \left(R + \frac{1}{2}l_{bin})\right)^2 \cdot \sin\frac{\alpha}{2}^2} \tag{5.17}$$

The colour of each detection mark indicates from how far away the detection was made. Markers from a larger distance are placed on top of sorter distance markers, since the focus is on the range of the first detection of a terrain feature. Several darker markers indicate clearly that both the upwards and downwards step in the terrain are well detected at long ranges, but the flat terrain following an upwards slope is less well covered.

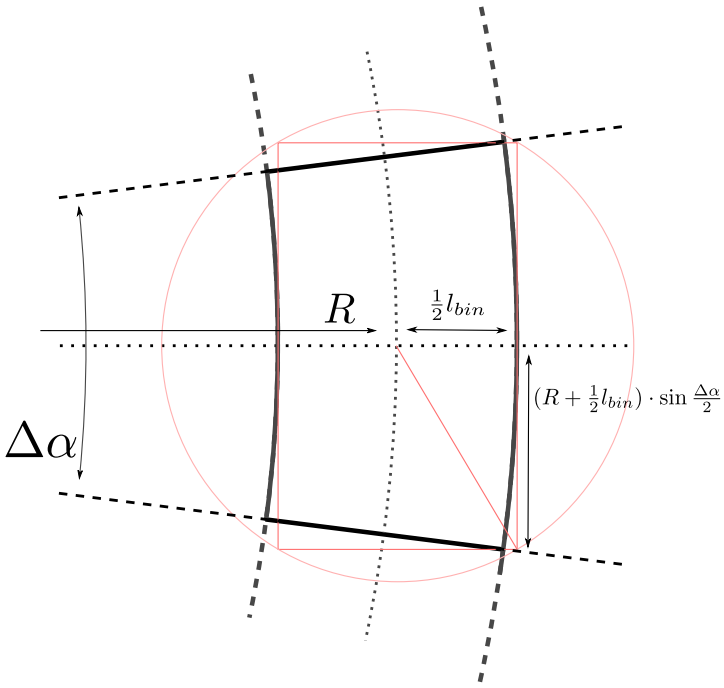

Figure 5.60: Maximum error estimate considering the beam opening angle $\Delta\alpha = 3^o$ and the bin length l_{bin}.

However, these areas are also of little concern for terrain tracking. The most surprising outcome is that both the downwards slope around the x-positions 40 m and 70 m are well detected. On the other hand the false detections shown in the selected section for Figure 5.58 can be clearly seen around x-position 65 m, causing a terrain over-estimate of ca. 0.5 m, which is improved through detections from a closer range.

To further investigate how much information is available for long-term planning (and had not been available before the analysis improvements), only detections with a minimum range of 3 m are shown in Figure 5.62, combined with an outline of the terrain structure that was obtained in the preparation of the Testwood lake experiments. Several early detections of the terrain step, that were shown to be vital in the comparison of the different detection timings (see Figure 5.31 with ca. 2 m and 1.8 m range), occur more accurately and at larger ranges than previously achieved.

Based on these results, the use of octomap and further processing of the data can now even further improve the terrain information, e.g. by fitting curves through the wider distributed points or dismissing the few remaining false detections due to their small number and distance to the rest of the terrain detection.

An path for further research would be the integration of both the detection ranges and the angle-independent detections from the terrain and the water surface in a shared probability map. Where existing mapping techniques are derived from techniques at the surface, assuming only one valid return exists, the complex sonar reflection behaviour

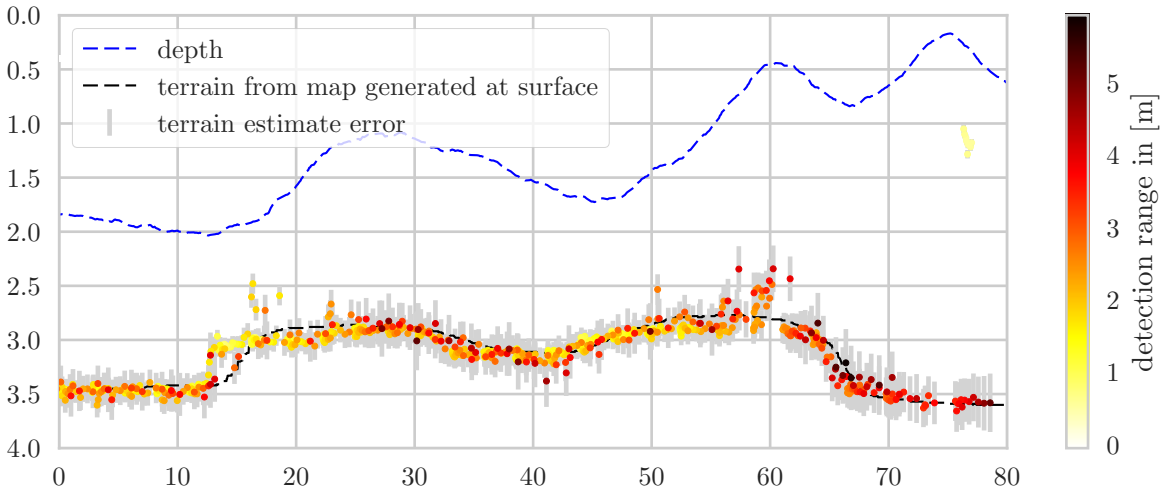

Figure 5.61: Global terrain map constructed from depth, pitch and sonar detection as well as an assumed constant x-velocity.

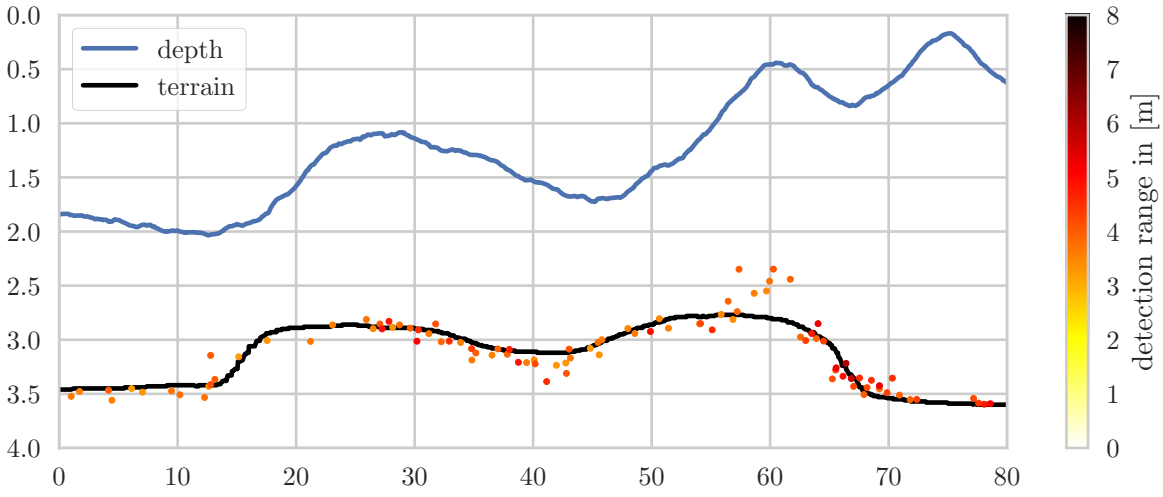

Figure 5.62: Comparison of surface map (black) with a mapping of the detections with a minimum range of 3 m, with the colour indicating the detection range.

could be used further to gain useful information from the data that is currently dismissed as noise.

Chapter 6

Conclusion and Future Work

The reported research determined that the altitude is a good proxy measure for the photographic survey success. The analysis of altitude tracking over complex terrain with flight style AUVs was performed in three analysis steps on vertical plane simulation data, Autosub6000 mission data, and Delphin2 lake experiments, followed by a development step focusing on the sonar analysis, which stood out as a detrimental factor for mission success, vehicle safety, and repeatability in the preceding analysis.

Four goals were pursued during the analysis: validating the altitude tracking systems model, particularly for control purposes, understanding which parameters are key for mission performance, identifying where further improvements will have the largest impact on the survey results, and establishing the suitability of a small test vehicle as a test platform for altitude tracking.

For quantitative comparison between different experiments and simulation data, the mission success and vehicle risk were used. On Delphin2, the propulsion method was varied, and the cost of transport was used quantify the impact of the actuation choice on the vehicle endurance, and consequently the cost of the photo survey.

It was shown that the delayed response of flight style vehicles to sternplane actions requires planning ahead over an order of magnitude of tens of metres. Several simulation methods for asserting the complexity and steepness of the terrain that can be surveyed by a flight style AUV were demonstrated and their limitations were discussed.

The detailed data analysis of Autosub6000 missions, the vertical plane flight style simulation, and the lake experiments with the Delphin2 vehicle all indicate that the challenge for improving the altitude tracking of flight style and hover capable vehicles is correctly recognising the terrain ahead. Improved terrain detection is also required to enable terrain tracking validation with small vehicles in shallow bodies of water; thus the further work was focused on the analysis of the acoustic forwards looking terrain detection.

This chapter links the conclusions of the work presented in this thesis with mission planning recommendations and suggestions for future development.

6.1 Photographic Mission Quantification

The introduced measures - mission risk and vehicle success - were established as valuable measures for quantifying photographic survey missions. Whilst full plots of missions will never be replaced by a single number, the mission success and vehicle risk were demonstrated as a valuable tool for comparing vehicle paths at a glance. When analysing Autosub6000 mission data, differences in altitude tracking success could easily be recognized from the vehicle depth plots with highlighted vehicle risk and mission success zones, despite the vertical exaggeration typical for such missions and even small risk zones were quickly identified and related to the terrain over which they occured. The numeric value was also used as a tool for the comparably large Delphin2 dataset from Testwood lake, to summarise the individual missions, before selecting individual experiments for visual and further more detailed examination, and extrapolating from the small scale experiments to full endurance missions based on the Cost Of Transport and available battery charge. The Delphin2 dataset demonstrates that the consideration of the battery capacity combined with the photo success gives a clearer picture, what can be expected from a vehicle deployment.

6.2 Autosub6000 Terrain Tracking Mission Analysis

The analysis of the data recorded with Autosub6000 goes hand in hand with the simulation of Autosub6000. The analysis of Autosub6000 data informed the simulation through providing vehicle surge estimates, detection range estimates and the vehicle state as validation data. The terrains reconstructed from missions M115 and M116, performed over the same terrain with no mission success (M115) and almost 100% mission success (M116), show a variation in the range of tens of centimetres, an inaccuracy of uncertain origin that needs to be considered during validation; conversely the simulation turned the attention of the mission data analysis towards the horizon detection as a cause for oscillation, which was then identified as the cause of the oscillation experienced during M114.
A recurring problem during Autosub6000 missions is reliable detection of the terrain. Whilst nominally the detection range is over 100 m, it was shown that this detection range is typically not achieved. Most altitude tracking missions have horizon detection range between 15 m and 45 m.

6.3 Autosub6000 Simulation

The vertical plane simulation was shown to be stable between 10 Hz and 20 Hz, with an upper limit introduced by the ROS software framework it is implemented with. The dynamic behaviour of the sternplane response simulation of Autosub1 matches existing

data. Considering the pitch limits of Autosub6000, the pitch error compared to the existing data is less than 15% and the depth error is below 6%. A steady state pitch study was performed to consider winglets that were added on Autosub6000 compared to Autosub1, the vehicle for which the model data was determined. Depending on the winglet correction, the steady state pitch angle for the 14.2 kg positively buoyant simulation at 1.6 m/s was shown to vary between $-1°$ and $-5.5°$.

The sternplane response study gives an impression of the manouvrability and response delay of the flight style vehicle. First estimates of the maximum terrain slope can be made based on the maximum ascend rate achieved with the extreme sternplane setpoint pattern. Next, a steep step response takes the altitude control loop into account in addition to the vehicle dynamics. This further limits the achieved ascend rate, and thus the step height that can safely be navigated. The variation in the control resonse when approaching the top of the terrain step also highlights that a single steep step is an oversimplification of the terrain, and in addition to criteria for assessing the vehicle performance, a better parametrization for the terrain, and a quantification of the terrain complexity are needed for a more detailed prediction of the performance of flight style AUVs over complex terrain. Turning from vehicle risk to mission success, the analysis of both the sternplane response and the small step response illustrate that a positively buoyant vehicle achieves better altitude tracking results when operating on an upward slope, since it can achieve faster ascend rates than descend rates. The two case studies also show that at a surge speed of 2 m/s the buoyancy has less impact on the vehicle manoeuvrability, and the overall manoeuvrability is better, even when comparing the vehicle path relative to the progress over terrain. The terrain step response study of the detection range and sonar scan angle offset shows several mechanisms through which an oscillation in the vehicle can be caused by inaccuracies in the sonar measurement or loss of detection. Based on these analysis results, the development of a better detection strategy and mapping was identified as a key goal for improving altitude tracking.

A comparison with M53, a mission where the obstacle avoidance system was not used, shows a close match between the vehicle and the simulated altitude, once the integral term for the depth controller is increased. This combined with a consistently ca. $4°$ larger pitch angle on the simulated vehicle indicated that an upward force on the simulated vehicle, most likely the buoyancy, is larger than during the actual mission.

The comparison of the simulation and mission data of M57, a mission using the obstacle avoidance system, again demonstrates the better mission performance on an upward slope, and the overestimate of forces towards the surface on the simulated vehicle. The observation that Autosub6000 was descending at its maximum pitch angle whilst no significant sternplane angle was recorded makes it likely that the vehicle buoyancy at depth was much closer to neutrally buoyant than the recorded positive buoyancy at the surface.

Whilst the vehicle recorded an average detection of 29 m, its performance was better matched to simulations with a lower detection range. It is therefore likely that the vehicle was underestimating the terrain ahead, e.g. due to an offset in the sonar head

position.

Overall, the simulation was successfully validated as a realistic simulation of altitude tracking, suitable for testing new altitude strategies, and identifying what needs to be further studied in experiment. However it was shown that the inability to accurately determine parameters such as the vehicle buoyancy, scanning sonar angle offsets, and detection range make the outcome of a specific experiment too unpredictable to simulate at this time.

6.4 Delphin2 as a Small Scale Test Platform

An analysis of the Reynolds number and Froude Number for the vehicle lenght and the Reynolds number for the sternplanes shows that Delphin2 operates in flow regime comparable to that of other flight style AUVs, so results from Delphin2 can be scaled and transferred to other vehicles. The Testwood experiments established that the experiments on Delphin2 are very repeatable and distinct between different vehicle configurations. As expected, the flight style behaviour of Delphin2 shows similar delayed effects as that of Autosub6000, and Delphin2 was demonstrated as a test platform for altitude tracking with a wide range of vehicles, both hover capable and flight style. The matching identification of sonar detection as the critical factor for photographic surveys both with Delphin2 and Autosub6000 further underpins the suitability of Delphin2 as a test platform for AUV photographic surveys. The experiments in a controlled environment have the added advantage that the terrain is well known, results can be compared, and the vehicle risk can be estimated more accurately than when relying on in-situ altitude tracking data only.

Using the forwards detection, the terrain step is on average detected from a distance of 3 m, however due to the sector scan time of the mechanical scanning sonar, this detection is varied by ± 1.4 m. Even though the terrain is underestimated at larger range, the earlier change in depth demand achieves significantly better altitude tracking results, with an error in the range of 0.2 m compared to 0.6 m for a detection at 1.5 m distance (tracking at 1 m altitude and 1 m/s surge). The detection range of 3 m scaled to Autosub6000 would be 8.3 m, this is less than half the minimum horizon detection range achieved on Autosub6000. To make Delphin2 more suited for testing altitude tracking behaviour of Autosub6000, an increase of the detection range is required.

The extrapolation of the photo survey success to a full battery charge showed that with the best detection performance the photographic survey success with obstacle avoidance (10.1 km) is doubled compared to the surveys using hover style actuation with obstacle avoidance (5.1 km). However, a variation of the detection threshold, and thus an increase in false detections, drastically reduces the outcome (3.4 km) below the results of hover capable actuation.

An analysis of the power consumption of the hover capable actuation verified that for

the positively buoyant Delphin2 the variation in power consumption is proportional to the altitude error, and thus a mission path with a positive slope, where the altitude error is mostly negative, will have a lower power consumption.

Experiments combining the two actuation methods at speed show that with the existing controller and limits in understanding the thruster forces at speed the thrusters hinder the vehicle manoeuvrability rather than improving it. Whilst hover capable actuation is a promising path for achieving a large area coverage whilst also being able to closely track steep steps in the terrain, the relationship between thruster force, surge velocity, and thruster position on the vehicle needs to be understood further.
Based on the Delphin2 experiments, keeping the different actuation modes separate and slowing down if the terrain complexity requires it was identified as the more promising path for further development. Thruster enhancement at flight style speeds may be possible with newer, less turbulent thruster technologies.

6.5 Key Mission Parameters

The buoyancy, surge velocity, sonar scan range and sonar scan angle offset were shown to be key mission parameters that need to be known when trying to simulate the altitude tracking behaviour of a flight style vehicle. Whilst the surge velocity is recorded well by the DVL, during Autosub6000 it was chosen very low compared to the vehicle's upper limit of 2 m/s. This increased the impact of the buoyancy on the pitch angle and overall manoeuvrability. Since the buoyancy is not known accurately enough, this is one of the main factors contributing to inaccuracies when modelling the vehicle dynamics.

The terrain slope is currently a mission parameter that is mostly out of the hands of the vehicle operators. The Autosub mission analysis, the simulation, the Delphin2 mission analysis clearly demonstrate that positively buoyant flight style vehicles perform worse, and that positively buoyant hover capable vehicles consume more energy on a downwards slope. Whilst the impact of some of these factors can be reduced, e.g. by reducing the conservative behaviours after achieving more reliable terrain detection, positively buoyant vehicles will always be at a disadvantage on a downwards slope.

Significant improvements can be achieved once this behaviour is recognised and considered in the mission plan. Figure 6.1 illustrated this on the example of a seamount. Small changes have been made to adapt the scan pattern to the terrain structure, increasing the proportion of the same length mission path that is spend on an upward slope and thus achieving almost 100% mission success for the area, whilst at the same time reducing the mission risk. Whilst the scientists using the recorded photos usually prefer a lawnmower pattern scan of an area, the example shows that with a lawnmower path of the vehicle no even coverage of the area is achieved, defeating the purpose of such a scan method. On the other hand the alternative path suggestion delivers a dense data grid, which could be re-sampled in post processing to only consider data that conforms

with a desired photo distribution.

To recognise an overall trend in the terrain slope over a several kilometre long vehicle path, a high resolution scan is not required, so even with the existing data better choices for the mission path can be made. Further improvement steps from here can aim to replace the human mission planner with an algorithm that optimises the waypoint placement, supervised by a vehicle operator before the vehicle launch. Finally the mission plan could even be developed as part of an adaptive mission, after an initial area scan at a higher altitude.

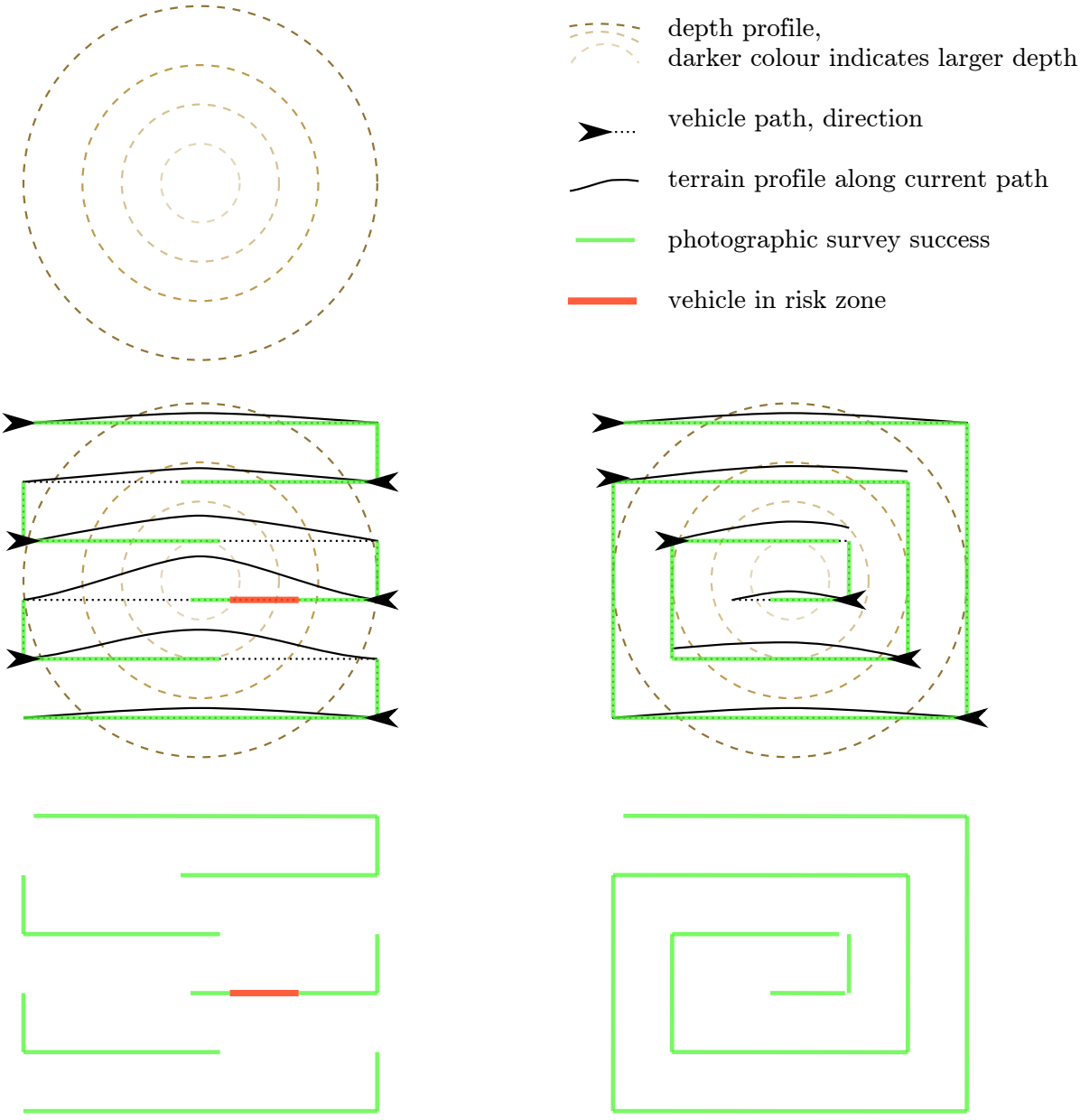

Figure 6.1: Considering low resolution terrain information can significantly improve photographic mission results whilst still maintaining a grid-like area coverage.

6.6 Altitude and Depth Control

Whilst the long delays between actuator action and vehicle response make the use of a more sophisticated controller very promising, even the best controller will not function successfully with a very unsteady control demand due to the terrain detection issues presented in this thesis. Before integrating the terrain tracking in the vertical plane control in the form of a variable depth limit, the problem of determining such a depth limit must first be solved.

The simulation validation using real Autosub6000 missions have clearly demonstrated that small parameter changes can have a significant impact on the vehicle behaviour. If a more advanced control, like Model Predictive Control, is to be applied successfully, these variations in system behaviour need to be reduced.

Reducing the variability, increasing the surge velocity, or finding methods for in-situ determination of these parameters can all contribute to limiting model uncertainty. However, many of these changes, like the depth based buoyancy change of the vehicle, are out of the control of the vehicle operator and can only be recognised through in-situ measurements on the vehicle. Others, like a sonar angle offset, may remain unnoticed or may even occur during the mission due to mechanical slips in the sensor or the sensor mount.

Future work on the in-situ sensing of a vehicle during the mission could include buoyancy change detection through analysis of a diving pattern close to the mission depth, or, as shown in the constant depth study and the statistical mission analysis, an analysis of the average pitch angle required to maintain a constant depth. The altimeter may be used to detect discrepancies between the measured altitude and the data recorded by the forwards looking sonar. Further vehicle developments could also include buoyancy engines to manipulate the vehicle model parameters, compensating for changes in buoyancy, or even adjusting the buoyancy of the vehicle for a downward- or upward slope.

6.7 Sonar Detection

With the analysis of Autosub6000 data, Autosub6000 simulation, and Delphin2 data all pointing towards the sonar detection as a key factor for obstacle avoidance, the continued work was focused on improving the sonar analysis. Methods for filtering false returns, particularly in shallow water, were introduced and demonstrated over Testwood data. A minimalistic predictive method for tracking an expected flat terrain was developed. Since the method mostly relies on mission configuration data, it only adds one tuning parameter compared to the existing thresholding method. Whilst a flat terrain assumption is made, terrain variations are detected well whilst false returns are dismissed. The range improvements were shown to double the detection range on the Testwood data from 3 m to over 6 m, making the shallow water experiment setup more

viable as a test platform.

A future development direction for mapping specificly with scanning sonars whilst moving in close proximity to terrain is suggested, using the information that is currently dismissed as noise. Evaluated in a probabilistic map, the consideration of angular symmetries, beam shapes, and known beam reflection paths within the vehicle could be used to generate a more detailed map of a complex environment, with less false detections.

The simulation results and analysis of the mechanical scanning sonar data acquisition show that a faster sonar detection would significantly improve the low altitude terrain tracking performance of flight style AUVs and reduce the variability of the mission outcome. The increased detection speed not only removes the delay in detecting a steep terrain step, it also reduces the unpredictability of the sonar scan timing and, as shown in the step studies, it can reduce or even fully remove the observed oscillations. Furthermore false detections will likely be easier to recognise and filter, and with better mapping capabilities misalignments of the sonar head can also be recognised and corrected easier.

Multibeam sonars provide a faster data acquisition, but the increase in detection speed comes at a cost, both literally and by introducing new limitations into the development process. Besides a significantly higher sensor cost, multibeam sonars have a higher energy consumption, thus increasing the cost of transport. The data post-processing is proprietary and thus not as accessible as on a mechanical scanning sonar. The higher amount of data acquired also means that often only a limited amount of the available data is logged, making an analysis after the end of the mission more difficult. Therefore mechanical scanning sonars are still expected to be widely used on altitude tracking vehicles, mostly for cost and energy efficiency purposes. New scanning methods may combine the horizon tracking method and the constant sector scan, to occasionally apply situation based changes to the scan sector, after a change in average pitch angle, altitude, or the horizon detection angle within the current scan sector.

With the noise based surface distance and altitude detection methods presented in this work, the mechanical scanning sonar has an extended application range as a cost and energy efficient multi-purpose sensor. There is still room for improvement in the terrain detection and further analysis of the collected data, particularly for faster moving vehicles. After profiling the reflection patterns of a sonar device in its mount position on the vehicles, the additional reflections may be used to enhance a probabilistic terrain map. Improvements and further work in this area will remain valuable to a large proportion of AUV users, and will also be applicable to the analysis of multibeam scan data.

References

Airfoiltools. URL http://airfoiltools.com/airfoil/details?airfoil=n0012-il.

26th ITTC Specialist Committee on Uncertainty Analysis. ITTC – Recommended Procedures ITTC – Recommended Procedures. *ITTC - Recommended Procedures*, 2011.

Derya Akkaynak, Tali Treibitz, Tom Shlesinger, Yossi Loya, Raz Tamir, and David Iluz. What is the Space of Attenuation Coefficients in Underwater Computer Vision? In *2017 IEEE Conference on Computer Vision and Pattern Recognition (CVPR)*, pages 568–577, Honolulu, HI, 2017. IEEE. ISBN 978-1-5386-0457-1. doi: 10.1109/CVPR.2017.68. URL http://ieeexplore.ieee.org/document/8099551/.

P G Allan. Cable Security in Sandwaves. 44(May):1–12, 2000.

R Bachmayer, N Ehrich Leonard, E Fiorellit, P Bhattat, and D Paleyf. Underwater Gliders : Recent Developments and Future Applications. *Proceedings of the 2004 International Symposium on Underwater Technology (IEEE Cat. No.04EX869)*, pages 195–200, 2003. doi: 10.1109/UT.2004.1405540.

Abhijit S Badwe, Ravindra D Gudi, Rohit S Patwardhan, Sirish L Shah, and Sachin C Patwardhan. Detection of model-plant mismatch in MPC applications q. *Journal of Process Control*, 19(8):1305–1313, 2009. ISSN 0959-1524. doi: 10.1016/j.jprocont.2009.04.007. URL http://dx.doi.org/10.1016/j.jprocont.2009.04.007.

Adrian Bodenmann, Blair Thornton, Ryota Nakajima, Hiroyuki Yamamoto, and Tamaki Ura. Wide Area 3D Seafloor Reconstruction and its Application to Sea Fauna Density Mapping. In *Proceedings of MTS/IEEE Oceans*, volume 13, 2013. ISBN 9780933957404.

Philip Bouxsein, Edgar An, Steven Schock, and P-P Beaujean. A SONAR simulation used to develop an obstacle avoidance system. In *OCEANS 2006-Asia Pacific*, pages 1–7. IEEE, 2007.

Mario Paulo Brito. Risk and reliability analysis of Autosub 6000, 2015.

Roy Burcher and Louis J Rydill. *Concepts in submarine design*, volume 2. Cambridge University Press, 1994.

Cesar Cadena, Luca Carlone, Henry Carrillo, Yasir Latif, Davide Scaramuzza, Jose Neira, Ian Reid, and John J. Leonard. Past, Present, and Future of Simultane-

ous Localization And Mapping: Towards the Robust-Perception Age. *IEEE Trans. Robotics*, 32(6):1309–1332, 2016. ISSN 1097-6256. doi: 10.1109/TRO.2016.2624754. URL http://arxiv.org/abs/1606.05830{%}0Ahttp://dx.doi.org/10.1109/TRO.2016.2624754.

C.V. Caldwell, D.D. Dunlap, and E.G. Collins. Motion planning for an autonomous Underwater Vehicle via Sampling Based Model Predictive Control. *Oceans 2010*, pages 1–6, 2010. doi: 10.1109/OCEANS.2010.5664470.

David W Caress, Hans Thomas, William J Kirkwood, Rob Mcewen, Richard Henthorn, David A Clague, Charles K Paull, Jenny Paduan, and Katherine L Maier. High-Resolution Multibeam, Sidescan, and Subbottom Surveys Using the MBARI AUV D. Allan B. *Marine Habitat Mapping Technology for Alaska*, pages 47–69, 2008. doi: 10.4027/mhmta.2008.04. URL http://seagrant.uaf.edu/bookstore/pubs/ak-sg-08-03/caress.html.

Jee Loong Chew and Mandar Chitre. Object Detection with Sector Scanning Sonar. In *2013 OCEANS - San Diego*, pages 1–8, San Diego, CA, 2013. IEEE. ISBN 9780933957404. doi: 10.23919/OCEANS.2013.6741056.

Brandon Cochenour, Linda Mullen, and John Muth. A modulated pulse laser for underwater detection, ranging, imaging, and communications. In *SPIE Defense, Security, and Sensing*, pages 83720S—-83720S. International Society for Optics and Photonics, 2012.

The Scipy Community. scipy.integrate.odeint, 2016. URL http://docs.scipy.org/doc/scipy-0.17.0/reference/generated/scipy.integrate.odeint.html.

Silvia Corchs and Raimondo Schettini. Underwater image processing: State of the art of restoration and image enhancement methods. *Eurasip Journal on Advances in Signal Processing*, 2010, 2010. ISSN 16876172. doi: 10.1155/2010/746052.

R J Cyr. Terrain obstacle avoidance sonar for autonomous vehicles. In *OCEANS 87 Proceedings: The Ocean - An International Workplace (Cat. No.87CH2498-4)*, pages 134–8 vol.1. IEEE; Marine Technol. Soc, 1987.

Matthew Dunbabin, Jonathan Roberts, Kane Usher, Graeme Winstanley, and Peter Corke. A hybrid AUV design for shallow water reef navigation. In *Proceedings - IEEE International Conference on Robotics and Automation*, pages 2105–2110, Barcelona, Spain, 2005. ISBN 078038914X. doi: 10.1109/ROBOT.2005.1570424. URL http://ieeexplore.ieee.org/document/6106913/.

Jennifer M. Durden, Brian J. Bett, Daniel O.B. Jones, Veerle A.I. Huvenne, and Henry A. Ruhl. Abyssal hills - hidden source of increased habitat heterogeneity, benthic megafaunal biomass and diversity in the deep sea. *Progress in Oceanography*, 137:209–218, 2015a. ISSN 00796611. doi: 10.1016/j.pocean.2015.06.006. URL http://dx.doi.org/10.1016/j.pocean.2015.06.006.

Jennifer M Durden, Brian J Bett, and Henry A Ruhl. Deep-Sea Research I The hemisessile lifestyle and feeding strategies of Iosactis vagabunda (Actiniaria , Iosactiidae), a dominant megafaunal species of the Porcupine Abyssal Plain. *Deep-Sea Research Part I*, 102:72–77, 2015b. ISSN 0967-0637. doi: 10.1016/j.dsr.2015.04.010. URL `http://dx.doi.org/10.1016/j.dsr.2015.04.010`.

Tou Hong Eng and Mandar Chitre. Minimum Speed Seeking Control for Nonhovering Autonomous Underwater Vehicles. *J. Field Robotics*, 33(5):706–733, 2015. ISSN 14746670. doi: 10.1002/rob.

Øystein Engelhardtsen. 3D AUV Collision Avoidance. (June):1–108, 2007.

Clark C Evans. The Official YAML Web Site, 2016. URL `http://www.yaml.org/`.

O. M. Faltinsen. *Sea Loads on Ships and Offshore Structures*. Cambridge University Press, Cambridge, 1999. ISBN 0 521 45870 6 paperback.

Thor I Fossen. *Marine Craft Hydrodynamics and Motion Control*. John Wiley & Sons, Chichester, 2011. ISBN 9781119991496.

Scott D. Foster, Geoffrey R. Hosack, Nicole A. Hill, Neville S. Barrett, and Vanessa L. Lucieer. Choosing between strategies for designing surveys: Autonomous underwater vehicles. *Methods in Ecology and Evolution*, 5(3):287–297, 2014. ISSN 2041210X. doi: 10.1111/2041-210X.12156.

Maaten E Furlong, Stephen D McPhail, and Miles Pebody. A New Collision Avoidance System for the Autosub6000 Autonomous Underwater Vehicle. In *Proceedings of the International Symposium on Unmanned Untethered Submersible Technology*, Durham, New Hampshire, 2009. Autonomous Undersea Systems Institute (AUSI).

Maaten E Furlong, Dave Paxton, Peter Stevenson, Miles Pebody, Stephen D McPhail, and James Perrett. Autosub Long Range: A long range deep diving AUV for ocean monitoring. In *Autonomous Underwater Vehicles (AUV), 2012 IEEE/OES*, pages 1–7. IEEE, 2012. ISBN 9781457720567. doi: 10.1109/AUV.2012.6380737.

Morton Gertler and Grant R Hagen. Standard Equations of Motion for Submarine Simulation. Technical report, Naval Ship Research and Deverlopment Center, 1967.

A G Glover, A J Gooday, D M Bailey, D S M Billett, P Chevaldonné, Ana Colaco, J Copley, Daphne Cuvelier, Daniel Desbruyeres, V Kalogeropoulou, and Others. Temporal change in deep-sea benthic ecosystems: a review of the evidence from recent time-series studies. *Advances in marine biology*, 58:1–95, 2010.

Yeqiang Han, Xiang Tian, Fan Zhou, Rongxin Jiang, and Yaowu Chen. A Real-Time 3-D Underwater Acoustical Imaging System. *Oceanic Engineering, IEEE Journal of*, 39(4):620–629, oct 2014.

Armin Hornung, Kai M. Wurm, Maren Bennewitz, Cyrill Stachniss, and Wolfram Burgard. OctoMap: An efficient probabilistic 3D mapping framework based on oc-

trees. *Autonomous Robots*, 34(3):189–206, 2013. ISSN 09295593. doi: 10.1007/s10514-012-9321-0.

Sarah E Houts and Stephen M Rock. Trajectory planning for motion-constrained AUVs in uncertain environments. *2014 Oceans - St. John's, OCEANS 2014*, 2015. ISSN 0197-7385. doi: 10.1109/OCEANS.2014.7003140.

Sarah E Houts, Stephen M Rock, and Rob McEwen. Aggressive terrain following for motion-constrained auvs. In *Autonomous Underwater Vehicles (AUV), 2012 IEEE/OES*, pages 1–7. IEEE, 2012. ISBN 9781457720567. doi: 10.1109/AUV.2012.6380749.

K L Howell, M Taylor, K Crombie, S Faithfull, N Golding, W A Nimmo-Smith, J Perrett, N Piechaud, R E Ross, N Stashchuk, D Turner, V Vlasenko, and N L Foster. RRS James Cook, Cruise No. JC136, 14th May – 23rd June, DEEPLINKS: Influence of population connectivity on depth-dependent diversity of deep-sea marine benthic biota., 2016.

Huachuan Huang, Rongbo Wang, Keding Yan, Zhengang Yan, Shouyu Wang, Zhenhua Li, and Zeren Li. High quality underwater imaging platform with laser range gated technique combining with image denoising and restoration. In *SPIE/COS Photonics Asia*, pages 92732D———92732D. International Society for Optics and Photonics, 2014.

Timothy Hughes, Timothy Henstock, James Pilgrim, Justin Dix, Thomas Gernon, and Charlotte Thompson. Effect of Sediment Properties on the Thermal Performance of Submarine HV Cables. 2014.

Inter IKEA Systems B.V. HYLLIS Shelving unit. URL `https://www.ikea.com/gb/en/products/storage-furniture/outdoor-organising/hyllis-shelving-unit-in-outdoor-art-00278578/`.

J S Jaffe. Computer modeling and the design of optimal underwater imaging systems. *Oceanic Engineering, IEEE Journal of*, 15(2):101–111, 1990. ISSN 03649059. doi: 10.1109/48.50695.

N I Kimber and W B Marshfield. Design and Testing of Control Surfaces for the Autosub Demonstrator Test Vehicle. Technical report, Institute of Oceanographic Sciences, Deacon Laboratory, Wormley, Surrey, UK, 1993.

Hayato Kondo and Tamaki Ura. Navigation of an AUV for investigation of underwater structures. *Control engineering practice*, 12(12):1551–1559, 2004.

W H Kwon, A M Bruckstein, and T Kailath. Stabilizing state-feedback design via the moving horizon method, 1983.

Alan Laux, Linda Mullen, Paul Perez, and Eleonora Zege. Underwater laser range finder. In *SPIE Defense, Security, and Sensing*, pages 83721B—-83721B. International Society for Optics and Photonics, 2012.

R. K. Lea, R. Allen, and S. L. Merry. A comparative study of control techniques for an underwater flight vehicle. *International Journal of Systems Science*, 30(9): 947–964, 1999. ISSN 0020-7721. doi: 10.1080/002077299291831. URL `http://www.tandfonline.com/doi/abs/10.1080/002077299291831`.

S D Ling, I Mahon, M P Marzloff, O Pizarro, C R Johnson, and S B Williams. Stereo-imaging AUV detects trends in sea urchin abundance on deep overgrazed reefs. *Limnology and Oceanography: Methods*, 14(5):293–304, 2016. ISSN 15415856. doi: 10.1002/lom3.10089. URL `http://doi.wiley.com/10.1002/lom3.10089`.

Tritech International Ltd. Software Notes for controlling and operating RS-232 Sonar * Heads. (August 2003):1–33, 2004.

Andreas Marouchos, Brett Muir, Russ Babcock, and Matthew Dunbabin. A shallow water AUV for benthic and water column observations. In *MTS/IEEE OCEANS 2015 - Genova: Discovering Sustainable Ocean Energy for a New World*, pages 1–7, Genoa, 2015. ISBN 9781479987368. doi: 10.1109/OCEANS-Genova.2015.7271362.

MathWorks. Matlab: Robot Operating System (ROS), 2016. URL `http://uk.mathworks.com/help/robotics/robot-operating-system-ros.html`.

O Matsebe, C Kumile, and N Tlale. A review of virtual simulators for autonomous underwater vehicles (auvs). *NGCUV, Killaloe, Ireland*, 2008.

Wes McKinney. Data Structures for Statistical Computing in Python. In Stéfan van der Walt and Jarrod Millman, editors, *Proceedings of the 9th Python in Science Conference*, pages 51–56, Austin, Texas, 2010. ISBN 0440877763224. URL `http://conference.scipy.org/proceedings/scipy2010/mckinney.html`.

S D McPhail, M Furlong, and M Pebody. Low-altitude terrain following and collision avoidance in a flight-class autonomous underwater vehicle. *Proceedings of the Institution of Mechanical Engineers, Part M: Journal of Engineering for the Maritime Environment*, 224(4):279–292, 2010a. URL `http://eprints.soton.ac.uk/169447/`.

Stephen D McPhail. Autosub6000: A Deep Diving Long Range AUV. *Journal of Bionic Engineering*, 6(1):55–62, mar 2009a. ISSN 1672-6529. doi: 10.1016/S1672-6529(08)60095-5.

Stephen D McPhail. Autosub6000: A Deep Diving Long Range AUV. *Journal of Bionic Engineering*, 6(1):55–62, mar 2009b. ISSN 1672-6529. doi: 10.1016/S1672-6529(08)60095-5.

Stephen D McPhail. RSS Discovery Cruise 343: Deepwater trials of the Autosub6000 AUV, HyBIS, and telemetry systems, 2010.

Stephen D McPhail and Miles Pebody. Navigation and control of an autonomous underwater vehicle using a distributed, networked, control architecture. *Underwater Technology*, 23(1):19–30, 1998. ISSN 0141-0814. doi: 10.3723/175605498783259975.

Stephen D McPhail, Maaten Furlong, Veerle Huvenne, and Peter Stevenson. Autosub6000: results of its engineering trials and first science missions. In *Proceedings UUVS 2008*, page [9p]. Reed Publishing, 2008. URL `http://eprints.soton.ac.uk/65904/`.

Stephen D McPhail, Maaten E Furlong, M Pebody, J R Perrett, P Stevenson, A. Webb, and D. White. Exploring beneath the PIG Ice Shelf with the Autosub3 AUV. *OCEANS '09 IEEE Bremen: Balancing Technology with Future Needs*, (January): 1–8, 2009. doi: 10.1109/OCEANSE.2009.5278170.

Stephen D McPhail, Peter Stevenson, Miles Pebody, Maaten Furlong, James Perrett, and Tim Lebas. Challenges of using an AUV to find and map hydrothermal vent sites in deep and rugged terrains. In *Autonomous Underwater Vehicles (AUV), 2010 IEEE/OES*, pages 1–8. IEEE, 2010b. ISBN 9781612849812. doi: 10.1109/AUV.2010.5779656.

Lashika Medagoda and Stefan B. Williams. Model predictive control of an autonomous underwater vehicle in an in situ estimated water current profile. *Program Book - OCEANS 2012 MTS/IEEE Yeosu: The Living Ocean and Coast - Diversity of Resources and Sustainable Activities*, 2012. doi: 10.1109/OCEANS-Yeosu.2012.6263604.

Anthony F Molland and Stephen R Turnock. *Marine rudders and control surfaces: principles, data, design and applications*. Elsevier, 2011.

Kirsty J Morris, Brian J Bett, Jennifer M Durden, Veerle A I Huvenne, Rosanna Milligan, Daniel O B Jones, Stephen McPhail, Katleen Robert, David M Bailey, and Henry A Ruhl. A new method for ecological surveying of the abyss using autonomous underwater vehicle photography. *Limnology and Oceanography: Methods*, 12:795–809, 2014. ISSN 1541-5856. doi: 10.4319/lom.2014.12.795.

Alan J Murphy and Maryam Haroutunian. USING BIO-INSPIRATION TO IMPROVE CAPABILITIES OF The current Status of AUV Technology The research challenge. In *17th International Unmanned Untethered Submersible Technology Conference*, number 17, pages 20–31, 2011.

W Naeem, R Sutton, J Chudley, F R Dalgleish, and S Tetlow. An online genetic algorithm based model predictive control autopilot design with experimental verification. *International Journal of Control*, 78(14):1076–1090, 2005. ISSN 0020-7179. doi: Doi10.1080/00207170500228483.

Ryota Nakajima, Hiroyuki Yamamoto, Shinsuke Kawagucci, Yutaro Takaya, Tatsuo Nozaki, Chong Chen, Katsunori Fujikura, Tetsuya Miwa, and Ken Takai. Post-Drilling Changes in Seabed Landscape and Megabenthos in a Deep-Sea Hydrothermal System, the Iheya North Field, Okinawa Trough. *PLoS ONE*, 10(4), 2015. ISSN 19326203. doi: 10.1371/journal.pone.0123095.

NASA. Mars Trek. URL `https://mars.nasa.gov/maps/explore-mars-map/`.

Y Nishida, T Ura, T Sakamaki, J Kojima, Y Ito, and Kangsoo Kim. Hovering type "Tuna-Sand" and its surveys on Smith caldera in Izu-Ogasawara ocean area. In *Oceans - San Diego, 2013*, pages 1–5, sep 2013.

Y Nishida, K Nagahashi, T Sato, A Bodenmann, B Thornton, A Asada, and T Ura. Development of an autonomous underwater vehicle for survey of cobalt-rich manganese crust. In *OCEANS 2015 - MTS/IEEE Washington*, pages 0–4, Washington, DC, 2015. ISBN 9780933957435. doi: 10.23919/OCEANS.2015.7404606. URL `http://ieeexplore.ieee.org/stamp/stamp.jsp?tp={&}arnumber=7404606{&}isnumber=7401802`.

Yuya Nishida, Ura Tamaki, Tomonori Hamatsu, Kenji Nagahashi, Shogo Inaba, and Takeshi Nakatani. Investigation method for the biomass of kichiji rockfish by hovering type AUV. In *OCEANS 2014 - TAIPEI*, pages 1–4, Taipei, apr 2014a. ISBN 9781479936465. doi: 10.1109/OCEANS-TAIPEI.2014.6964503.

Yuya Nishida, Tamaki Ura, Tomonori Hamatsu, Kenji Nagahashi, Shogo Inaba, and Takeshi Nakatani. Resource investigation for Kichiji rockfish by autonomous underwater vehicle in Kitami-Yamato bank off Northern Japan. *ROBOMECH Journal*, 1(1):1–6, 2014b. ISSN 2197-4225. doi: 10.1186/s40648-014-0002-y. URL `http://www.robomechjournal.com/content/1/1/2{%}5CnFile://localhost/Users/jescartin/WORK/Referencias/pdfs/Nishida2014.pdf`.

NOAA. U.S. Bathymetric and Fishing Maps. URL `https://maps.ngdc.noaa.gov/viewers/fishmaps/`.

OpenStreetMap. OpenStreetMap. URL `https://www.openstreetmap.org`.

Yuto Otsuki, Blair Thornton, Toshihiro Maki, Yuya Nishida, Adrian Bodenmann, and Kazunori Nagano. Real-time Autonomous Multi Resolution Visual Surveys Based on Seafloor Scene Complexity. In *2016 IEEE/OES Autonomous Underwater Vehicles (AUV)*, pages 330–335, Tokyo, 2016. ISBN 9781509057160. doi: 10.1109/AUV.2016.7778692.

Gwyneth E. Packard, Roger Stokey, Reed Christenson, Frederic Jaffre, Mike Purcell, and Robin Littlefield. Hull inspection and confined area search capabilities of REMUS autonomous underwater vehicle. In *MTS/IEEE Seattle, OCEANS 2010*, pages 1–4, Seattle, WA, 2010. ISBN 9781424443321. doi: 10.1109/OCEANS.2010.5664593. URL `http://ieeexplore.ieee.org/stamp/stamp.jsp?tp={&}arnumber=5664593{&}isnumber=5663781`.

Alistair Palmer, Grant E Hearn, and Peter Stevenson. Experimental Testing of an Autonomous Underwater Vehicle with Tunnel Thrusters. In Kourosh Koushan and Sverre Steen, editors, *First International Symposium on Marine Propulsion*, pages 569–575, Trondheim, Norway, 2009. MARINTEK (Norwegian Marine Technology Research Institute).

M Pebody. Autonomous underwater vehicle collision avoidance for under-ice explo-

ration. *Proceedings of the Institution of Mechanical Engineers, Part M: Journal of Engineering for the Maritime Environment*, 222(2):53–66, 2008.

A B Phillips, L V Steenson, E Rogers, S R Turnock, C Harris, M Furlong, T H E Transactions, O F The, and O F Naval. Delphin2: An over actuated autonomous underwater vehicle for manoeuvring research, 2013. ISSN 17400716.

Mario Prats, Javier Pérez, J Javier Fernández, and Pedro J Sanz. An open source tool for simulation and supervision of underwater intervention missions. In *Intelligent Robots and Systems (IROS), 2012 IEEE/RSJ International Conference on*, pages 2577–2582. IEEE, 2012.

Isabelle Quidu, H Alain, Yann Dupas, and S Lefevre. AUV (REDERMOR) obstacle detection and avoidance experimental evaluation. In *OCEANS 2007-Europe*, pages 1–6. IEEE, 2007.

Morgan Quigley, Ken Conley, Brian Gerkey, Josh Faust, Tully Foote, Jeremy Leibs, Rob Wheeler, and Andrew Y Ng. ROS: an open-source Robot Operating System. *ICRA workshop on open source software*, 3(3.2):5, 2009.

J Urick Robert. *Principles of Underwater Sound for Engineers*. McGraw-Hill Book Company, New York, 1967.

Henry A Ruhl. RRS Discovery Cruise 377 & 378: Autonomous ecological surveying of the abyss: understanding mesoscale spatial heterogenety at the Porcupine Abyssal Plain. Technical report, Southampton, 2013. URL `http://eprints.soton.ac.uk/350696/`.

Sophia M Schillai, Stephen R Turnock, Eric Rogers, Alexander B Phillips, and Catherine A Harris. Evaluation of Terrain Collision Risks for Flight Style Autonomous Underwater Vehicles. In *IEEE/OES Autonomous Underwater Vehicles (AUV)*, pages 311–318, Tokyo, 2016. ISBN 9781509024421. doi: 10.1109/AUV.2016.7778689. URL `http://eprints.soton.ac.uk/400679/`.

Hanumant Singh, Roy Armstrong, Fernando Gilbes, Ryan Eustice, Chris Roman, Oscar Pizarro, and Juan Torres. Imaging Coral I: Imaging Coral Habitats with the SeaBED AUV. *Subsurface Sensing Technologies and Applications*, 5(1):25–42, 2004a. ISSN 1566-0184. doi: 10.1023/B:SSTA.0000018445.25977.f3. URL `http://deepblue.lib.umich.edu/handle/2027.42/86034`.

Hanumant Singh, Ali Can, Ryan Eustice, Steve Lerner, Neil McPhee, Oscar Pizarro, and Chris Roman. Seabed AUV Offers New Platform for High-Resolution Imaging. *Eos, Transactions American Geophysical Union*, 85(31):160, 2004b. ISSN 1098-6596. doi: 10.1017/CBO9781107415324.004.

Dan A Smale, Gary A Kendrick, Euan S Harvey, Timothy J Langlois, Renae K Hovey, Kimberly P Van Niel, Kris I Waddington, Lynda M Bellchambers, Matthew B Pember, Russ C Babcock, Mathew A Vanderklift, Damian P Thomson, Michael V Jakuba, Oscar Pizarro, and Stefan B Williams. Regional-scale benthic monitoring for ecosystem-

based fisheries management (EBFM) using an autonomous underwater vehicle (AUV). *ICES Journal of Marine Science*, 69:1108–1118, 2012.

L V Steenson, S R Turnock, A B Phillips, C Harris, M E Furlong, E Rogers, L Wang, K Bodles, and D W Evans. Model predictive control of a hybrid autonomous underwater vehicle with experimental verification. *Proceedings of the Institution of Mechanical Engineers, Part M: Journal of Engineering for the Maritime Environment*, 228(2): 166–179, 2014. ISSN 1475-0902. doi: 10.1177/1475090213506185.

Leo Vincent Steenson, Alexander B Phillips, Maaten E Furlong, Eric Rogers, and Stephen R Turnock. The performance of vertical tunnel thrusters on an autonomous underwater vehicle operating near the free surface in waves. In Moustafa Abdel-Maksoud, editor, *Second International Symposium on Marine Propulsors*, number June, pages 499–507, Hamburg, 2011. Institute for Fluid Dynamics and Ship Theory (FDS) - Hamburg University of Technology (TUHH), German Society for Maritime Technology (STG). URL `http://eprints.ecs.soton.ac.uk/22165/`.

Kantapon Tanakitkorn, Philip A Wilson, Stephen R Turnock, and Alexander B Phillips. Depth Control for an Over-Actuated , Hover-Capable Autonomous Underwater Vehicle with Experimental Verification. *Mechatronics*, 41:67–81, 2016.

Kantapon Tanakitkorn, Philip A Wilson, Stephen R Turnock, and Alexander B Phillips. Sliding Mode Heading Control of an Over-Actuated , Hover-Capable Autonomous Underwater Vehicle with Experimental Verification. *Journal of Field Robotics*, 35(3): 396–415, 2017. doi: 10.1002/rob.21766. URL `https://onlinelibrary.wiley.com/doi/abs/10.1002/rob.21766`.

Blair Thornton. Presentation slides on "Systemizing deep-sea exploration", FEE, University of Southampton, may 2015.

Blair Thornton, Tamaki Ura, Yoshiaki Nose, and Stepehen Turnock. Zero-G class underwater robots: Unrestricted attitude control using control moment gyros. *IEEE Journal of Oceanic Engineering*, 32(3):565–583, 2007. ISSN 03649059. doi: 10.1109/JOE.2007.899274.

N Tolimieri, M E Clarke, H Singh, and C Goldfinger. Evaluating the SeaBED AUV for Monitoring Groundfish in Untrawlable Habitat. *Marine Habitat Mapping Technology for Alaska*, pages 129–142, 2008. doi: 10.4027/mhmta.2008.09. URL `http://www.alaskaseagrant.org/bookstore/pubs/AK-SG-08-03.html`.

Thomas Tosik and Erik Maehle. MARS: A simulation environment for marine robotics. In *Oceans-St. John's, 2014*, pages 1–7. IEEE, 2014.

Thomas Tosik and Erik Maehle. MARS: A simulation environment for marine robotics. *2014 Oceans - St. John's, OCEANS 2014*, pages 0–6, 2015. doi: 10.1109/OCEANS.2014.7003008.

Tritech International Ltd. Micron Echosounder Ultra Compact Under-

water Altimeter. URL http://www.tritech.co.uk/media/products/tritech-micron-echo-sounder-ultra-compact-altimeter.pdf.

Stéfan van der Walt, Johannes L Schönberger, Juan Nunez-Iglesias, François Boulogne, Joshua D Warner, Neil Yager, Emmanuelle Gouillart, Tony Yu, and The scikit-image contributors. scikit-image: image processing in {P}ython. *PeerJ*, 2:e453, 2014. ISSN 2167-8359. doi: 10.7717/peerj.453. URL http://dx.doi.org/10.7717/peerj.453.

Ashley D Waite. *Sonar for practising engineers*. Wiley London, third edition, 2005.

Steven Weinberg. A comparison of coral reef survey methods. *Bijdragen tot de Dierkunde*, 51(2):199–218, 1981. ISSN 0067-8546. URL http://apps.isiknowledge.com.libproxy1.nus.edu.sg/full{_}record.do?product=WOS{&}search{_}mode=GeneralSearch{&}qid=2{&}SID=3AJLhmcb7P64ik1DIAN{&}page=2{&}doc=16{#}output{_}options.

S B Williams, Oscar R Pizarro, Ian Mahon, and Matthew Johnson-Roberson. Simultaneous localisation and mapping and dense stereoscopic seafloor reconstruction using an AUV. *Experimental robotics*, pages 407–416, 2009a. ISSN 1610-7438. doi: 10.1007/978-3-540-73958-6_2.

Stefan B Williams, Oscar Pizarro, Martin Howy, Duncan Mercer, George Powell, Justin Marshally, and Roger Hanlon. Surveying noctural cuttlefish camouflage behaviour using an AUV. In *Proceedings - IEEE International Conference on Robotics and Automation*, pages 214–219, Kobe, Japan, 2009b. IEEE. ISBN 9781424427895. doi: 10.1109/ROBOT.2009.5152868.

Stefan B Williams, Oscar Pizarro, Michael Jakuba, and Neville Barrett. *AUV benthic habitat mapping in south eastern Tasmania*, volume 62 of *Springer Tracts in Advanced Robotics*. Springer, Berlin, Heidelberg, 2010a. ISBN 978-3-642-13407-4. doi: 10.1007/978-3-642-13408-1_25.

Stefan B. Williams, Oscar Pizarro, Michael V. Jakuba, Ian Mahon, Scott D. Ling, and Craig R. Johnson. Repeated AUV surveying of urchin barrens in north eastern Tasmania. *Proceedings - IEEE International Conference on Robotics and Automation*, pages 293–299, 2010b. ISSN 10504729. doi: 10.1109/ROBOT.2010.5509604.

Stefan B Williams, Oscar R Pizarro, Michael V Jakuba, Craig R Johnson, Neville S Barrett, Russel C Babcock, Gary A Kendrick, Peter D Steinberg, Andrew J Heyward, Peter J Doherty, Ian Mahon, Matthew Johnson-Roberson, Daniel Steinberg, and Ariell Friedman. Monitoring of Benthic Reference Sites: Using an Autonomous Underwater Vehicle. *Robotics and Automation Magazine, IEEE*, 19 (1):73 – 84, 2012. ISSN 1070-9932. doi: 10.1109/MRA.2011.2181772. URL http://ieeexplore.ieee.org.ezproxy2.library.usyd.edu.au/ielx5/100/6173573/06174326.pdf?tp={&}arnumber=6174326{&}isnumber=6173573{%}5Cnhttp://ieeexplore.ieee.org.ezproxy2.library.usyd.edu.au/stamp/stamp.jsp?tp={&}arnumber=6174326{&}tag=1.

Margaret F J Wilson, Brian O'Connell, Colin Brown, Janine C Guinan, and Anthony J Grehan. Multiscale terrain analysis of multibeam bathymetry data for habitat mapping on the continental slope. *Marine Geodesy*, 30(1-2):3–35, 2007. ISSN 0149-0419. doi: 10.1080/01490410701295962.

M Woolsey, V L Asper, A-R Diercks, and K McLetchie. Enhancing NIUST ' s SeaBED Class AUV , Mola Mola. In *2010 IEEE/OES Autonomous Underwater Vehicles*, pages 1–5, Monterey, CA, USA, 2010. IEEE. doi: 10.1109/AUV.2010.5779667.

Russell B Wynn, Veerle A I Huvenne, Timothy P Le Bas, Bramley J Murton, Douglas P Connelly, Brian J Bett, Henry A Ruhl, Kirsty J Morris, Jeffrey Peakall, Daniel R Parsons, Esther J Sumner, Stephen E Darby, Robert M Dorrell, and James E Hunt. Autonomous Underwater Vehicles (AUVs): their past, present and future contributions to the advancement of marine geoscience. *Marine Geology*, 352:451–468, 2014. ISSN 00253227. doi: 10.1016/j.margeo.2014.03.012. URL `http://dx.doi.org/10.1016/j.margeo.2014.03.012`.

Mingxi Zhou, Ralf Bachmayer, and Brad Deyoung. Mapping for control in an underwater environment using a dynamic inverse-sonar model. In *OCEANS 2016 MTS/IEEE Monterey, OCE 2016*, 2016. ISBN 9781509015375. doi: 10.1109/OCEANS.2016.7761190.

Appendix A

Heading Error Impact on Terrain Detection

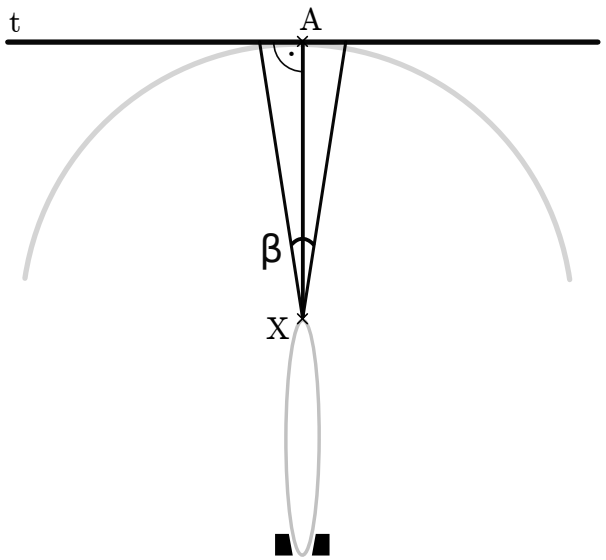

Figure A.1: Ideal detection of a terrain step t at a distance $\overline{XA}$ (top view).

The vertical plane simplification assumes that the edge of a terrain step t is orthogonal to the direction of movement, or that the horizontal opening angle β of the scanning sonar is negligibly small (see Figure A.1). In reality, the opening angle of the scanning sonar on Delphin2 and Autosub6000 is significant, and terrain steps are not always perfectly aligned with the vehicle path. On the one hand, this can make the detection of an obstacle less clear. It can also reduce the estimated distance to the terrain, if the terrain is closer to the vehicle at a position irrelevant for terrain tracking, but within the opening angle of the sonar beam. In case of repeated experiments over a terrain step, the repeatability of an experiment will be reduced through heading inaccuracy. This section analyses the scale of the step distance underestimate that can be caused by a

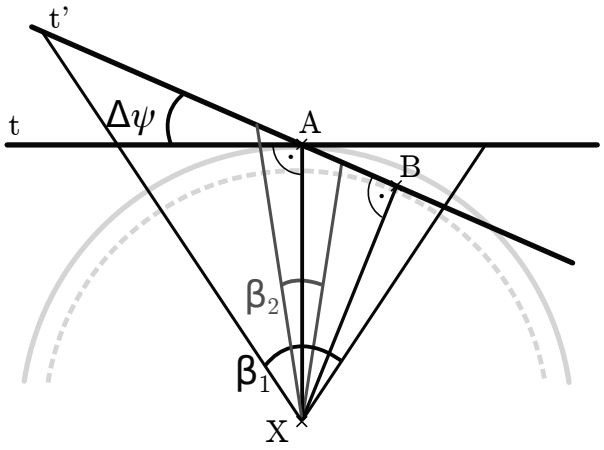

Figure A.2: Impact of heading error and beam width variation on terrani detection.

heading error.

Figure A.2 shows the detection of a terrain step at position t without heading error, and how the same terrain step appears at position t' when it is approached with a heading error of $\Delta\Psi$. The dashed circle shows the smallest distance between t' and the vehicle position X. This is the shortest distance at which the terrain step could be detected. This error in detection range can be reduced if the opening angle of the mechanical scanning sonar is so small that the position B of the minium detection range is outside of the sonar beam. The effect of the sonar beam opening angle is illustrated in Figure A.2 with the two opening angles β_1 and β_2: a scanning sonar with opening angle β_1 will detect t' at the distance $\overline{XA}$, whilst for the smaller opening angle β_2 the step distance error will be reduced.

Thus, the distance $\overline{XB}$ is used as an upper limit for the detection range error. Since t' is the tangent of a circle, the triangle XAB is rectangular (see Figure A.3). Angle identities and right angles show that the angle of the triangle at x is equal the heading error $\Delta\psi$. The upper limit estimate of the terrain detection error $\overline{XA}-\overline{XB}$ can therefore be derrived as:

$$\begin{aligned} \cos(\Delta\psi) &= \frac{\overline{XB}}{\overline{XA}} \\ \overline{XB} &= \overline{XA} \cdot \cos(\Delta\psi) \\ \overline{XA} - \overline{XB} &= \overline{XA}\,(1 - \cos(\Delta\psi)) \end{aligned} \tag{A.1}$$

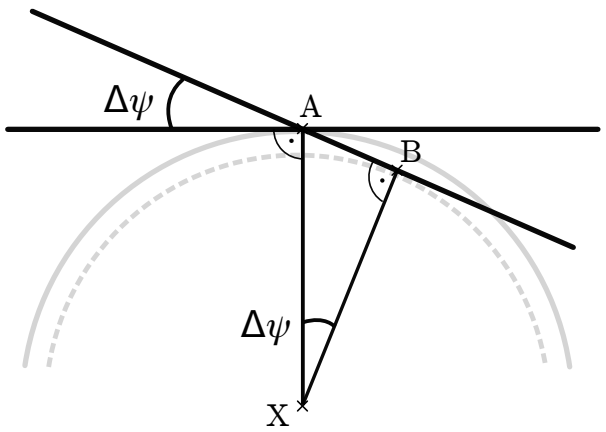

Figure A.3: Upper limit estimate of the terrain step detection error.

Appendix B

Roll Error Impact on Terrain Detection

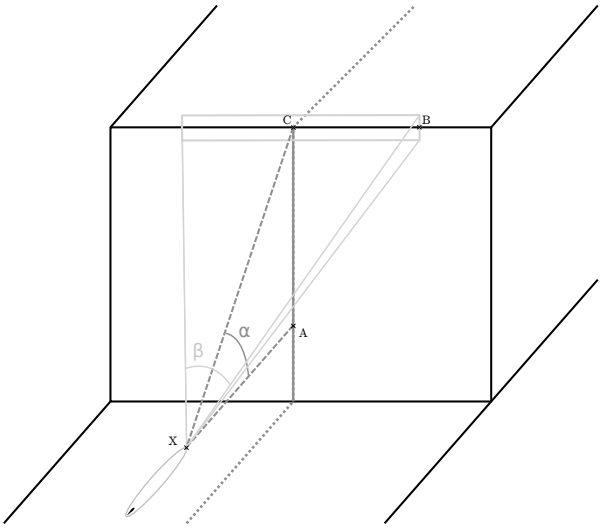

Figure B.1: Simplified terrain detection with no roll error.

In the ideal case of zero roll, the sonar scan direction is parallel to the z-Axis, and the sonar beam hits the terrain ahead completely horizontally. All areas of the beam represent the same terrain height (see Figure B.1.
However, if the vehicle has a roll angle $\phi \neq 0$ (see Figure B.2, the sonar scan axis rotates with the vehicle and two effects increase the value of the largest scan angle that detects the terrain: The horizontal beam opening is no longer orthogonal to the vertical plane, and the sonar scan direction is no longer parallel to the z-Axis. When the horizontal beam is no longer orthogonal to the vertical plane, its lowest point actually represents a lower terrain height than is assumed. With the scan direction no longer parallel to the z-Axis, the scan direction represents a longer distance than the terrain height. As a result, the terrain height is overestimated from the increased sonar scan angle $\alpha*$.

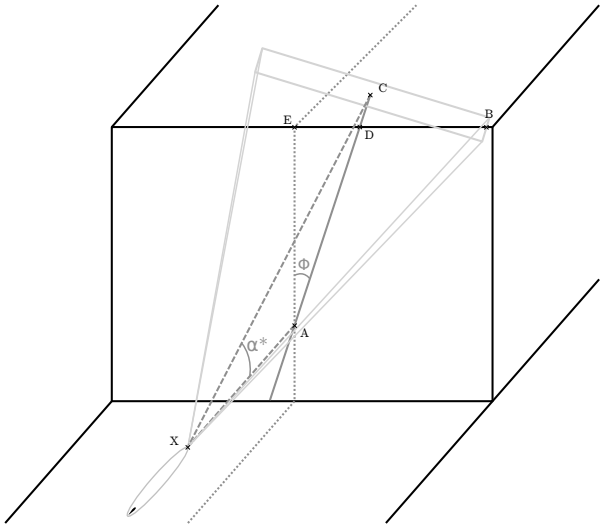

Figure B.2: Simplified terrain detection with roll error.

The calculation of the overestimate of the terrain is thus split into two separate calculations calculating the errors from both these effects. It is parametrized using the distance to the detected horizon $\overline{XA}$ and the height from the vehicle fixed surge axis $\overline{AE}$. The sonar beam and the terrain detection on it is assumed to lead to a detection as soon as any area of the beam hits the terrain step. In reality, this will overestimate the error, since a larger section of the beam will have to hit the terrain to cause a detection.

First the effect of the sonar beam opening angle β is considered, with the sonar scan angle α assumed to be zero (Figure B.3). From geometry, the additional detection height $\overline{AC}$ is calculated:

$$\begin{aligned} \tan\phi &= \frac{\overline{AC}}{\overline{BC}} \\ \overline{AC} &= \overline{BC} \cdot \tan\phi \end{aligned} \tag{B.1}$$

It is assumed that the increased detection does not significantly increase the detection range $\overline{XC}$ compared to the original detection range $\overline{XA}$, and the width of the sonar beam $2 \cdot \overline{CB}$ does not increase significantly:

$$\begin{aligned} \overline{BC} &= \overline{XC} \cdot \sin\frac{\beta}{2} \\ \overline{XC} &\approx \overline{XA} \\ \overline{BC} &\approx \overline{XA} \cdot \sin\frac{\beta}{2} \\ \overline{AC} &\approx \overline{XA} \cdot \sin\frac{\beta}{2} \cdot \tan\phi \end{aligned} \tag{B.2}$$

Next, the effect of the misalignment of the vertical plane and the scanning plane is

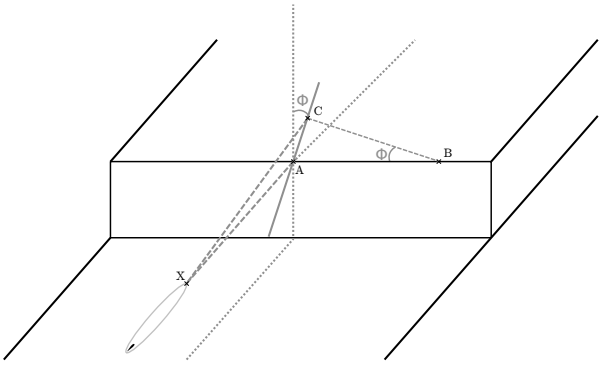

Figure B.3: Simplified terrain detection with roll error, assuming terrain detection at zero degree sonar scanning angle.

analysed for a sonar beam opening angle of $\beta = 0$ (Figure B.4):

$$\begin{aligned} \cos\phi &= \frac{\overline{AD}}{\overline{AE}} \\ \overline{AD} &= \frac{\overline{AE}}{\cos\phi} \\ \overline{AD} - \overline{AE} &= \overline{AE} \cdot \left(\frac{1}{\cos\phi} - 1 \right) \end{aligned} \tag{B.3}$$

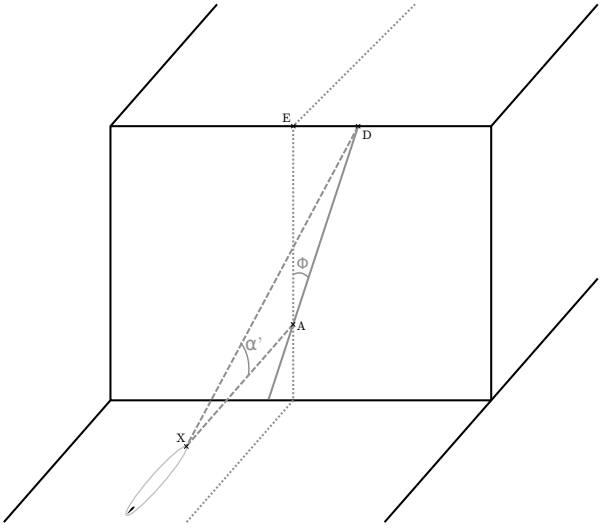

Figure B.4: Simplified terrain detection with roll error, assuming zero beam opening angle.

When combining the two cases, the detection range $\overline{XA}$ in Figure B.3 needs to be replaced with the detection range $\overline{XD}$, which is calculated using Pythagoras and inserting

B.3:

$$\begin{aligned} \overline{XD}^2 &= \overline{XA}^2 + \overline{AD}^2 \\ \overline{XD} = \sqrt{\overline{XA}^2 + \overline{AD}^2} &= \sqrt{\overline{XA}^2 + \left(\frac{\overline{AE}}{\cos\phi}\right)^2} \end{aligned} \tag{B.4}$$

The combination of Equations B.2, B.3, and B.4 yields the detection error Δ_ϕ:

$$\begin{aligned} \Delta_\phi = \overline{AC} - \overline{AE} \approx &\left[\sqrt{\overline{XA}^2 + \left(\frac{\overline{AE}}{\cos\phi}\right)^2} \cdot \sin\frac{\beta}{2} \cdot \tan\phi\right] \\ &+ \left[\overline{AE} \cdot \left(\frac{1}{\cos\phi} - 1\right)\right] \end{aligned} \tag{B.5}$$

Appendix C

Boldrewood Towing Tank Considerations

Bolderwood Towing Tank was considered as a test location for performing Delphin2 experiments. In the end, the Testwood Lake test location was used, since the heading error in Boldrewood Towing Tank caused problems with the obstacle detection. This appendix outlines the original experiment plans, and explains the obstacle detection issues in detail.

For testing and validating various vehicle state controllers Boldrewood Towing Tank is a valuable tool. However, during flight style experiments it had already been observed that it is difficult to maintain a constant heading along the towing tank. This is most likely due to magnetic disturbances from the towing tank structure.

The initial plan was to add an obstacle at the bottom of the towing tank, which would then be crossed along the length of the towing tank with various control and obstacle detection configurations. To create an obstacle with good visibility in a sonar scan, a 0.60 mx0.27 mx1.40 m metal shelf (IKEA HYLLIS, [Inter IKEA Systems B.V.]) was wrapped in bubble wrap C.1.

The available Qualisys motion capture set up for underwater motion tracking can be used to accurately determine the obstacle position and the vehicle movement across it over a section of several metres, adding an external observation perspective to the experiment analysis. However, while navigating along the towing tank, this data is not available to the AUV. Instead it has to rely on compass and accelerometer measurements to keep a constant heading. Even when choosing a very short distance of 5 m for reaching a steady state, detecting the obstacle, and returning to the goal altitude after the obstacle, a heading error of ten degrees will lead to a collision with the towing tank wall before the end of the experiment path.

At the same time, a heading error reduces the distance at which the towing tank wall is registered by the forwards looking sonar. Whilst the sonar beam is very slim in the

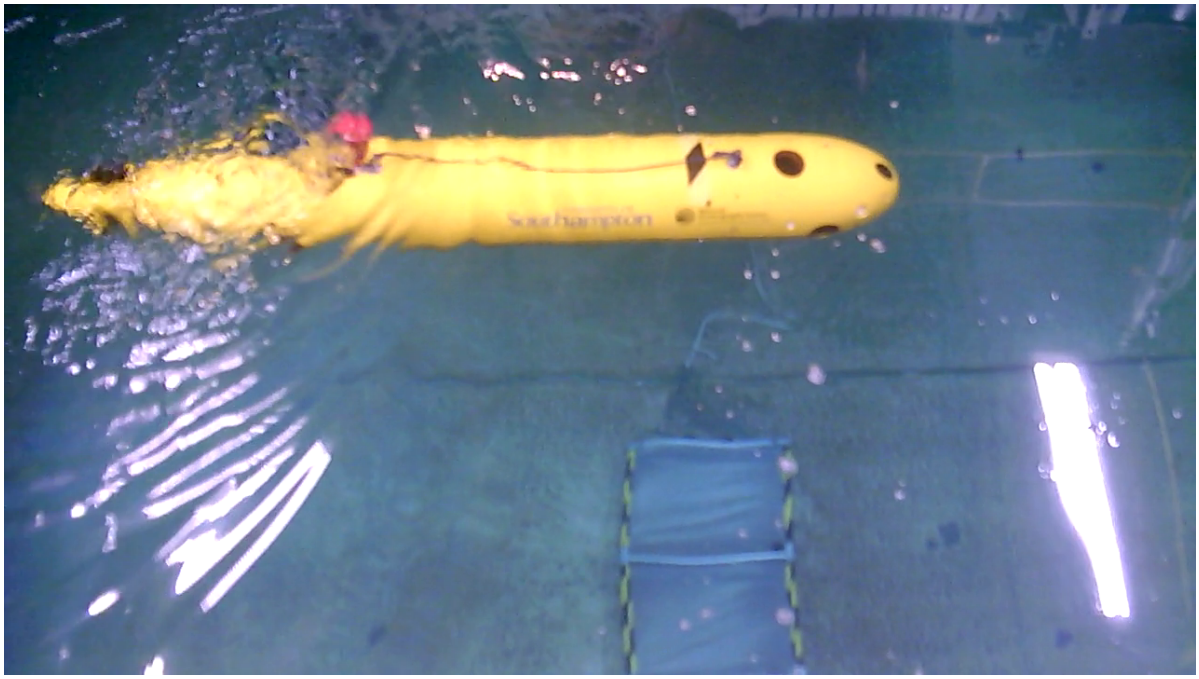

Figure C.1: Delphin2 in towing tank with a step obstacle made from metal shelf and bubble wrap.

scanning direction, it has a wide horizontal opening angle. From the sonar data it cannot be determined if a reflection of the sonar beam comes from the walls or the bottom of the towing tank. Even when the AUV is perfectly centred, the sonar beam detects the towing tank walls at a distance of less than 10 m. This distance shortens drastically with heading error and position offset relative to the centreline of the towing tank. The effects of the sonar beam width and the heading error are illustrated to scale in Figure C.2.

Combined with the likelihood of large heading errors, achieving a large number of passes over the obstacle with repeatable detection conditions is impossible without further navigation aids for the AUV.

To improve the navigation accuracy, the addition of a red rope at the bottom of the towing tank as a guide line was considered. In the end this option for improving the vehicle alignment relative to the towing tank was dismissed since no functioning driver for the cameras on Delphin2 could be found, and adding more recent camera models would have required significant modifications to the vehicle to get additional connections through the pressure hull of the vehicle.

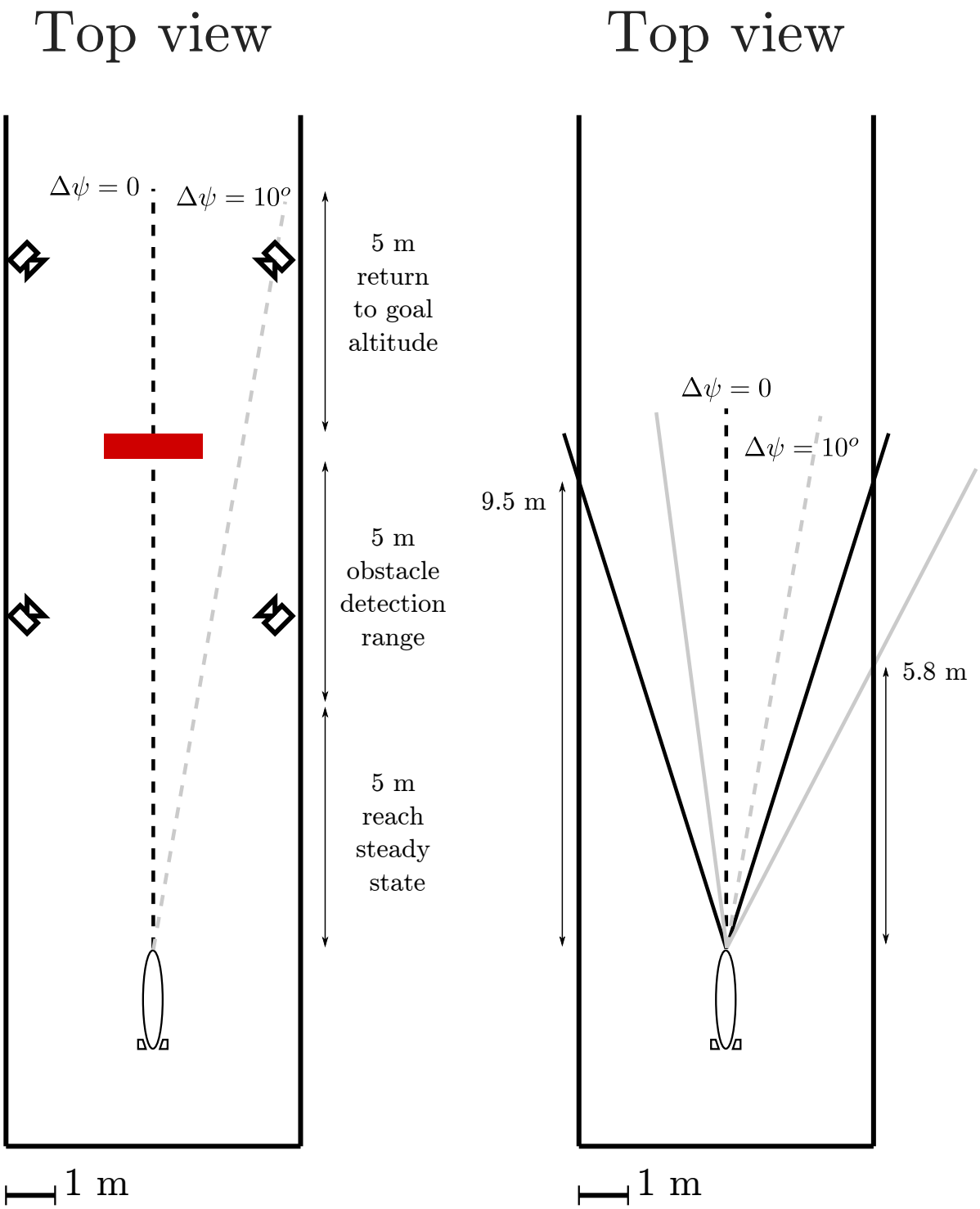

(a) Minimum length experiment path along the Boldrewood Towing Tank and Delphin2 path with a ten degree heading error.

(b) Mechanical scanning horizontal beam width in the Boldrewood Towing Tank, with correct heading along the towing tank and a ten degree heading error.

Figure C.2: Heading error sensitivity of experiment set up in Boldrewood Towing Tank.

Appendix D

Overview of Available Autosub6000 Mission Files

Tables D.2 and D.4 below give a full list of all Autosub6000 missions available for this work, as well as the vehicle configurations that were identified for each mission. Several missions were dismissed for simulation validation and more detailed analysis, the reasons are given in table D.2. Most of the mission data was extracted from the mission script ('*.ms') and mission configuration ('*.mcfg') text files of the individual missions using regular expressions and python. Further information was extracted from mission summary word documents, as well as additional word documents with software screenshots and further engineers' notes. If a missing value was filled in by assuming it has not changed between the previous or next mission, it is marked with a $*$. If multiple conflicting values were found, they are detailed in a footnote.

The following values are read from files that are assumed to have been used to configure Autosub6000: Waypoints ('*.ms') , goal altitudes ('TrackAtAltitude' in '*.ms'), and propeller power ('GL_MOTOR_CRUISE_POWER' in '*.ms'). For the D343 and D377 cruises further values were included in these files: pitch angle limits ('ncPitchLims' in '*.mcfg'), use of the forwards scanning obstacle avoidance ('ncAvoidanceActive' in '*.mcfg'), and a list of timings ('*.mcfg'). Furthermore, for the D343 and D377 the '*.mcfg' file contained information that was manually added as comments: The Depth control coefficients ('ncDepthCfs', an array containing P_z, D_z, TC_z, Max. I_z, Min. I_z, P_θ, and D_θ) and the scale factor for the fowards looking obstacle avoidance ('fwd scale'). For the JC136 and JC142 the obstacle avoidance settings and depth control coefficients are no longer included in all mission scripts and configuration files, they can be found in sreenshots instead. One pre-cruise document each gives settings at the start (though depth control is missing for JC136). If variables were changed, further word documents with screenshots and annotations indicated the change and before which misison it occurred. as well as some more screenshots indicating the variables that were changed and before which mission this change was appled. The obstacle avoidance settings and depth control coefficients were taken from these screenshot documents.

	altitude demands	OAS beam steering	OAS output used	collision noted	avg. speed over ground	surface buoyancy (positive)	reason for not using
M14	10-60m	False	False [a]	-	-	12 kg	Too many undefined parameters
M15	20-200m	True [b]	True	-	0.91 m/s	12 kg	No altitude tracking below 15 m.
M16	20-200m	True [c]	True	-	1.21 m/s	12 kg	No altitude tracking below 15 m.
M17	-	False	False	-	-	12 kg ∗	No altitude tracking
M18	-	False	False	-	-	16.6 kg	No altitude tracking
M19	-	False	-	-	-	16.6 kg ∗	No altitude tracking
M20	100m	True	True	-	-	16.6 kg ∗	No altitude tracking below 15 m.
M21	50m	True	True	-	-	16.6 kg ∗	No altitude tracking below 15 m.
M22	-	True	True	-	-	16.6 kg ∗	No altitude tracking
M23	3-200m	True	True ∗	-	-	16.6 kg ∗	
M24	-	True	True ∗	-	-	16.6 kg ∗	No altitude tracking
M25	3-50m	True	True	-	-	16.6 kg ∗	
M26	-	True [d]	True	-	-	16.6 kg ∗	No altitude tracking
M27	-	True [e]	True	-	-	16.6 kg ∗	No altitude tracking
M49	3-10m	False	-	-	-	-	Mission aborted before altitude tracking: Battery failure.
M50	2.7-10m	True	False	-	1.18 m/s	9.6 kg	
M51	2.7-10m	True	False	-	1.28 m/s	9.6 kg	
M52	100m	True	False	-	1.28 m/s	9.6 kg	No altitude tracking below 15 m.
M53	3m	True	False	1	1.15 m/s	9.6 kg	
M54	3m	True	False	-	1.13 m/s	14.2 kg	
M55	3.2-100m	True	False	-	1.12 m/s	14.2 kg	
M56	3.2-100m	True	False	-	-	14.2 kg [f]	
M57	3.5-20m	True	True	3	1.09 m/s	14.2 kg	
M58	3.2-50m	True	True [g]	-	1.29 m/s	14.2 kg	
M59	-	-	-	-	-	-	No mission data in folder
M114	50-90m	True	True	-	0.98 m/s	13.5 kg	No altitude tracking below 15 m.
M115	3m	True ∗	True	-	0.97 m/s	13.5 kg	
M116	3-110m	True ∗	True	1	1.0 m/s	13.5 kg	
M117	15-70m	True	True	-	0.9 m/s	13.5 kg	No altitude tracking below 15 m.
M118	70-100m	True	True	-	1.02 m/s	13.5 kg	No altitude tracking below 15 m.
M119	70m	True ∗	True	-	0.81 m/s	13.5 kg	No altitude tracking below 15 m.
M120	3m	True	True	-	0.96 m/s	13.5 kg	
M121	110m	True ∗	True	-	0.98 m/s	13.5 kg	No altitude tracking below 15 m.
M122	3-90m	True ∗	True	-	0.96 m/s	13.5 kg	
M123	15m	True	True	-	0.78 m/s	13.5 kg	No altitude tracking below 15 m.
M124	15m	True	True	-	0.89 m/s	13.5 kg	No altitude tracking below 15 m.
M133	3-25m	True ∗	True	-	0.88 m/s	17 kg	
M134	3m	True	True	-	0.69 m/s	17 kg	
M138	4-10m	True	True	-	0.94 m/s	17 kg	
M139	3-25m	True	True	-	1.01 m/s	17 kg	
M140	3-30m	True	True	-	0.86 m/s	17 kg	

Table D.2: Overview of Autosub6000 altitude tracking missions.

[a] OAS setting were changed during mission, using continuous scanning, beam steering and beam steering with output use

[b] M15 screenshot: beam steering on, output used; '*.mcfg' file: OAS not used

[c] M16 screenshot: beam steering on, output used; '*.mcfg' file: OAS not used

[d] M26 screenshot: beam steering on, output used; '*.mcfg' file: OAS not used

[e] M27 screenshot: beam steering on, output used; '*.mcfg' file: OAS not used

[f] Missuon summary lists 13kg and 14.2kg

[g] M58 screenshot & mission summary: beam steering on, output used; '*.mcfg' file: OAS not used

Autosub mission	P_z	D_z	TC_z	Max. I_z	Min. I_z	P_θ	D_θ	Max. θ	Min. θ	scale factor	motor power
M14								0.5	-0.5 [a]		270 W
M15								1.0	-1.0		270 W
M16								1.0	-1.0		270 W
M17								1.0	-0.5		270 W
M18								1.0	-0.5		270 W
M19								1.0	-0.5		270 W
M20	0.03	0.0	60	0.2	-0.1	2.2	6.0	0.6	-0.5	1.1	350 W
M21	0.03	0.0	60	0.2	-0.1	2.2	6.0	0.6	-0.5	1.1	350 W
M22	0.06	0.1	60	0.4	-0.1	2.2	6.0	0.6	-0.5	1.05	- W
M23	0.06	0.1	60	0.4	-0.1	2.2	6.0	0.6	-0.5	1.05	300 W
M24	0.02	0.0	60	0.4	-0.1	2.2	6.0	0.6	-0.5	1.05	320 W
M25	0.06	0.1	60	0.4	-0.1	2.2	6.0	0.6	-0.5	1.05	270 W
M26	-						-	-	-		
M27	-						-	-	-		
M49	0.05	0.1	60	0.1	-0.1	2.2	6.0	0.3	-0.3	1.5	230 W
M50	0.05 $*$	0.1$*$	60$*$	? [b]	-0.1$*$	2.2$*$	6.0$*$	0.3$*$	-0.3$*$	1.5$*$	230 W
M51	0.05	0.1	60	0.03	-0.03	2.2	6.0	0.3	-0.3	1.5	250 W
M52	0.05	0.1	60	0.03	-0.03	2.2	6.0	0.3	-0.25	1.5	250 W
M53	0.035	0.1	60	0.3	-0.05	2.2	6.0	1.0	-0.25	1.5	180 W
M54	0.03	0.1	60	0.4	-0.05	2.2	6.0	1.0	-0.25	1.5	180 W
M55	0.04	0.1	90	0.05	-0.05	2.2	6.0	0.6	-0.3	1.5	180 W
M56	0.04	0.1	90	0.05	-0.05	2.2	6.0	0.6	-0.3	1.5	180 W
M57	0.04	0.1	70	0.4	-0.15	2.2	6.0	1.2	-0.3	1.0	180 W
M58	0.04	0.1	90	0.1	-0.1	2.2	6.0	0.4	-0.3	1.0	230 W
M59											
M114	0.04	0.1	90	0.1	-0.1	2.2	6.0	0.4	-0.3	1.0	220 W
M115	0.04	0.1	90	0.1	-0.1	2.2	6.0	0.4	-0.3	1.0	220 W
M116	0.04	0.1	90	0.1	-0.1	2.2	6.0	0.4	-0.3	1.0	220 W
M117	0.04	0.1	90	0.1	-0.1	2.2	6.0	0.4	-0.3	1.0	220 W
M118	0.04	0.1	90	0.1	-0.1	2.2	6.0	0.4	-0.3	1.0	220 W
M119	0.04	0.1	90	0.1	-0.1	2.2	6.0	0.4	-0.3	1.0	220 W
M120	0.04	0.1	90	0.1	-0.1	2.2	6.0	0.4	-0.3	1.0	220 W
M121	0.04	0.1	90	0.1	-0.1	2.2	6.0	0.4	-0.3	1.333	220 W
M122	0.04	0.1	90	0.1	-0.1	2.2	6.0	0.4	-0.3	1.333	220 W
M123	0.04	0.1	90	0.1	-0.1	2.2	6.0	0.4	-0.3	1.333	220 W
M124	0.04	0.1	90	0.1	-0.1	2.2	6.0	0.4	-0.3	1.333	220 W
M133	0.04	0.1	90	0.1	-0.1	2.2	6.0	0.4	-0.3	1.333	220 W
M134	0.04	0.1	90	0.1	-0.1	2.2	6.0	0.4	-0.3	2.0	220 W
M138	0.04	0.1	90	0.1	-0.1	2.2	6.0	0.4	-0.3	2.333	220 W
M139	0.04	0.1	90	0.1	-0.1	2.2	6.0	0.4	-0.3	2.333	220 W
M140	0.04	0.1	90	0.1	-0.1	2.2	6.0	0.4	-0.3	2.333	220 W

Table D.4: Overview of depth control coefficients and propeller power for available Autosub6000 missions.

[a] Max. pitch 1.0, min. pitch -0.4 in mission summary word document

[b] No sources for this value could be found, whilst the others remain unchanged in previous and next settings, 0.1 or 0.03 are plausibe

Appendix A: list of all Testwood lake terrain following experiments

To this date, the following tests have been performed and analysed with Delphin2 at Testwood lakes:

Day	Time	Goal altitude	Propeller setpoint	Direction	Altitude tracking algorithm	Note
25.10.2017	11:27	-	10	forwards and reverse	-	at surface
25.10.2017	11:51	1.0	10	forwards	altitude tracking	
25.10.2017	12:22	1.0	10	forwards	altitude tracking	
25.10.2017	12: 7	1.0	10	reverse	altitude tracking	
25.10.2017	13:17	1.0	16	forwards	altitude tracking	
25.10.2017	13:40	1.0	16	forwards	altitude tracking	
25.10.2017	13:27	1.0	16	reverse	altitude tracking	
25.10.2017	13:50	1.0	16	reverse	altitude tracking	
25.10.2017	14:30	1.0	22	forwards	altitude tracking	
25.10.2017	14:42	1.0	22	forwards	altitude tracking	
25.10.2017	14:38	1.0	22	reverse	altitude tracking	
25.10.2017	14:46	1.0	22	reverse	altitude tracking	
01.11.2017	9:39	1.0	10	forwards	horizon tracking	
01.11.2017	9:54	1.0	10	forwards	horizon tracking	
01.11.2017	10:07	1.0	10	reverse	horizon tracking	
01.11.2017	10:24	1.0	10	reverse	horizon tracking	
01.11.2017	10:46	0.6	10	forwards	horizon tracking	
01.11.2017	11:10	0.6	10	forwards	horizon tracking	
01.11.2017	10:59	0.6	10	reverse	horizon tracking	
01.11.2017	11:21	0.6	10	reverse	horizon tracking	
01.11.2017	11:36	1.0	16	forwards	horizon tracking	
01.11.2017	11:48	1.0	16	forwards	horizon tracking	aborted early
01.11.2017	12:04	1.0	16	forwards	horizon tracking	
01.11.2017	11:43	1.0	16	reverse	horizon tracking	
01.11.2017	11:54	1.0	16	reverse	horizon tracking	
01.11.2017	12:18	0.6	16	forwards	horizon tracking	
01.11.2017	12:31	0.6	16	forwards	horizon tracking	
01.11.2017	12:24	0.6	16	reverse	horizon tracking	
01.11.2017	12:37	0.6	16	reverse	horizon tracking	
01.11.2017	13:15	1.0	22	forwards	horizon tracking	
01.11.2017	13:30	1.0	22	forwards	horizon tracking	
01.11.2017	13:43	1.0	22	forwards	horizon tracking	
01.11.2017	13:52	1.0	22	forwards	horizon tracking	
01.11.2017	13:07	1.0	22	reverse	horizon tracking	
01.11.2017	13:20	1.0	22	reverse	horizon tracking	
01.11.2017	13:35	1.0	22	reverse	horizon tracking	
01.11.2017	13:48	1.0	22	reverse	horizon tracking	
01.11.2017	13:56	1.0	22	reverse	horizon tracking	
01.11.2017	14:02	0.6	22	forwards	horizon tracking	
01.11.2017	14:12	0.6	22	forwards	horizon tracking	
01.11.2017	14:08	0.6	22	reverse	horizon tracking	
01.11.2017	14:17	0.6	22	reverse	horizon tracking	
01.11.2017	14:27	0.6	22	forwards	horizon tracking	sonar threshold 75
01.11.2017	14:33	0.6	22	reverse	horizon tracking	sonar threshold 75
01.11.2017	14:40	0.6	22	forwards	horizon tracking	
01.11.2017	14:46	0.6	22	reverse	horizon tracking	
01.11.2017	14:54	0.6	22	forwards	horizon tracking	
01.11.2017	15:01	0.6	22	reverse	horizon tracking	
06.12.2017	09:34	0.6	10	+1	horizon tracking	
06.12.2017	09:44	1.0	10	-1	horizon tracking	
06.12.2017	10:43	1.0	22	+1	horizon tracking	
06.12.2017	10:50	1.0	22	-1	horizon tracking	
06.12.2017	10:56	1.0	22	+1	horizon tracking	
06.12.2017	11:01	1.0	22	-1	horizon tracking	
06.12.2017	12:38	1.0	22	+1	horizon tracking	sonar threshold 85
06.12.2017	12:44	1.0	22	-1	horizon tracking	sonar threshold 85
06.12.2017	12:49	1.0	22	+1	horizon tracking	sonar threshold 85
06.12.2017	12:54	1.0	22	-1	horizon tracking	sonar threshold 85
06.12.2017	13:03	1.0	22	+1	horizon tracking	sonar threshold 75
06.12.2017	13:09	1.0	22	-1	horizon tracking	sonar threshold 75
06.12.2017	13:13	1.0	22	+1	horizon tracking	sonar threshold 75
06.12.2017	13:29	1.0	22	+1	horizon tracking	
06.12.2017	13:36	1.0	22	-1	horizon tracking	
06.12.2017	13:41	1.0	22	+1	horizon tracking	
06.12.2017	13:46	1.0	22	-1	horizon tracking	
06.12.2017	13:57	1.0	22	+1	horizon tracking	
06.12.2017	14:04	1.0	22	-1	horizon tracking	
06.12.2017	14:09	1.0	22	+1	horizon tracking	
06.12.2017	14:13	1.0	22	-1	horizon tracking	
06.12.2017	15:06	1.0	22	+1	horizon tracking	slide threshold base 95, slide 7
06.12.2017	15:11	1.0	22	-1	horizon tracking	slide threshold base 99, slide 7
06.12.2017	15:18	1.0	22	+1	horizon tracking	slide threshold base 99, slide 7
06.12.2017	15:23	1.0	22	-1	horizon tracking	slide threshold base 99, slide 7

Appendix E

Overview Plots of All Autosub6000 Missions

To select experiments of interest, key data for all available Autosub6000 missions was plotted. The scales for all plots were chosen the same, to make comparison easier. Rather than speed, which varies between a range of 0.7 m/s and 1.3 m/s, the time in seconds since reaching an altitude below 10 m was chosen. The depth plot is centred around the median depth spend after first reaching an altitude below 10 m.

Besides the vehicle depth and altitude, the vehicle heading change rate, pitch angle and the mechanical scanning sonar head angle were included in the plots. Whilst the heading is assumed constant during the altitude tracking missions, the actual vehicle path is split in several sections following a grid as shown in the overview maps in figure 4.11. The heading change rate indicates when a corner of the path is reached. The vehicle pitch gives an impression how steady the vehicle was during the terrain following. The mechanical scanning sonar angle indicates if the altitude tracking was used. If the altitude tracking was not used, it continuously scans between the maximum and minimum angle limit.

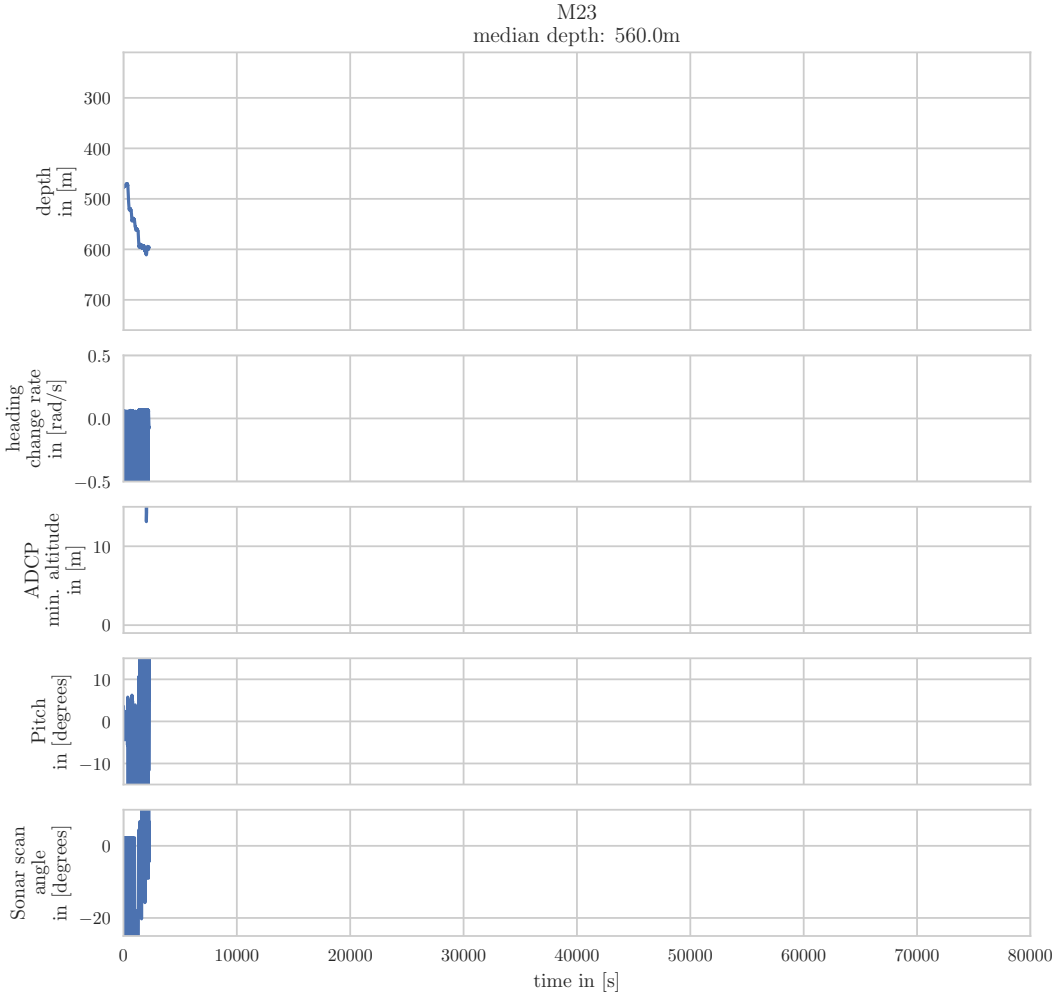
M23
median depth: 560.0m
depth in [m]
300
400
500
600
700
heading change rate in [rad/s]
0.5
0.0
−0.5
ADCP min. altitude in [m]
10
0
Pitch in [degrees]
10
0
−10
Sonar scan angle in [degrees]
0
−20
0
10000
20000
30000
40000
50000
60000
70000
80000
time in [s]

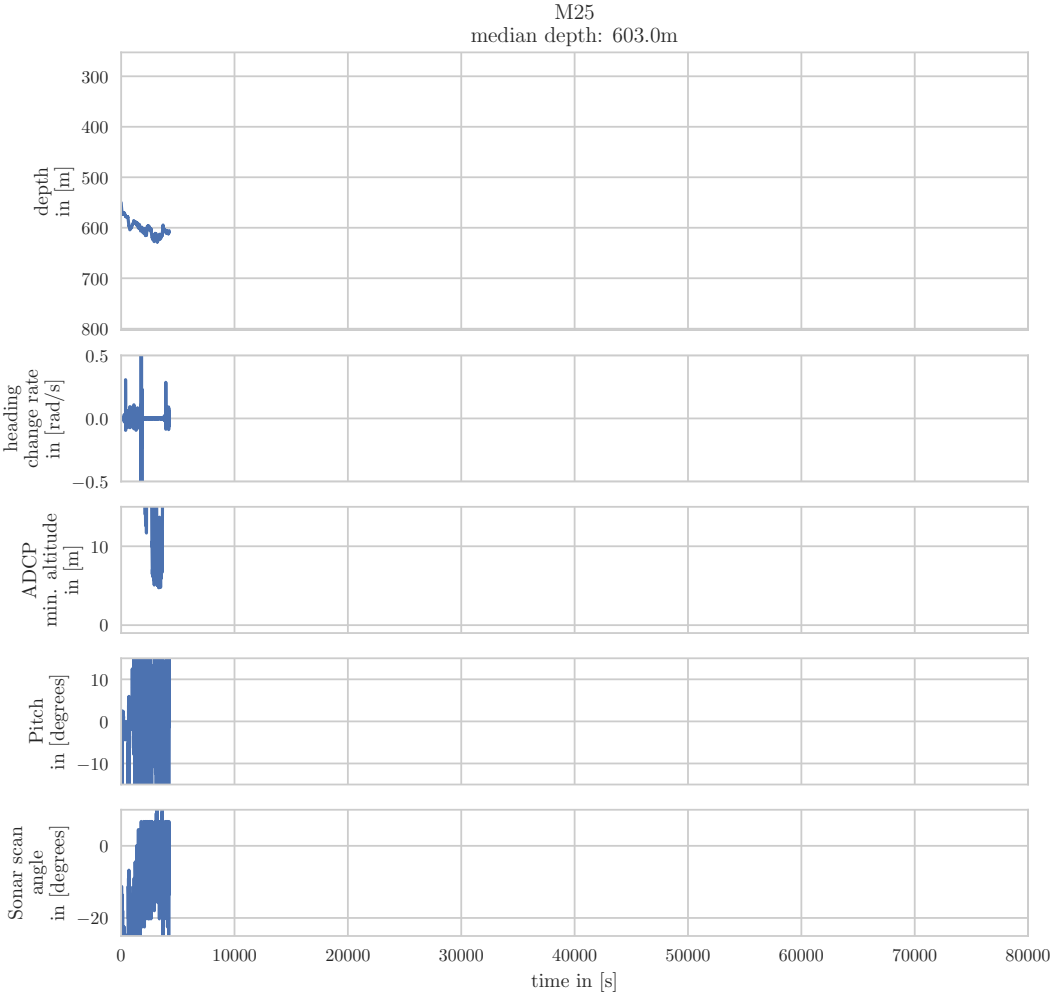
M25
median depth: 603.0m
depth in [m]
300
400
500
600
700
800
heading change rate in [rad/s]
0.5
0.0
−0.5
ADCP min. altitude in [m]
10
0
Pitch in [degrees]
10
0
−10
Sonar scan angle in [degrees]
0
−20
0
10000
20000
30000
40000
50000
60000
70000
80000
time in [s]

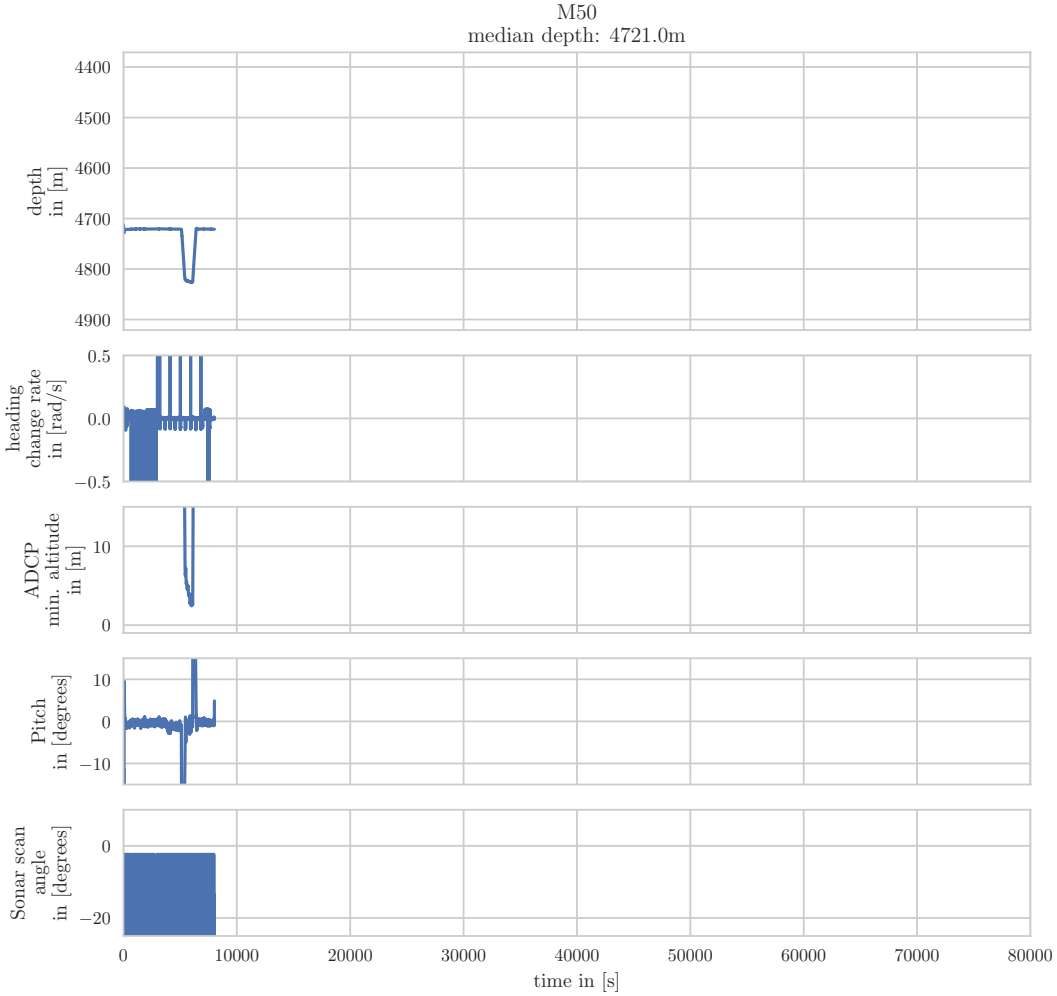
M50
median depth: 4721.0m
depth in [m]
4400
4500
4600
4700
4800
4900
heading change rate in [rad/s]
0.5
0.0
−0.5
ADCP min. altitude in [m]
10
0
Pitch in [degrees]
10
0
−10
Sonar scan angle in [degrees]
0
−20
0
10000
20000
30000
40000
50000
60000
70000
80000
time in [s]

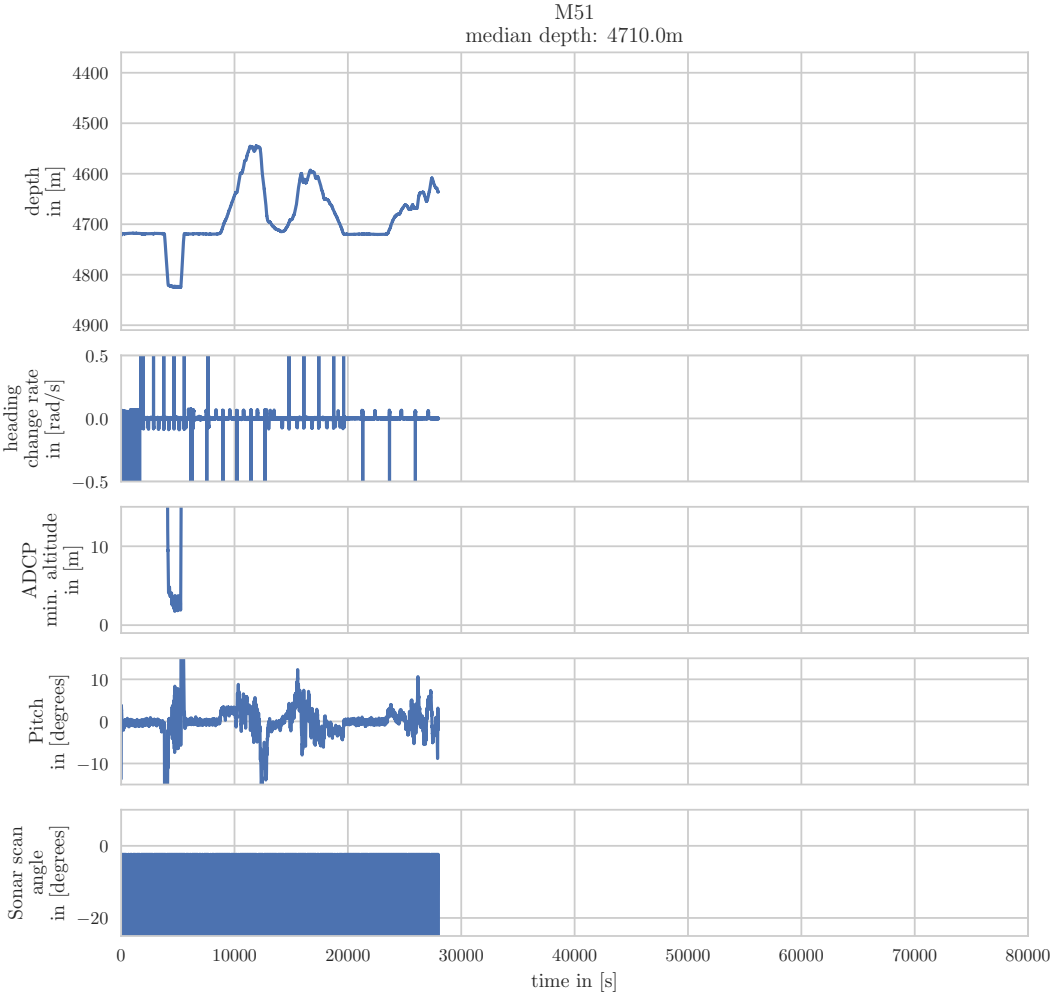
M51
median depth: 4710.0m
depth in [m]
4400
4500
4600
4700
4800
4900
heading change rate in [rad/s]
0.5
0.0
−0.5
ADCP min. altitude in [m]
10
0
Pitch in [degrees]
10
0
−10
Sonar scan angle in [degrees]
0
−20
0
10000
20000
30000
40000
50000
60000
70000
80000
time in [s]

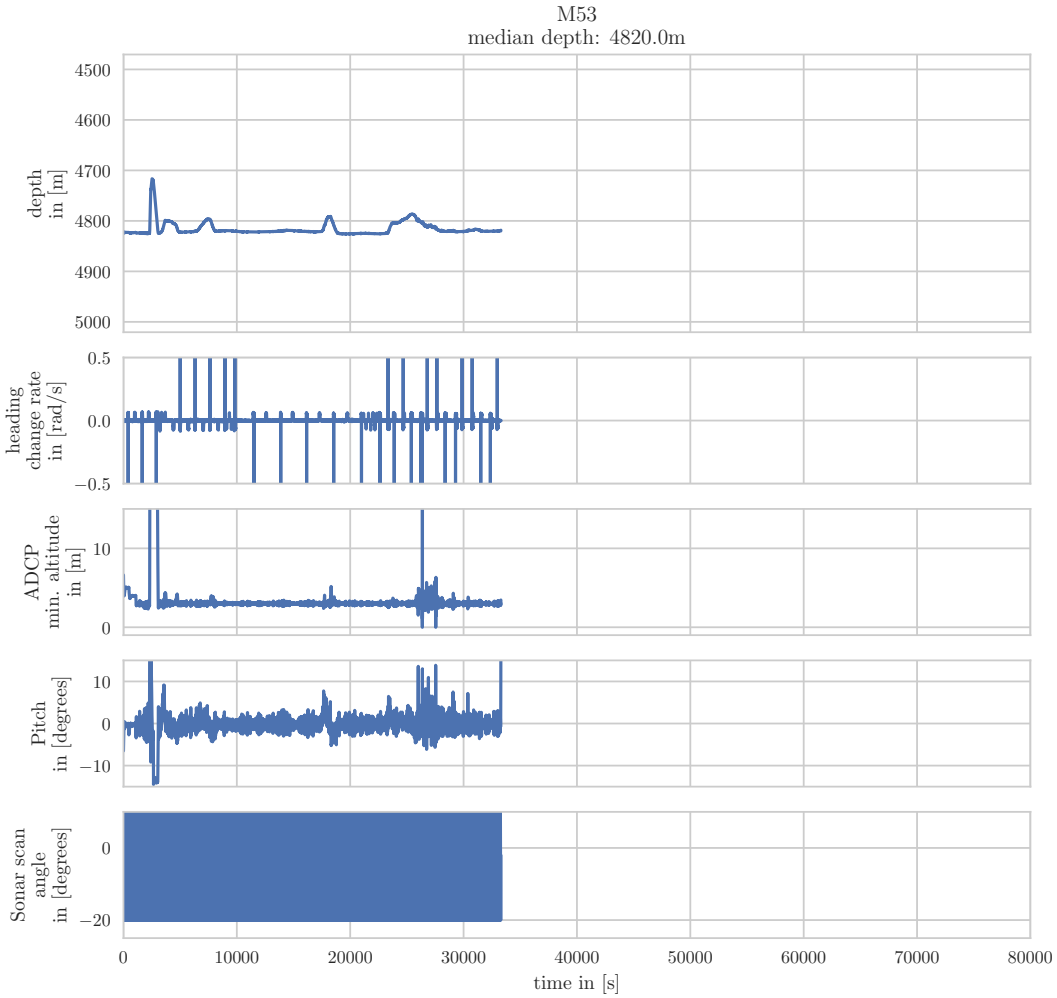
M53
median depth: 4820.0m
depth in [m]
4500
4600
4700
4800
4900
5000
heading change rate in [rad/s]
0.5
0.0
−0.5
ADCP min. altitude in [m]
10
0
Pitch in [degrees]
10
0
−10
Sonar scan angle in [degrees]
0
−20
0
10000
20000
30000
40000
50000
60000
70000
80000
time in [s]

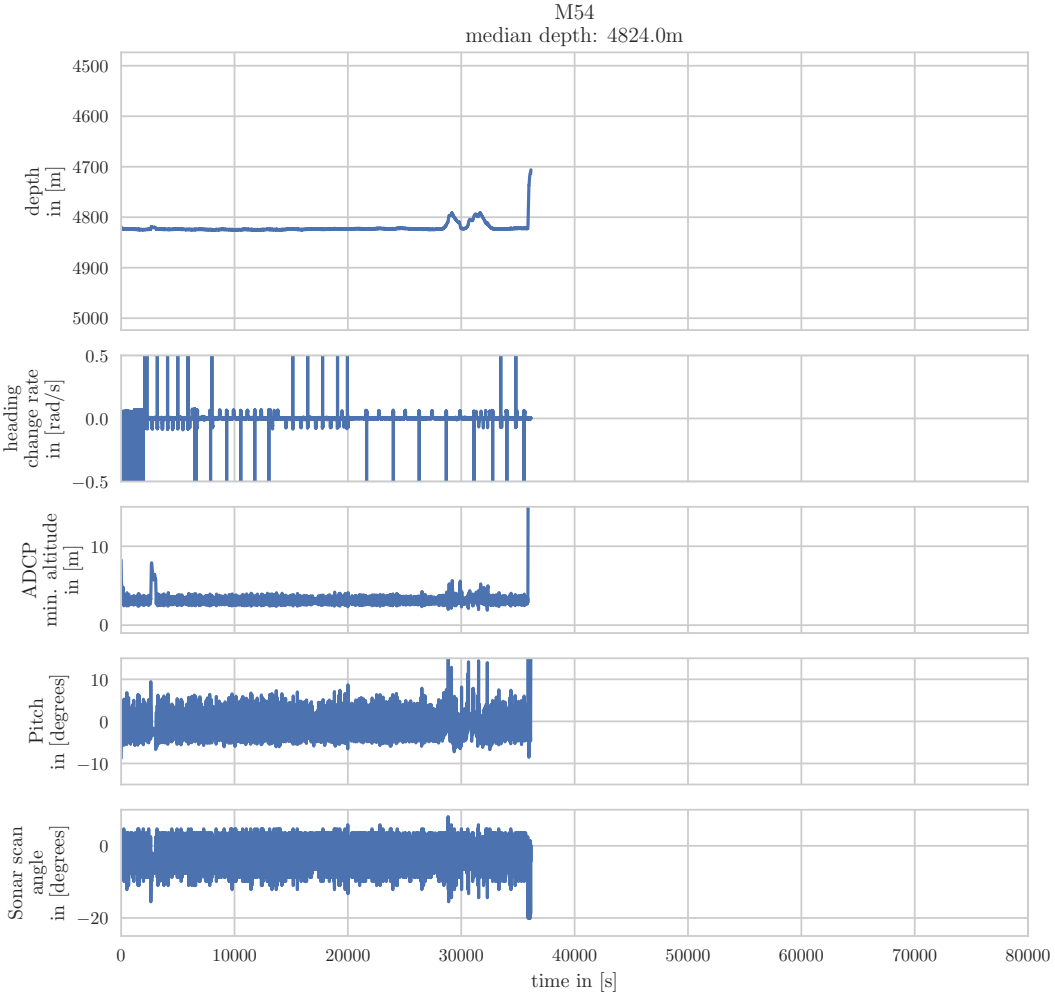
M54
median depth: 4824.0m
depth in [m]
4500
4600
4700
4800
4900
5000
heading change rate in [rad/s]
0.5
0.0
−0.5
ADCP min. altitude in [m]
10
0
Pitch in [degrees]
10
0
−10
Sonar scan angle in [degrees]
0
−20
0
10000
20000
30000
40000
50000
60000
70000
80000
time in [s]

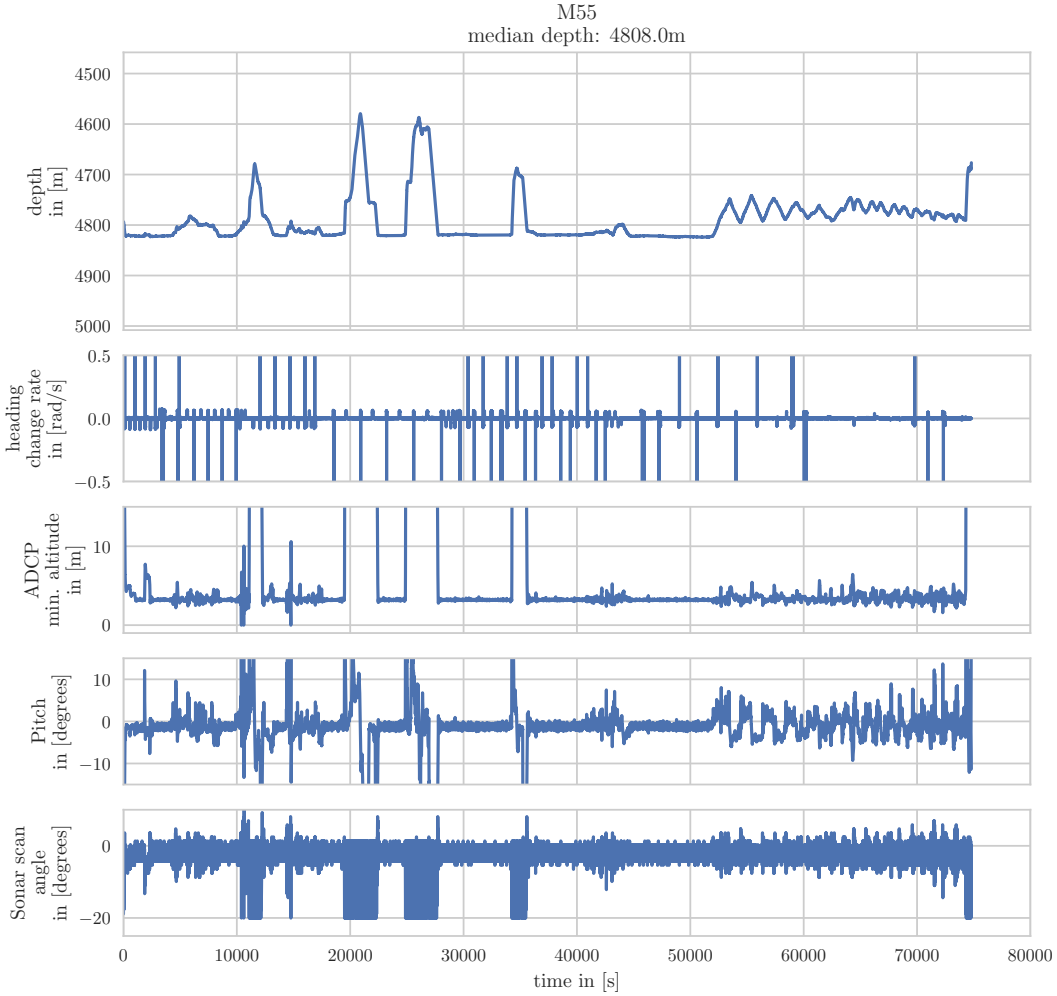
M55
median depth: 4808.0m
depth in [m]
4500
4600
4700
4800
4900
5000
heading change rate in [rad/s]
0.5
0.0
−0.5
ADCP min. altitude in [m]
10
0
Pitch in [degrees]
10
0
−10
Sonar scan angle in [degrees]
0
−20
0
10000
20000
30000
40000
50000
60000
70000
80000
time in [s]

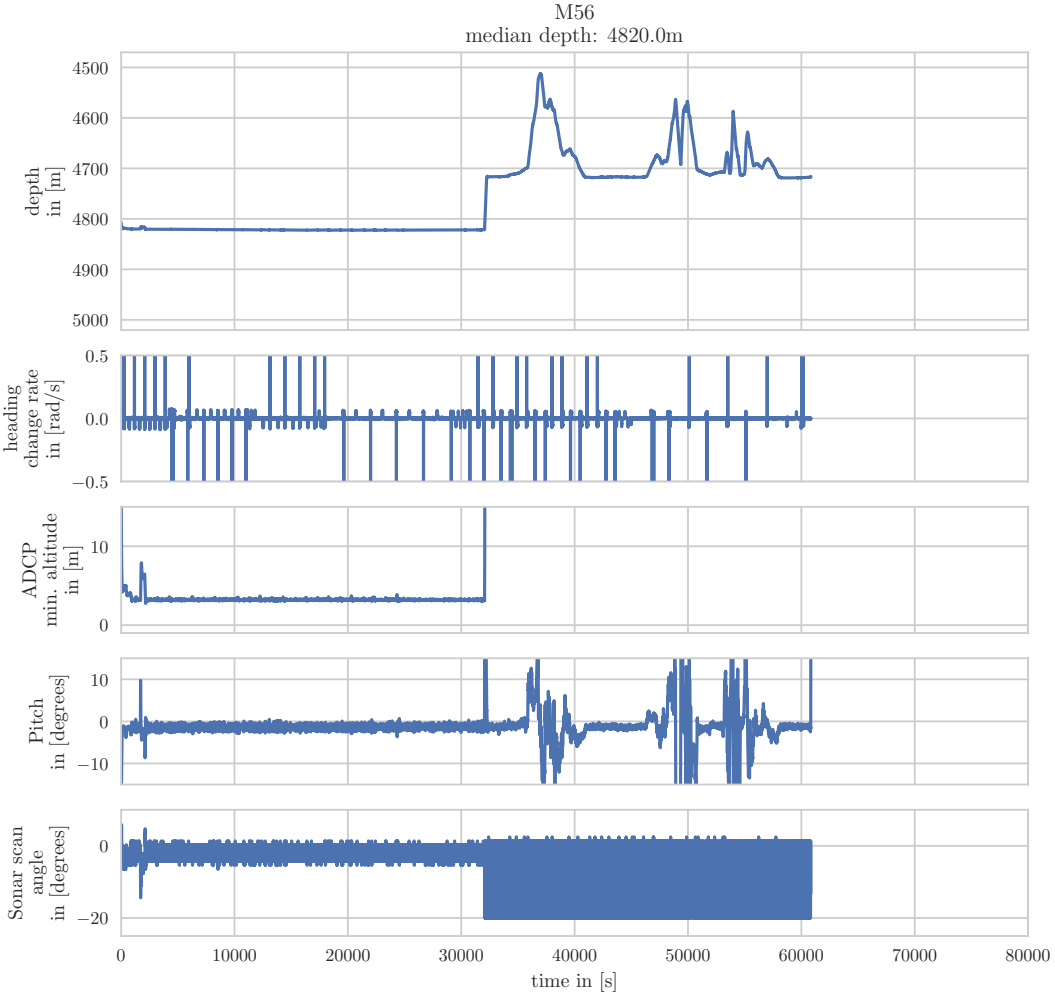
M56
median depth: 4820.0m
depth in [m]
4500
4600
4700
4800
4900
5000
heading change rate in [rad/s]
0.5
0.0
−0.5
ADCP min. altitude in [m]
10
0
Pitch in [degrees]
10
0
−10
Sonar scan angle in [degrees]
0
−20
0
10000
20000
30000
40000
50000
60000
70000
80000
time in [s]

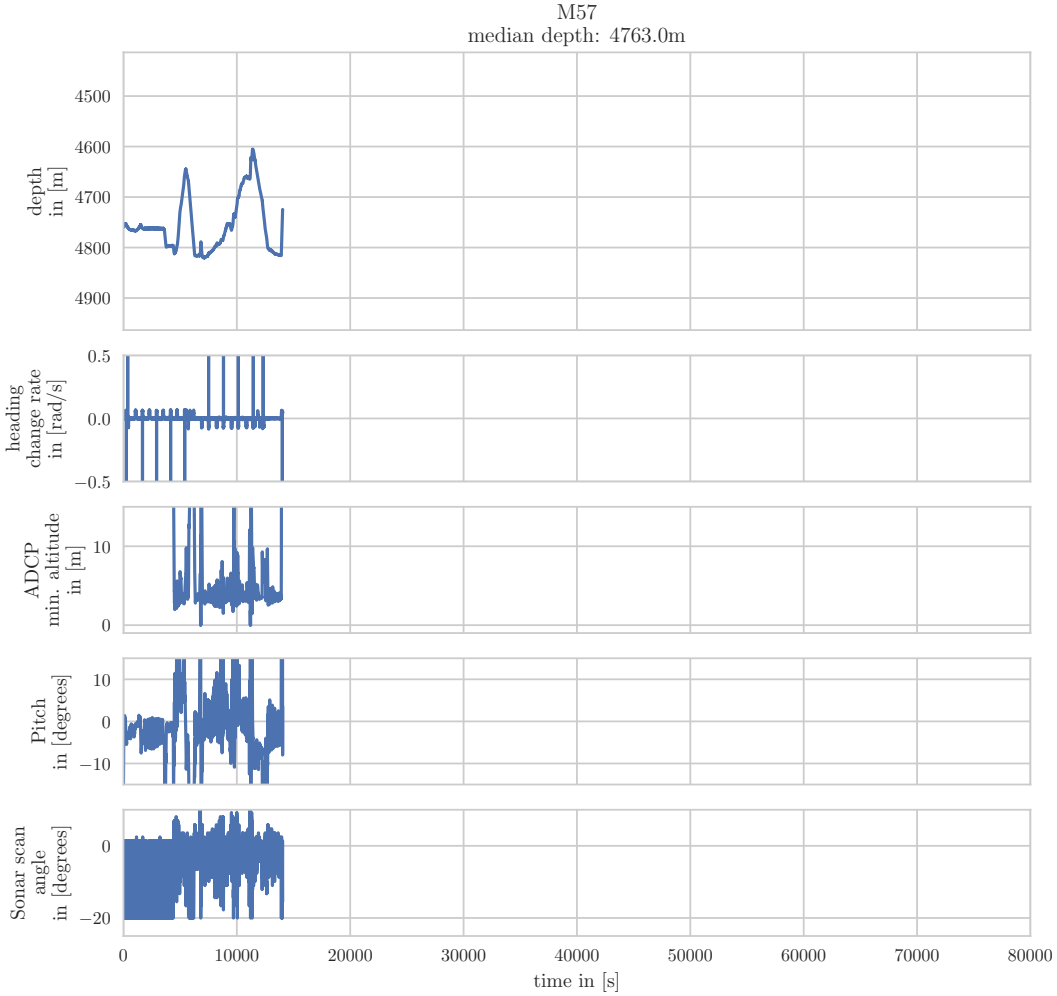
M57
median depth: 4763.0m
depth in [m]
4500
4600
4700
4800
4900
heading change rate in [rad/s]
0.5
0.0
−0.5
ADCP min. altitude in [m]
10
0
Pitch in [degrees]
10
0
−10
Sonar scan angle in [degrees]
0
−20
0
10000
20000
30000
40000
50000
60000
70000
80000
time in [s]

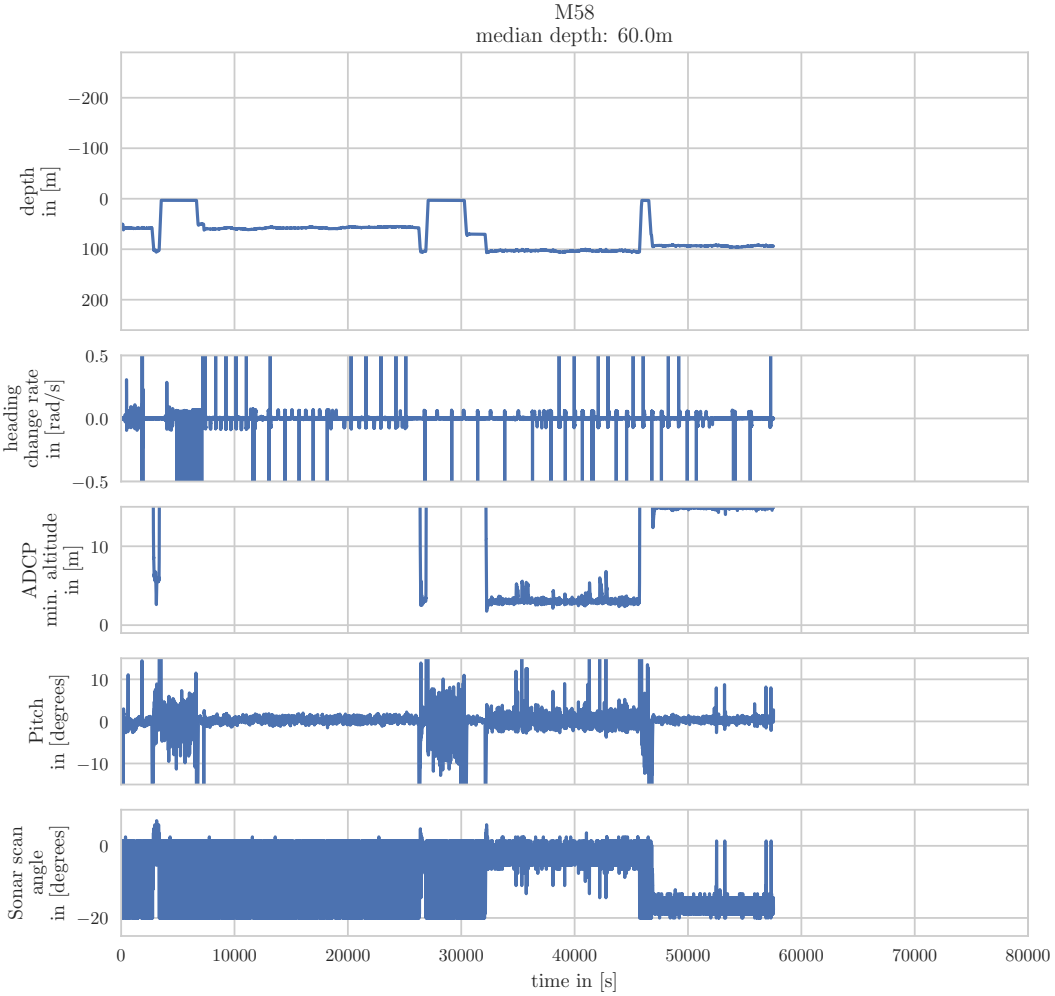
M58
median depth: 60.0m
depth in [m]
−200
−100
0
100
200
heading change rate in [rad/s]
0.5
0.0
−0.5
ADCP min. altitude in [m]
10
0
Pitch in [degrees]
10
0
−10
Sonar scan angle in [degrees]
0
−20
0
10000
20000
30000
40000
50000
60000
70000
80000
time in [s]

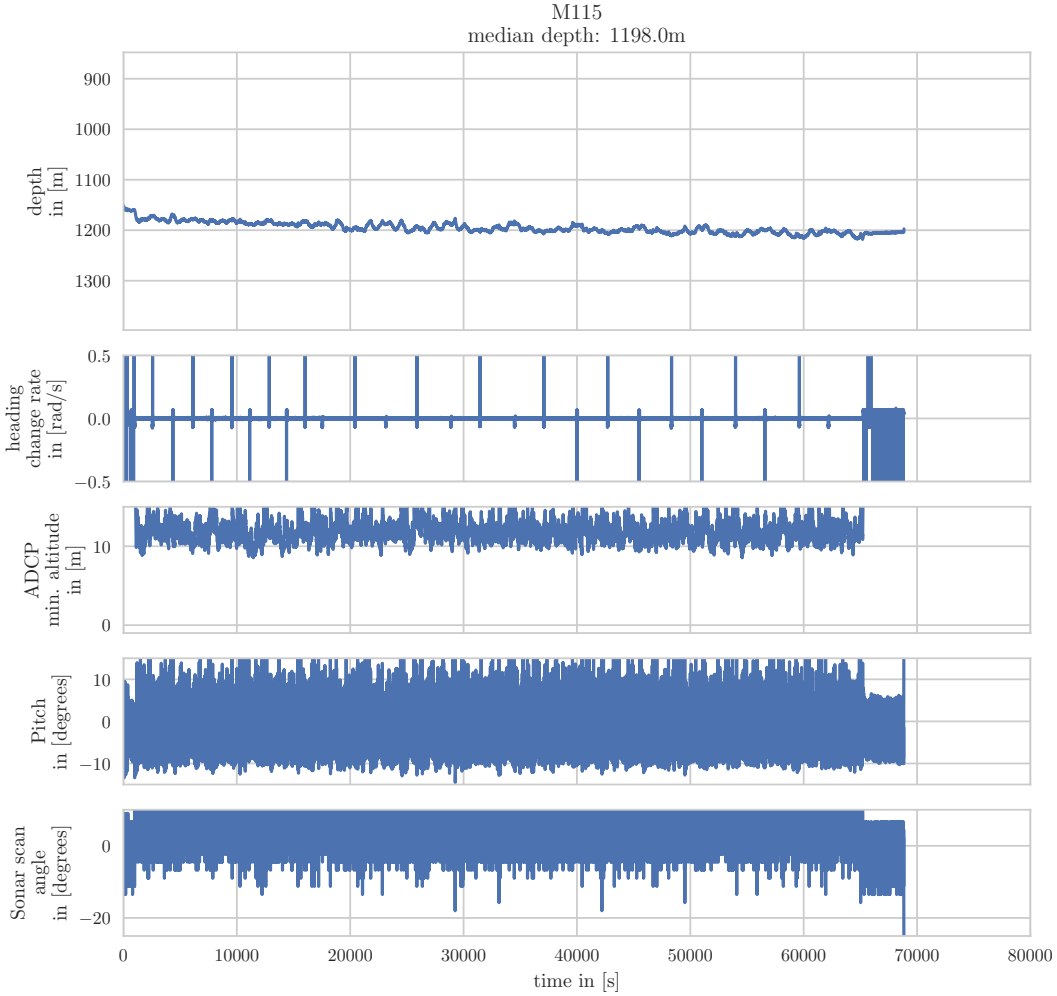
M115
median depth: 1198.0m
depth in [m]
900
1000
1100
1200
1300
heading change rate in [rad/s]
0.5
0.0
−0.5
ADCP min. altitude in [m]
10
0
Pitch in [degrees]
10
0
−10
Sonar scan angle in [degrees]
0
−20
0
10000
20000
30000
40000
50000
60000
70000
80000
time in [s]

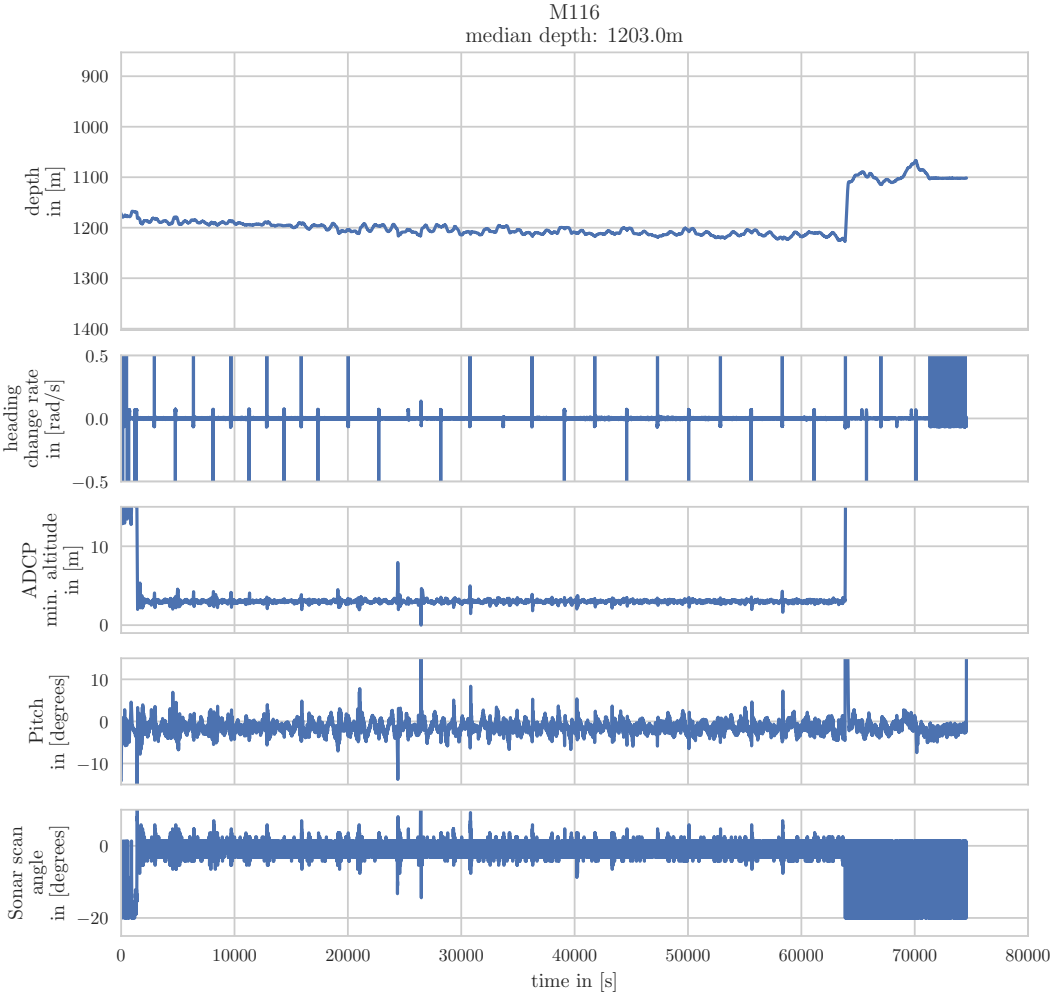
M116
median depth: 1203.0m
depth in [m]
900
1000
1100
1200
1300
1400
heading change rate in [rad/s]
0.5
0.0
−0.5
ADCP min. altitude in [m]
10
0
Pitch in [degrees]
10
0
−10
Sonar scan angle in [degrees]
0
−20
0
10000
20000
30000
40000
50000
60000
70000
80000
time in [s]

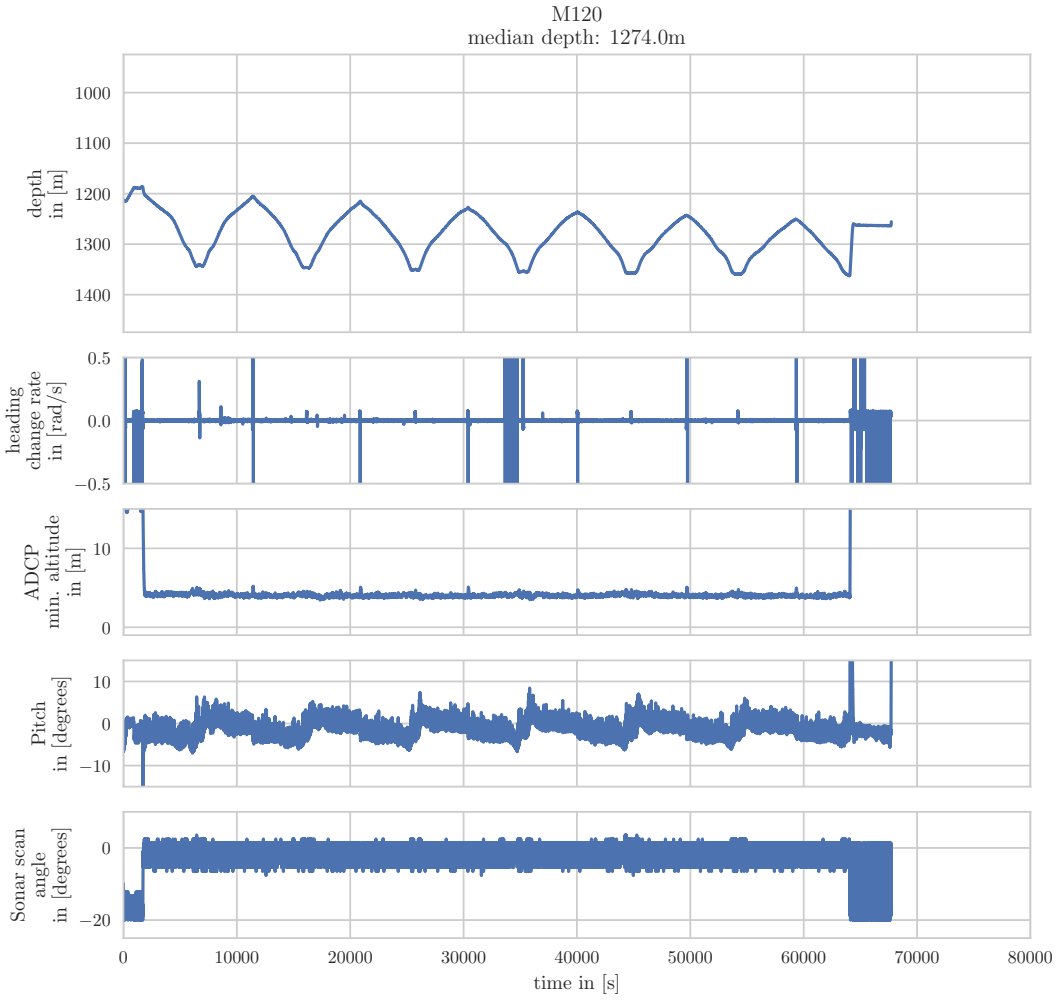
M120
median depth: 1274.0m
depth in [m]
1000
1100
1200
1300
1400
heading change rate in [rad/s]
0.5
0.0
−0.5
ADCP min. altitude in [m]
10
0
Pitch in [degrees]
10
0
−10
Sonar scan angle in [degrees]
0
−20
0
10000
20000
30000
40000
50000
60000
70000
80000
time in [s]

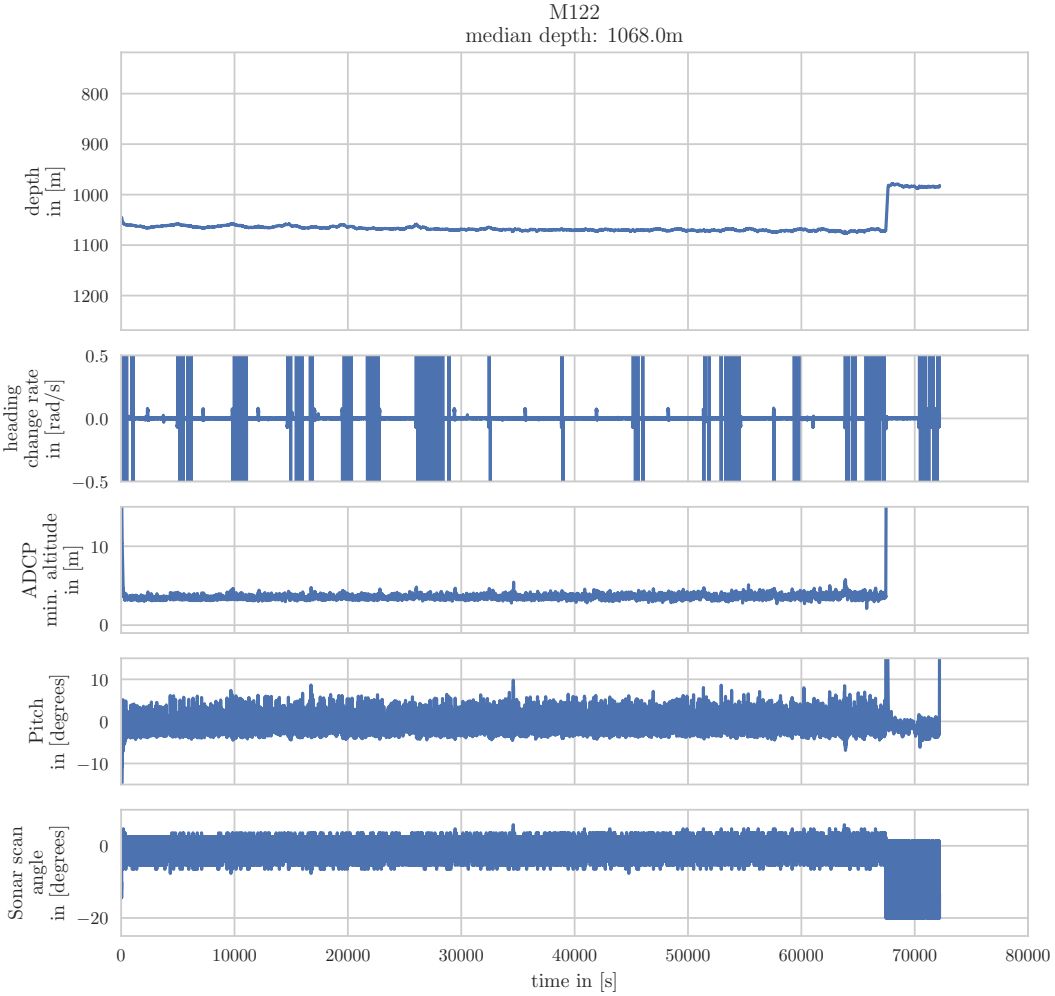
M122
median depth: 1068.0m
depth in [m]
800
900
1000
1100
1200
heading change rate in [rad/s]
0.5
0.0
−0.5
ADCP min. altitude in [m]
10
0
Pitch in [degrees]
10
0
−10
Sonar scan angle in [degrees]
0
−20
0
10000
20000
30000
40000
50000
60000
70000
80000
time in [s]

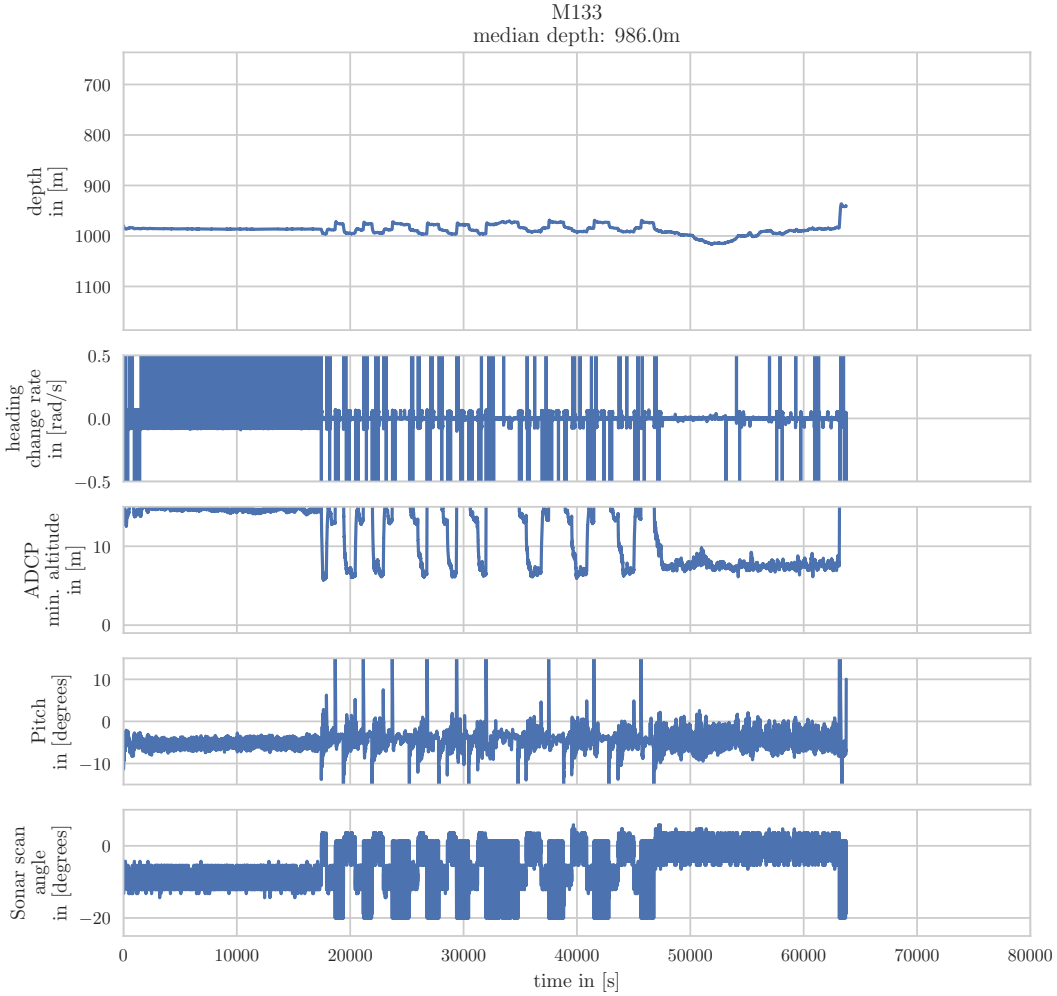
M133
median depth: 986.0m
depth in [m]
700
800
900
1000
1100
heading change rate in [rad/s]
0.5
0.0
−0.5
ADCP min. altitude in [m]
10
0
Pitch in [degrees]
10
0
−10
Sonar scan angle in [degrees]
0
−20
0
10000
20000
30000
40000
50000
60000
70000
80000
time in [s]

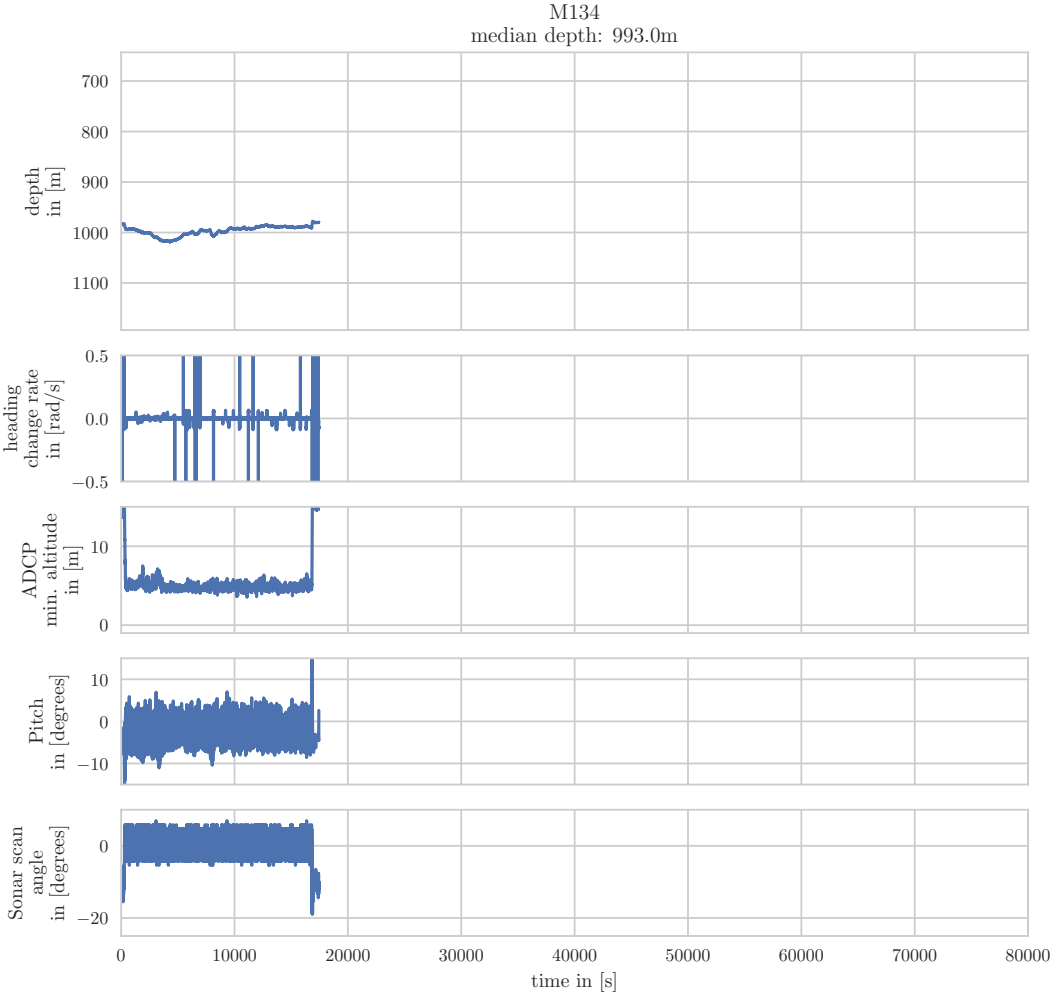
M134
median depth: 993.0m
depth in [m]
700
800
900
1000
1100
heading change rate in [rad/s]
0.5
0.0
−0.5
ADCP min. altitude in [m]
10
0
Pitch in [degrees]
10
0
−10
Sonar scan angle in [degrees]
0
−20
0
10000
20000
30000
40000
50000
60000
70000
80000
time in [s]

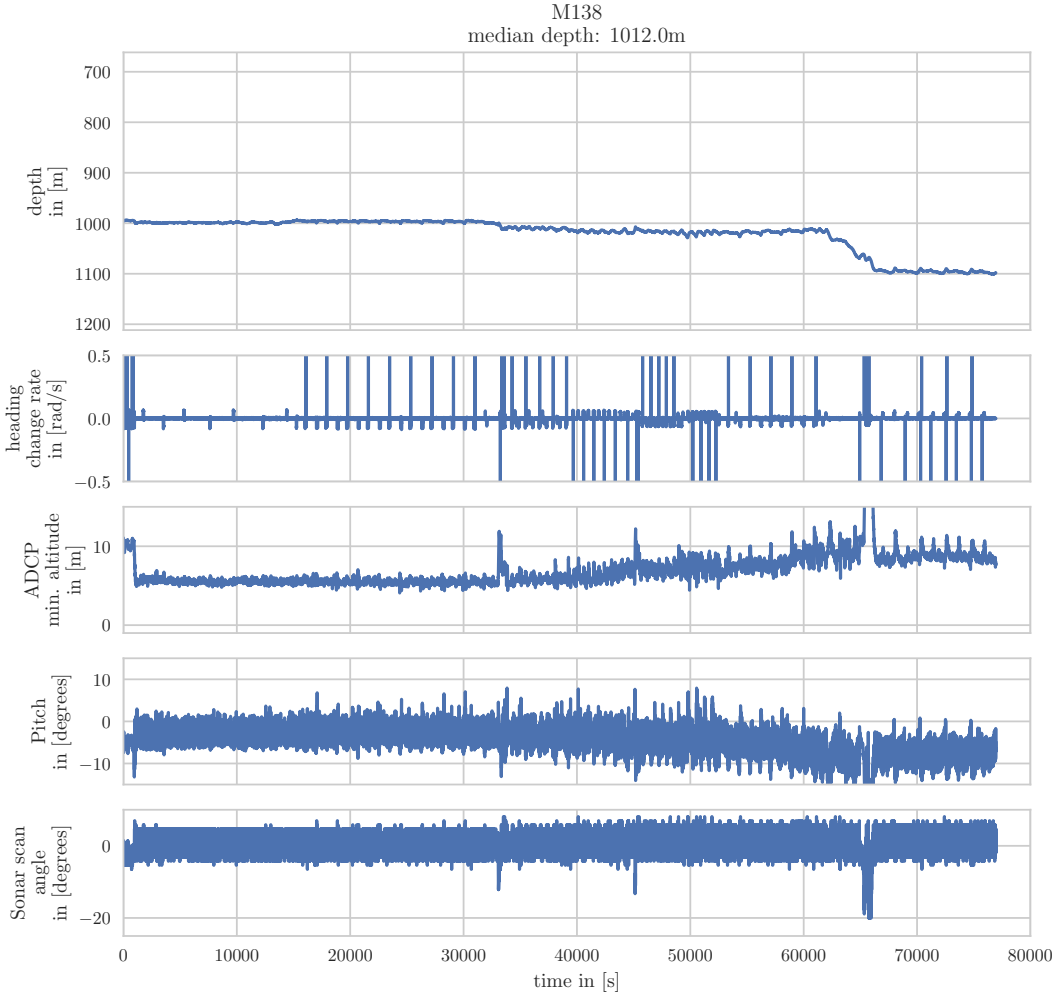
M138
median depth: 1012.0m
depth in [m]
700
800
900
1000
1100
1200
heading change rate in [rad/s]
0.5
0.0
−0.5
ADCP min. altitude in [m]
10
0
Pitch in [degrees]
10
0
−10
Sonar scan angle in [degrees]
0
−20
0
10000
20000
30000
40000
50000
60000
70000
80000
time in [s]

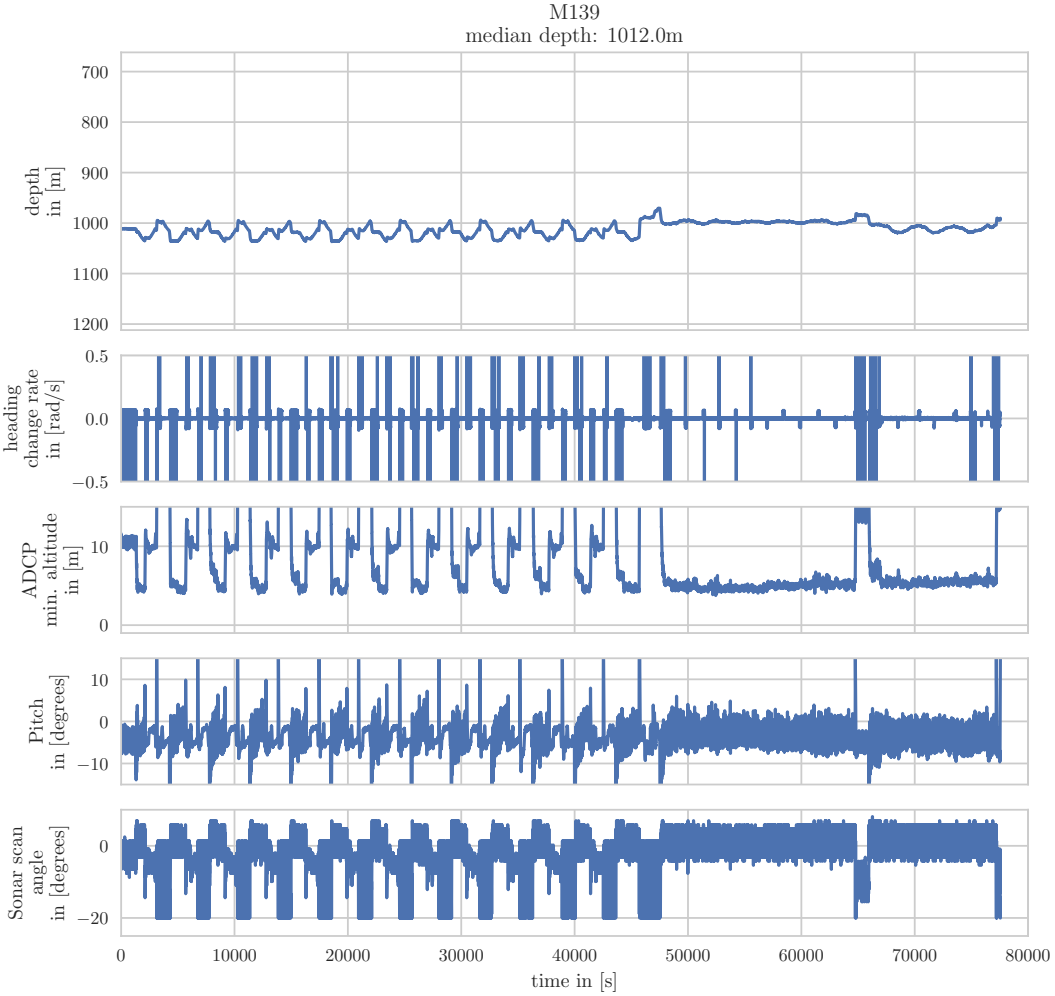
M139
median depth: 1012.0m
depth in [m]
700
800
900
1000
1100
1200
heading change rate in [rad/s]
0.5
0.0
−0.5
ADCP min. altitude in [m]
10
0
Pitch in [degrees]
10
0
−10
Sonar scan angle in [degrees]
0
−20
0
10000
20000
30000
40000
50000
60000
70000
80000
time in [s]

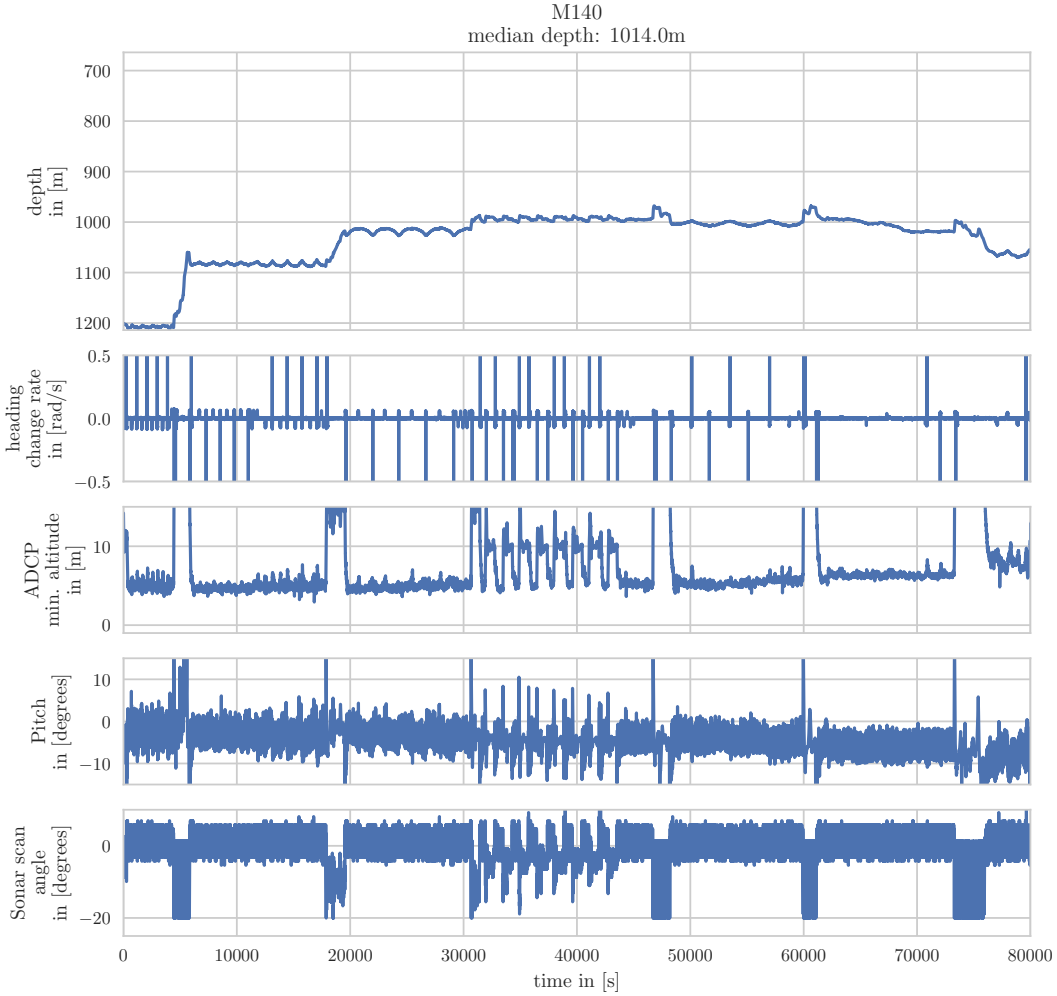
M140
median depth: 1014.0m
depth in [m]
700
800
900
1000
1100
1200
heading change rate in [rad/s]
0.5
0.0
−0.5
ADCP min. altitude in [m]
10
0
Pitch in [degrees]
10
0
−10
Sonar scan angle in [degrees]
0
−20
0
10000
20000
30000
40000
50000
60000
70000
80000
time in [s]

Appendix F

Statistics for All Available Autosub6000 Missions

mission		23	25	50	51	53	54	55	56	57	58
surge avg	in $[\frac{m}{s}]$	1.50	1.48	1.30	1.37	1.21	1.19	1.18	1.17	1.17	1.38
mission length	in [km]	0.94	0.94	0.89	1.53	39.01	41.93	85.66	36.62	10.81	18.19
altMin avg	in [m]	22.57	9.28	4.08	3.04	4.06	3.09	10.15	3.15	5.18	3.00
altMin std	in [m]	3.42	5.26	1.43	0.74	9.24	0.52	21.42	0.49	5.00	0.49
riskMin	in %	0.00	0.00	0.00	0.00	0.41	0.00	0.11	0.00	1.12	0.00
risk	in %	0.00	0.00	0.00	0.00	0.01	0.00	0.02	0.00	0.09	0.00
success	in %	0.00	0.00	55.52	89.32	95.90	96.71	82.98	97.25	59.98	94.56
alt avg	in [m]	24.72	10.15	4.27	3.21	5.85	3.27	11.37	3.30	10.58	3.16
alt std	in [m]	3.68	5.78	1.52	0.77	38.26	0.55	28.80	0.55	68.59	0.51
depthError avg	in [m]	3.73	0.29	13.87	1.79	-0.68	-0.18	-0.86	-0.02	-1.64	-0.08
depthError std	in [m]	49.17	4.80	105.59	12.94	9.99	1.98	8.81	1.05	6.73	0.69
pitch avg	in [degree]	-0.70	-0.49	-0.58	-0.15	-0.24	-1.42	-1.39	-1.51	-1.70	0.37
pitch std	in [degree]	7.93	8.04	2.10	3.36	3.56	2.38	4.39	0.79	8.01	1.39
roll avg	in [degree]	-0.58	-0.38	0.80	1.02	2.78	0.98	1.07	0.20	1.50	-0.22
roll std	in [degree]	1.30	0.58	0.43	0.58	0.47	0.60	0.55	0.57	0.52	0.67
horizonRange avg	in [m]	41.24	41.57	17.77	15.99	2 4.66	23.83	25.61	25.25	28.68	33.57
horizonRange std	in [m]	15.49	19.72	4.41	5.25	3.58	3.58	3.67	3.43	7.08	6.07
beamAngle avg	in [degree]	-1.54	-2.76	-20.12	-19.92	-3.49	-1.78	-2.83	-2.08	-2.81	-2.13
beamAngle std	in [degree]	5.39	5.30	9.99	10.04	9.89	2.69	3.41	1.32	4.45	1.75
pseudoAlt avg	in [m]	5.96	4.53	3.37	2.46	1.27	2.24	2.46	2.40	5.66	5.41
pseudoAlt std	in [m]	7.08	5.99	1.76	1.12	0.94	1.17	1.13	0.68	3.59	2.45
pseudoAltCorrected avg	in [m]	6.26	4.75	5.06	3.68	1.91	3.37	3.69	3.60	5.66	5.41

mission		115	116	120	122	133	134	138	139	140
surge avg	in $[\frac{m}{s}]$	1.13	1.17	1.19	1.19	0.95	1.25	1.04	1.09	1.00
mission length	in [km]	71.19	71.48	72.96	78.84	14.71	20.12	77.18	31.19	83.02
altMin avg	in [m]	11.02	2.87	3.85	3.43	7.06	4.60	6.35	5.21	7.37
altMin std	in [m]	1.24	0.23	0.18	0.27	0.48	0.41	1.92	1.92	5.30
riskMin	in %	0.00	0.05	0.00	0.01	0.00	0.00	0.00	0.00	0.00
risk	in %	0.00	0.03	0.00	0.00	0.00	0.00	0.00	0.00	0.00
success	in %	0.00	99.29	82.87	96.76	0.00	2.16	0.00	0.47	0.76
alt avg	in [m]	11.91	3.08	4.05	3.61	7.63	4.92	6.94	5.63	8.06
alt std	in [m]	1.39	8.06	0.20	0.28	0.54	0.46	2.30	2.11	5.85
depthError avg	in [m]	-1.68	-0.00	-0.12	-0.12	-0.23	-0.27	-0.29	-0.28	-0.46
depthError std	in [m]	6.07	1.13	1.50	0.58	1.05	1.70	15.36	2.00	2.68
pitch avg	in [degree]	-1.53	-1.43	-1.45	-1.33	-4.72	-3.34	-5.01	-4.06	-5.02
pitch std	in [degree]	5.78	1.50	1.99	1.65	1.63	2.76	2.99	2.24	3.27
roll avg	in [degree]	0.78	0.40	0.45	0.23	-1.86	-1.04	-1.33	-1.97	-1.90
roll std	in [degree]	0.40	0.24	0.22	0.21	0.38	0.45	0.53	0.49	0.49
horizonRange avg	in [m]	61.82	30.33	35.91	37.69	42.66	32.76	40.70	36.02	37.86
horizonRange std	in [m]	37.80	3.15	4.47	5.84	4.62	5.83	5.65	5.63	6.06
beamAngle avg	in [degree]	5.56	-0.83	-1.49	-0.43	-0.66	0.78	0.68	0.70	-0.55
beamAngle std	in [degree]	4.57	1.49	1.75	1.84	1.84	2.44	2.66	3.31	4.73
pseudoAlt avg	in [m]	5.78	4.50	3.26	2.72	3.27	2.11	2.33	2.15	2.75
pseudoAlt std	in [m]	6.35	1.57	0.76	0.91	1.01	1.43	1.78	2.28	3.14
pseudoAltCorrected avg	in [m]	5.78	4.50	3.26	3.63	4.36	4.22	5.44	5.02	6.42

Table F.2: Statistical analysis to get an overview of all Autosub missions.

Appendix G

Figures without permission to share digitally

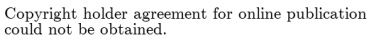

5.1m altitude

4.1m altitude

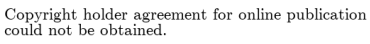

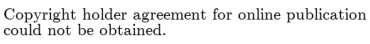

3.2m altitude

2m altitude

Figure G.1: Photos of Amperima (see fig. G.2, E) recorded at various altitudes. The photos were manually post-processed by researches for their analysis. Images collected as part of the AESA project.

Figure G.2: Examples of species recorded by Autosub6000 during RRS Discovery research cruises D377 & D378 as part of the AESA project. An analysis of the photographic survey is presented in [Morris et al., 2014].

Figure G.3: Two anemones that can be recognised in an image captured at approximately 2 m Altitude. Size of the anemone highlighted with the arrow is less than 2 cm. Image collected as part of the AESA project during research cruises D377 & D378.

Figure G.4: Multiple sonar transducers above a multibeam sonar, placed on the REDERMOR AUV for improved obstacle information at low computational cost, from [Quidu et al., 2007].

Glossary

actuator Electromechanical device changing the speed and direction of motion of the AUV or moving parts of the AUV relative to itself.

airfoil Cross section shape of an object that experiences flow of fluids like water and air, e.g. wings of airplanes or sternplanes of flight style underwater vehicles. The different speeds of the liquid over the surface induce forces on the object.

altitude Distance between the vehicle and the terrain, parallel to the heave direction in the vehicle fixed reference frame. Typically given relative to the position of the sensor on the vehicle that is measuring the altitude.

Autosub1 Torpedo shaped, flight style underwater vehicle, on which Autosub6000 is based. Hydrodynamic coefficients were obtained with a 3/4 scale model in a towing tank..

Autosub6000 5.5m long, torpedo shaped, flight style underwater vehicle. Autosub6000 has succesfully performed photographic surveys and this work is focused on better understanding and improving its terrain following performance.

benthic zone Region at the bottom of a lake or ocean.

bin Discretization unit of the sonar measurement. The time between emitting the sonar pulse and receiving the return signal indicates a distance. Since the continuous measurement of return signal has to be discretized for further processing, the wait time (sonar range) is split into a fixed number of bins.

bin length The distance equivalent of the measurement time of one bin of the sonar return.

blanking distance Short range from the origin of the sonar within which reverberations of the sonar device itself, and reflection inside the vehicle cause a high levels of noise. Usually the measurements within the blanking distance is ignored in the further analysis of the sonar returns.

Centre of Buoyancy The point where the sum of all buoyant forces act. Usually volumetric centre of the submerged part of the vehicle. In case of a fully submerged vehicle, the centre of volume of the vehicle.

Centre of Gravity The point where the sum of all graviational foces act.

collision distance Shortest distance between the bounding box containing the vehicle and the terrain.

cruising AUVs Common alternative description for flight style AUVs.

Delphin2 1.96 m long, torpedo shaped, flight style underwater vehicle, based on the design of Autosub6000. Used for experiments in lakes and test tanks..

depth Distance to the water surface (or, in case of the simulations, a freely defined reference zero depth), measured parallel to the z-axis of the global reference frame.

flight style Attribute describbting underwater vehicles that typically use only one thruster, for generating forwards motion, and rely on sternplanes for changing depth and heading. Similar to airplanes, the vehicles have to maintain a forwards speed to be able to dive and control their motion. This speed is typically around 1 m/s.

grazing angle Angle between the sonar beam and the seabed from where it is reflected.

heave Axis in the vehicle fixed coordinate frame, positive heave direction is the downwards direction of the vehicle.

horizon tracking Following the horizon with the sonar beam angle, or following the height of the horizon with a vehicle by adjusting the altitude control based on the horizon height.

hover capable Attribute describing underwater vehicles that are equipped with sufficient thrusters to hover in a fixes position and manouevre at slow speeds.

pitch Rotation around the sway axis in the vehicle fixed coordinate frame. A positive pitch angle moves the AUV towards the water surface, in the negative heave direction.

pseudo altitude Distance parallel to the heave direction, measuring the height of the horizon in the vehicle fixed coordinate frame.

roll Rotation around the surge direction in the vehicle fixed coordinate frame. Neglected for the vertical plane considerations.

sector scan period The time (or x-progress) for one full scan between the sonar angle maximum and minimum limits (e.g. from the maximum angle to the minimum angle and back again).

sector scan time The time required by the mechanical scanning sonar to perform a full scan from the maximum angle limit to the minimum angle limit and back again.

sheet laser A laser source combined with optical grids or lenses to project a line shape or grid, rather than a single focused beam.

sternplanes Movable surfaces that have airfoils shaped cross sections, used to control vehicle motion in the vertical and horizontal plane.

surge Axis in the vehicle fixed coordinate frame, positive surge direction is the forwards direction of the vehicle.

sway Axis in the vehicle fixed coordinate frame, positive sway direction is the starboard direction of the vehicle. Neglected for the vertical plane considerations.

terrain Term used in vehicle operations describing the lake bed or sea bed the vehicle is navigating over.

terrain detection Detecting the shape of the terrain ahead of the vehicle with a sensor, in this thesis typically a mechanical scanning sonar.

terrain tracking Following the outline of the terrain closely with a vehicle by keeping a constant altitude.

yaw Rotation around the heave direction of the vehicle fixed coordinate frame. Neglected for the vertical plane considerations.